Measurement of Jet Cross Sections in $D^{*\pm}$ Photoproduction at HERA

Takanori Kohno

Department of Physics, University of Tokyo
7-3-1 Hongo, Bunkyo-ku, Tokyo 113-0033 Japan

A thesis submitted in partial fulfillment
of the requirements
for the doctor's degree of science

December 19, 2003

Abstract

Inclusive jet cross sections in $D^{*\pm}$ photoproduction at HERA has been measured in photon-proton center of mass energy from 130 GeV to 280 GeV. The analysis is based on the integrated luminosity of 78.6 pb^{-1} taken by the ZEUS detector. $D^{*\pm}$ was measured in the kinematic region $p_T(D^*) > 3$ GeV/c and $|\eta(D^*)| < 1.5$. Jet cross sections have been measured with the aim to have better correspondence between the observable (jet) and the outgoing parton, and also to extend the measurement towards the proton direction. Differential cross sections as a function of the transverse energy (E_T^{jet}) and the pseudo-rapidity (η^{jet}) of jets were measured in the range $E_T^{jet} > 6$ GeV and $-1.5 < \eta^{jet} < 2.4$. The η^{jet} cross sections are reasonably described by the next-to-leading order (NLO) QCD calculation corrected for hadronization effect. The measured cross sections are larger than the NLO QCD predictions, but agrees within the theoretical uncertainty except for the highest measured E_T^{jet} where an excess of 3σ is observed. At high E_T^{jet}, by studying the ratio of the transverse momentum of the D^* to its matching jet, $p_T(D^*)/E_T^{jet}$, it is found that the excess is related to relatively low $p_T(D^*)$ than expected from the fragmentation function of the D^* which indicates the contribution from a secondary charm production in photoproduction at HERA.

Contents

Chapter 1

Introduction

It has been known since some time that fundamental particles in this world are the *quarks*, the *leptons* and the *gauge bosons* [1]. The interaction between the quarks and the leptons is mediated by the gauge bosons. There are six quarks : *up* (u), *down* (d), *strange* (s), *charm* (c), *bottom* (b) and *top* (t), where they become heavier in this order. However, these quarks are not directly observable and they are confined inside hadrons (mesons; a bound state of quark anti-quark pair, and baryons; a bound state of three quarks).

The matter which we are familiar with in the everyday life consists of u and d quarks which are the lightest two quarks. Bound states involving other four quarks have very short lifetimes so that they decay into u or d quarks and do not exist as stable particles. Although the heavier quarks decay into lighter quarks by the weak interaction, from the point of view of the strong interaction, all quarks behave similarly except for their mass differences. The gauge boson of the strong interaction, the *gluon*, couples in exactly the same way to all flavors of quarks in the context of *Quantum Chromodynamics* (QCD), the theory of strong interaction. This enables the production of heavy quarks from light quarks, e.g. $u\bar{u} \to g \to c\bar{c}$.

Based on the QCD, the interaction of high energy hadron collision in general, i.e. not restricting to heavy quark production, can be explained as a collision between the constituents of the hadrons (*partons*). The perturbation theory becomes applicable to QCD at high energy due to the property of *asymptotic freedom* [2, 3]. The QCD coupling constant α_S is *running* as it becomes smaller at higher energies. In the framework of QCD, the cross section of hadron-hadron collision is calculated as a convolution of parton densities inside hadrons and the parton-parton cross section which can be calculated by QCD perturbatively. The study based on perturbative analysis of QCD is often called *perturbative QCD* (pQCD) [4]. Usually, the hard scale in hadron-hadron collision is provided by the transverse momentum of out-going partons. Parton densities of hadrons are not calculable by pQCD and they must be measured experimentally. However, if pQCD is the proper framework to describe high energy hadron collisions, parton density functions

(PDFs) can be used for any calculation as they are universal. The PDFs of the proton has been determined precisely from the data of electron-proton deep inelastic scattering (DIS) measured by H1 and ZEUS collaborations, in a wide kinematic region.

It is expected that the heavy quark production[1] can be also explained by QCD, similarly to processes involving light quarks. In this case, the mass of the heavy quark, m_Q provides an additional hard scale for the pQCD calculation. Therefore, the heavy quark production in hadron interaction can be used to test pQCD with an additional hard scale m_Q. Also, as the heavy quark is not the major constituents of stable hadrons, its production becomes sensitive to the gluon density in the hadron. This means that it can be used to obtain further information about the gluon density, which is not constrained precisely compared to light quark densities.

The measurements of heavy quark production in hadron interaction have been performed at various fixed target and collider experiments with various CM energies. From these studies, it was found that measurements at collider experiments overshoot the pQCD prediction by several factors. Discrepancies were found to be larger in b production. Cross sections of B meson production in $p\bar{p}$ collisions measured by CDF [7] and D0 [8] experiments were underestimated by the pQCD predictions by a factor of $2-3$. The cross section of $\gamma\gamma \to b\bar{b}$ measured at LEP [9, 10] also showed an excess of the measurement by a factor of 3

Recently, photoproduction of D^* meson ($\gamma p \to D^* + X$) had been studied at HERA and showed deviation to the NLO QCD calculation, in particular in the proton direction [14]. The measured cross section became significantly larger than theoretical prediction for low transverse momentum and for positive pseudo-rapidity. Also the D^* production in DIS by ZEUS [15] indicated that the interaction between D^* and the proton remnant may change the pseudo-rapidity distribution such that the distribution gets shifted into the proton direction.

In this study, in order to reduce soft hadronization effect and make better comparison with pQCD predictions, it is proposed to measure jet cross section for the events containing a D^* ($\gamma p \to D^* + jets + X$). A jet consists of a group of particles created by the fragmentation of the parton which are well collimated around the direction of the original parton. By reconstructing a jet, all particles fragmenting from the original parton are measured, so it is less dependent on the fragmentation process. Jets are expected to have better correspondence to the outgoing partons.

There is also another benefit to study jets in D^* events, practical side. Since the D^* is identified by reconstructing the invariant mass with the tracking information, the measured kinematic region is limited to the central region. On the other hand, jets can be measured by the calorimeter in wider kinematic region. Especially, it is interesting to extend the measurement of particle distritubion towards the proton direction, where the

[1] Hearafter, by heavy quarks, we only consider c and b quarks

discrepancy between the measured D^* cross section and the NLO QCD prediction seems to be larger.

Jet cross sections are measured as a function of the transverse momentum E_T^{jet} and the pseudo-rapidity of the jet (η^{jet}). The theoretical prediction of the measurement, has been obtained based on the NLO calculation done in the massive scheme, with applying all selection cuts used in the experiment. The effect of the hadronization process was studied using MC simulation to correct the theoretical calculation to hadron level. Measured cross sections are compared to the NLO QCD prediction.

In the next chapter, theoretical overview of the heavy quark production in hadronic interaction and the experimental studies performed are given. In chapter 3, the experimental setup with which the measurement had been performed, is explained. In chapter 4, Monte Carlo (MC) simulations used in the analysis is explained. The reconstruction of the measured quantities and the event selection are described in chapter 5. The properties of the selected events and the comparison with MC are shown in chapter 6. Chapter 7 explains the unfolding method to obtain the cross section and the systematic uncertainties. Results are presented in chapter 8 compared to NLO QCD predicitions. The analysis presented in chapter 6, 7 and 8 are the main contribution of the author. Summary and conclusion are given in chapter 9.

Chapter 2

Heavy quark production in hadronic interactions

In this chapter, we introduce the kinematics of ep collision and give an overview of a general ep scattering. The concept of parton density functions and factorization are reviewed. In section 2.4, the heavy quark production mechanism in hadronic interaction is explained. Experimental results on heavy quark production in hadronic collisions are reviewed in section 2.5. In the last section, the measurement performed in this analysis and the aim of the analysis are presented.

2.1 Kinematics of ep scattering

In this section, kinematic variables used in this analysis are introduced. The electron[1] and proton deep inelastic scattering (DIS) is a process where an electron scatters off a proton and the proton becomes a hadronic system X.

$$e(k) + P(p) \rightarrow e'(k') + X. \tag{2.1}$$

The 4-momenta of particles are indicated by the characters in the parentheses. In the quark parton model, DIS is interpreted as a process in which the photon emitted from the electron scatters off a parton inside the proton. Figure 2.1 shows a schematic diagram of this process. The 4-momentum of the photon emmited from the incoming electron is given by $q = k - k'$.

The center of mass energy of the electron and the proton, s is given by

$$s = (p + k)^2. \tag{2.2}$$

[1]The term electron is used for both electron and positron.

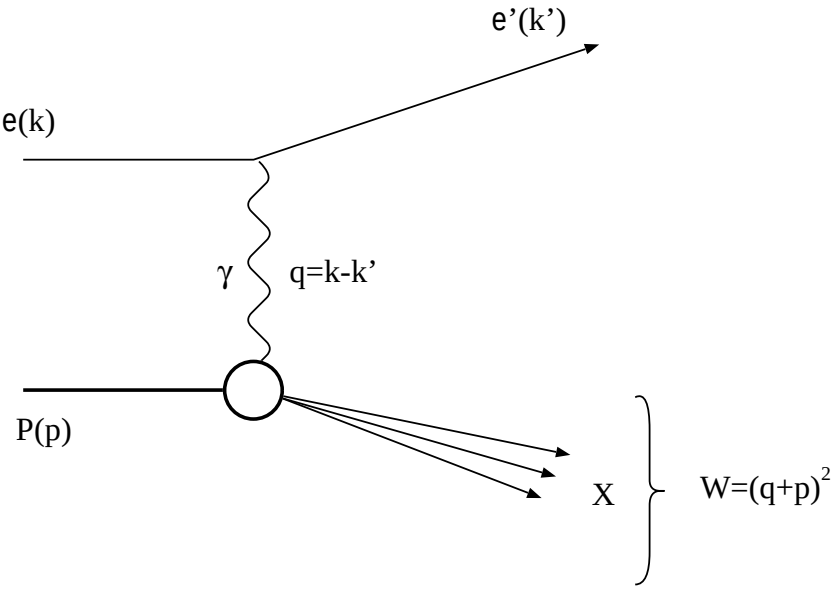

Figure 2.1: A diagram of a general NC event.

The negative mass squared of the virtual photon is written as Q^2, which is given by

$$Q^2 = -q^2 = -(k - k')^2. \tag{2.3}$$

Q^2 represents the energy scale which the proton is probed at.

The Bjorken scaling variable x and another dimensionless variable y is defined as

$$x = \frac{Q^2}{2p \cdot q}, \tag{2.4}$$

$$y = \frac{p \cdot q}{p \cdot k}. \tag{2.5}$$

In the naive quark parton model (QPM), x represents the fractional momentum of the proton carried by the quark struck by the virtual photon. In the proton rest frame, the four momentum of the proton can be expressed as $p = (m_p, 0, 0, 0)$ where m_p represents the proton mass, thus y can be written as $y = (E_e - E'_e)/E_e$. In this frame, y represents the fraction of energy transfered to the exchanged photon with respect to the energy of the incoming electron. Since $s = (p + k)^2 = m_p^2 + Q^2/xy + m_e^2$, by neglecting the proton mass m_p and the electron mass m_e, Q^2, x and y are related to each other by

$$Q^2 \simeq sxy. \tag{2.6}$$

hence only two of these variables are independent.

The invariant mass of the exchanged photon and the proton W is given by

$$W^2 = (p+q)^2 = m_p^2 + sy - Q^2 \quad (2.7)$$
$$\simeq sy - Q^2. \quad (2.8)$$

In the kinematic range relevant to this study ($Q^2 < 1$ GeV^2), only the first term in the last equality becomes dominant. Therefore, W can be written as

$$W = \sqrt{s \cdot y}. \quad (2.9)$$

The energy transfer of the electron in the proton rest frame, ν is defined as

$$\nu = \frac{p \cdot q}{m_p} \quad (2.10)$$

We also use variable called *pseudo-rapidity* (denoted as η), which is defined using the polar angle θ as

$$\eta = -\ln(\tan(\theta/2)). \quad (2.11)$$

It is identical to *rapidity* ($y = 1/2 \cdot \ln((E - p_z)/(E + p_z))$) for a massless particle.

2.2 DIS cross section and structure functions

The DIS cross section can be written as

$$\frac{d^2\sigma}{dxdy} \propto L_{\alpha\beta} W^{\alpha\beta}, \quad (2.12)$$

where $L_{\alpha\beta}$ and $W^{\alpha\beta}$ are the leptonic and hadronic tensor, respectively. The leptonic tensor can be calculated by *quantum electrodynamics* (QED) which gives

$$L_{\alpha\beta} = 4e^2(k_\alpha k'_\beta + k_\beta k'_\alpha - g_{\alpha\beta} k \cdot k'). \quad (2.13)$$

Although the exact form of the hadronic tensor depends on the structure of the proton, a general expression of $W^{\alpha\beta}$ is given, by using two functions W_1 and W_2, as

$$W^{\alpha\beta}(p,q) = \left(g^{\alpha\beta} - \frac{q^\alpha q^\beta}{q^2}\right) W_1(x,Q^2) + \left(p^\alpha + \frac{1}{2x}q^\alpha\right)\left(p^\beta + \frac{1}{2x}q^\beta\right) W_2(x,Q^2). \quad (2.14)$$

All information about the structure of the proton is contained in the functions W_1 and W_2. It is common to redefine the functions W_1 and W_2 as

$$F_1(x,Q^2) = W_1(x,Q^2), \quad (2.15)$$
$$F_2(x,Q^2) = \nu W_2(x,Q^2). \quad (2.16)$$

Then, taking into account the overall normalization factor, the DIS cross section is given by

$$\frac{d^2\sigma}{dxdQ^2} = \frac{4\pi\alpha^2}{Q^4}\left[\left\{1+(1-y)^2\right\}F_1(x,Q^2) + \frac{1-y}{y}\left(F_2(x,Q^2) - 2xF_1(x,Q^2)\right)\right]. \quad (2.17)$$

The functions $F_1(x,Q^2)$ and $F_2(x,Q^2)$ are called *structure functions*.

In QPM, structure functions are related to parton density functions (PDF), $f_q(x,Q^2)$ by

$$F_2(x,Q^2) = \sum_{q,\bar{q}} e_q^2 x f_q(x), \quad (2.18)$$

$$2xF_1(x,Q^2) = 2xF_2(x,Q^2). \quad (2.19)$$

The PDF describes the probability to find a parton q inside a proton with a fractional momentum x. In the naive QPM, the structure function is only a function of x and does not depend on Q^2. However, as we will see in the next section, once we take into account QCD effects (gluon radiation from quarks and gluon splitting into $q\bar{q}$ pair), it depends on Q^2 and the evolution of stucture function with respect to Q^2 is calculable by pQCD.

2.3 Photoproduction

Electron-proton collision at very low Q^2 ($\simeq 0$) can be regarded as a collision between a real photon and a proton. Therefore this process is called *photoproduction*.

Theoretical calculation of photoproduction in ep scattering is based on the *Weizsäcker-Williams* or *Equivalent Photon Approximation* (EPA) [16]. In this approximation, the ep cross section is factorized into the photon spectrum in the electron and the γp cross section as

$$d\sigma(ep \to X) = \int_0^1 dy f_{\gamma/e}(y) d\sigma(\gamma p \to X). \quad (2.20)$$

In eq. (2.20), the variable y represents the fraction of momentum carried by the photon with respect to the electron ($= (E_e - E'_e)/E_e$), which corresponds to y defined in eq. (2.5) as discussed in the previous chapter. The function $f_{\gamma/e}(y)$ is calculable in QED and is given by

$$f_{\gamma/e}(y) = \frac{\alpha}{2\pi}\left[\frac{1+(1-y)^2}{y}\ln\frac{Q^2_{max}}{Q^2_{min}} + 2m_e^2 y\left(\frac{1}{Q^2_{min}} - \frac{1}{Q^2_{max}}\right)\right], \quad (2.21)$$

where α and m_e are the electomagnetic coupling constant and the mass of the electron, respectively. Q^2_{min} and Q^2_{max} are the minimum and maximum Q^2 allowed which are given

by

$$Q^2_{min} = \frac{m_e^2 y^2}{1-y}, \tag{2.22}$$

$$Q^2_{max} = 1 \text{ GeV}^2. \tag{2.23}$$

In order to calculate the cross section of eq. (2.20), we must also know the form of the γp cross section. A proton is known to have a substructure in forms of quarks and gluons). In the QPM, the γp scattering can be interpreted as a scattering of the photon off partons in the proton.

The parton level cross section can be calculated by pQCD for *hard* photoproduction, where the term *hard* indicates that the process involves a certain energy scale which is larger than the QCD scale ($\Lambda_{QCD} \simeq 200$ MeV). Due to the property of asymptotic freedom, given a hard energy scale, the process is calculable perturbatively. In case of hard photoproduction, the hard scale is provided by the transverse momentum, p_T of outgoing partons.

The γp cross section can be written down as a convolution of the perturbatively calculable cross section $\sigma(\gamma q \to X)$ and the non-perturbative PDF as

$$d\sigma(\gamma p \to X) = \sum \int_0^1 dx_p f_{q/p}(x_p, \mu_F) d\sigma(\gamma q \to X) \tag{2.24}$$

where $f_{q/p}(x_p, \mu_F)$ is the PDF when probed at a scale μ_F (*factorization scale*).

Eq. (2.24) is not the only contribution to the γp cross section. It is known that a photon reveals its hadronic structure when probed at a hard scale. This hadronic contribution is called *resolved photon process*, while the contribution from a point-like photon is called *direct photon process*. Taking into accout the resolved photon process, the cross section can be written as

$$d\sigma(\gamma p \to X) = \sum_{q_1, q_2} \int dx_\gamma \int dx_p f_{q_1/\gamma}(x_\gamma, \mu_F) f_{q_2/p}(x_p, \mu_F) d\sigma(q_1 q_2 \to X) \tag{2.25}$$

where $f_{q_1/\gamma}(x_\gamma, \mu_F)$ is the PDF of the photon which descibes the probability of finding a parton q_1 within a photon with a fractional momentum x_γ when probed at a scale μ_F. Figure 2.2 shows examples of Feynmann diagrams in direct and resolved processes.

2.3.1 QCD evolution equation

The Q^2 evolution of the structure function is determined by the parton processes. Let us consider the contribution of the gluon radiation process $q \to qg$ where the parent quark has fractional momentum ξ of the proton. After emitting a gluon, the fractional momentum of the proton carried by the quark becomes x ($x < \xi$) with a non-zero transverse momentum.

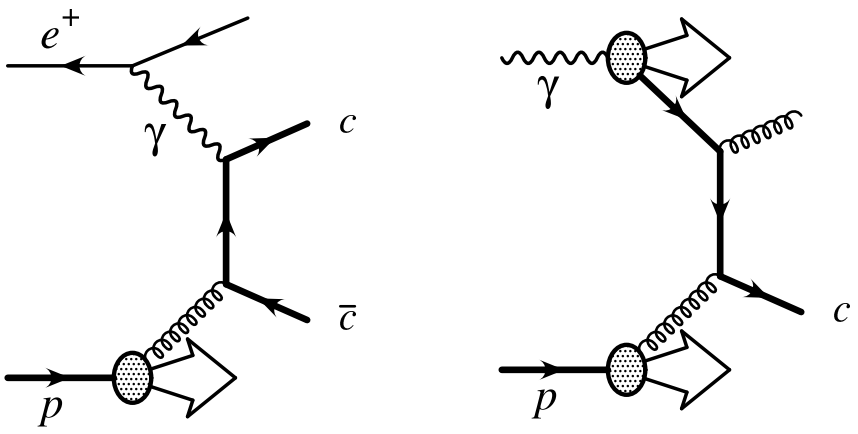

Figure 2.2: Feynman diagram of direct photon process (left) and resolved photon process (right).

The maximum transverse momentum which the quark can obtain is limitted by Q^2 since $(k+q)^2$ is massless. This means that, the density of the quark which interact with the photon is a sum of the original distribution $q_0(x)$ and the contribution from quarks with larger fractional momentum $\xi > x$ which radiates gluons. The result of the $\mathcal{O}(\alpha_S)$ calculation is given by

$$q(x,\mu^2) = q_0(x) + \frac{\alpha_S}{2\pi}\int_x^1 \frac{d\xi}{\xi} q_0(\xi)\left\{P\left(\frac{x}{\xi}\right)\ln\frac{\mu^2}{\kappa^2} + C\left(\frac{x}{\xi}\right)\right\} \tag{2.26}$$

where $C(x)$ is a calculable finite function. κ^2 is an *ad hoc* cut off introduced to regularize the expression. The μ is the factorization scale. $P(x/\xi)$ is known as the *splitting function* which is given by

$$P(z) = C_F\frac{1+z^2}{1-z} \tag{2.27}$$

Thus PDF becomes dependent to the factorization scale after including higher order QCD effects.

Up to now we have only considered the effect of gluon radiation from a quark. Taking into account other QCD processes, such as gluon splitting into $q\bar{q}$ pair, QCD predicts the scale dependence of the PDF as

$$\frac{dq(x,\mu^2)}{d\ln(\mu)} = \frac{\alpha_S}{2\pi}\sum_{q,\bar{q}}\int_x^1 \frac{d\xi}{\xi}P_{qq}\left(\frac{x}{\xi}\right)q(\xi,\mu^2) + \int_x^1\frac{d\xi}{\xi}P_{qg}\left(\frac{x}{\xi}\right)g(\xi,\mu^2), \tag{2.28}$$

$$\frac{dg(x,\mu^2)}{d\ln(\mu)} = \frac{\alpha_S}{2\pi}\sum_{q,\bar{q}}\int_x^1 \frac{d\xi}{\xi}P_{gq}\left(\frac{x}{\xi}\right)q(\xi,\mu^2) + \int_x^1\frac{d\xi}{\xi}P_{gg}\left(\frac{x}{\xi}\right)g(\xi,\mu^2). \tag{2.29}$$

where $q(x,\mu^2)$ and $g(x,\mu^2)$ are the quark and gluon PDFs. This is known as the DGLAP equation or the evolution equation [17]. The splitting functions are given as follows at

$\mathcal{O}(\alpha_S)$.

$$P_{qq}(z) = \frac{4}{3}\left[\frac{1+z^2}{1-z} + \frac{3}{2}\delta(1-z)\right] \quad (2.30)$$

$$P_{qg}(z) = \frac{z^2+(1-z)^2}{2} \quad (2.31)$$

$$P_{gq}(z) = \frac{4}{3}\left[\frac{1+(1-z)^2}{z}\right] \quad (2.32)$$

$$P_{gg}(z) = 6\left[\frac{z}{1-z} + \frac{1-z}{z} + z(1-z)\right] + \left(\frac{11}{2} - \frac{n_f}{3}\right)\delta(1-z) \quad (2.33)$$

where n_f denotes the number of quark flavors. Given the PDF at a certain scale Q_0^2, the PDF at different Q^2 can be calculable by the DGLAP equation.

The QCD evolution equation also applies to the photon PDFs. However, there is another contribution to the photon PDF, due to the direct coupling of the photon to $q\bar{q}$ pair $\gamma \to q\bar{q}$. The evolution equation is modified as

$$\frac{dq(x,\mu^2)}{d\ln(\mu)} = \frac{\alpha}{2\pi}P_{\gamma q}(x) + \frac{\alpha_S}{2\pi}\sum_{q,\bar{q}}\int_x^1 \frac{d\xi}{\xi}P_{qq}\left(\frac{x}{\xi}\right)q(\xi,\mu^2) + \int_x^1 \frac{d\xi}{\xi}P_{qg}\left(\frac{x}{\xi}\right)g(\xi,\mu^2) \quad (2.34)$$

$$\frac{dg(x,\mu^2)}{d\ln(\mu)} = \frac{\alpha}{2\pi}P_{\gamma q}(x) + \frac{\alpha_S}{2\pi}\sum_{q,\bar{q}}\int_x^1 \frac{d\xi}{\xi}P_{gq}\left(\frac{x}{\xi}\right)q(\xi,\mu^2) + \int_x^1 \frac{d\xi}{\xi}P_{gg}\left(\frac{x}{\xi}\right)g(\xi,\mu^2) \quad (2.35)$$

Measurements of the structure function has been carried out in wide kinematic region, by various experiments including fixed target and H1 and ZEUS at HERA. The structure function is well fitted by the DGLAP equation, from which the PDF of the proton has been extracted. There are several groups performing the global fit and various PDFs are available [18].

The photon structure function has been measured at e^+e^- scattering where the photon emitted from the electron (or positron) is probed by the photon emitted by the positron (or electron) with high virtuality. Various PDFs of the photon are also available [19, 20].

2.4 Photoproduction of heavy quarks

The cross section of photoproduction process with high transverse energy (E_T) jets is calculable in the framework of pQCD as described in the previous section. Here we consider the case in which a heavy quark (c or b) is produced. In this case, an additional energy scale is provided by the mass of the heavy quark, m_c ($\simeq$ 1.5 GeV/c^2) or m_b ($\simeq$ 5 GeV/c^2). Due to its large mass of the heavy quark, there are two approaches to the theoretical calculation of heavy quark production. Here we explain these approaches breifly for charm production.

In the massive scheme, the mass of the charm quark is kept finite in the calculation of the matrix element and only light quarks (u, d and s) and gluons are considered as active flavors in the proton and the photon. Therefore, charm is only produced dynamically, i.e. only appears in the final state. The leading order contributions are given by

$$\gamma g \to c\bar{c}, \tag{2.36}$$

$$gg \to c\bar{c}, q\bar{q} \to c\bar{c}. \tag{2.37}$$

The process in eq. (2.36) is called the *boson-gluon fusion* (BGF) which is the dominant process contributing to charm production in direct photon process. The left diagram in figure 2.2 shows the diagram of BGF.

At low p_T, this approach is expected to provide reliable calculation since it is reasonable to neglect the PDF of the charm quark. The finite mass of the charm quark introduces a natural cut off for the divergence arising from the collinear emission of gluon from the charm quark as $\ln(p_T^2/m_c^2)$. However, this term becomes significantly large at $p_T \gg m_c$, thus spoiling the perturbative calculation. It is not clear where the term becomes non-negligible, however, it is expected at 20-25 GeV [21].

The other approach, the massless scheme, set the charm quark to be massless and considers charm as an active flavor in the hadrons. The scheme is expected to be reliable at $p_T \gg m_c$, since the mass of the charm becomes less important and it becomes natural to consider the light flavors and the charm in a smililar manner. The divergent term $\ln(p_T^2/\mu^2)$ is absorbed in the PDF of the charm quark, as usually done for light flavors. In this approach a flavor excitation process $cg \to cg$ also contribute to the cross section.

These two approaches do not make much difference for the physical cross section [21], although the contribution from direct and resolved processes differ in the two approaches.

2.4.1 Next-to-leading order program FMNR

The next-to-leading order (NLO) QCD calculation of charm photoproduction used in this analysis was developed by Frixione et al [5]. The calculation is based on the massive scheme. The FORTRAN code implementing this calculation is available from the authors (S. Frixione, M. Magano, P. Nason and G. Ridolfi) [22, 23]. Taking the initial letters of the authors, we call this program FMNR. This calculation includes the parton level processes summarized in table 2.1.

Figure 2.3 shows the LO diagrams calculated in FMNR. Figure 2.4 shows some examples of diagrams at NLO, involved in the direct process. Figure 2.4 (a) shows an example of the virtual correction, which involves a loop integral. Figure 2.4 (b)-(d) show examples of real corrections. Although the FMNR does not explicitly consider the charm PDF in the photon, a diagram like the one shown in figure 2.4 (b),(c) partially include this effect. The definition of direct and resolved process depends order-by-order in perturbative

direct process		
LO	NLO	
$\gamma g \to c\bar{c}$	virtual correction	$\gamma g \to c\bar{c}$
	real correction	$\gamma g \to c\bar{c}g$ $\gamma q \to c\bar{c}q$
resolved process		
LO	NLO	
$gg \to c\bar{c}$ $q\bar{q} \to c\bar{c}$	virtual correction	$gg \to c\bar{c}$ $q\bar{q} \to c\bar{c}$
	real correction	$gg \to c\bar{c}g$ $q\bar{q} \to c\bar{c}q$ $qg \to c\bar{c}q$ $\bar{q}g \to c\bar{c}\bar{q}$

Table 2.1: Parton level processes included in FMNR.

calculation.

The FMNR is implemented as a "parton" event generator available in FORTRAN code [22, 23]. The calculation is performed in such a way that the cancellation of soft and collinear singularities takes place under the integral sign. This enables us to apply various cuts performed in the experiment, thus allowing the calculation of jet cross sections.

2.4.2 Fragmentation of a heavy quark

In theoretical calculation, cross section is calculated for the production of partons. However, in experiments, partons are not direct observables due to color confinement. Partons are observed in the form of colorless hadrons which are produced after the *fragmentation* or the *hadronization* process.

A hadron which contains a heavy quark has a large fractional momentum of the parent quark. The fragmentation of heavy quarks are called to be hard in this sense. In order to model the momentum distribution of the meson from c or b quark, the *fragmentation function* is used. The fragmentation function is a phenomenological function which are obtained by a fit to experimental data of the fractional momentum carried by the hadron with respect to the parent quark (denoted by z in eq. (2.38). One of the commonly used function, the Peterson function [24] is given by

$$f(z) = \frac{1}{z\left(1 - \frac{1}{z} - \frac{\epsilon}{1-z}\right)^2}. \tag{2.38}$$

The parameter ϵ is obtained by fitting the Peterson function to the fragmentation func-

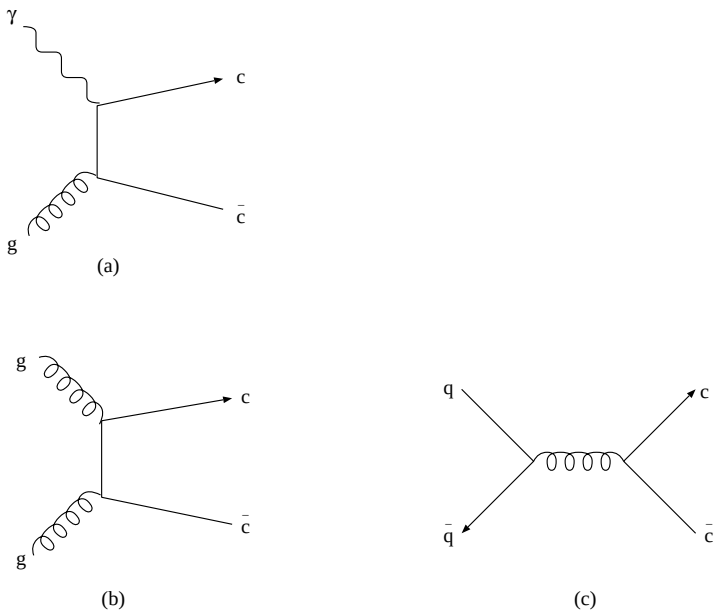

Figure 2.3: Examples of LO diagrams of charm production.

tion measured by experiments. In the theoretical calculation used in this analysis, the ϵ parameter has been set to 0.035 which was obtained by an NLO fit [25] to ARGUS data [26].

2.5 Experimental results on heavy quark production

Experimental studies of heavy quark production has been performed in various experiments. In high energy collider experiments such as LEP, Tevatron and HERA, it is generally observed that, the theoretical calculation underestimates the measurement. The discrepancy between the measurement and the calculation is larger for b production where a factor of 2-3 difference of B meson production has been reported by CDF [7] and D0 [8] experiments. Two photon collision at LEP experiment also show an excess of data by a factor of 3 for the total cross section of $e^+e^- \to e^+e^- b\bar{b}$ [9, 10].

Charm production shows better agreement between the data and the NLO QCD calculations. For example, the total cross section of $e^+e^- \to e^+e^- c\bar{c}$ reported by LEP experiments [11, 12, 13] show a general agreement although the large theoretical uncertainty. However, a trend of the measured cross sections being larger than theoretical prediction is also observed in several experiments.

Charm production in DIS has been studied by both H1 [27] and ZEUS collaborations [15]. They showed a good agreement to theoretical prediction showing that the dominant

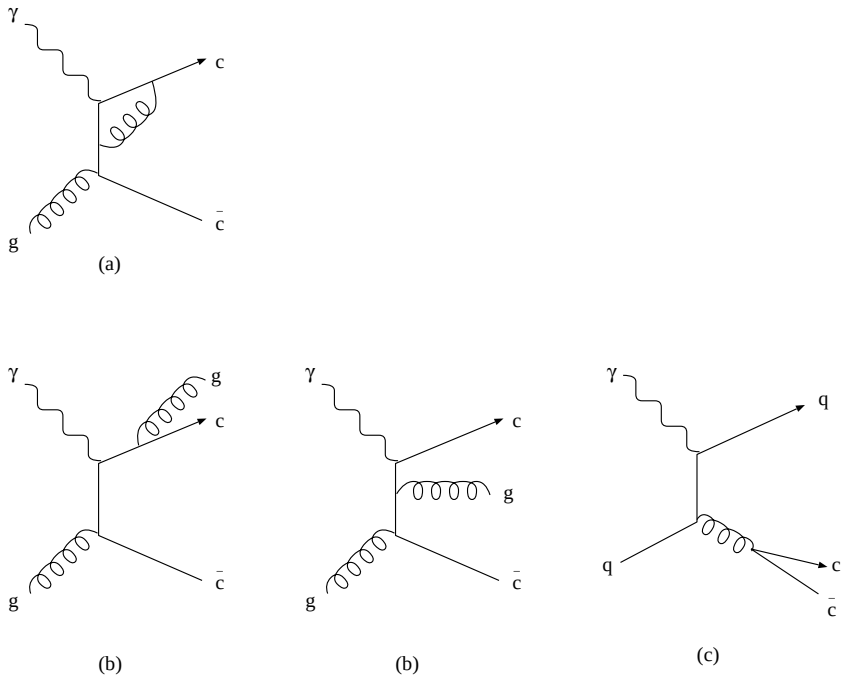

Figure 2.4: Examples of diagrams involved in NLO correction for direct photon process. Virtual correction to BGF diagram (a), and real corrections (b) and (c). are shown.

process in charm production is the BGF process. On the other hand, charm production in photoproduction was also studied at HERA [28, 29], and some discrepancies were observed, which are shown in the next section.

2.5.1 $D^{*\pm}$ photoproduction at ZEUS

Several measurements have been done on D^* photoproduction at HERA. Here we summarize the results of two recent measurements performed by ZEUS Collaboration.

Inclusive D^* cross section in photoproduction

Measurements of differential cross sections of D^* meson in the photoproduction regime have been performed by ZEUS Collaboration [14]. The measurement was performed in the kinematic region of $Q^2 < 1$ GeV^2 and $130 < W < 300$ GeV with the D^* selected in $|\eta(D^*)| < 1.6$ and $p_T(D^*) > 1.9$ GeV/c. The measurement was compared to massive scheme NLO calculation and massless scheme fixed order next-to-leading-log (FONLL) calculation [30]. Cross sections as a function of the pseudo-rapidity of the D^*, $\eta(D^*)$ in bins of $p_T(D^*)$ are shown in figure 2.5, where positive η is the direction of the proton.

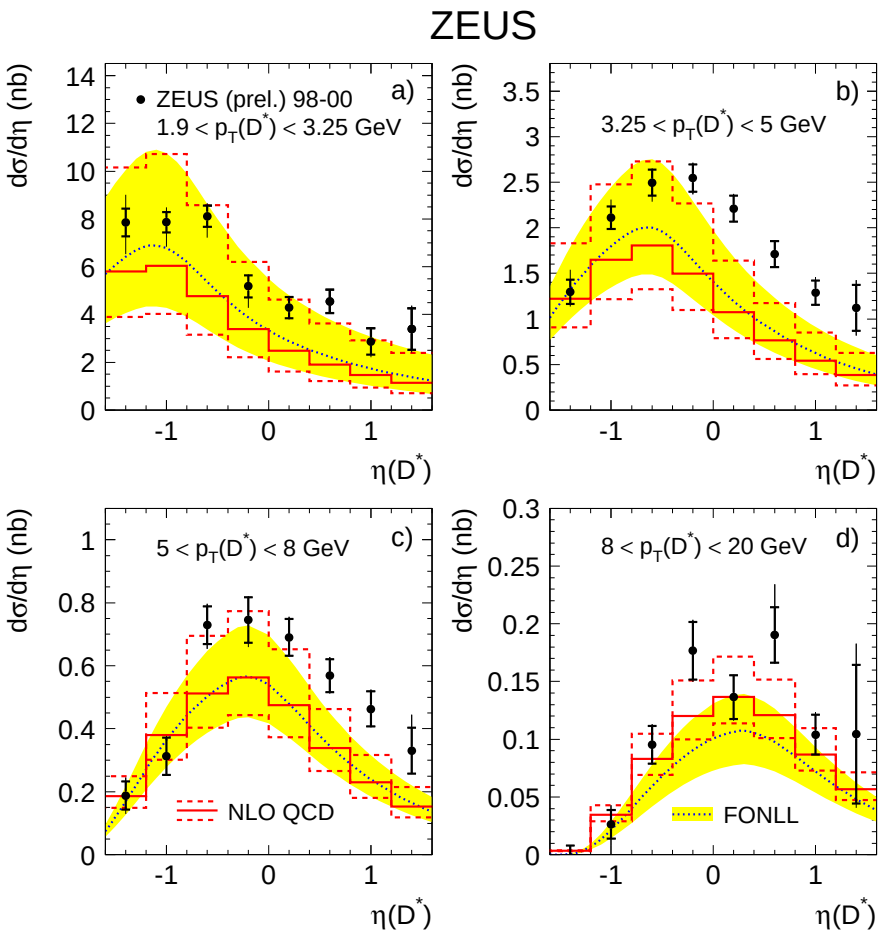

Figure 2.5: Differential cross section of D^* photoproduction with respect to $\eta(D^*)$ measured by ZEUS Collaboration. Measured cross sections (dots) are compared to the NLO calculation (solid histograms) with its uncertainty shown as dashed histograms, and to the FONLL predictions (dotted curves and shaded bands).

The black dotted lines with the yellow bands show the prediction of the FONLL calculation and its errors, while the red thick solid lines and the dashed lines show the prediction of the NLO calculation and its errors. The calculations have large errors originating from the scale uncertainty but both of them underestimate the cross section in almost the whole kinematic region. In particular, the disagreement becomes large at medium $p_T(D^*)$ values and large $\eta(D^*)$ region (figure 2.5 b)).

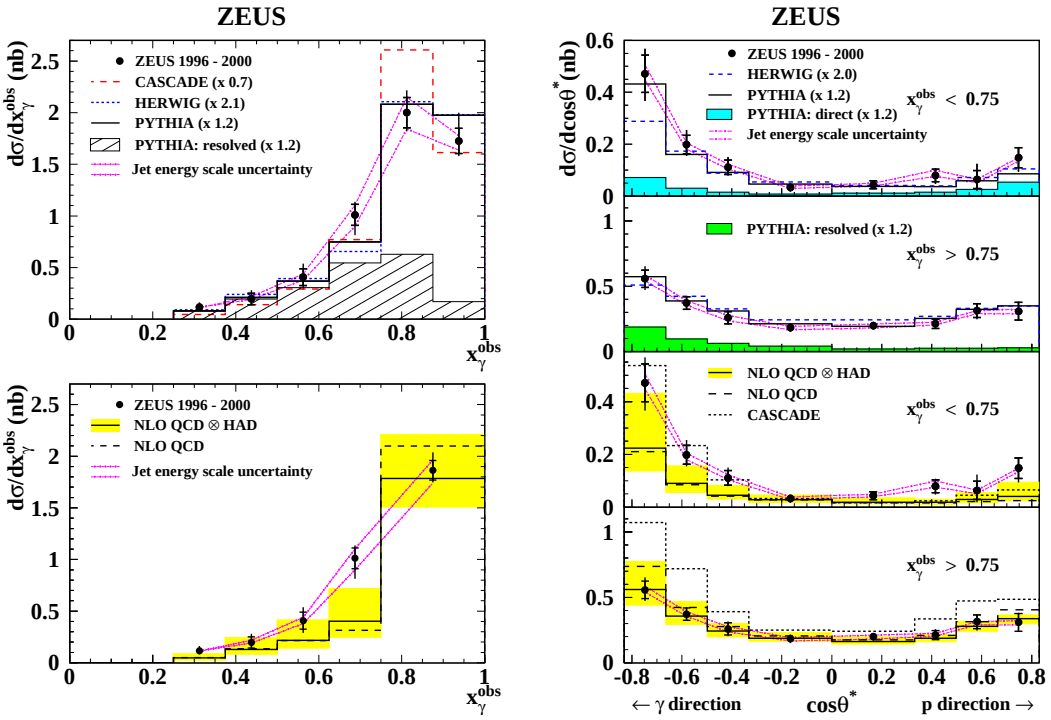

Figure 2.6: Differential cross sections of dijet events in D^* photoproduction with respect to x_γ^{OBS} (left) and $\cos\theta^*$ (right) as measured by ZEUS. The measurement is compared to LO MC predictions (upper half) and to the NLO prediction (lower half).

Dijet angular distribution in D^* photoproduction

Angular distribution of dijet events with charm has been studied by ZEUS Collaboration [31]. Results were presented in terms of variables x_γ^{obs} and $\cos\theta^*$ which are calculated by dijet variables as

$$x_\gamma^{obs} = \frac{\sum_{jets} E_{T,jet}\exp(-\eta_{jet})}{2yE_e}, \tag{2.39}$$

$$\cos\theta^* = \tanh\left(\frac{\eta_{jet1}-\eta_{jet2}}{2}\right). \tag{2.40}$$

The variable x_γ^{obs} represents the fractional momentum of the photon contributing to the production of the two jets. $\cos\theta^*$ is the scattering angle of the dijets in its rest frame. In direct photoproduction, x_γ^{obs} is close to unity since all energy of the photon contributes to the hard scattering. For resolved processes, x_γ^{obs} is reconstructed at low values. Direct (resolved) enriched sample can be obtained by selecting events with $x_\gamma > 0.75$ ($x_\gamma < 0.75$).

The angular distribution is sensitive to the spin of the exchanged particle. While a quark propagater gives $1/(1-|\cos\theta^*|)$ dependence of the cross section, a gluon propagator

the cross section increases as $1/(1-|\cos\theta^*|)^2$ at $|\cos\theta^*| \simeq 1$, and hence gives steeper angular dependence.

The left plots of figure 2.6 shows $d\sigma/dx_\gamma^{obs}$, seperated at $x_\gamma = 0.75$. The $d\sigma/d\cos\theta^*$ for direct enriched sample and resolved enriched sample are compared to the NLO QCD calculation in the right plots. The sign of $\cos\theta^*$ is defined by taking the photon direction as $\cos\theta^* = -1$.

In the $\cos\theta^*$ distribution, in all cases, it shows a mild rise towards $|\cos\theta^*| = 1$ as expected from quark exchange, except for the resolved-enriched sample. In this sample, the cross section rises steeply in the photon direction ($\cos\theta^* = -1$), as expected from gluon exchange. This observation indicates that the charm originating from the photon is the dominant component in the resolved photoproduction of dijet events with charm.

2.6 Inclusive jet cross section in $D^{*\pm}$ photoproduction

As an extension to previous studies, the main theme of this analysis is the measurement of differential jet cross sections in D^* photoproduction. A jet whose transverse energy, E_T^{jet}, are greater than 6 GeV and in the pseudo-rapidity region $-1.5 < \eta^{jet} < 2.4$ are selected inclusively, i.e. events with more or equal to one jet are selected. Measured cross sections are presented as functions of the transverse energy of the jet ($d\sigma/E_T^{jet}$) and pseudo-rapidity of the jet ($d\sigma/\eta^{jet}$).

Jets are further divided into D^* *jets* and *other jets* using a D^*-jet matching criterion as described in section 6.1. The D^* jet is defined to be the jet nearest to the D^* in $\eta-\phi$ plane, with $\Delta R = \sqrt{(\phi_{jet}-\phi_{D^*})^2+(\eta_{jet}-\eta_{D^*})^2} < 0.6$. The remaining jets are classified as other jets. The cross sections ($d\sigma/dE_T^{jet}$ and $d\sigma/d\eta^{jet}$) are shown seperately for D^* jets and other jets. As shown in section 6.5.4, LO MC shows that contribution of resolved process becomes dominant in the forward region for other jets. Therefore, cross sections measured seperately for D^* jets and other jets have some sensitivity to the parton level contribution to charm photoproduction.

The aim of this study is to test the framework of pQCD in charm photoproduction. One of the motivation for this study came from the observed excess in the forward direction in inclusive D^* cross section. Although the D^* cross section can be calculated by convoluting the parton cross section with the fragmentation function, at relatively low p_T, the effect of the hadronization may be sizeable. By measuring a jet, one can have better correspondence to the outgoing parton and become less sensitive to the fragmentation process. Conversely, by studying the relation between the D^* and the jet, one can obtain information about the fragmentation of the D^* from the parton. Jet measurement also allows to investigate the distribution of other particles as well as the D^*. Especially,

this allows to measure particle flow in the forward region outside the acceptance of the tracking detector, which extends the measured pseudo-rapidity range compared to the inclusive D^* cross section.

In order to examine the description of the jet cross section in D^* photoproduction, theoretical prediction has been calculated using the program FMNR, which is based on the NLO QCD calculation in massive scheme. Details are explained in section 8.1.

Chapter 3

Experimental setup

The experiment has been performed using the electron proton collider HERA (Hadron-Elektron Ring Anlage) at the Deutches Electronen Synchrotron (DESY) in Hamburg, Germany. Collision data were collected by the ZEUS detector. In this chapter, the experimental devices used are explained.

3.1 The HERA accelerator

HERA (Hadron-Elektron Ring Anlage) is the first and the only lepton-proton collider in the world. A schematic layout of HERA accelerator is shown in figure 3.1. The circumference of HERA is 6.3 km with 4 experimental halls. It accelerates electrons or positrons up to 27.56 GeV and protons up to 920 GeV 820 GeV before 1998). Two beams are accelerated in opposite directions and brought into collision with the center of mass energy of 318 GeV.

There are two collider experiments, H1 and ZEUS which take place at North Hall and South Hall, respectively. Two fixed target experiments HERMES and HERA-B take place at East Hall and West Hall, respectively. HERMES studies the spin structure of the nucleon by scattering longitudinally polarized electron beam off a polarized gas target. HERA-B was built to study the B mesons using the proton beam and a wire target.

Electrons or positrons are subsequently accelerated by the linear accelerator LINAC, the synchrotron DESY II and PETRA III. After being accelerated up to 14 GeV, they are injected into HERA and accelerated up to 27.5 GeV. Protons are first accelerated in the form of negative hydrogen ions (H^-) by the linear accelerator up to 50 MeV. After stripping off the electrons, protons are injected into DESY III and PETRA II and accelerated up to 40 GeV. Finally they are injected into HERA and accelerated up to 920 GeV.

In order to get high luminosity, HERA is operated in multi-bunch mode. 220 bunches can be filled at maximum for each ring. The time between the two bunch crossings are

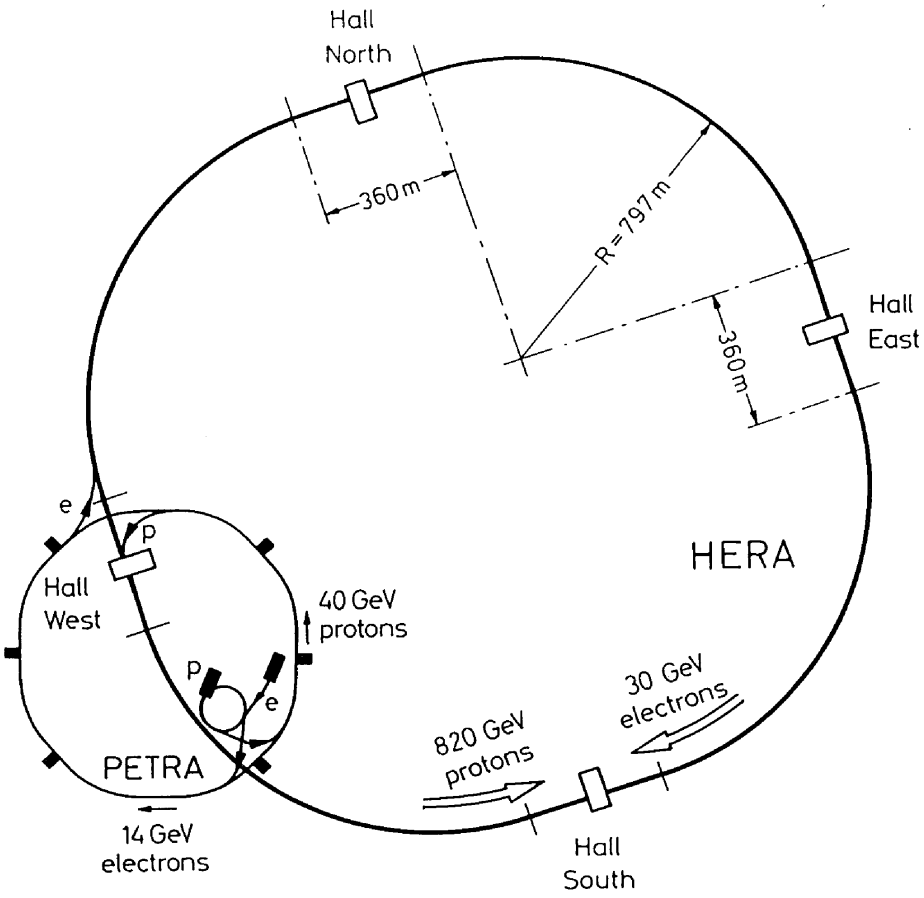

Figure 3.1: Layout of HERA and other accelerators.

	electron ring	proton ring
circumference	6336m	
nominal energy	30 GeV	920 GeV
c.m. energy	314GeV	
circulating current	60 mA	160 mA
number of particles/beam	0.8×10^{13}	2.1×10^{13}
number of bunch packets	220	220
number of bunches	210	210
current/bunch	0.3 mA	0.8 mA
time between beam crossings	96ns	
Beam size at interaction point (σ_x)	0.286 mm	0.28 mm
Beam size at interaction point (σ_y)	0.06 mm	0.058 mm
Beam size at interaction point (σ_z)	0.85 cm	19 cm
luminosity	$1.5 \times 10^{31}\mathrm{cm}^{-2}\mathrm{s}{-}1$	
specific luminosity	$3.3 \times 10^{29}\mathrm{cm}^{-2}\mathrm{s}^{-1}$	
polarization time at E_e=30GeV	25 min.	

Table 3.1: Design parameters of HERA during '98 - '00 data taking period.

only 96 ns. Some of these bunches are kept empty (*pilot bunches*) which can be used to study backgrounds from beam-gas interactions.

The design paremeters of HERA are summarized in table 3.1.

The history of the integrated luminosity taken by the ZEUS experiment is shown in figure 3.2. During the preiod of 1998 to April 1999, HERA delivered electron beams. Since May 1999 to 2000, HERA deliverd positron beams. This analysis is based on data taken by ZEUS in 1998 to 2000, which corresponds to a total integrated luminosity of about 78.6 pb^{-1} (e^+p: 13.5 pb^{-1}, e^-p: 65.1 pb^{-1}).

3.2 ZEUS detector

The ZEUS detector [32] is a multipurpose particle detector to measure final state particles produced in ep collision. It covers 99.7 % of 4π solid angle around the interaction point of $e^{\pm}p$ collisions and measures final state particles produced from the collision. Figures 3.3 and 3.4 show the schematic view of the ZEUS detector.

First of all, we define a coordinate system used in this analysis. The positive z direction is taken as the direction of the proton beam with the origin at the nominal interaction point. The positive x direction is taken as the horizontal direction pointing from the origin to the center of the HERA ring. As we use a right-handed coordinate system,

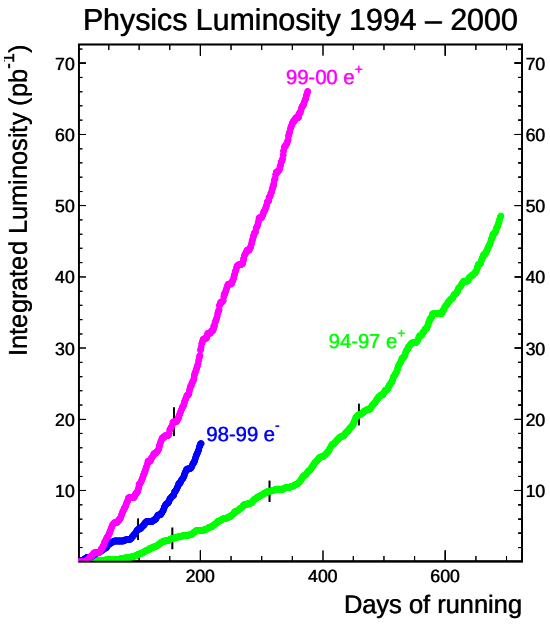

Figure 3.2: Integrated luminosity taken by ZEUS in 1994-2000 data taking period.

the y direction corresponds to the direction pointing upwards. The positive (negative) z direction is sometimes refered to as *forward* (*rear*) direction, i.e. the incoming proton (electron) direction. The polar angle θ is defined with respect to the positive z axis. The azimuthal angle ϕ is defined with respect to the positive x axis in the $x - y$ plane.

The ZEUS detector consists of several subcomponents. From inside to outside, there resides, the Central Tracking Detector (CTD), the Uranium Calorimeter (UCAL) and the Muon chamber (MUON). Between the CTD and the UCAL, there exists the solenoid which provides 1.43 T magnetic field at the center for particle tracking in the CTD. The iron yoke outside the UCAL is used as the return path of the magnetic field and as the absorber of the Backing Calorimeter (BCAL), which measures the energy depost escaping the main calorimeter. There are special purpose detectors to veto backgrounds from non-physics events, those are the Veto Wall (VETO), the C5 counter (C5) There are some other detectors far away from the interaction point which are not shown in figure 3.3. One of such detectors relevant for this study is the lumniosity monitor (LUMI) by which we measure the luminosity.

In the following sections, detector components important for this study, i.e. the CTD, the UCAL and the LUMI, are explained in more detail,

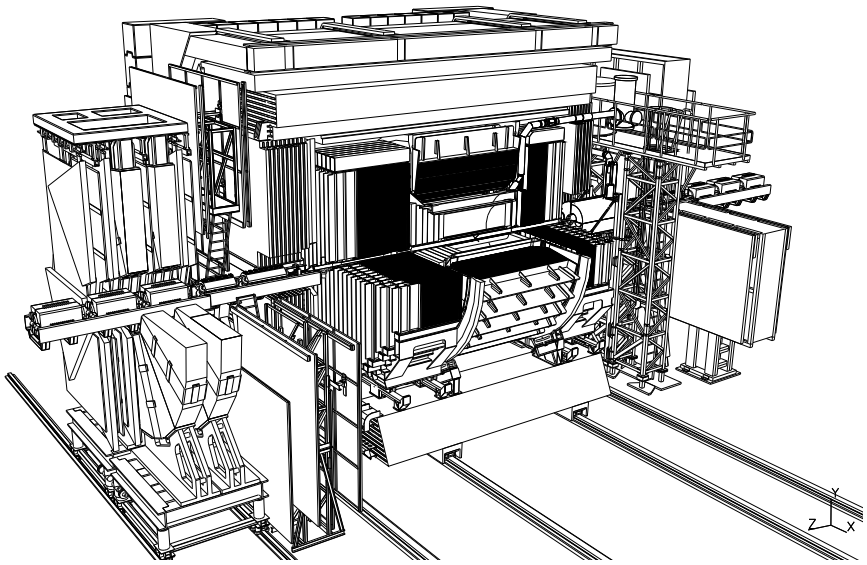

Figure 3.3: The ZEUS detector.

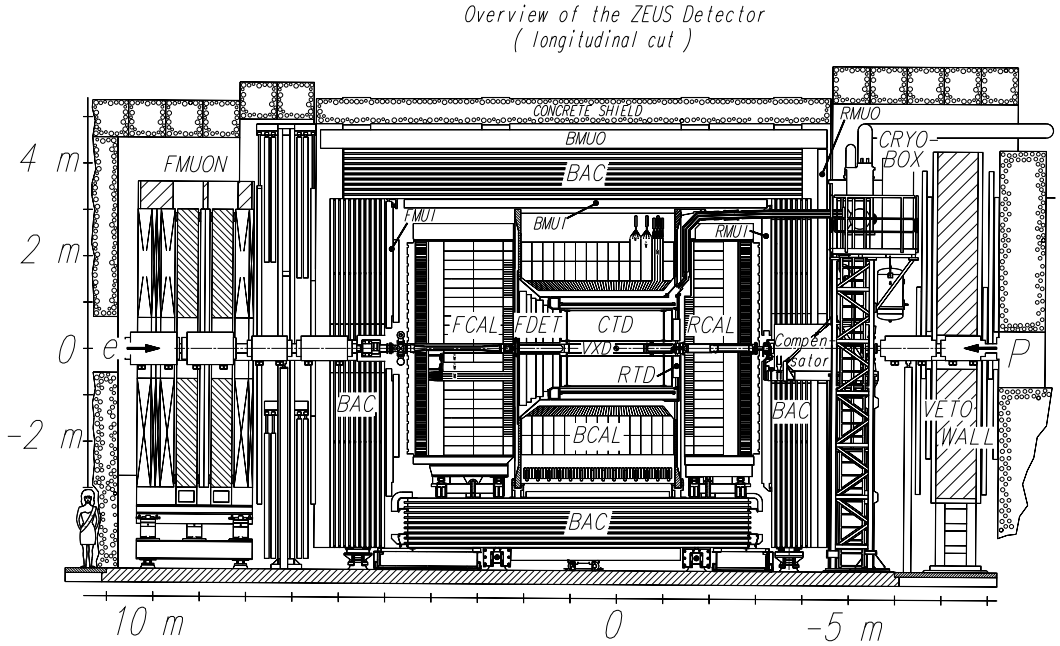

Figure 3.4: $y - z$ view of the ZEUS detector.

3.2.1 The central tracking detector

The CTD [33] is a cylindrical drift chamber operated in magnetic field. The active region of the CTD extends from -100 cm to $+105$ cm in z direction with the inner and outer radii of 18.2 cm and 89.4 cm respectively. The CTD is filled with a gas mixture of Ar (90 %), CO_2 (8 %) and ethane (2 %).

The CTD consists of 72 cylindrical layers arranged in 9 *superlayers* (SL), each containing 8 layers of sense wires. One octant of the CTD is shown in figure 3.5 together with the wire configuration. The CTD has a Lorentz angle of 45° due to the high magnetic field. The wire plane is rotated by 45° with respect to the radial direction to make the drift direction perpendicular to the wire plane.

The numbering of the SLs is defined such that the number 1 is the inner most SL. SLs with odd numbers have wires parallel to the z axis. Wires in SLs with even numbers have stereo angle of $\pm 5°$ to measure the z position.

The resolution of the CTD for a full-length track is given by

$$\frac{\sigma(p_T)}{p_T} = 0.0058 p_T \oplus 0.0065 \oplus \frac{0.0014}{p_T} \tag{3.1}$$

where p_T is measured in GeV/c and the symbol $\oplus$ indicating the quadric sum. The first term on the right hand side is the uncerntainty from of the hit resolution. The second and third terms are the uncertainties from the multiple scattering inside and outside the CTD. The vertex of an event can be measured with a typical resolution of 0.4 (0.1) cm in the longitudinal (transverse) direction.

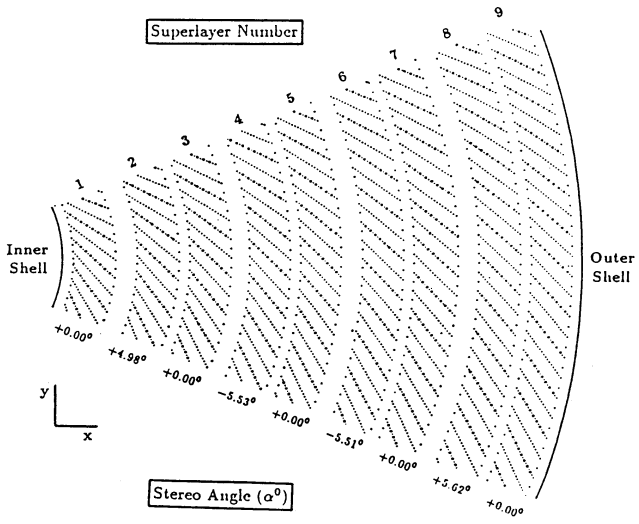

Figure 3.5: CTD wires.

In this analysis, only tracks traversing more than 3 SLs are used. This requirement limits the acceptance of the CTD in the central region of the detector.

3.2.2 The uranium-scintillator calorimeter

The ZEUS calorimeter [34] was designed to have good resolution for hadronic energy measurement. In order to have good resolution for hadrons, it is essential to have same response to electromagnetic particles and to hadrons. In this condition, the effect of the multiplicity fluctuation of electromagnetic components in hadron shower is reduced in the measurement of the energy depsoit. In order to realize this property, ZEUS selected a sampling calorimeter with depleted uranium (DU) for the absorber and plastic scintillator for the active material. The thickness of one layer was determiened as 3.3 mm for DU and 2.6 mm for scintillators. By selecting these values, the ratio of the responses to electrons to that to hadrons (e/h) was found to be $e/h = 1.00 \pm 0.03$ from beam tests. The energy resolutions for electrons and hadrons measured at beam tests are given by

$$\frac{\sigma(E)}{E} = \frac{18\%}{\sqrt{E\ [\mathrm{GeV}]}} \oplus 1\% \text{ for electrons} \tag{3.2}$$

$$\frac{\sigma(E)}{E} = \frac{35\%}{\sqrt{E\ [\mathrm{GeV}]}} \oplus 2\% \text{ for hadrons} \tag{3.3}$$

The UCAL is divided into 3 regions: forward (FCAL), barrel (BCAL) and rear (RCAL) regions, as shown in figure 3.6. Due to the asymmetric beam energies, final state particles produced in ep collision are boosted into the forward direction. Therefore three regions have different thickness. FCAL, BCAL and RCAL have thickness of 7λ, 5λ and 4λ respectively, where λ is the interaction length. The calorimeter system surrounds completely the CTD and covers 99.7 % of the 4π solid angle.

Each part of the UCAL consists of *modules*. Each module consists of *towers* whose transverse size is 20 cm $\times$ 20 cm. This is shown schematically in figure 3.7 in case of FCAL. An FCAL module is a collection of towers aligned vertically as shown in the figure. A tower can be divided longitudinally into one electromagnetic section (EMC) and two (one in RCAL) hadronic sections (HAC1 and HAC2). For the FCAL, the thickness of the EMC section is $\simeq 1\lambda$ and that of the two HAC sections are $\simeq 3\lambda$ each. The structure of the RCAL is similar to that of the FCAL. The BCAL consists of 32 wedge shaped modules, each covering 11.25° in azimuth. The EMC section of FCAL and BCAL is further divided into 4 *cells* (RCAL is divided into 2 cells). HAC1 and HAC2 sections make cells by themselves. Angular coverage and thickness of each section in FCAL, BCAL and RCAL are summarized in table 3.2.

The light output from the scintillator is transmitted to the photomultiplier tubes (PMT) through the wavelength shifter (WLS) from both sides of the cell. Thus the signal from each cell is readout by 2 PMTs from the left and right sides.

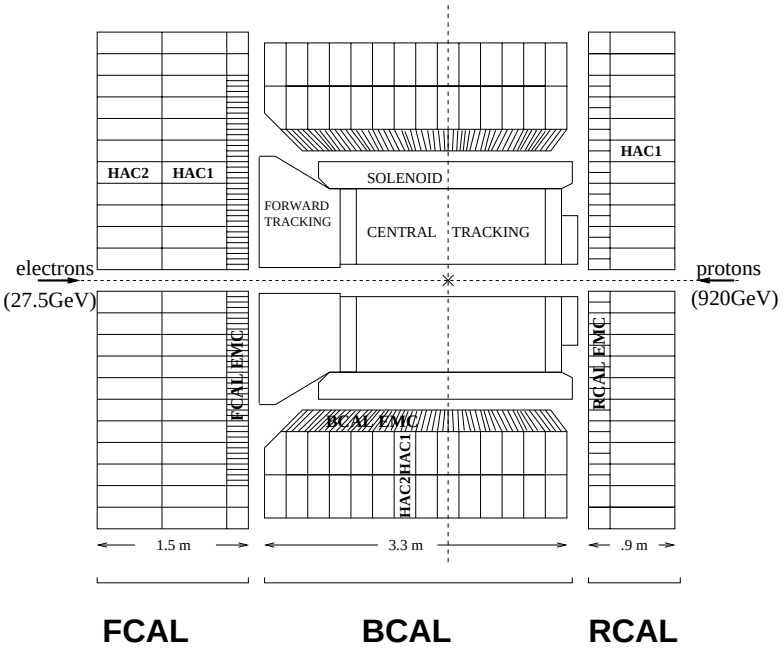

Figure 3.6: An y-z view of the CAL.

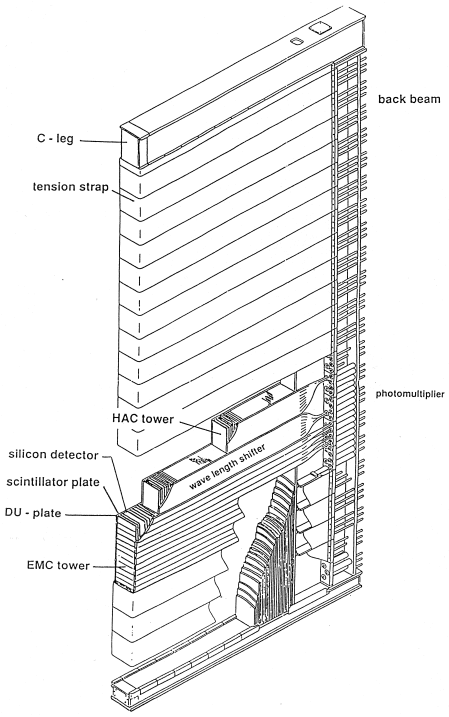

Figure 3.7: Structure of an FCAL module.

	FCAL			BCAL			RCAL	
	EMC	HAC1	HAC2	EMC	HAC1	HAC2	EMC	HAC1
Thickness (cm)	24.1	64.0	64.4	21.3	42.2	42.4	22.6	64.4
Radiation length (X_0)	25.9	84.2	84.2	24.6	51.5	51.5	24.3	84.2
Interaction length (λ)	0.84	3.09	3.09	0.85	2.03	2.04	0.90	3.09
Angular coverage	$2.2° - 39.9°$			$36.7° - 129.1°$			$128.1° - 176.5°$	

Table 3.2: Parameters of each setion of the CAL.

3.2.3 Noise suppression for the UCAL

A noise suppression for CAL cells is performed to remove cells in which the signal in the PMTs comes from the electronics, PMT or the radioactivity of the uranium.

In the standard calorimeter reconstruction routine, the energy of a cell is set to zero if the energy is less than 60 (110) MeV for EMC (HAC) cell. For isolated cells, which are surrounded by zero-energy cells, the energies are set to zero if they are less than 80 (140) MeV for EMC (HAC) cells. These thresholds were determined based on a study using randomly triggered events.

PMTs sometimes discharge spontaneously and produce a large signal (PMT spark). In order to reject cells from PMT spark, cells are rejected if the energy imbalance $(E_R - E_L)/(E_R + E_L)$ is larger than 0.9, where $E_{R/L}$ is the energy measured by PMTs on right/left side.

Furthermore, run-by-run stability of cells are monitored, and noisy or *hot cells* are identified based on the frequency of its appearance and the energy distribution [35]. Hot cells are rejected in the offline analysis.

3.2.4 The luminosity detector

The luminosity is measured by counting the rate of the bremsstrahlung process $ep \to ep\gamma$. The theoretical prediction of this process is known with an accuracy of $\simeq 0.5$ %, enabling precise determination of the luminosity. Electron and photon are scattered at very small angle and are measured by the LUMI system [36]. The photon is detected by the photon calorimeter located at $z = -107$ m as shown in figure 3.8. It is a lead-scintillator sampling calorimeter whose transverse size is 18 cm $\times$ 18 cm. It consists of 22 layers of 5.7 mm lead and 2.8 mm plastic scintillator, corresponding to 22 X_0. A carbon filter with a thickness of $2X_0$ is inserted in front of the photon calorimeter to absorb the large flux of photons from the synchrotron radiation. The resolution of the photon calorimeter is $24\%/\sqrt{E(\mathrm{GeV})}$. The electron calorimeter located at $z = -35$ m is used for the cross check of the luminosity measurement.

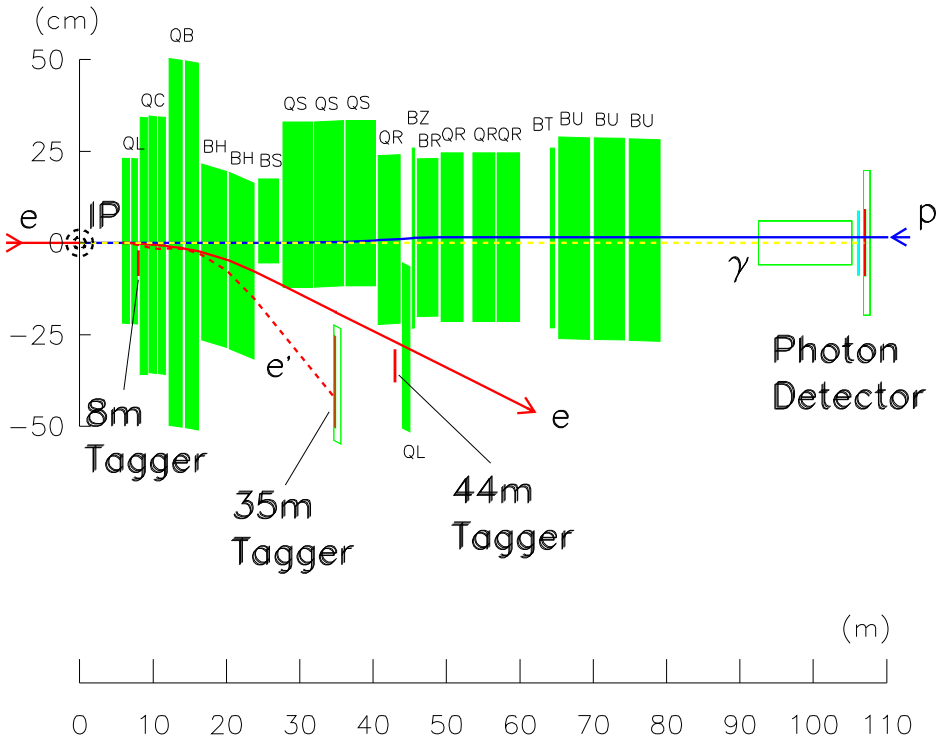

Figure 3.8: The luminosity detector.

The luminosity (L) is calculated from the counting rate in the photon calorimeter (R) and the theoretical cross section of the bremsstrahlung process (σ), using the relation $R = L\sigma$. The major background in the measurement is the bremsstrahlung photon from the electron and the residual gas in the beampipe. This background is subtracted statistically using the electron pilot bunches. The rate of the ep bremsstrahlung photon, R_{ep}, is obtained from the total rate, R_{total}, and the rate from electron pilot bunches, $R_{e-pilot}$, as

$$R_{ep} = R_{total} - k \cdot R_{e-pilot}, \tag{3.4}$$

where the factor k ($= I_e^{coll}/E_e^{pilot}$) is the ratio of the total electron current in the colliding bunches (I_e^{coll}) to that in the pilot bunches (I_e^{pilot}).

The main sources of the systematic error on the luminosity measurement are the geometrical acceptance (0.8 %), the theoretical uncertainty on the cross section (0.6 %), the background subtraction (0.1 %) and the energy scale uncertainty (1.1 %). The overall uncertainty is estimated to be 2 % [37].

3.2.5 Trigger and data acquisition system

The ZEUS data acquisition (DAQ) system has to cope with the high bunch crossing rate (10.41 MHz) and the large data size of an event ($\simeq$ 100 kB). Despite the high frequency of the bunch crossing, events which are interesting for studying physics is low. The rate of those events depends on the cross section, where some of them are $\simeq$ 100 Hz while for rare process only few events are expected in an year.

On the other hand, there are events where particles tranverse into the detector, such as the interaction between beam particles and the residual gas molecule inside the beampipe (*beam-gas* events), halo muons from the upstream of the proton beam or cosmic events. The background rate reaches about 100 kHz, where the contribution from proton beam-gas events is dominant.

In order to efficiently trigger on physics events and to reject non-*ep* events, the ZEUS DAQ system uses a trigger system consisting of three levels, the First Level Trigger (FLT), the Second Level Trigger (SLT) and the Third Level Trigger (TLT) [38]. A schematic diagram of the trigger and the DAQ system is shown in figure 3.9.

First Level Trigger

The task of the first level trigger (FLT) is to reduce the event rate from the bunch crossing rate 10.41 MHz to about 1 kHz. In order to achieve this goal without introducting significant deadtime, the FLT uses a pipeline structure. The FLT consists of component FLTs and the Global FLT (GFLT). The component FLTs process their data and send them to the GFLT within 26 bunch crossing. For example, the Calorimeter FLT (CFLT) calculates total and regional energy sums etc. with a special trigger hardware, and send them to the GFLT. After receiving data from all component FLTs, the GFLT makes the final decision within 20 bunch crossings. During this period, the raw data of each component are stored in analog- or digital-pipelines.

There are about 700 component data (bits) sent to GFLT from CTD, CAL and veto detectors. The GFLT makes an extensive use of Memory Lookup Tables (MLTs) to make fast decision and produces an output consisting of 64 bits. Each outbit corresponds to a decision of the GFLT with a certain logic, which are called *slots*. The final decision of the GFLT is the OR of the 64 slots.

If the GFLT makes a positive decision, an accept signal is sent to all components, and the components start to read the raw data stored in pipelines.

Second Level Trigger

The SLT further reduces backgrounds using the readout data from various components, such as CAL timing information. At the SLT, an order of 10 ms is avaiable to make the decision, so the SLT is able to perform more sophisticated calculation with CPUs, thus

providing quantities with better resolutions. To make the system flexible, DSP (Digital Signal Processor) and transputers are used for the data processing.

The event rate is reduced by a factor of 10, i.e. from 1 kHz to 100 Hz. If the GSLT issues a positive decision, data are sent to the Event Builder (EVB). The EVB combines all data from the components and sends them to the TLT.

Third Level Trigger

The task of the TLT is to further reject background events using timing information and to select particular types of physics events. The TLT has an access to full data from all components and a part of the offline reconstruction code is used.

Since large amount of computing power is needed, the TLT consists of a farm of SGI workstations. Events passing the TLT are sent to the data storage system and then written on the disk. The output of the TLT must be less than 5 Hz.

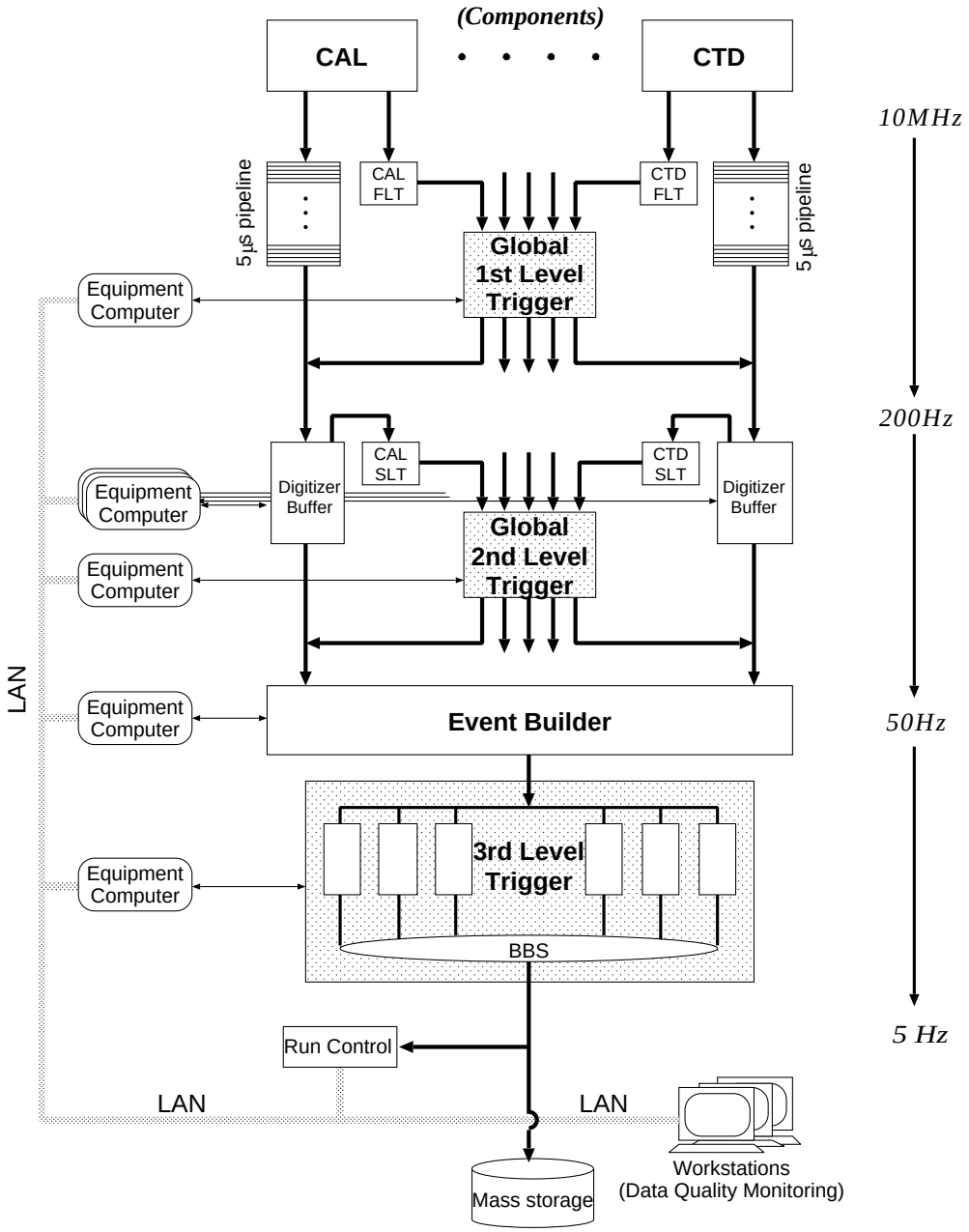

Figure 3.9: Data flow of the trigger and DAQ system.

Chapter 4

Monte Carlo simulation

The kinematic variables reconstructed from the measured quantities can be different from their true values due to detector effects (resolution, energy loss, etc). Variables can have different values at different levels of definitions or measurements. Three levels are used to describe events, the *parton level*, the *hadron level* and the *detector level*.

Parton level describes the event using the 4-momentum of final state partons. This is the output of the NLO QCD calculation. The partons are fragmented into the final state particles consisting of hardons. Variables calculated from the 4-momentum of final state hadrons are defined to be at *hadron level*. At *Detector level*, variables are reconstructed from the quantities measured by the detector.

Parton level information is what is calculable in pQCD. However, partons are not directly observed and only hadrons go through the detector. Therefore, what we can measure are hadron level quantities. Since the hadronization process is not calculable in pQCD, in order to relate parton level quantities to hadron level quantities, a certain correction must be applied to pQCD calculation.

Monte Carlo (MC) simulation is used to undertand the relation of variables at different levels. Detector level quantities should be corrected for if necessary. The MC simulation is also used to estimate the trigger and selection efficiencies.

The simulation proceeds in two steps : (1) event generation and (2) detector simulation. Each step is described in the next sections.

4.1 Simulation of D^* production in photoproduction

4.1.1 Event generation

In MC event generator, events with particular final states are generated such that the distribution of kinematic variables for many events reproduce the differential cross section of the process. For the QCD process, such as D^* photoproduction, the simulation is

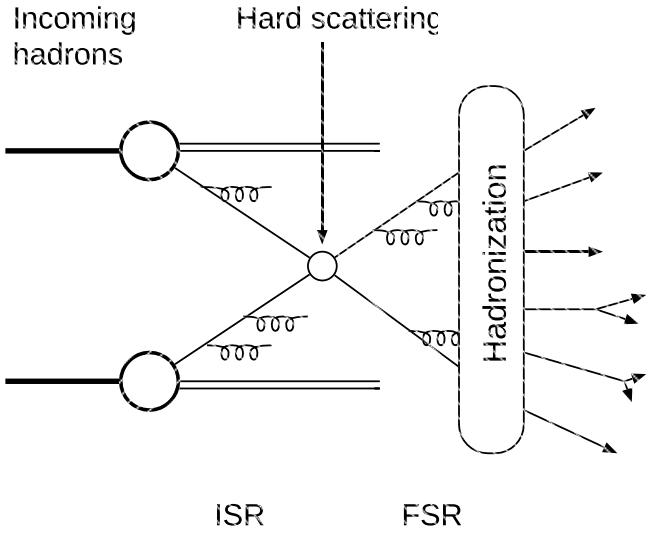

Figure 4.1: A schematic diagram of the processes involved in event simulation.

performed by a combination of parton densities of the incoming hadrons, matrix element of the parton-parton scattering, initial and final state radiation, and the hadronization processes [39]. This is schematically shown in figure 4.1.

Usually, event generators implement the leading order (LO) matrix element calculations. There are some phase space regions where higher order contributions become important, e.g. the region where two partons are collinear. Initial and final state radiation (ISR and FSR) takes this into account by simulating the parton branching process predicted by pQCD. The radiation process is also called a parton shower, as many partons are emitted after this stage. Finally, the partons are fragmented into hadrons. The hadronization process is not calculable by pQCD, so a certain model is needed. The string fragmentation model and cluster fragmentation model are the most commonly used. These models are found to describe well the measured particle flow in e^+e^- experiments.

Finally, the final state partons are fragmented into hadrons and the decay of hadrons are also simulated.

Events were generated by HERWIG [40] and PYTHIA [41] event generators by considering the following processes,

$$
\begin{aligned}
q\bar{q} &\rightarrow Q\bar{Q} \\
gg &\rightarrow Q\bar{Q} \\
\gamma g &\rightarrow Q\bar{Q} \\
Qq &\rightarrow Qq \text{ (flavor excitation in a proton or a photon)} \\
Qg &\rightarrow Qg \text{ (flavor excitation in a proton or a photon)}
\end{aligned}
$$

$$\gamma Q \rightarrow gQ \text{ (flavor excitation in a proton)}$$

The cluster model and the string model of hadronization are implemented in HERWIG and PYTHIA respectively. The direct photon process and resolved photon process were generated seperately in both HERWIG and PYTHIA, according to the LO cross sections. The PDFs, CTEQ5L [18] for the proton and GRV-G LO [19] for the photon were used.

In the production of MC samples, one of the charm quarks were required to fragment into a $D^{*\pm}$ meson. In order to study effect of other charm particles, the eight decay modes listed in table 4.1 and their charge conjugates were considered.

modes	p_T cut [GeV/c]
$D^{*+} \rightarrow D^0\pi_s^+ \rightarrow K^-\pi^+\pi_s^+$	1.25
$D^{*+} \rightarrow D^0\pi_s^+ \rightarrow K_0^S\pi^+\pi^-\pi_s^+$	1.35
$D^{*+} \rightarrow D^0\pi_s^+ \rightarrow K^-\pi^+\pi^+\pi^-\pi_s^+$	2.3
$D^0 \rightarrow K^-\pi^+$	2.6
$D_s^+ \rightarrow K^+K^-\pi^+$	1.7
$D^+ \rightarrow K^+K^-\pi^+$	1.7
$D^+ \rightarrow K^-\pi^+\pi^+$	2.8
$\Lambda_c^+ \rightarrow pK^-\pi^+$	2.8

Table 4.1: Eight decay modes generated in MC sample.

Charm mesons may be produced from b quark production, where B meson decays into a charm meson. In order to study contribution from b production, MC samples of b production with a charmed meson in the final state has been generated as well by HERWIG and PYTHIA.

Events corresponding to 886 pb^{-1} (350 pb^{-1}) were generated by HERWIG (PYTHIA) for each charm and bottom production.

4.2 ZEUS detector simulation

After generating the final state particles by the event generator, those particles are input to the detector simulation. The simulation of the ZEUS detector is performed by the program (MOZART) which is based on the GEANT3.13 package [42]. MOZART simulates the interaction of particles and the detector materials and outputs the signal measured in the detector. From the simulated signals, trigger simulation and event reconstruction are performed. The same offline reconstruction is used for both data and MC events.

Chapter 5

Reconstruction and event selection

5.1 Overview of the event selection

The event selection of the study of charm photoproduction with a jet consists of the following three requirements:

- the selection of photoproduction events,
- reconstructing the D^* meson, and
- jet finding.

An example of a typical event of interest is shown in figure 5.1. There is a large hadronic activity in the forward region (left side) due to the proton remnant. There is a bunch of particles going into a particular region which forms a jet. In figure 5.1, two jets are observed back-to-back. A D^* is reconstructed from the tracks by reconstructing its invariant mass. Note that there is no scattered electron found in the detector, as the electron scatters at very low angle and escape through the beam pipe in photoproduction. As seen in the figure, the final state consists of hadronic activities. Therefore, the reconstruction of the kinematic variables should be made from these.

In this chapter, first, we explain how the hadronic final state is reconstructed, where kinematic variables and the jets are reconstructed from the hadronic final state. Then we explain how the events were selected.

5.2 Reconstruction of the hadronic final state

The hadronic final state is reconstructed from the information of both the CTD and the CAL. At ZEUS experiment, such objects which represents final state particles are called *energy flow objects (EFOs)* [43]. Details of the algorithm to reconstruct EFOs is described

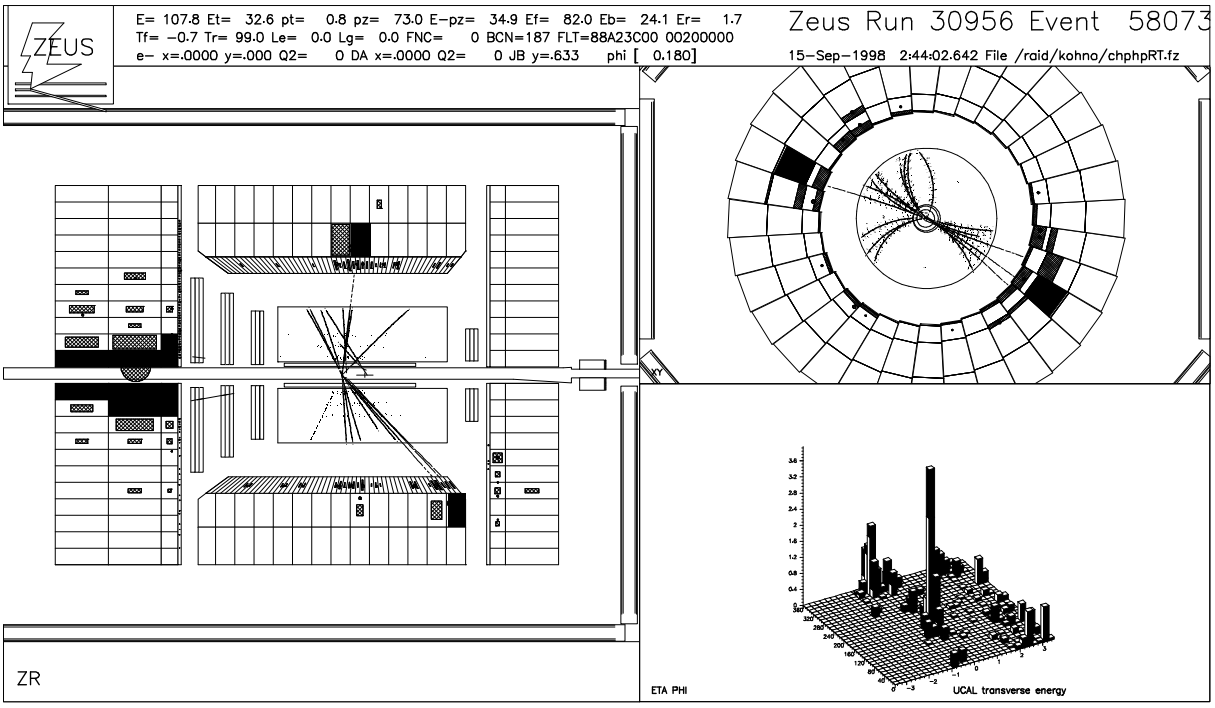

Figure 5.1: A D^* photoproduction event with a jet as seen by the ZEUS detector.

in appendix A. As seen from eq. (3.1)-(3.3), the CTD has better momentum resolution of charged particles at low momentum, while the CAL has better energy resolution at high momentum. This crossover takes place at momentum around 10 GeV. The momentum of an object is determined by using the CTD or the CAL depending on the resolution. For all charged objects a mass of a charged pion is assumed.

If there is a CAL cluster without any matching tracks to it, it is identified as neutral particle such as photon, neutron, etc. Neutral particles are only measured by the CAL. Therefore, energy and angle of the object is measured from the CAL and momenta is determined by assuming it as a massless object.

The output of the EFO algorithm is a collection of objects representing the final state particle. EFOs can be categorized into the following 3 types according to the source of measurement used to determine the 4-momentum of the EFO.

- 4-momentum is reconstructed from the CAL measurement.
- 4-momentum is reconstructed from the momentum measured in the CTD.
- the energy measured by the CAL and the angular information from the CTD are combined.

In this study, kinematic variables y, W and jets are reconstructed from EFOs. This gives better resolution than only using CAL cells for the reconstruction.

5.3 Reconstruction of Kinematic variables

In photoproduction, the electron is scattered at very small angle, so it escapes through the beampipe and is not detected in the central detector. So the kinematic variables must be reconstructed from the hadronic final state. The method to determine kinematic variables from the hadronic system is called *Jacquet-Blondel* method [44]. In this method, kinematic variables y and W are reconstructed from the 4-momentum of the hadronic system as

$$y_{JB} = \frac{E - P_z}{2E_e} \tag{5.1}$$

$$W_{JB} = \sqrt{s \cdot y_{JB}} \tag{5.2}$$

where $E - P_z$ is the sum over the whole hadronic system. Variables reconstructed by Jacquet-Blondel method are indicated by the subscript "JB".

When the scattered electron is detected, variable y can be calculated as

$$y_{el} = 1 - \frac{E'_e(1 - \cos\theta_e)}{2E_e} \tag{5.3}$$

where E'_e and θ_e are the energy and angle of the scattered electron.

5.3.1 Correction of y_{JB}

Figure 5.2 shows the correlation of reconstructed y_{JB} and true y (y_{true}) for events with $Q^2 \leq 1\text{GeV}^2$ in HERWIG MC. There is a good correlation between them with the following relation.

$$y_{JB} = 0.86 \times y_{true} + 0.02 \tag{5.4}$$

The inverse of eq. (5.4) is used to correct the value of y_{JB}. The corrected value will be denoted as y^{cor}. The W obtained from the y^{cor} is denoted by W^{cor}.

The distribution of $(y^{cor} - y_{true})/y_{true}$ is shown in figure 5.3 in different y_{true} ranges. The distribution peaks at zero except for the $0.1 < y_{true} < 0.2$. The standard deviation is about 12 % and is weakly dependent to the value of y_{true}.

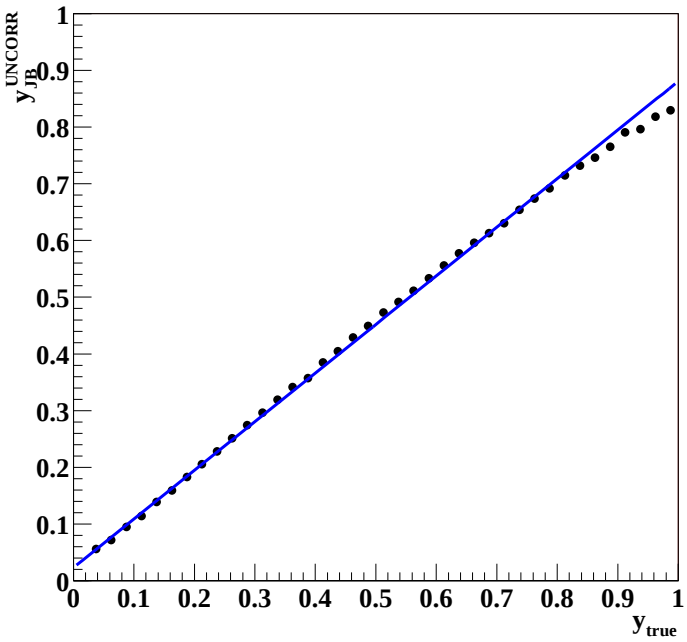

Figure 5.2: Correlation between y_{JB} and y_{true}.

5.4 Reconstruction of jets

5.4.1 Inclusive k_T algorithm

The longitudinally invariant k_T algorithm [45] was used in the inclusive mode to reconstruct jets. Given a list of objects, the procedure of jet finding is the following.

1. All objects are considered to be massless. Momentum of objects are scaled so that it equals to the energy of the object. The algorithm starts with these massless objects in the list.

2. Calculate the resolution variable d_{kB} for each object k and d_{ij} for each pair of objects i and j, which are given by,

$$d_{kB} = E_T^2, \tag{5.5}$$
$$d_{ij} = min(E_{T,i}, E_{T,j})^2 \cdot \Delta R_{ij}, \Delta R_{ij}^2 = (\eta_i - \eta_j)^2 + (\phi_i - \phi_j)^2. \tag{5.6}$$

   In the small angle limit, these variables reduce to the minimal relative transverse momentum of one object to the other like $d_{kB} \simeq k_{\perp,kB}^2$ and $d_{ij} \simeq k_{\perp,ij}^2$ respectively.

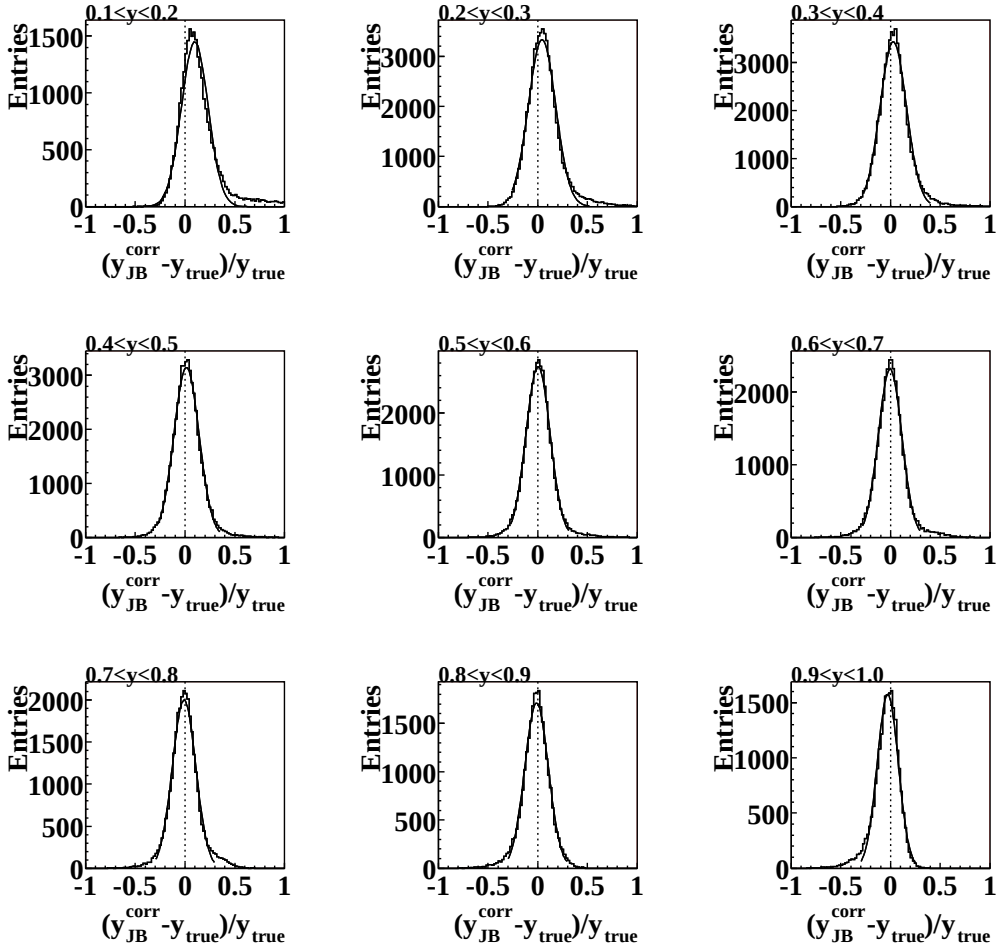

Figure 5.3: Distribution of $(y^{cor} - y_{true})/y_{true}$ in bins of y_{true} evaluated by HERWIG.

3. Find the smallest value among $\{d_{kB}, d_{ij}\}$. If d_{kB} is the smallest, the object k is considered to be a jet and is removed from the list. If d_{ij} is the smallest value, the objects (i,j) are merged into a new object. Momentum of the new object is given by

$$E_T = E_{T,i} + E_{T,j} \tag{5.7}$$

$$\eta = \frac{E_{T,i} \cdot \eta_i + E_{T,j} \cdot \eta_j}{E_T} \tag{5.8}$$

$$\phi = \frac{E_{T,i} \cdot \phi_i + E_{T,j} \cdot \phi_j}{E_T} \tag{5.9}$$

   Then objects i and j are replaced by the new object.

4. Continue the procedure from step 2, until there are no more entries in the list.

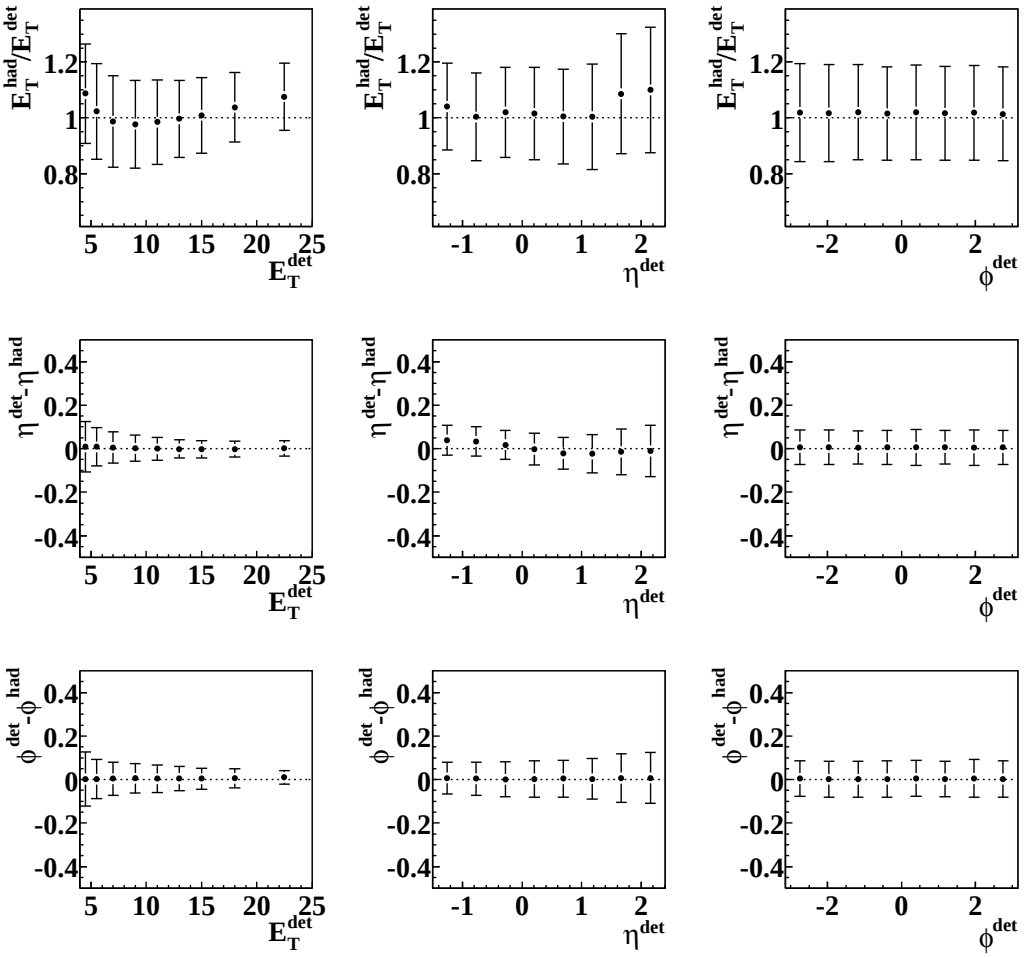

Figure 5.4: Correlation of jet variables between detector and hadron level.

Jet finding was performed in the laboratory frame. At the detector level, jet finder was run over the EFOs. In the MC, jet finder was run over the final state hadrons or the partons. It was also applied to the partons in the NLO QCD program.

At hadron level, since the decay particles of a D^* are known, we use a D^* meson instead of its decay products, as the input to the jet finder.

5.4.2 Correlation of jet variables between detector and hadron level

The correlation between jet variables measured by detector and the ones at the hadron level were checked using HERWIG MC. The event sample used for this study passes all selection cuts except for cuts related to jets. The detector level jets with $E_T^{det} > 4$ GeV

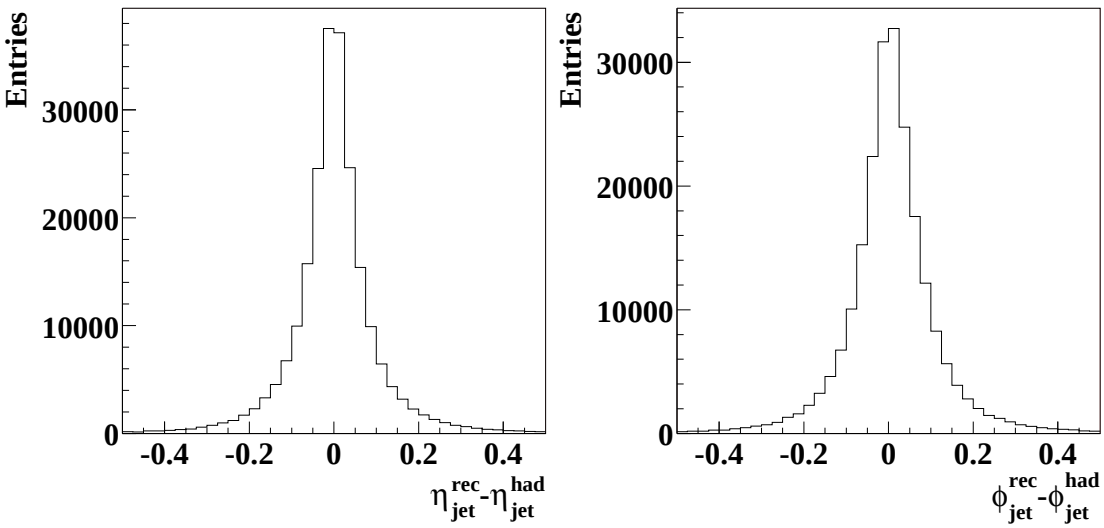

Figure 5.5: Resolution of η_{jet} and ϕ_{jet}.

and hadron level jets with $E_T^{had} > 3$ GeV are used for this check. For each detector level jet the closest hadron level jet is matched to it if $\Delta R < 1$, where the closeness between jets (ΔR) are defined by $\Delta R = \sqrt{(\eta^{det} - \eta^{had})^2 + (\phi^{det} - \phi^{had})^2}$.

The mean value of E_T^{had}/E_T^{det}, $\eta^{det} - \eta^{had}$ and $\phi^{det} - \phi^{had}$ are plotted as functions of E_T^{det}, η^{det} and ϕ^{det} in figure 5.4. The error bars on the points represent the RMS of the distribution.

The figure shows that there is no dependence on ϕ. The difference of η shows some strucure with respect to the η itself. However, the shift of the difference between detector and hadron levels are not so significant. As shown in the figure, E_T^{had} is larger that E_T^{det} in all η region. This is expected due to the energy loss of particles as they travel to the CAL. The E_T ratio is slightly η^{det} dependent. The difference is small in the central rapidity region and becomes larger in forward and in rear regions. This structure can be qualitatively explained by the fact that we use the EFOs to reconstruct jets. In the central region, information from the CTD, which is less affected by the energy loss of particles and has better resolution that the CAL, can be used. Therefore E_T^{det} remains close to E_T^{had}. Whereas outside the CTD acceptance, jets are reconstructed from EFOs with the measurement from the CAL, thus become more affected by energy losses of particles. Therefore the E_T^{had}/E_T^{det} becomes larger.

From these observations, we only correct the jet transverse energy. The correction of the jet transverse energy is discussed in section 6.2.

5.5 Trigger selection

The trigger logic used for this analysis is described in appendix B in detail. Here only a general strategy of trigger chain is explained.

At the FLT and the SLT, the trigger were designed to select hard photoproduction events. The FLT required a large energy deposit in the CAL and a good FLT track. Two trigger slots were used in a logical OR: one with tighter cuts on CAL energies and a loose tracking requirement, the other with lower thresholds on CAL energies and tighter requirement on the tracking.

At the SLT, events with high E_T and good vertex tracks are triggered. The selection cuts are similar to those in the offline selection with looser thresholds. At the TLT, full tracking information were available and a modified version of the offline tracking code was used. A D^* was reconstructed from the tracks as described in section 5.6.3 with wider mass windows.

5.6 Offline selections

5.6.1 Selection of photoproduction events

Photoproduction is characterized by $Q^2 < 1$ GeV^2. However, Q^2 can not be reconstructed with sufficient precision at low Q^2 without the measurement of the scattered electron. So the selection of photoproduction events must be performed by other methods.

Although Q^2 can not be well reconstructed without the electron, the absence of the scattered electron is a clear signal of photoproduction events. If the event does not have any electron candidate, it is likely to be a photoproduction event. The electron finding was performed using the standard electron finder at the ZEUS experiment, the SINISTRA [48]. This is based on a neural network algorithm to identify an electromagnetic cluster in the CAL from the energy deposits in cells. The electromagnetic cluster found by the SINISTRA is required to have a matching track, if it exists inside the CTD acceptance. The electromagnetic cluster and the track passing these conditions are identified as a scattered electron. The efficiency of the SINISTRA is greater than 99 % for electrons with energy greater than 10 GeV [49].

Considering these facts, the following cuts were used to select photoproduction events.

1. $-50 < Z_{vtx} < 50$ cm
   This cut on the Z coordinate of the interaction vertex is required to reject non-physics backgrounds such as proton beam-gas interaction or cosmic events.

2. If there is at least one electron candidate with $y_{el} < 0.7$, it is considered to be a real electron and that event is rejected.

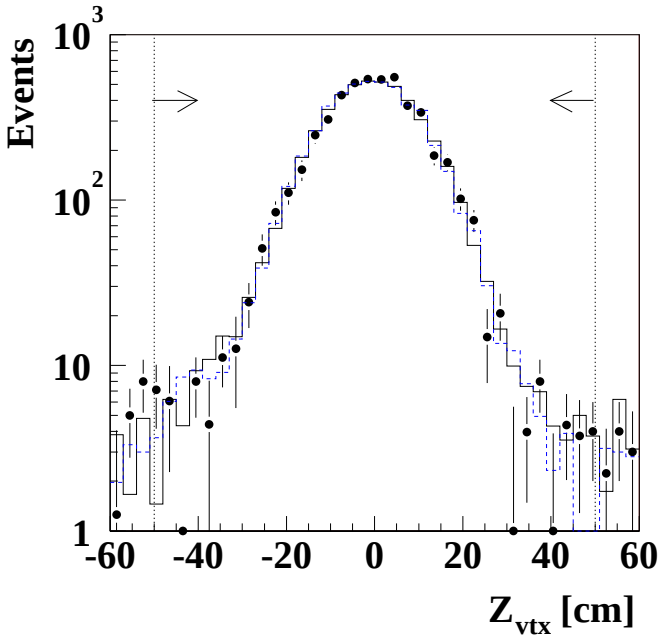

Figure 5.6: Z_{vtx} Distribution of data (dots) compared to HERWIG (solid line) and PYTHIA (blue dashed line).

When photoproduction events contain an electromagnetic cluster in the CAL, for example π^0 or η mesons from the hadronic final state, the energy of the cluster is in general lower than the scattered electron in NC DIS events. Therefore y_{el} defined by eq. (5.3) has higher values than DIS events. On the other hand, DIS cross section has the dependence $1/y^2$ so most of the DIS events are concentrated at low y_{el} region. From these considerations, the electron candidate with $y_{el} > 0.7$ are regarded as a fake electron and the event is considered to be a photoproduction event.

3. $130 < W^{cor} < 280$ GeV
   Since W_{JB} is related to y_{JB} by eq. (5.2), this cut corresponds to requiring $0.16 < y_{JB} < 0.69$. The lower cut on y_{JB} is required to reject further contribution from proton beam-gas interaction, which are mostly boosted to the positive Z direction and therefore characterized by $E - P_z \simeq 0$. The upper cut is required to reject contribution from NC DIS events where the electron finder couldn't identify the scattered electron. In this case, electromagnetic cluster in the CAL is taken as a part of the hadronic final state. Due to the conservation of $E - P_z$, the total $E - P_z$ of the hadronic system peaks at 2 times the electron energy, $2E_e$, hence $y_{JB} \simeq 1$.

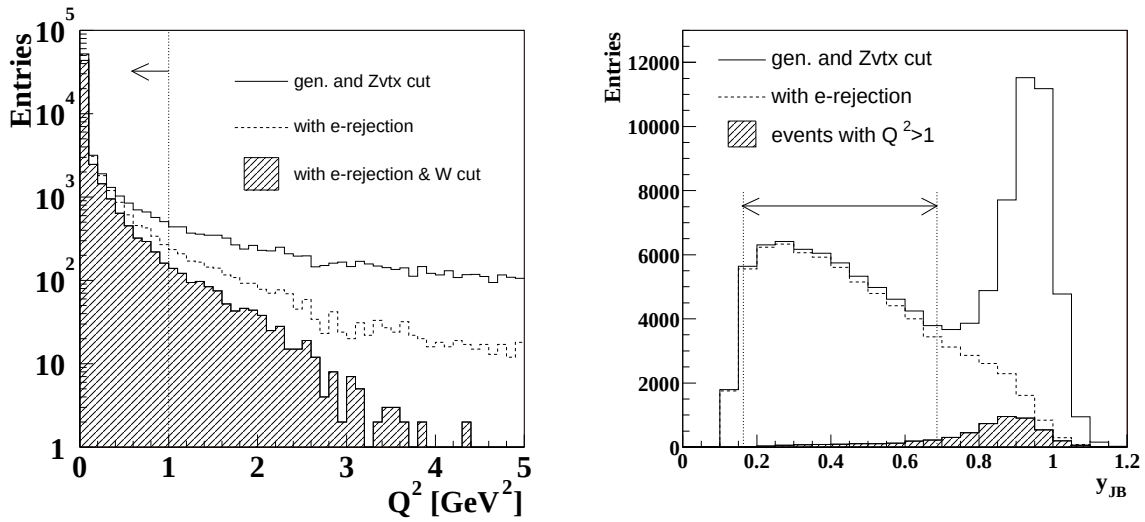

Figure 5.7: Distributions of Q^2 (left) and y_{JB} (right) after photoproduction selections. The solid line shows the distribution applying all selections except for electron rejection and the W cut. Dashed lines in both plots show distributions after rejecting events with the scattered electron. The hatched histogram on the left plot shows the distribution after the W cut. The hatched histogram on the right plot shows the contamination of events with $Q^2 > 1$ GeV^2 after electron rejection.

Z_{vtx} distribution is shown in figure 5.6 together with the MC distributions normalized to data. The distribution is well described by the MCs (HERWIG and PYTHIA). The arrows indicate the selected region.

The left plot of figure 5.7 shows the Q^2 distribution after the photoproduction selections using HERWIG. The solid line shows the distribution of Q^2 after all cuts except for the electron rejection and the W cut. The dashed line shows the distribution of events, in which no electron was detected. The hatched histogram shows the distribution after applying the W cut. As can be seen in the figure, after applying all cuts, events with $Q^2 > 1$ GeV^2 were reduced significantly. The right plot of figure 5.7 shows the distribution of y_{JB}. The solid line shows the distribution with all cuts except for the electron rejection and the W cut. A big peak close to $y_{JB} = 1$ come from the DIS event as already explained. The dashed line shows the distribution after removing events in which the electron was found. This removes most of the DIS events. However, there is still some contamination of DIS events which is shown by the hatched histogram. The cuts applied to y_{JB} corresponding to the W cut are indicated by the arrow. After all requirements, the contamination of events with $Q^2 > 1$GeV^2 in the final sample was estimated to be 1.9 % using HERWIG. Since the contamination of DIS events is small, no subtraction was

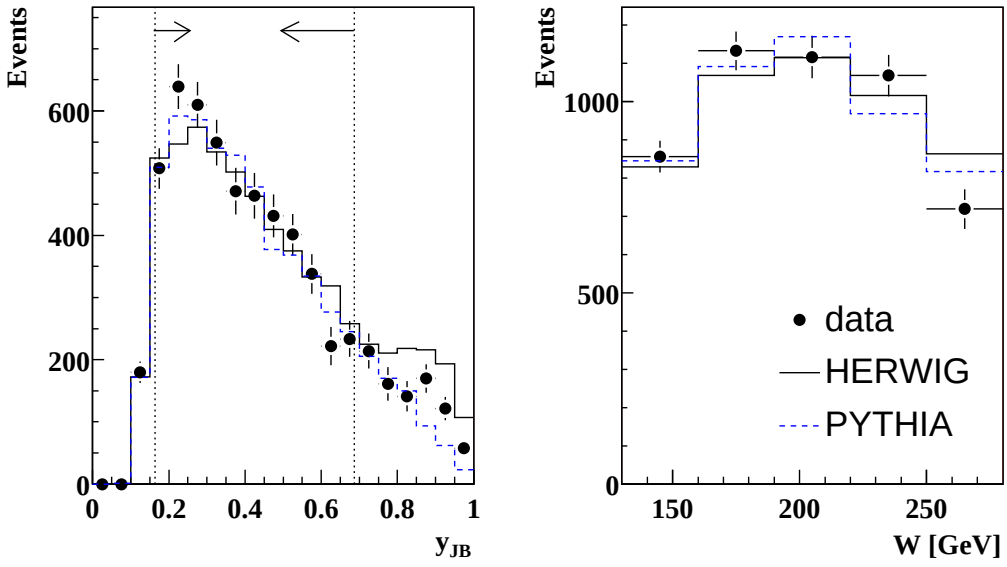

Figure 5.8: Distribution of y_{JB} and W^{cor}. Data (dots) are compared to HERWIG (solid line) and PYTHIA (dashed line).

performed.

The reconstructed y_{JB} with all selections except for the W cut, and W^{cor} after all selections are shown in figure 5.8, together with the expected distribution of MCs. HERWIG describes better the distribution.

5.6.2 Selection of charm events

Identification of charm event is done by measuring a charmed meson in the final state. In this analysis, $D^{*\pm}$ meson is reconstructed in the following decay mode[1].

$$D^{*\pm} \to D^0 \pi_s^{\pm} \to K^{\mp}\pi^{\pm}\pi_s^{\pm} \tag{5.10}$$

The branching ratios of these decay modes are given by,

$$Br(D^{*+} \to D^0 \pi_s^+) = 67.7 \pm 0.5\%, \tag{5.11}$$
$$Br(D^0 \to K^-\pi^+) = 3.80 \pm 0.09\%, \tag{5.12}$$

according to the Particle Data Group [46]. Thus the overall branching ratio of this decay chain, $D^* \to K^-\pi^+\pi_s^+$, is 2.57 %. The branching ratio of a charm quark to fragment into

[1]charge conjugate is always implied.

a $D^{*\pm}$ is given by [47]

$$f(c \to D^{*+}) = 23.5\ \%. \tag{5.13}$$

Although the branching ratio is small, this decay chain has several advantages. In order to reconstruct the invariant mass of the D^* meson, all decay products must be measured with a good precision. The decay products of eq. (5.10) are all charged particles so that their momenta can be measured by the CTD with good resolution. Furthermore, the main advantage of this decay mode is that two mass constraints, the mass of the D^0 and the mass difference of the D^* and the D^0, Δm. They were reconstructed by, $m(K\pi)$ for the D^0 mass and

$$\Delta m \;\; = \;\; m(K\pi\pi_s) - m(K\pi). \tag{5.14}$$

5.6.3 Reconstruction of $D^{*\pm}$ meson

In hard photoproduction events, we typically measure about 20 tracks in one event. The high multiplicity of charged tracks gives rise to combinatorial backgrounds in the D^0 mass distribution. However, since the mass difference Δm is very small and just above the charged pion mass, backgrounds from random combinations of pions and kaons which lies in the mass window of the D^* signal can be reduced significantly. Since pion emitted from the $D^{*\pm}$ decay have small momentum in the D^* rest frame, it is refered to as *slow* pion (denoted by π_s) to distinguish it from a pion from the $\bar{D}^0$ decay.

D^* mesons are reconstructed from charged tracks measured by the CTD which are also associated to the event vertex. Tracks measured by the CTD are also required to be in the central region $\eta(track) < 1.75$ tranversing at least three superlayers.

Among the CTD tracks, two charged particles with opposite charges with $p_T > 0.4$ GeV/c are combined to form a D^0 candidate. Since the ZEUS detector can not distinguish between charged pions and kaons, to calculate the invariant mass of these two particles, pion and kaon masses were assumed in turn for each particle. After forming a D^0 candidate, the slow pion was required to have $p_T > 0.12$ GeV/c and was searched for from tracks with a charge opposite to the kaon. The selection of tracks to form D^* candidates can be summarized as

- $\eta(track) < 1.75$
- $p_T(K)$, $p_T(\pi) > 0.4$ GeV/c
- $p_T(\pi_s) > 0.12$ GeV/c

Figure 5.9 shows the correlation of $p_T(D^*)$ and $p_T(\pi_s)$ (left) or $p_T(\pi, K)$ (right) evaluated by HERWIG. There is a strong correlation between $p_T(D^*)$ and $p_T(\pi_s)$. The dashed lines indicate the cuts applied to transverse momenta. It can be seen that once we apply a

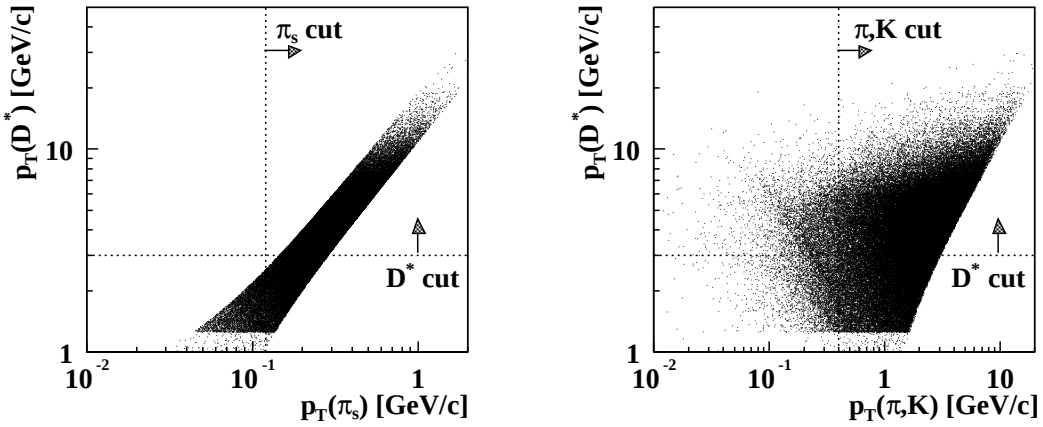

Figure 5.9: Correlation of transverse momentum of D^* and the decay particles. The left plot shows the correlation between $p_T(D^*)$ and $p_T(\pi_s)$. The right plot shows the correlation between $p_T(D^*)$ and $p_T(\pi)$ or $p_T(K)$. The cuts on the transverse momenta are indicated by arrows and dashed lines.

cut on $p_T(D^*)$, the cut on $p_T(\pi_s)$ does not remove further events. However, in data due to the finite resolution of the reconstruction of invariant masses, the correlation is smeared, so the cut on $p_T(\pi_s)$ may remove some events. There is no strong correlation between $p_T(D^*)$ and $p_T(\pi, K)$ as shown in the right plot of figure 5.9. The cuts on $p_T(\pi, K)$ are also indicated in the figure.

Figure 5.10 shows the transverse momentum distributions of π_s, π K and D^* compared to HERWIG and PYTHIA. In these plots, contribution from combinatorial backgrounds are subtracted according to the procedure described later. Both MCs describes the distributions reasonably well, although HERWIG reproduces the shape of the η distributions better.

The difference of the reconstructed values of $p_T(D^*)$ and $\eta(D^*)$ to the true values are shown in figure 5.11. There is no bias in the reconstruction.

D^* signal extraction

In order to estimate the contribution of combinatorial backgrounds, wrong charge combinations of kaons and pions, i.e. the same charge tracks, from $\bar{D}^0$ decay are used. In figure 5.12, the distribution of Δm is shown together with the distribution of the wrong charge background which is shown by the filled histogram. The cut on $m(K\pi)$ (eq. (5.18)) was imposed to create the distribution. Wrong charge background distributions are normalized to right charge distributions in the range $0.15 < \Delta m < 0.17$ and $2.0 < m(D^0) < 2.15$ for

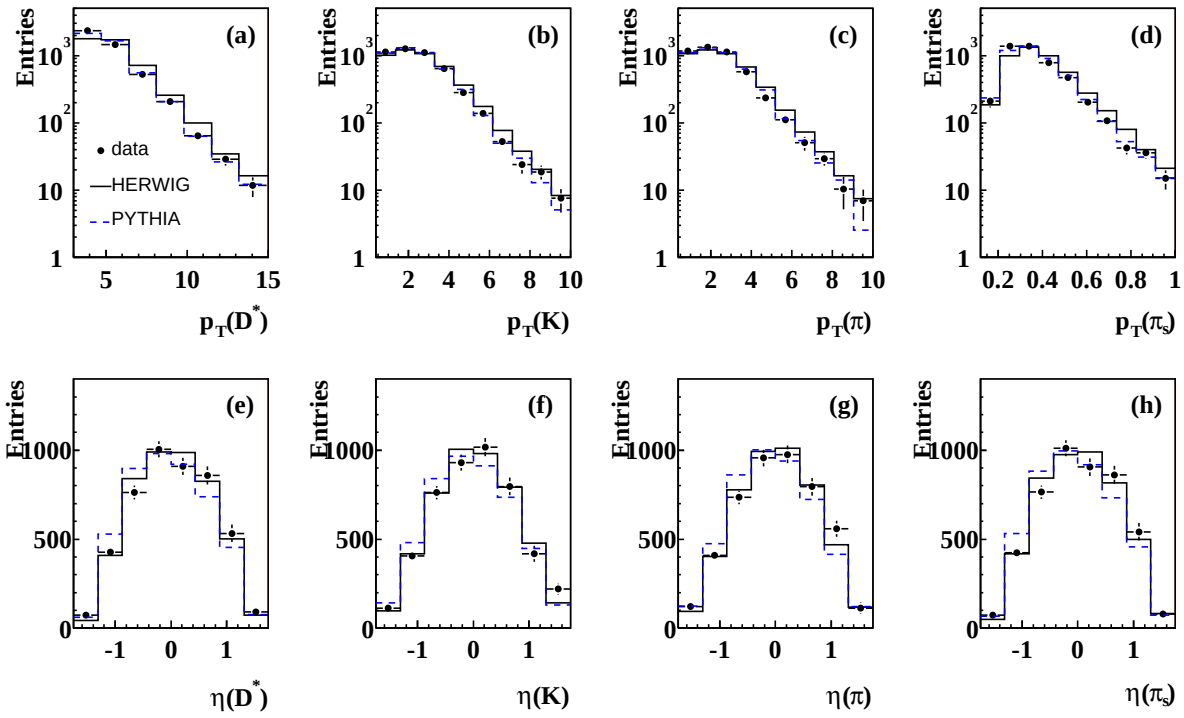

Figure 5.10: Distributions of transverse momentum of (a) D^*, (b) K, (c) π and (d) π_s, and pseudo-rapidity of (e) D^*, (f) K, (g) π and (h) π_s. Data (dots) are compared to HERWIG (solid line) and PYTHIA (dashed line).

Δm and $m(K\pi)$ distributions respectively. The functional form fitted to Δm distribution is a Gaussian plus a background function given by,

$$\left(\frac{dN}{d\Delta m}\right)_{BG} = p_0 \cdot (\Delta m - m_\pi)^{p_1}. \tag{5.15}$$

where m_π is the mass of a charge pion.

The distribution of $m(K\pi)$ is shown in figure 5.13 together with the distribution of wrong charge combination. The cut on Δm is imposed to create the distribution. The function fitted to $m(K\pi)$ distribution is a Gaussian plus a background function given by

$$\left(\frac{dN}{dm(K\pi)}\right)_{BG} = p_0 e^{-p_1 m(K\pi)}. \tag{5.16}$$

The fit was performed in the range from 1.7 GeV/c^2 to 2.2 GeV/c^2. The distribution of $m(K\pi)$ for wrong charge combination shows discrepancy between the right charge combination at low mass region. This is due to the reflection of other decay modes of D^0, where some decay particles were not observed, e.g. $D^0 \to K^-\pi^+\pi^0$, where the neutral

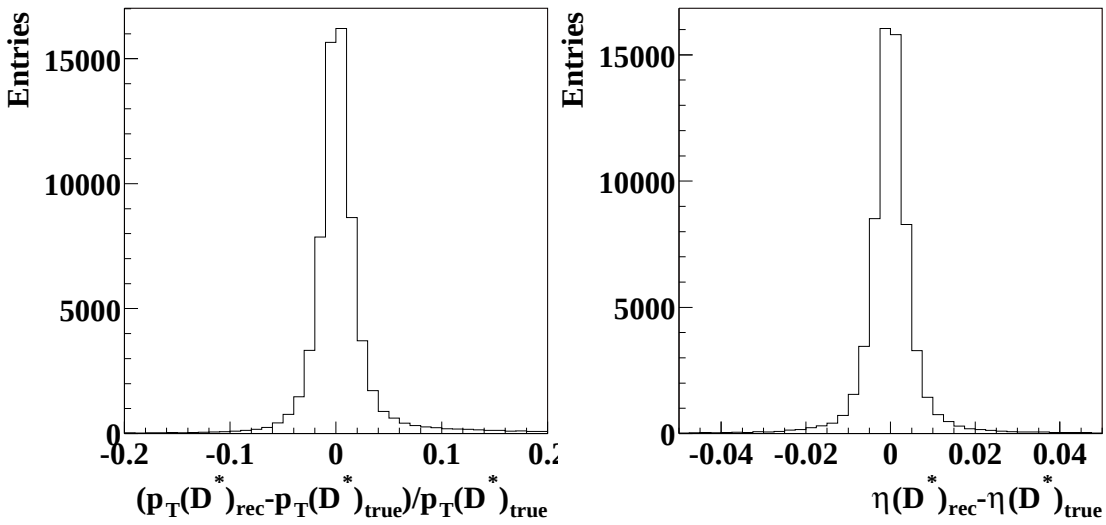

Figure 5.11: Differences of reconstructed values and the true values of $p_T(D^*)$ (left) and $\eta(D^*)$ (right).

pion was not observed. Then the invariant mass of kaon and pion is resonstructed below the nominal D^0 mass, making a broad peak at $m(K\pi) < m(D^0)$.

The signal regions are defined as

$$0.143 < \Delta m < 0.148 \text{ GeV/c}^2, \tag{5.17}$$

$$1.80 < m(D^0) < 1.92 \text{ GeV/c}^2. \tag{5.18}$$

D^* signal is extracted by subtracting the background contribution in the signal region of Δm distribution. The background contribution is estimated from the wrong charge distribution after normalizing it to the right charge distribution in the control region, $0.15 < \Delta m < 0.17$. Suppose that the number of events in the control region ($0.15 < \Delta m < 0.17$ GeV/c^2) are N_{ctrl}^{right} and N_{ctrl}^{wrong} for right and wrong charge distributions, respectively and the number of events in the mass window ($0.143 < \Delta m < 0.148$ GeV/c^2) are N_{win}^{right} and N_{win}^{wrong} for right and wrong charge distributions, respectively. Then the number of D^* signal and its error are given by

$$N_{D^*} = N_{win}^{right} - (N_{ctrl}^{right}/N_{ctrl}^{wrong})N_{win}^{wrong}, \tag{5.19}$$

$$\delta N_{D^*} = \left(N_{win}^{right} + N_{win}^{wrong} N_{ctrl}^{right} \cdot \frac{N_{win}^{wrong} + N_{ctrl}^{right} + N_{win}^{wrong} N_{ctrl}^{right}/N_{ctrl}^{wrong}}{N_{ctrl}^{wrong2}} \right)^{1/2} \tag{5.20}$$

Number of singal can also be obtained by fitting the Δm distribution with a signal+background function. We use the wrong charge background as a default method to extract D^* signal. Signal extraction by fit is used only for a cross check.

The total number of events after all selections was

$$N_{D^*} = 4891 \pm 113$$

obtained from wrong charge background subtraction.

The values of Δm and $m(D^0)$ obtained from the fit was $\Delta m = 145.5$ MeV/c^2 and $m(D^0) = 1.862$ GeV/c^2, respectively. They agree well with values from the PDG ($\Delta m(PDG) = 145.421 \pm 0.010$ MeV/c^2 and $m(D^0)(PDG) = 1864.5 \pm 0.5$ MeV/c^2). The width of the distribution is dominated by the resolution of the tracking.

In the measurement of the differential cross sections, combinatorial background is subtracted statistically in each bin.

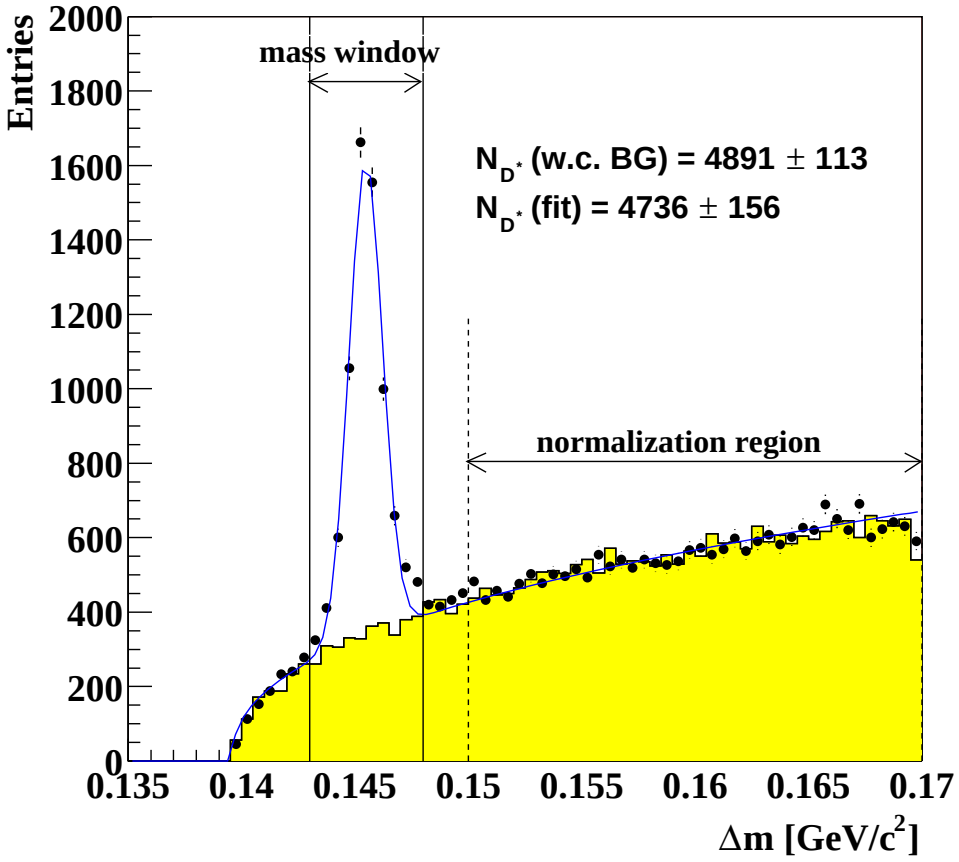

Figure 5.12: The Δm distribution after all selections. A cut on $m(K\pi)$ was imposed to create this plot. Hatched histograms are the distribution of wrong charge background normalized to right charge distribution in the region described in the text (also indicated in the plot).

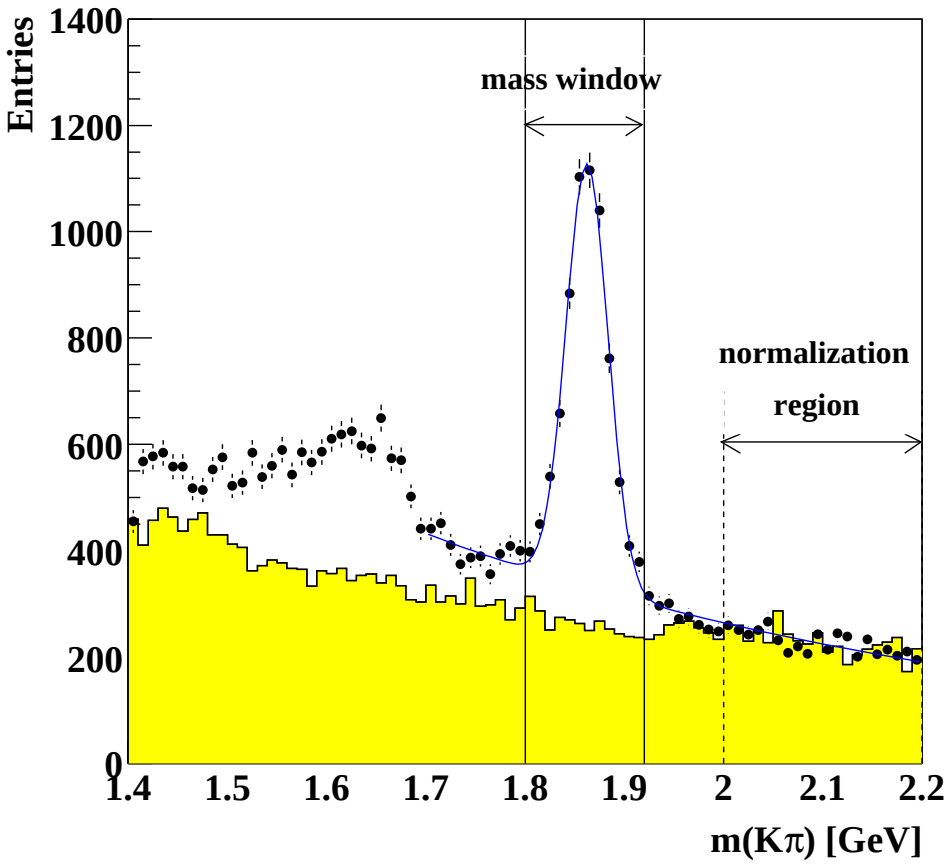

Figure 5.13: $m(K\pi)$ distribution after all selections. A cut on Δm is imposed to create this plot. Hatched histograms are the distributions of wrong charge background normalized to right charge distributions in the region described in the text (also indicated in the plot).

5.7 Summary of the offline selection

Offline selection cuts are summarized in table 5.1.

	Cuts
Vertex	$\lvert Z_{vtx}\rvert < 50$ cm
Photoproduction	No electron
	$130 < W^{cor} < 280$ GeV
D^* selection	$\lvert\eta(track)\rvert < 1.75$
	$p_T(\pi_s) > 0.12$ GeV/c
	$p_T(\pi) > 0.4$ GeV/c
	$p_T(K) > 0.4$ GeV/c
	$1.80 < m(D^0) < 1.92$ GeV/c^2
	$0.143 < \Delta m < 0.148$ GeV/c^2
Jet selection	$E_T > 6$ GeV
	$-1.5 < \eta^{jet} < 2.4$

Table 5.1: Summary of the offline selection cuts.

Chapter 6

Jets in D^* events

In the previous chapter, selction of events containg a D^* and jets in the kinematic region $Q^2 < 1$ GeV^2 and $130 < W < 280$ GeV has been described. In this chapter, we investigate the properties of jets in this event sample.

6.1 D^* - jet matching

In this analysis, D^* and jets are reconstructed independently. However, both D^* and jets are originated from the outgoing partons of the hard scattering. So D^* is likely to exist inside a jet. Figure 6.1 shows the ΔR distribution of D^* and the jets, where ΔR is defined by

$$\Delta R(D^*, jet) = \sqrt{(\eta_{jet} - \eta_{D^*})^2 + (\phi_{jet} - \phi_{D^*})}. \tag{6.1}$$

There is a large peak at $\Delta R(D^*, jet) = 0$ as expected. Another peak around $\Delta R = 3.1$, appears when the jet associated with the D^* was rejected by the E_T cut, and the D^* is matched to the other jet. For example, suppose there is a charm quark with transverse momentum 6 GeV which fragments into a D^* meson with $p_T(D^*) > 3$ GeV/c, if the transverse energy of the jet produced from this charm quark was measured to be less than 6 GeV and another jet had E_T larger than 6 GeV, the matching jet to the D^* can be rejected.

In photoproduction, the lowest order diagram to produce charm quark have 2 outgoing partons. Since the transverse momentum must conserve, two jets from these partons exist in opposite direction in azimuthal angle. Therefore when the matching jet to the D^* was rejected, the jet closest to the D^* becomes the jet in the opposite direction, which peaks at $\Delta\phi = \pi$. Note that our sample consists of events which have at least one jet.

We define D^* *jet* and *other jet* as follows.

- D^* jet
  Jets whose distance between the D^*, $\Delta R(jet, D^*)$, is less than 0.6.

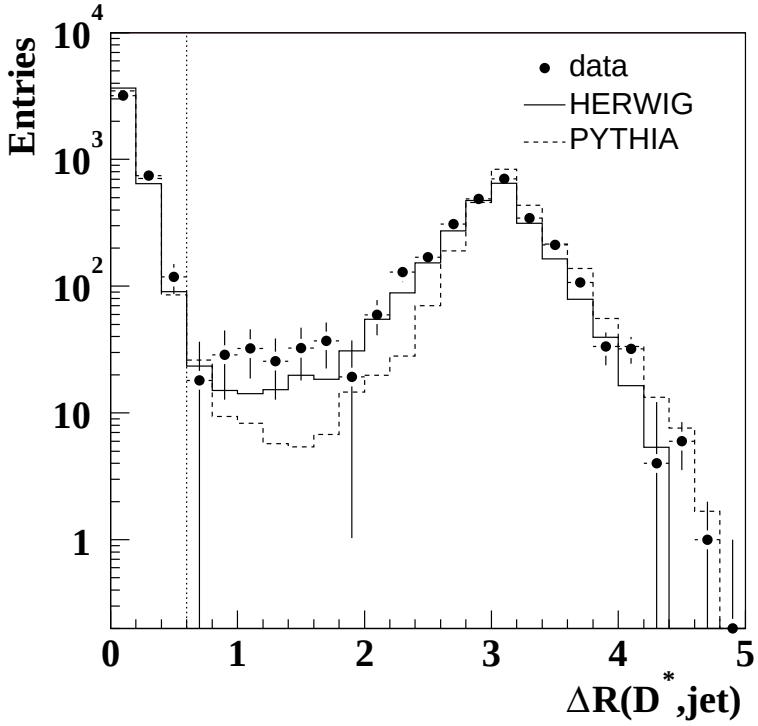

Figure 6.1: ΔR of D^* and the jets. All jets are included. Data (black dots), HERWIG (solid line) and PYTHIA (dashed line) are shown together.

- other jet
  All other jets which are not identified as D^* jet.

The interpretation of the other jet is not trivial. It is just defined as a jet not matched to the D^*. Depending on the parton level sub-process, the origin of the other jets may be c-quark, gluon or light quarks. In direct photon process, it is mainly c-quark, as BGF is the dominant sub-process. Therefore both D^* jet and other jet are charm jets. In resolved photon process, according to LO MC, they are gluon and light quarks which are identified as other jets, since the charm excitation from the photon is the main contribution.

Figure 6.2 shows the distribution of the ratio of the transverse momentum of the D^* to the transverse energy of the matching D^* jet, $p_T(D^*)/E_T^{jet}$. This variable represents the fraction of the jet momentum taken by the D^*. Therefore, the distribution reflects the shape of the fragmentation function where the D^* carries a large fraction of the momentum of the jet. It can be seen that HERWIG (solid line) has harder fragmentation function than the data, while PYTHIA (dashed line) reproduces the distribution better.

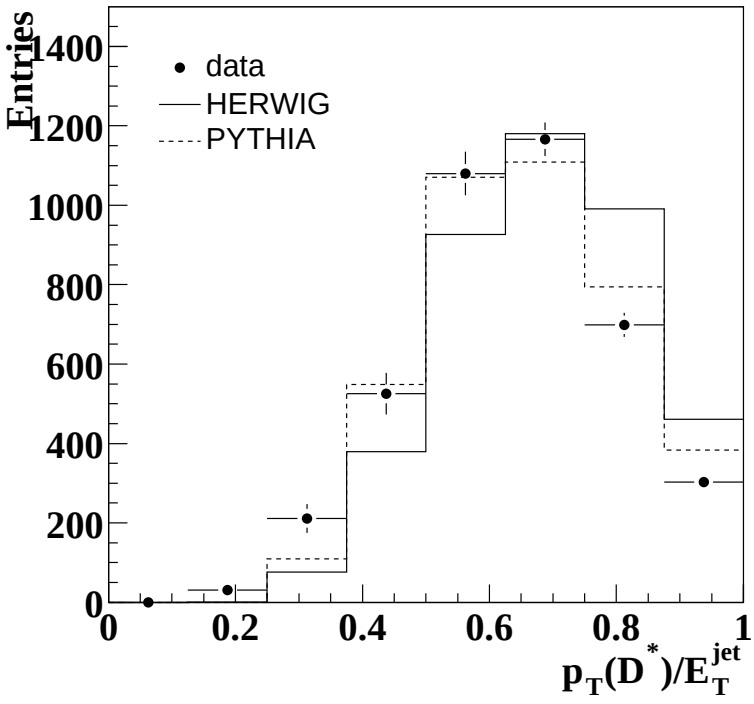

Figure 6.2: The $p_T(D^*)/E_T^{jet}$ distribution for the D^* and the matching D^* jet. Data (black dots), HERWIG (solid line) and PYTHIA (dashed line) are shown together.

6.2 Correction of jet transverse energy

The correlation of jet quantities at detector level and hadron level was already shown at sec 5.4.2. It was found that transverse energy E_T of jets need corrections, where the correction factor depends on E_T and η.

In order to determine the correction factors, there might be differences between D^* jet and other jets. Since D^* is tagged by its decay into charged particles, Other jets may be a charm jet, gluon jet or light quark jets. When the other jets originates from charm, any decay mode can take place including semi-leptonic decay modes. When the charm quark in the other jet decays semi-leptonically, E_T measured in the detector E_T^{det} is expected to be smaller than the E_T at hadron level E_T^{had}. According to PDG, the branching ratio of $c \to e + anything$ and $c \to \mu + anything$ is about 20 %.

Figure 6.4 shows the distribution of the fraction of transverse energy carried by neutrino with respect to jet transverse energy. The figure shows the distribution for D^* jets

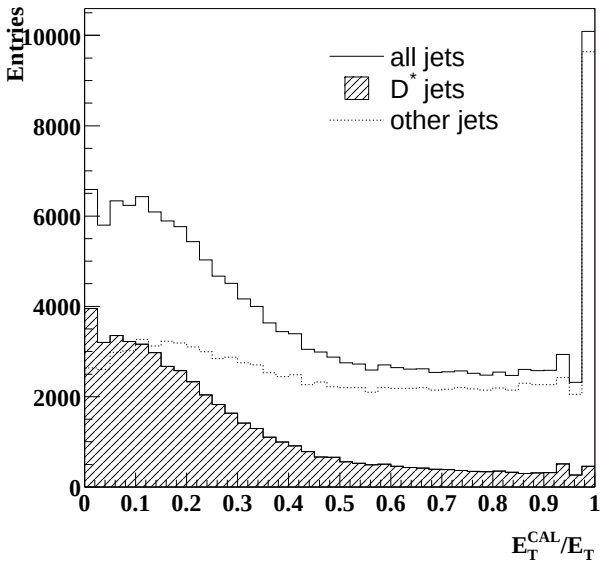

Figure 6.3: The fraction of E_T using the CAL information to the total E_T,$E_T CAL/E_T$. Distributiosn are shown seperately for all jets (solid line), D^* jets (hatched histogram)and other jets (dotted line).

(hatched histogram)and other jets (dotted line) seperately. Note that only jets which include a neutrino contribute to the plot. As expected, the neutrino in the other jet takes non-negligible amount of E_T of the jet.

Another effect is that D^* jet is expected to have more track information in E_T measurement than other jets. We select the D^* decay mode into 3 charged particles while charmed particle in other jet can decay into neutral particles. Therefore, D^* jet is expected to have more tracks than normal jets. Figure 6.3 shows the fraction of E_T measured using the CAL information E_T^{CAL} to the total E_T of the jet, E_T^{CAL}/E_T. The distribution is shown for D^* jets and other jets seperately. As shown in the figure, indeed less information of CAL is used in the E_T measurement for D^* jets, while E_T^{CAL}/E_T distributes almost uniformly form zero to unity for other jets. The effect of energy losses due to the inactive materials in front of the detector is higher for the CAL measurement than the CTD measurement. Therefore, from the distribution in figure 6.3, it is expected that D^* jets have smaller correction to hadron level than other jets.

In spite of these differences, due to combinatorial backgrounds, it is not possible to distinguish between D^* jet and other jet for individual jets at detector level. Therefore the same correction procedure is applied to all jets. Above effects are all included in MC.

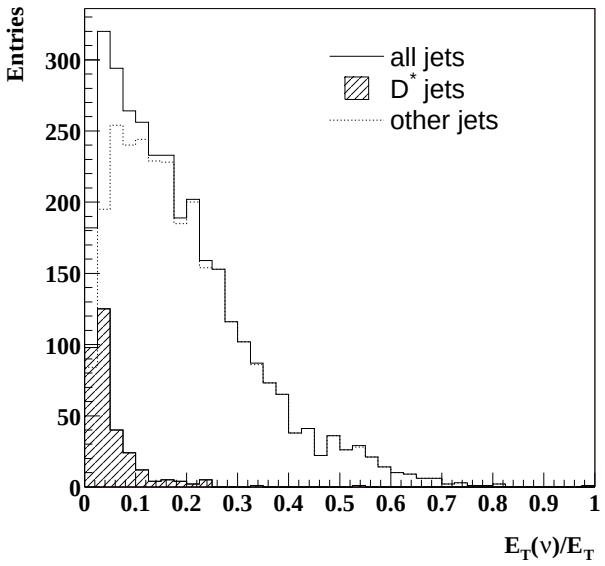

Figure 6.4: The fraction of E_T taken by the neutrino inside a jet, as evaluated by HERWIG. The distribution for all jets, D^* jets and other jets are plotted in solid line, hatched histogram and dotted histogram, respectively.

6.2.1 Method of E_T correction

We consider a correction of E_T by multiplying a factor which is dependent on E_T^{det} and η^{det} as

$$E_T^{cor} = C(E_T^{det}, \eta^{det}) \cdot E_T^{det} \tag{6.2}$$

The correction factor $C(E_T^{det}, \eta^{det})$ was determined as

$$C(E_T^{det}, \eta^{det}) = \left\langle \frac{E_T^{had}}{E_T^{det}} \right\rangle . \tag{6.3}$$

where $\langle\rangle$ denotes the average.

In order to determine the correction factor $C(E_T^{det}, \eta^{det})$, η range, $-1.5 < \eta < 2.4$, is divided into 8 subranges. Then the profile of the ratio $\left\langle E_T^{had}/E_T^{det} \right\rangle$ with respect to E_T^{det} is investigated in each η subregion. Dividing η region into subregions is justified since η^{det} agrees well with η^{had} and also, from figure 5.4, the dependence of correction factor on η is not steep.

In figure 6.5, the profile of $\left\langle E_T^{had}/E_T^{det} \right\rangle$ with respect to E_T^{det} is shown. Curves on the figure shows the fit to the profile with the following functional form used for the correction factors.

$$C(E_T^{det}) = p_0 + p_1 \exp^{-p_2 E_T^{det}} - p_3 \exp^{-p_4 E_T^{det}} \tag{6.4}$$

The second term in eq. (6.4) describes the feature that the ratio $< E_T^{had}/E_T^{det} >$ decreases as E_T increases. This is because the energy loss is larger for low energy particles. The last term in eq. (6.4) was added to describe the feature that the ratio $< E_T^{had}/E_T^{det} >$ increases at high E_T.

In the central rapidity region, the correction factor drops to unity at intermediate E_T. Here the CTD information is available so the measurement is less affected by energy loss of particles. The increase of the correction factor at high E_T can be understood since the contribution from CAL measurement increases as the energy of particles increases. This is due to the EFO algorithm. It can be seen that the constant term is large at some η regions ($0.6 < \eta < 1.2$ and $1.2 < \eta < 1.8$). This is because that the there are more dead materials in from of the CAL at these rapidity regions.

6.2.2 Effect of jet transverse energy correction

The effect of the transverse energy correction can be seen by checking the difference between the reconstructed E_T and E_T of the hadron level jet before and after correction. This is shown in figure 6.6 in 4 bins of E_T^{cor}. These E_T regions correspond to the binning used in the cross section measurement. The differences without correction are shown by dashed lines and ones after correction are shown by solid lines. Gaussian fits to the distribution after correction are shown together where mean and σ of the Gaussian fits (fitted $\pm 2\sigma$ around the mean) are indicated in the figure. It is seen that we have better correspondece between reconstructed E_T and hadron level E_T after the correction at high E_T.

Figure 6.7 shows the dependence of mean and σ, with respect to E_T^{cor}, where the mean and the σ were obtained by fitting a Gaussian in the range, $\pm 2\sigma$ around the mean of the distribution. Black dots show the points considering all jets. Open circles and open squares show the mean and σ for D^* jets and other jets respectively. As expected, mean of E_T is larger for D^* jets than other jets by about 3 % in the low E_T region. The difference gets smaller at high E_T.

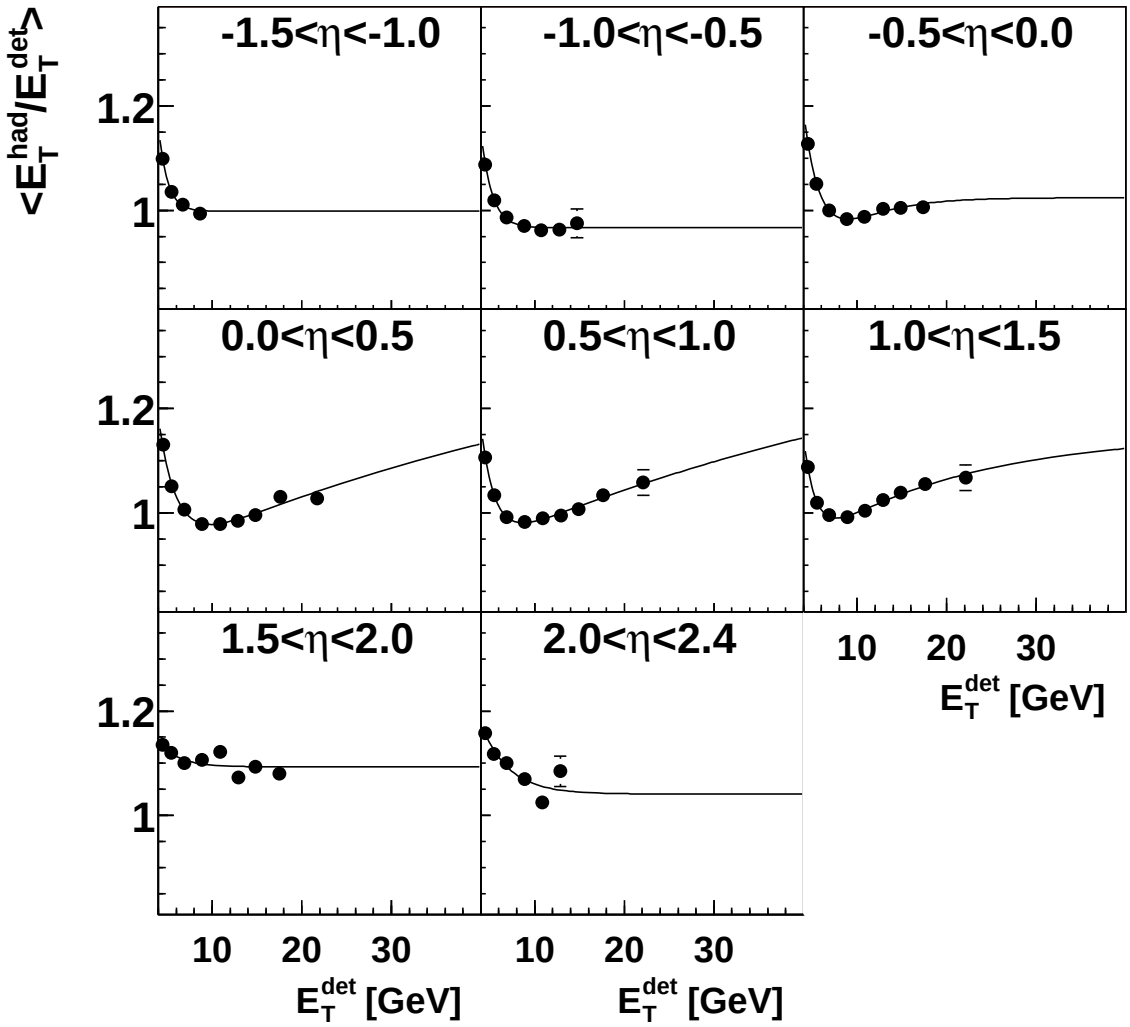

Figure 6.5: Correction factors obtained by HERWIG for each bin in η. The η ranges are indicated in each plot. The curve shows the result of a fit with a functional form given in eq. (6.4)

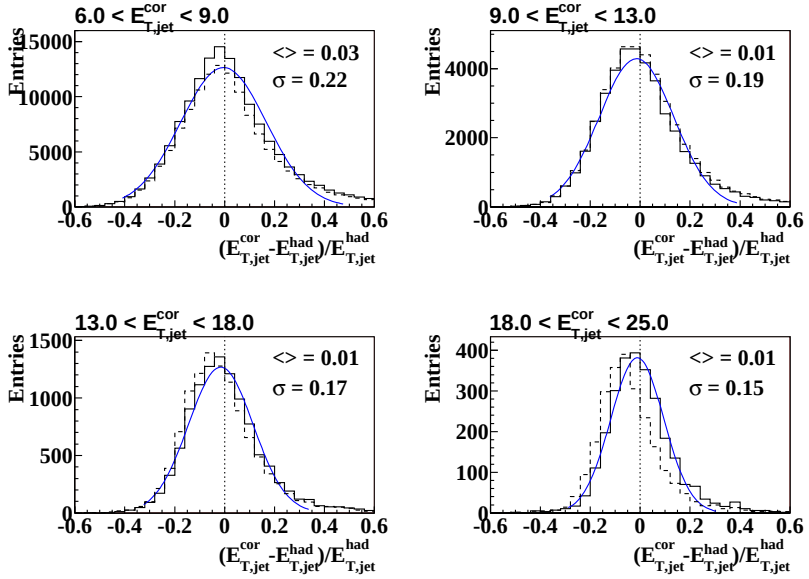

Figure 6.6: Comparison of the corrected jet transverse energy, E_T^{cor} to that of hadron level, E_T^{had}, in bins of E_T^{cor}.

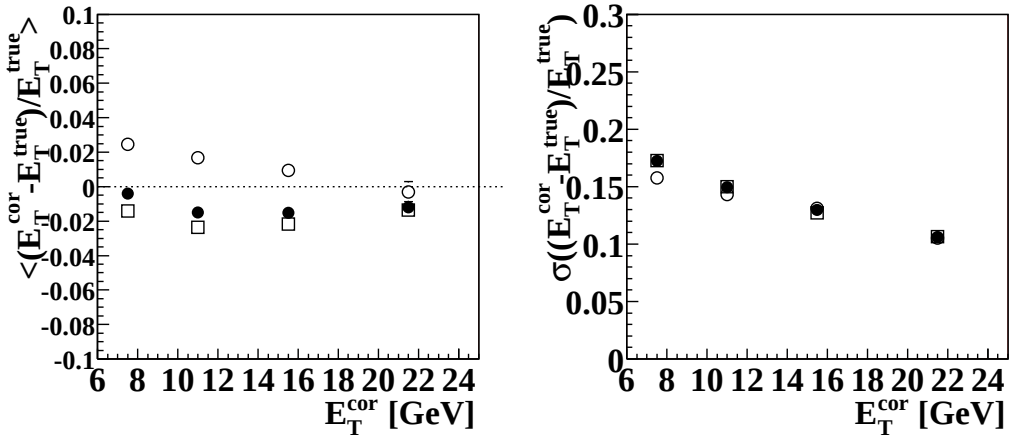

Figure 6.7: Difference (left) and resolution (right) of $(E_T^{cor} - E_T^{had})/E_T^{had}$ as a function of E_T^{cor}.

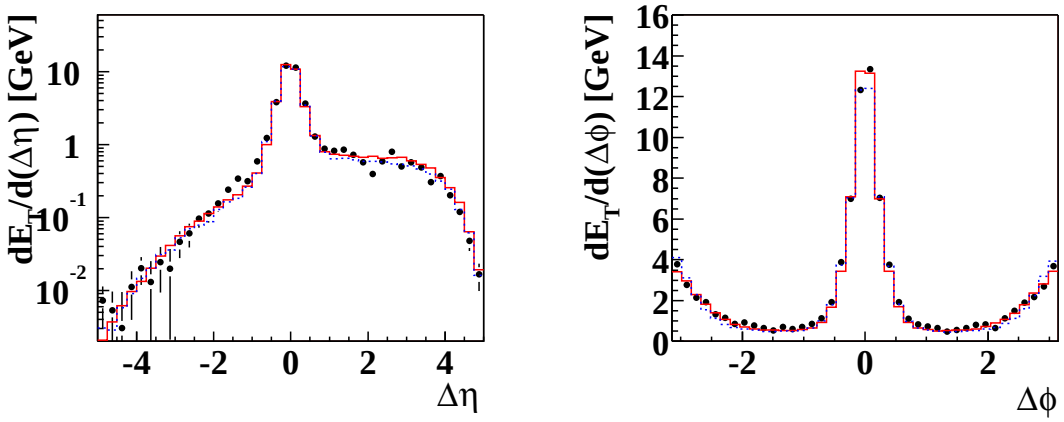

Figure 6.8: Transverse energy flow around the jet is shown as a function of $\Delta\eta$ (left) and $\Delta\phi$ (right). Data (dots) are compared to HERWIG (solid line) and PYTHIA (dashed line).

6.3 Transverse energy flow around the jet

In order to check that the quality of MC simulations, *jet profile* which is the transverse energy flow around the jet, has been compared between data and simulations. The transverse energies of EFOs are measured as a function of the difference of pseudo-rapidity or azimuthal angle between the EFO and the jet, $\Delta\eta = \eta_{EFO} - \eta_{jet}$ or $\Delta\phi = \phi_{EFO} - \phi_{jet}$. Only EFOs in the range $\Delta\phi < 1$ ($\Delta\eta < 1$) are used when plotting $dE_T/d(\Delta\eta)$ ($dE_T/d(\Delta\phi)$). In order to study the jet profile in charm events, contribution from combinatorial backgrounds are subtracted statistically in the plots. The measured $dE_T/d(\Delta\eta)$ and $dE_T/d(\Delta\phi)$ are are compared to HERWIG and PYTHIA in figure 6.8.

There are more transverse energy flow in the forward region ($\Delta\eta > 0$) of the jet. This is due to the interaction between the outgoing parton and the proton remnant, which creates hadrons within the gap. In figure 6.9, $dE_T/d(\Delta\eta)$ is shown in several bins of η^{jet}. The peak at the forward edge is an artifact due to the edge of the CAL. The energy flow in the rear direction increases for jets produced in forward directions. The jet profile is simulated well by the MC in the whole region.

In figure 6.10, jet profile is compared to HERWIG with contribution from direct and resolved processes shown seperately. Data distribution (dots), HERWIG (direct+resolved) (solid line), HERWIG (direct) (dashed line) and HERWIG (resolved) (dotted line) are shown together. The resolved process has more energy flow in the backward region, due to the photon remnant which goes into the backward region. On the other hand, if we only take into account the direct process, then the MC fails to describe the energy flow

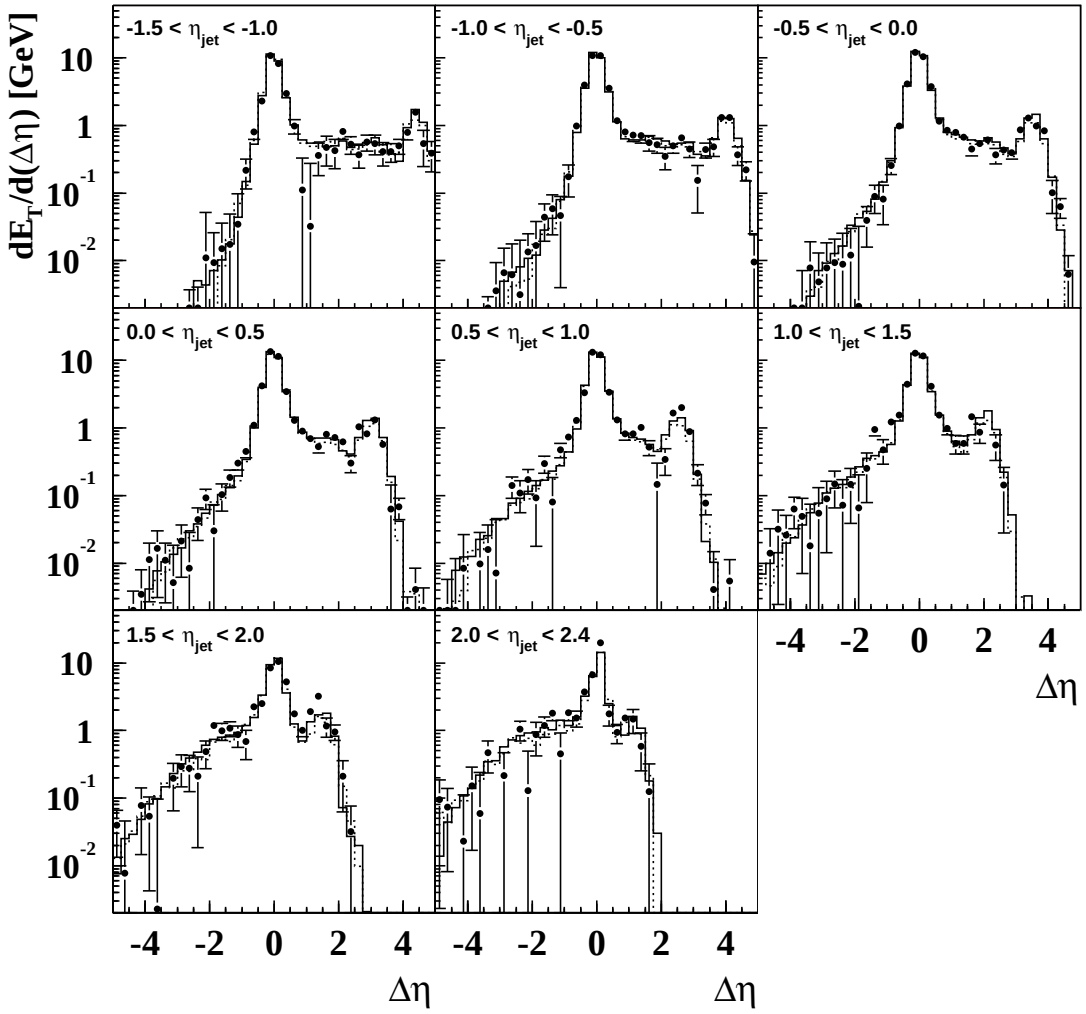

Figure 6.9: Jet profile in different bins of η_{jet}. The η^{jet} ranges are shown in each plot. Data points are shown by dots, HERWIG by the solid line and PYTHIA by dashed line.

in the $\Delta\eta < 0$ region. The fact that the transverse energy flow is described well justifies the ratio of direct to resolved process in the MC, which were generated according to the LO cross sections. The contribution from direct and resolved process after all cuts were found to be 65 % : 35 %, in HERWIG.

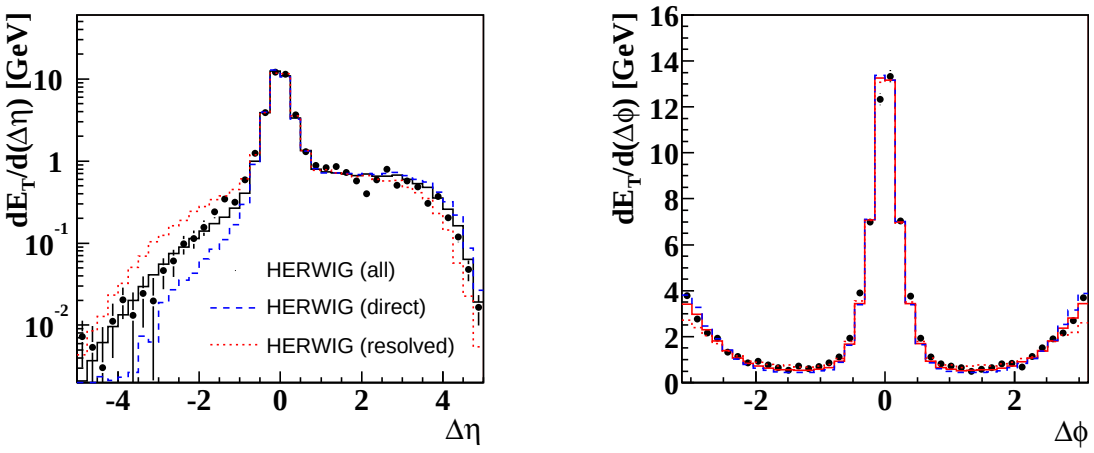

Figure 6.10: Jet profile of data (dots) are compared to HERWIG all (solid line), direct-only (dashed line) and resolved-only (dashed line).

6.4 Contribution from b-quark production

A D^* can be also produced from the decays of B-mesons. The contribution from b-quark production has been estimated by the MC. Figure 6.11 shows the E_T and η distribution of HERWIG (charm+bottom) and HERWIG (bottom). The b fraction is about 3 % at low E_T and increases as E_T get larger up to 12 % at the highest E_T.

The contribution is smaller than the statistical uncertainty in most of the bins and furthermore there is a large theoretical uncertainty in b quark production, therefore, we do not subtract b contribution. The measured cross section is defined as the cross section with a D^* regardless of its origin, so that the contribution from b-decay is included.

6.5 Jet distributions

After transverse energy of jets are corrected, reconstructed jet distributions are compared to MC expectations. These distributions are obtained for D^* events, by subtracting non-D^* backgrounds statistically for each bin.

The Δm signal is shown for each bin of E_T^{jet} and η^{jet} distributions in figures 6.12 and 6.13, respectively. The clear peak is observed in all bins shown in the figures. A peak exist even at the highest E_T^{jet} bin of $18 < E_T^{jet} < 25$ GeV. Figure 6.13 shows that the fraction of the combinatorial background increases as the jet goes to the forward region. This is due to the fact that there are more energy flow, so as the track, in the positive η region. When jets are produced in the forward region, the probability of having ramdom

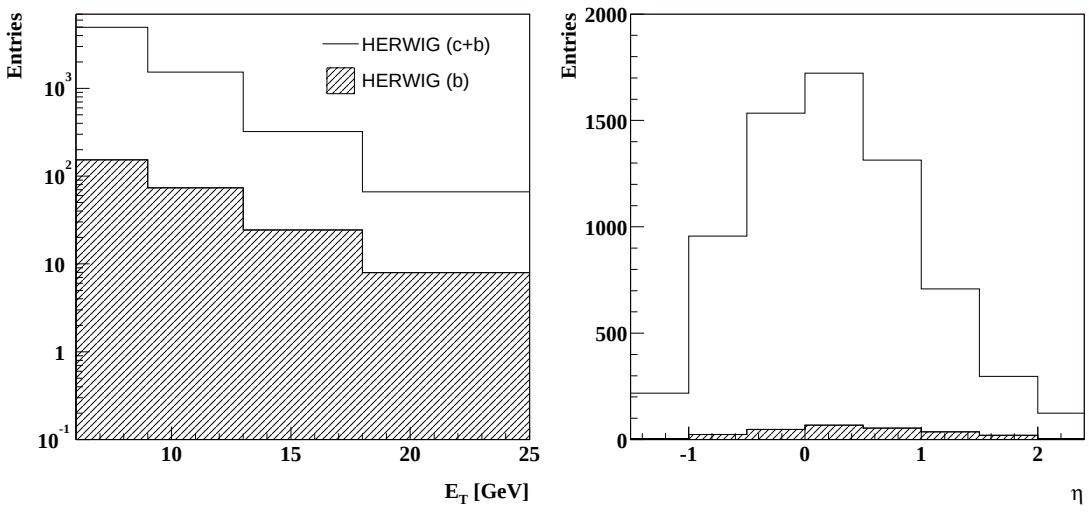

Figure 6.11: Distribution of E_T^{jet} and η^{jet}. Distributions of HERWIG (charm+bottom) and HERWIG (bottom) are shown in solid lines and hatch histograms respectively.

combination of tracks in the mass window increases. Algthough the background increases, the signal is still clearly seen.

In the rest of the sections in this chapter, we show the kinematical distributions of jets, to compare between data, HERWIG and PYTHIA. The MC sample includes both charm and beauty contributions.

It was found that both MCs underestimate the reconstructed distribution, when they are normalized by the luminosities. These MCs are used for unfolding the detector effects so that, in the comparison, we are only interested in the shape of the distributions. For this purpose, HERWIG and PYTHIA plots are scaled by 2.4 and 1.5 respectively.

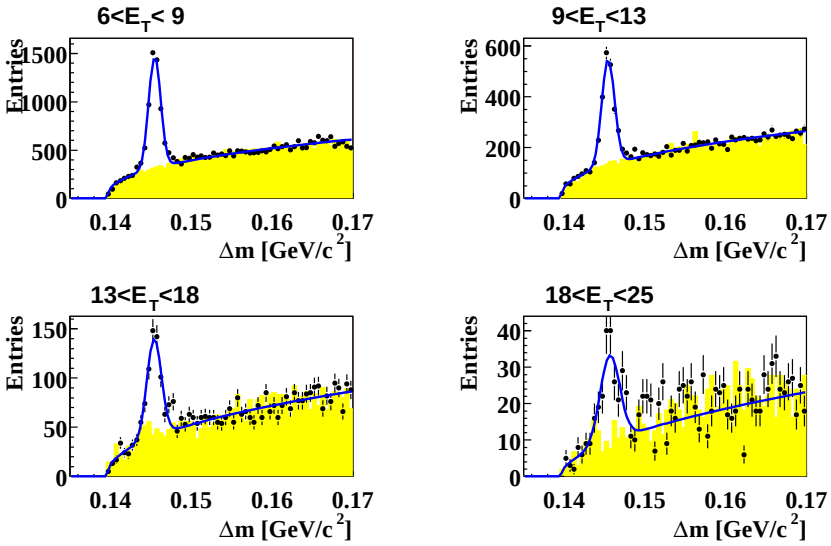

Figure 6.12: Δm distribution for each bin of E_T^{jet}.

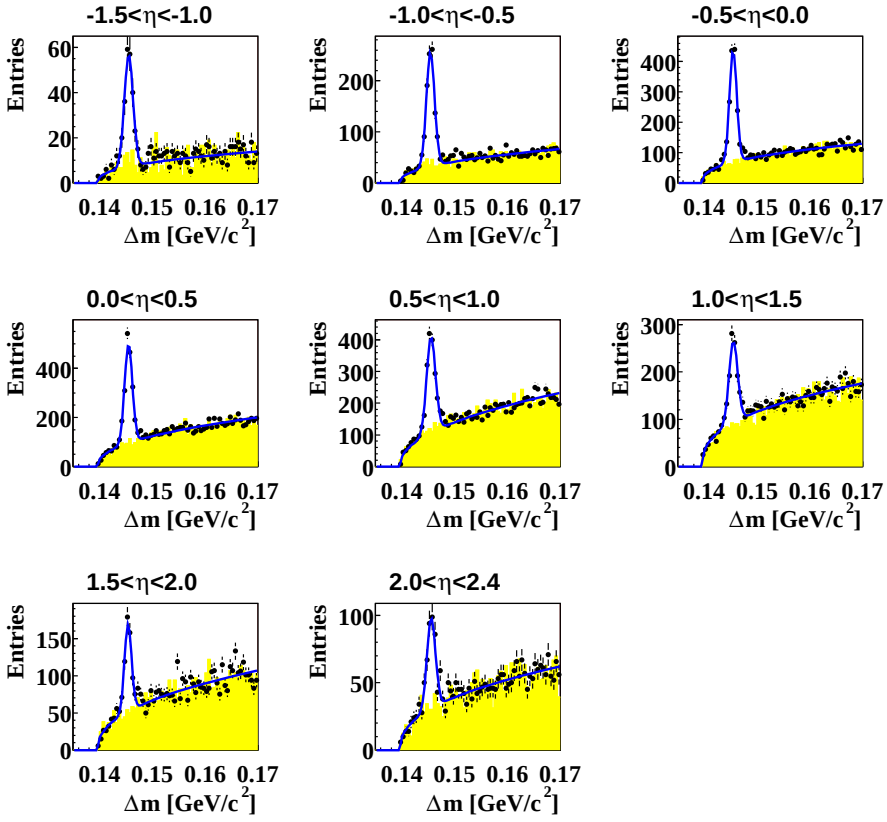

Figure 6.13: Δm distribution for each bin of η^{jet}.

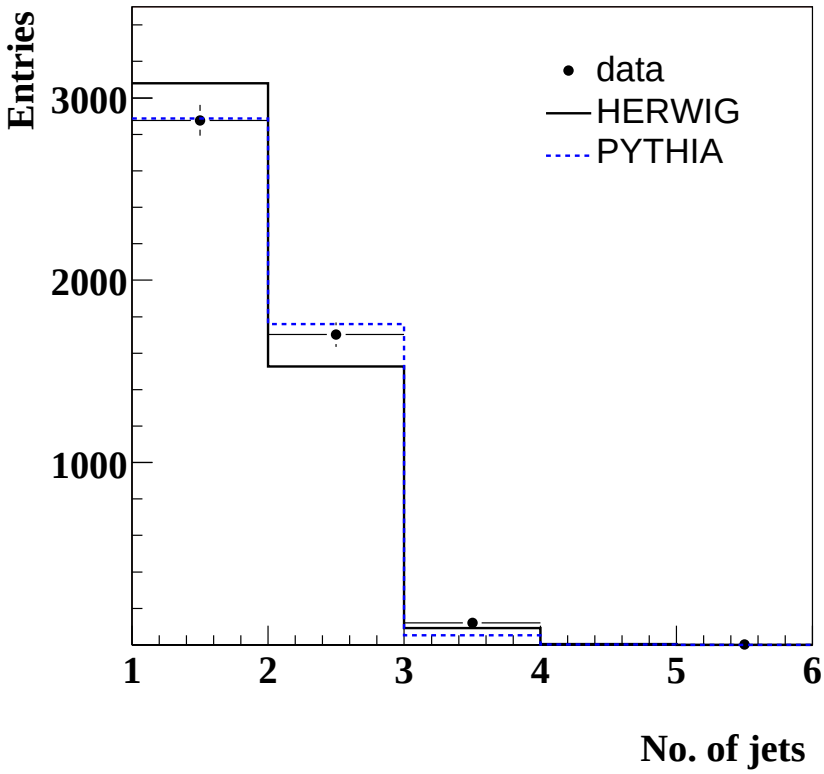

Figure 6.14: The distribution of jet multiplicity in the final sample.

6.5.1 Jet multiplicity

The jet multiplicity in each event is shown in figure 6.14 together with the expectation of HERWIG and PYTHIA. The black dots represent the data, solid line represents HERWIG and dashed line represent the expectation of PYTHIA. About 60 % of the events are one-jet events. Data agrees well to PYTHIA, while HERWIG predicts a larger fraction of one-jet events.

6.5.2 E_T^{jet} distributions

In figure 6.15, E_T^{jet} distribution in $-1.5 < \eta^{jet} < 2.4$ is shown. The distribution is described well by both MC except for the highest E_T^{jet} bin, where both MC lies below data. Figure 6.16 shows E_T^{jet} distributions in restricted ranges of η^{jet}: $-1.5 < \eta^{jet} < -0.5$, $-0.5 < \eta^{jet} < 0.5$, $0.5 < \eta^{jet} < 1.5$ and $1.5 < \eta^{jet} < 2.4$. The distribution is in reasonable agreement with MC. In $1.5 < \eta^{jet} < 2.4$, data is higher than the MC expectations.

6.5.3 η^{jet} distributions

Figure 6.17 shows the η^{jet} distribution in $E_T^{jet} > 6$ GeV. As for the E_T^{jet} distribution, data (dots) is compared to HERWIG (solid histogram) and PYTHIA (dashed histogram). Also the HERWIG resolved contribution (hatched histogram) is shown together. Data distribution is shifted to the forward direction compared to both MC. HERWIG describes the data slightly better.

The distribution of η^{jet} in low and high E_T^{jet} regions, $6 < E_T^{jet} < 9$ GeV and $E_T^{jet} > 9$ GeV are shown in figure 6.18, showing reasonable agreement between data and MC.

The contribution of the resolved photon process increases at forward region, since only part of the photon energy participates in the hard scattering and the system is boosted towards the forward direction. On the other hand, the rear region is dominated by the direct photon process.

6.5.4 D^* jets and other jets

Distributions for D^* jets and other jets are presented. E_T^{jet} distribution is shown figure 6.19. Both distributions are described reasonably well by the MC. As in the inclusive jet distribution, an excess of data is observed at the highest E_T^{jet} bin.

Figure 6.20 (a), (c) and (e) shows the η^{jet} distributions of D^* jet in $E_T^{jet} > 6$ GeV, $6 < E_T^{jet} < 9$ GeV and $E_T^{jet} > 9$ GeV, respectively. D^* jet is always reconstructed in the central part independent of direct or resolved, because a D^* needs to be tagged in $|\eta(D^*)| < 1.5$.

Same distributions for other jets are shown in figure 6.20 (b), (d) and (f). As can be seen in the plots, resolved photon contribution becomes dominant at forward region, where the shape of the distribution is different from the total distribution. Therefore, it might have some sensitivity to the parton level processes involved.

Although data is shifted towards forward direction in most of the plots, MC describes the data rather well.

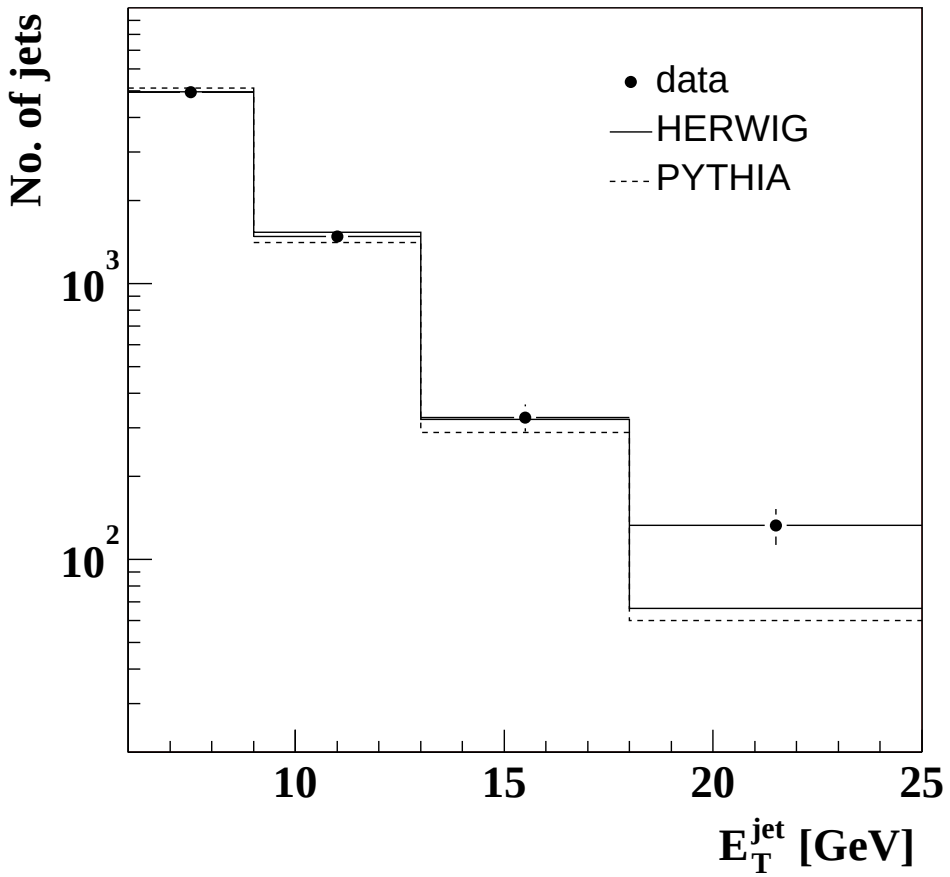

Figure 6.15: The E_T^{jet} distribution in $-1.5 < \eta^{jet} < 2.4$. Data (dots) is compared to HERWIG (solid histogram) and PYTHIA (dashed histogram), where both MC includes contribution from c and b production.

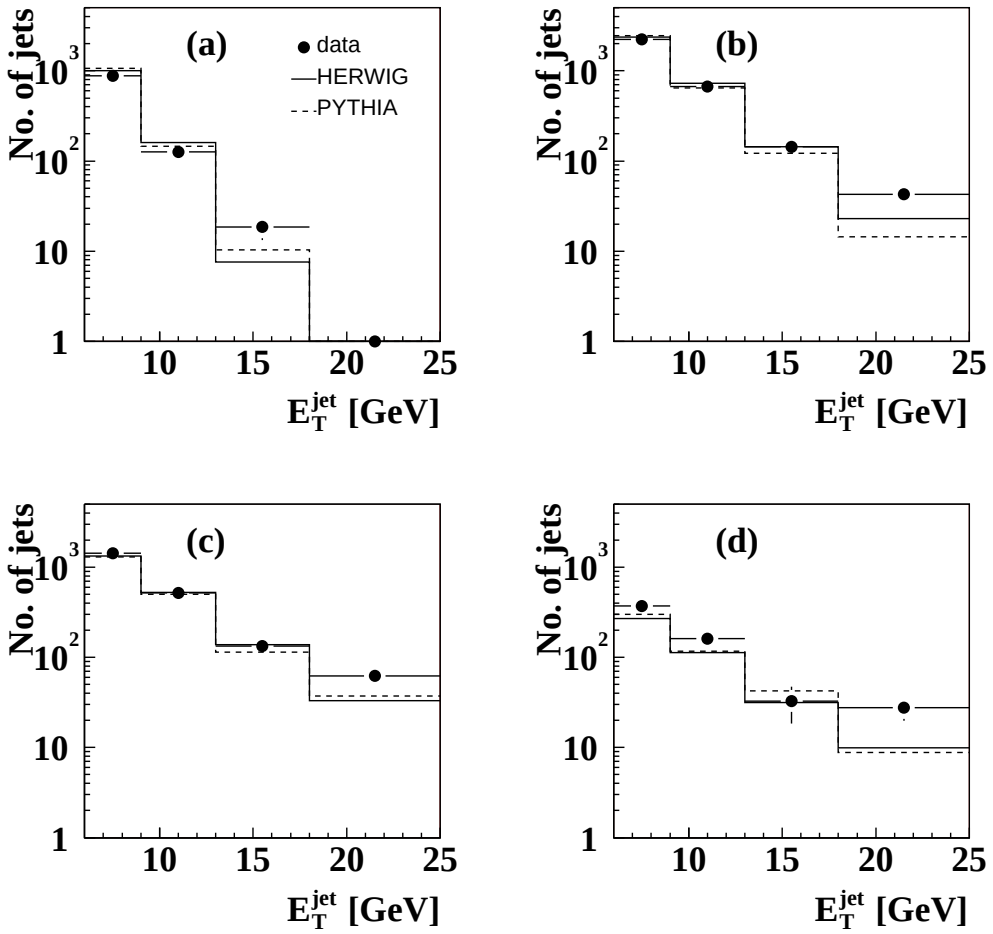

Figure 6.16: The E_T^{jet} distribution in (a) $-1.5 < \eta^{jet} < -0.5$, (b) $-0.5 < \eta^{jet} < 0.5$, (c) $0.5 < \eta^{jet} < 1.5$ and (d) $1.5 < \eta^{jet} < 2.4$. Data (dots) is compared to HERWIG (solid histogram) and PYTHIA (dashed histogram), where both MC includes contribution from c and b production.

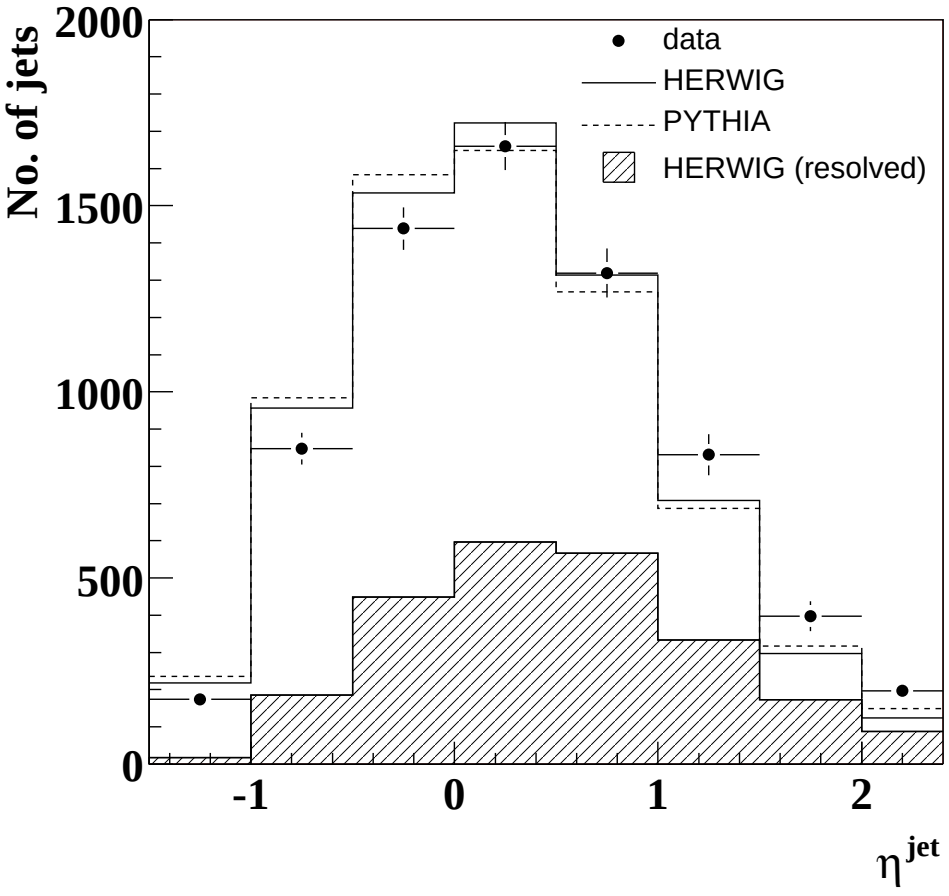

Figure 6.17: η^{jet} distribution in $E_T^{jet} > 6$ GeV. Data (dots) is compared to HERWIG (solid histogram) and PYTHIA (dashed histogram). The HERWIG resolved contribution is shown as a hatched histogram.

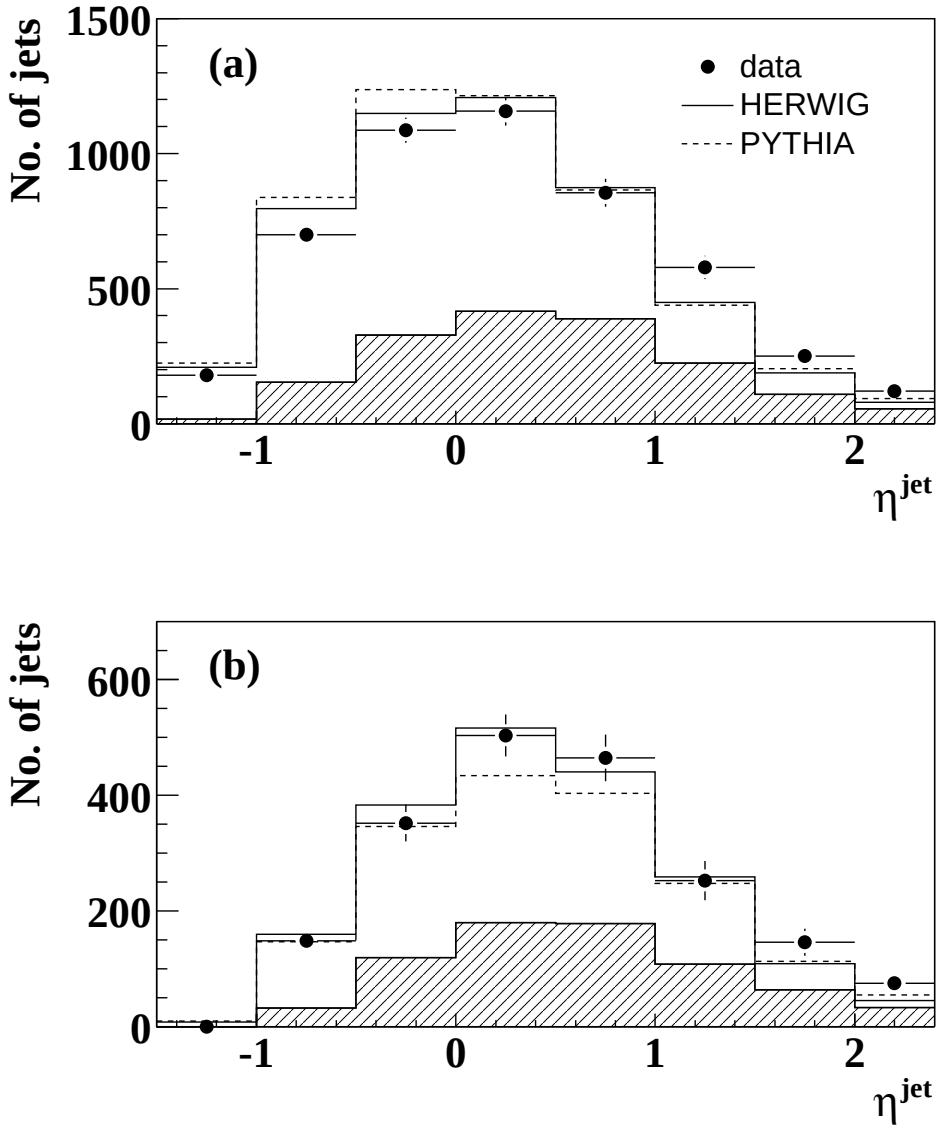

Figure 6.18: The η^{jet} distribution in (a) $6 < E_T^{jet} < 9$ GeV and (b) $E_T^{jet} > 9$ GeV. Data (dots) is compared to HERWIG (solid histogram) and PYTHIA (dashed histogram). The HERWIG resolved contribution is shown as a hatched histogram.

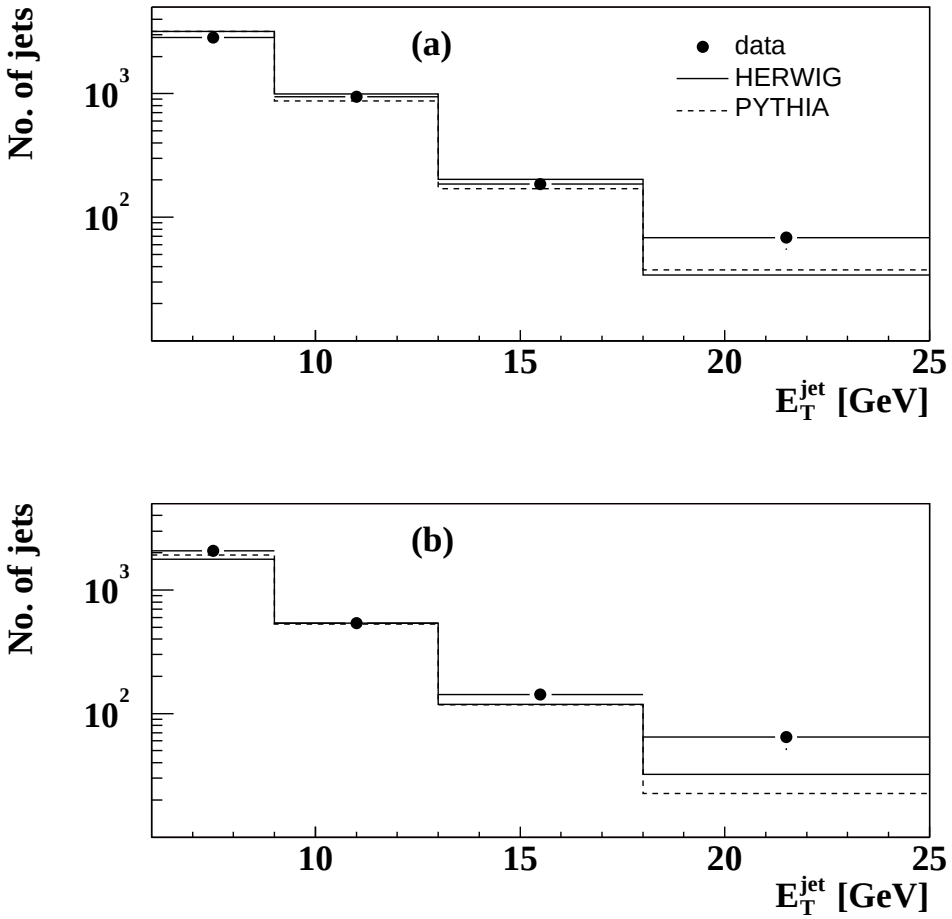

Figure 6.19: The E_T distribution of jets in $-1.5 < \eta^{jet} < 2.4$ for (a) D^* jets and (b) other jets. Data (dots) is compared to HERWIG (solid histogram) and PYTHIA (dashed histogram).

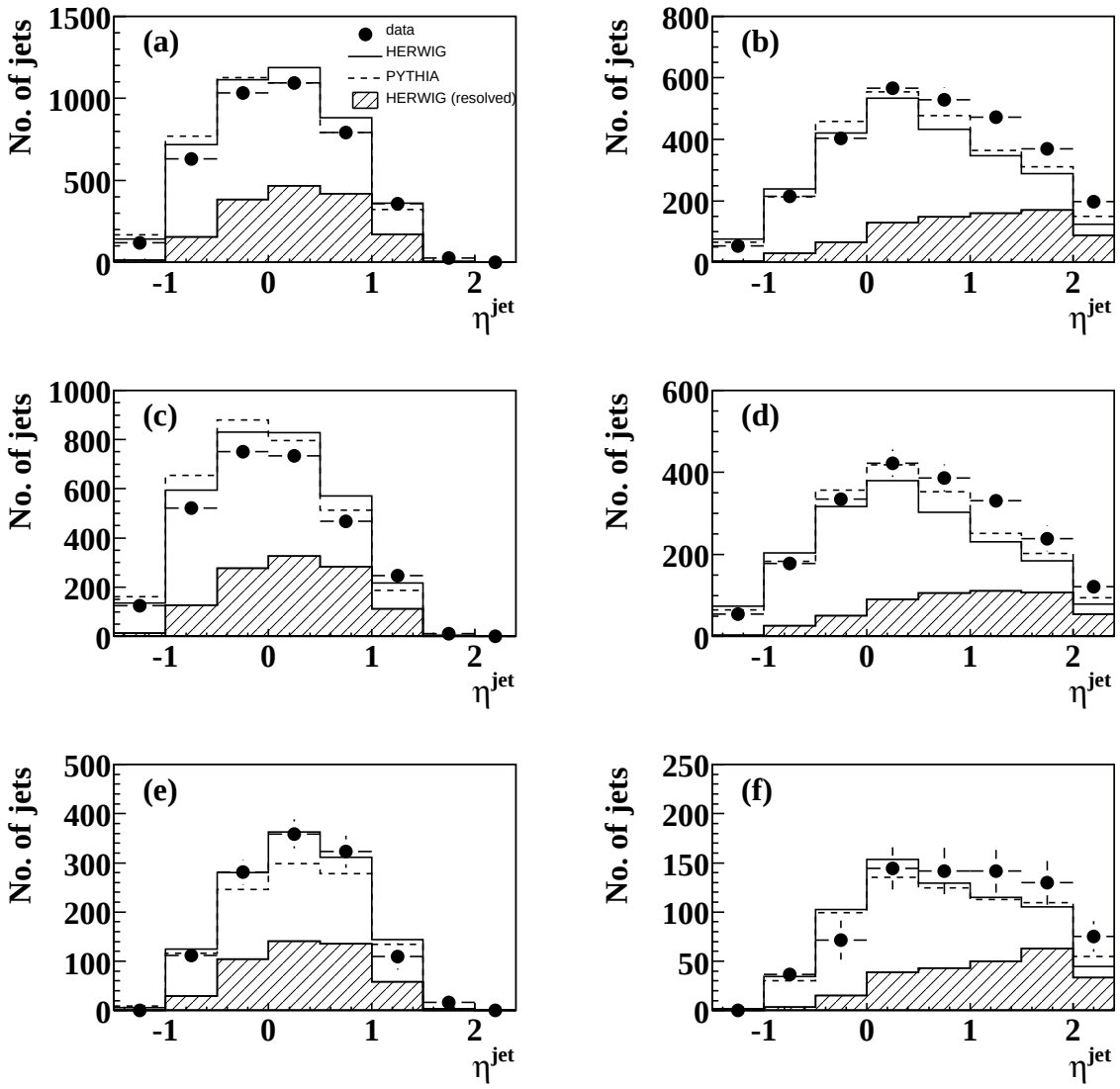

Figure 6.20: The η^{jet} distribution of D^* jets for (a) $E_T^{jet} > 6$ GeV, (c) $6 < E_T^{jet} < 9$ GeV and (e) $E_T^{jet} > 9$ GeV, and that of other jets for (b) $E_T^{jet} > 6$ GeV, (d) $6 < E_T^{jet} < 9$ GeV and (f) $E_T^{jet} > 9$ GeV. Data (dots) is compared to HERWIG (solid histogram) and PYTHIA (dashed histogram). The HERWIG resolved contribution is shown as a hatched histogram.

Chapter 7

Cross section measurement

In the previous two chapters, events containing a D^* meson and a jet were selected. Corrections on y_{JB} and jet transverse energy have been made. Detector level distributions of selected events were compared to MC models showing reasonable agreement. In this chapter, first, the cross sections to be measured are defined. Then the method to unfold the cross section from the detector level distribution is described.

7.1 Definition of cross sections

Inclusive jet cross secions with a D^* in the final state are measured as a function of E_T^{jet} ($d\sigma/dE_T^{jet}$) and η^{jet} ($d\sigma/d\eta^{jet}$) in the following kinematic region.

$$Q^2 < 1 \text{ GeV}^2 \tag{7.1}$$

$$130 < W < 280 \text{ GeV} \tag{7.2}$$

$$p_T(D^*) > 3 \text{ GeV/c} \tag{7.3}$$

$$|\eta(D^*)| < 1.5 \tag{7.4}$$

$$E_{T,jet} > 6 \text{ GeV} \tag{7.5}$$

$$-1.5 < \eta_{jet} < 2.4 \tag{7.6}$$

The jet cross section are *inclusive* so that, for example, dijet events contribute twice (one for each jet). Differential cross sections $d\sigma/dE_T^{jet}$ and $d\sigma/d\eta^{jet}$ are measured in the kinematic region defined in eq. (7.1) to (7.6).

The cross section $d\sigma/dE_T^{jet}$ is also shown in seperate η^{jet} regions, $-1.5 < \eta^{jet} < -0.5$, $-0.5 < \eta^{jet} < 0.5$, $0.5 < \eta^{jet} < 1.5$ and $1.5 < \eta^{jet} < 2.4$. The cross section $d\sigma/d\eta^{jet}$ is shown for low and high E_T^{jet} regions, $6 < E_T^{jet} < 9$ GeV and $E_T^{jet} > 9$ GeV.

We also obtain the cross sections seperately for D^* jets and other jets, where association of D^* and jets are done based the seperation in $\eta - \phi$ plane (ΔR), such that D^* jet is defined as the closest jet to the D^* with in $\Delta R < 0.6$. Jets not identified as a D^* jet is

defined as other jet. The distribution of D^* jets are limited in the central region because of the $|\eta(D^*)| < 1.5$ requirement. In LO MC, distributions of other jets showed some sensitivitiy to the parton level processes contritubing to charm photoproduction, as seen in figure 6.20, where resolved contribution is enhanced in the forward region. Although at NLO, the distinction between direct and resolved processes are more ambiguous, it is worthwhile to see whether there are any differences of the shape of $d\sigma/d\eta^{jet}$ between data and NLO prediction for other jets. Cross sections of D^* jets and other jets are also presented as a function of E_T^{jet} or η^{jet} in the kinematic region defined for inclusive jets, except for $d\sigma/dE_T^{jet}$, which is shown only for the entire region of η^{jet}, due to the limited statistics.

7.2 Unfolding method

Cross sections are obtained from the detector level distributions by a bin-by-bin unfolding procedure. For a differential cross section with respect to a variable X, the number of jets observed in a certain bin i, N_i^{obs}, is unfolded to the number of jets in that bin at hadron level N_i^{had} taking into account the detector effects and selection efficiencies. N_i^{had} is obtained from N_i^{obs} by

$$N_i^{had} = \mathcal{C}_i \cdot N_i^{obs}, \tag{7.7}$$

where the acceptance correction factors $\mathcal{C}_i$ are estimated from the MC simulation. We use HERWIG as the default MC and PYTHIA as a cross check. The correction factors are obtained by the MC as the ratio of the cross section at hadron level and detector level.

$$\mathcal{C}_i = \left(\frac{d\sigma_i^{had}}{d\sigma_i^{det}}\right)_{MC} \tag{7.8}$$

Differential cross section in the bin i, $(\sigma/dX)_i$, is calculated from the number of observed jets N_i^{obs}, the integrated luminosity $\mathcal{L}$, i.e. 78.6 pb^{-1} and the correction factor defined in eq. (7.8) as

$$\left(\frac{d\sigma}{dX}\right)_i = \mathcal{C}_i \cdot \frac{N_i^{obs}\cdot}{\mathcal{L} \cdot \mathcal{B}r(D^* \to K\pi\pi) \cdot \Delta X}, \tag{7.9}$$

where $\mathcal{B}r(D^* \to K\pi\pi)$ is the overall branching ratio of a D^* decaying into $K\pi\pi$ mode which is given by the product of eq. (5.11) and (5.12) as $\mathcal{B}r(D^* \to K\pi\pi) = 2.57$ %.

In order to qualify the correction factors $\mathcal{C}_i$, efficiency $\mathcal{E}_i$ and purity $\mathcal{P}_i$ of each bin i are checked. They are defined as

$$\mathcal{E}_i = \frac{N_i^{had\cap \det}}{N_i^{had}}, \tag{7.10}$$

$$\mathcal{P}_i = \frac{N_i^{had\cap \det}}{N_i^{det}}, \tag{7.11}$$

where $N_i^{had \cap \mathrm{det}}$ is the number of jets generated in bin i and also reconstructed at the detector level in that bin. Efficiency represents the probability to reconstruct a jet in the same bin as the bin which it was generated in. Purity represents the fraction of jets which were generated in that bin with respect to the number of reconstructed jets in that bin.

The acceptance correction factor $\mathcal{C}_i$ is related to $\mathcal{E}_i$ and $\mathcal{P}_i$ by

$$\mathcal{C}_i = \frac{\mathcal{P}_i}{\mathcal{E}_i}. \tag{7.12}$$

Efficiencies of measured cross sections as a function of E_T^{jet} (η^{jet}) are shown in figure 7.1 (figure 7.2). The efficiency is around 30 %. It decrease slowly towards high E_T^{jet}. As a function of η^{jet}, the efficiency drops at $\eta^{jet} < -1$ or $\eta^{jet} > 1$. This is mainly due to the selection of a D^* in $|\eta| < 1.5$. As described in the next section, the requirement on the D^* decay products worsen the efficiency. The efficiency is a product of the efficiency of cuts applied to select events $\mathcal{E}_i^{sel}$ and the one due to the migration between neighboring bins $\mathcal{E}_i^{mig}$. The selection efficiency $\mathcal{E}_i^{sel}$ is discussed in the next section. The migration efficiency is about 60 % as the bin size is taken as about 2 times the resolution.

Purities of measured cross sections as a function of E_T^{jet} (η^{jet}) are shown in figure 7.3 (figure 7.4). Purity is around 60 %, being flat with respect to E_T^{jet}. This is consistent with the fact that the size of the bins were taken as, approximatelty, two times the resolution. The purity drops at the most backward and forward regions, due to the worse resolution or η^{jet} at these regions, similar to the efficiency.

Correction factors for measured cross sections as a function of E_T^{jet} (η^{jet}) are shown in figure 7.5 (figure 7.6). The size of the correction is typically 2-3.

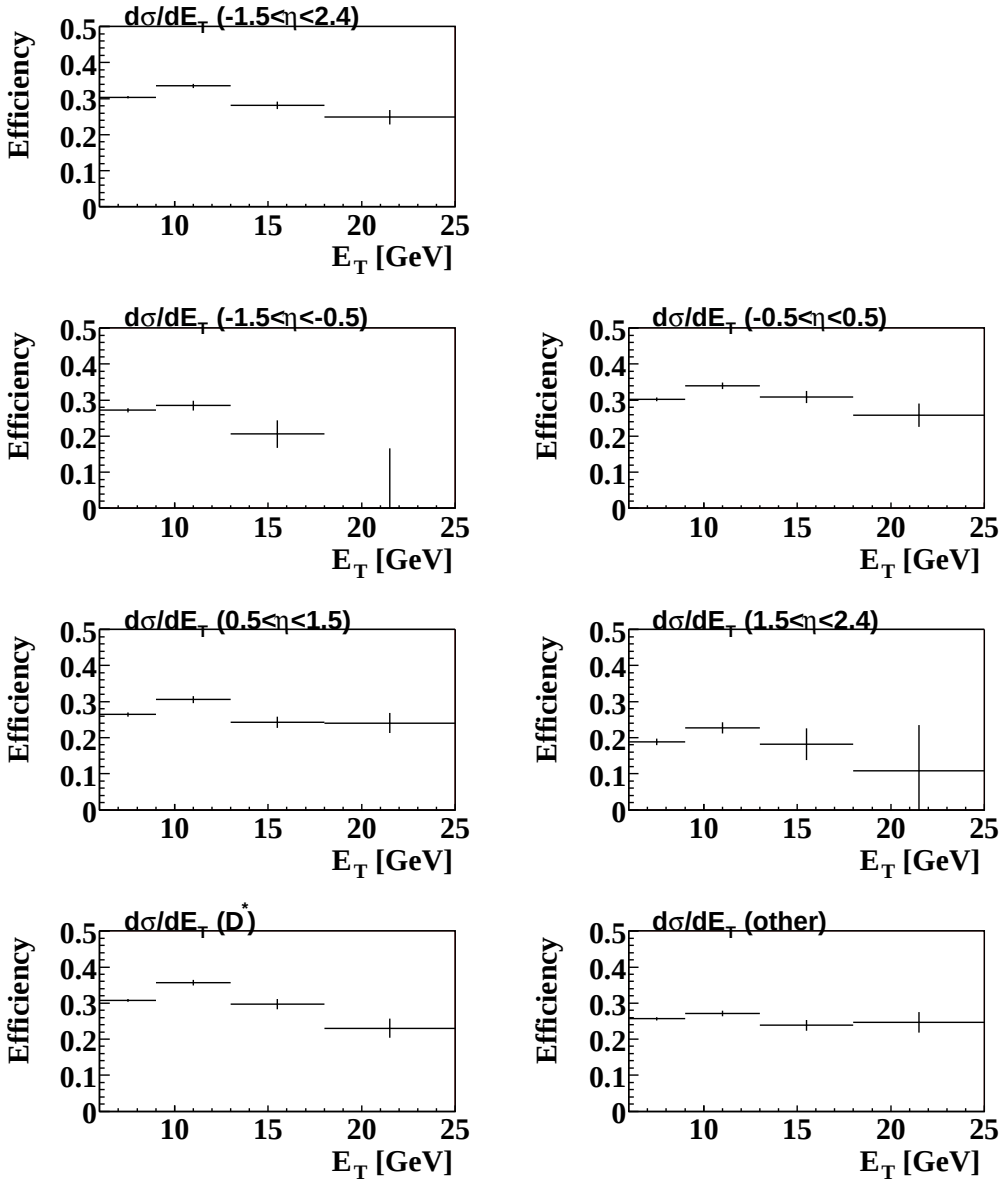

Figure 7.1: Efficiencies for the $d\sigma/dE_T^{jet}$ measurements. The η^{jet} ranges are shown at the top of each plot.

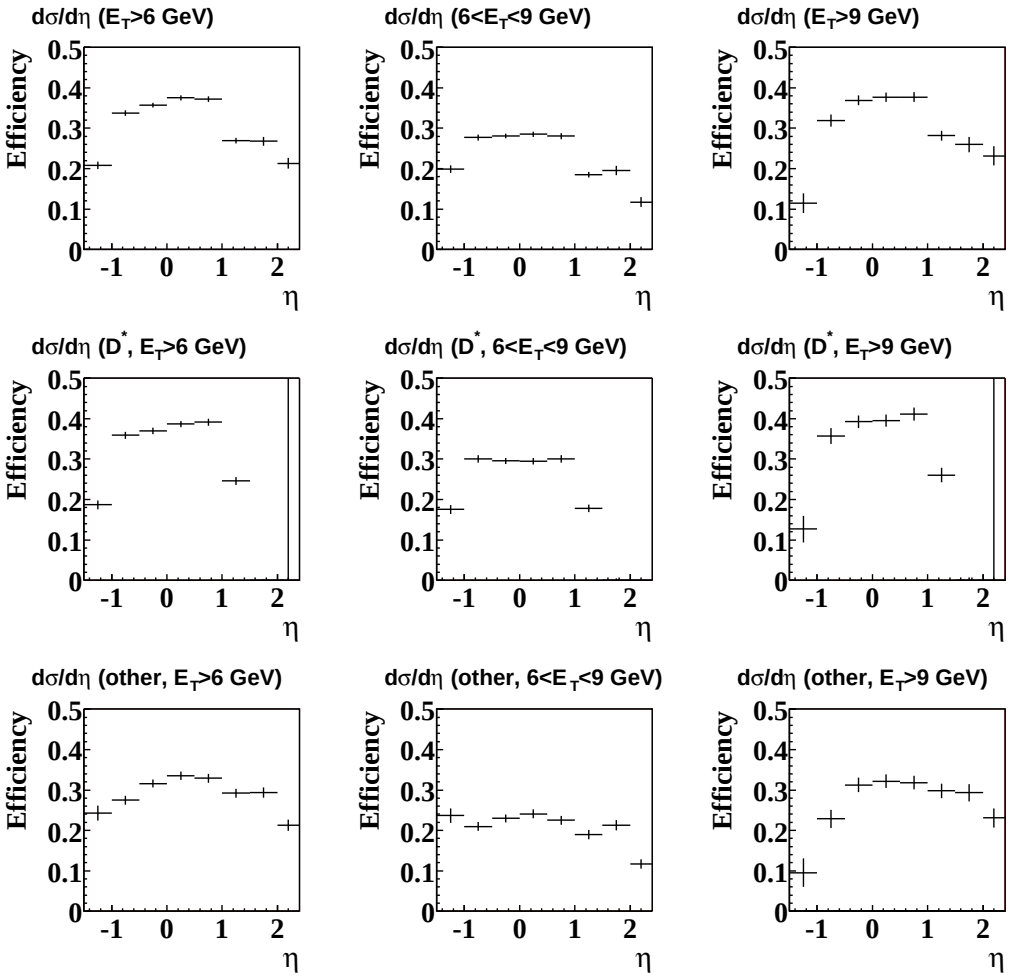

Figure 7.2: Efficiencies for the $d\sigma/d\eta^{jet}$ measurements. The E_T^{jet} ranges are shown at the top of each plot.

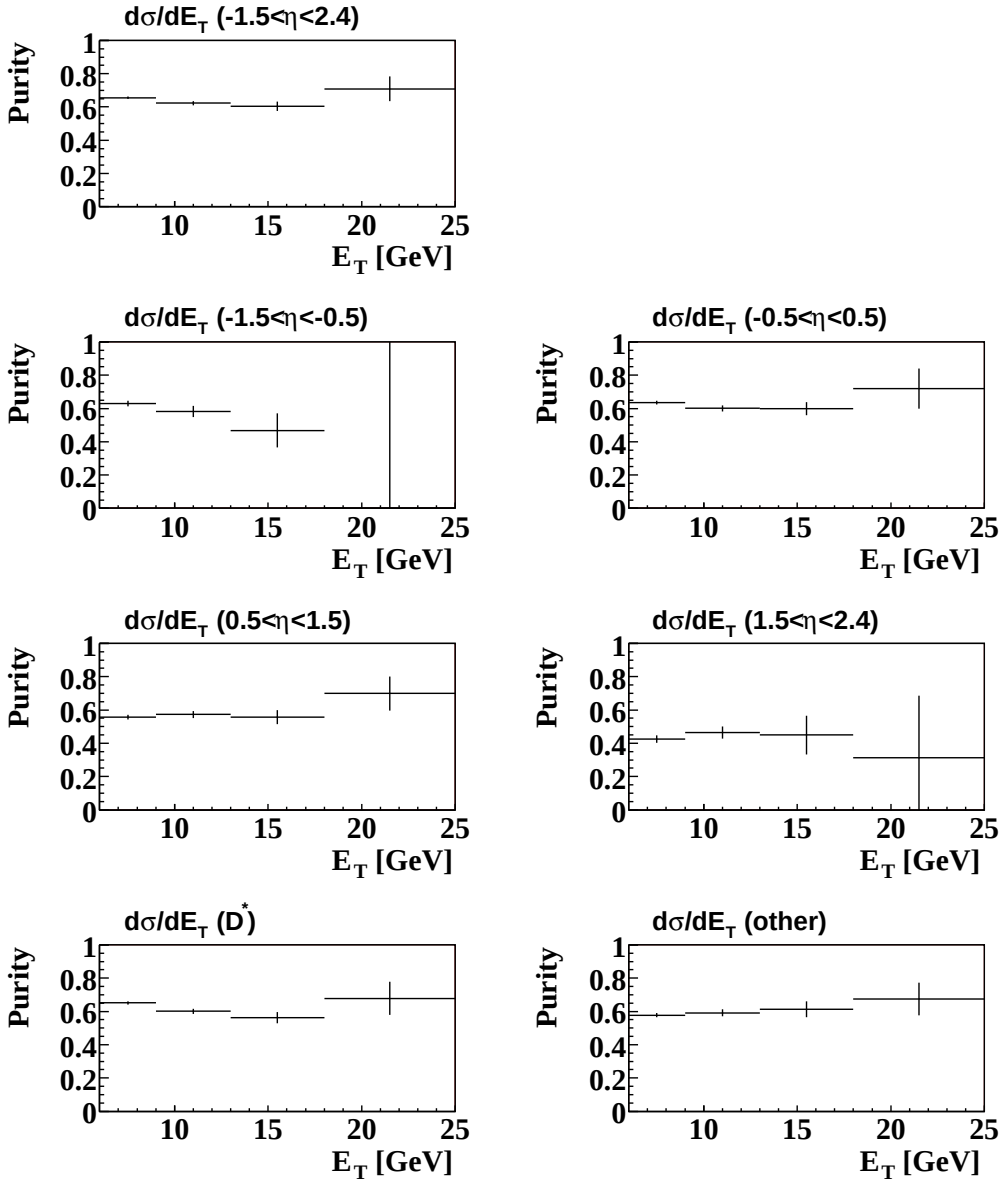

Figure 7.3: Purities for the $d\sigma/dE_T^{jet}$ measurements. The η^{jet} ranges are shown at the top of each plot.

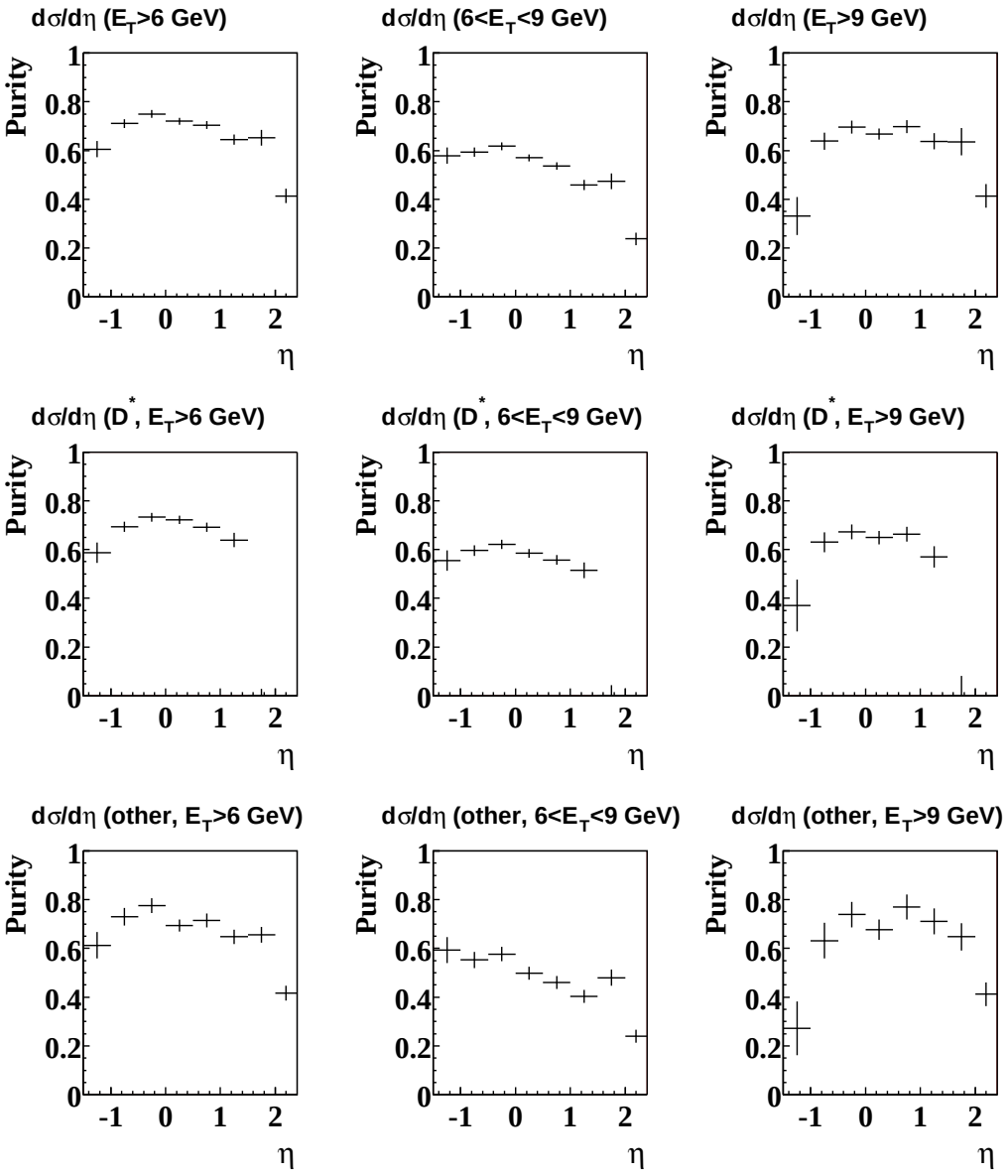

Figure 7.4: Purities for the $d\sigma/d\eta^{jet}$ measurements. The E_T^{jet} ranges are shown at the top of each plot.

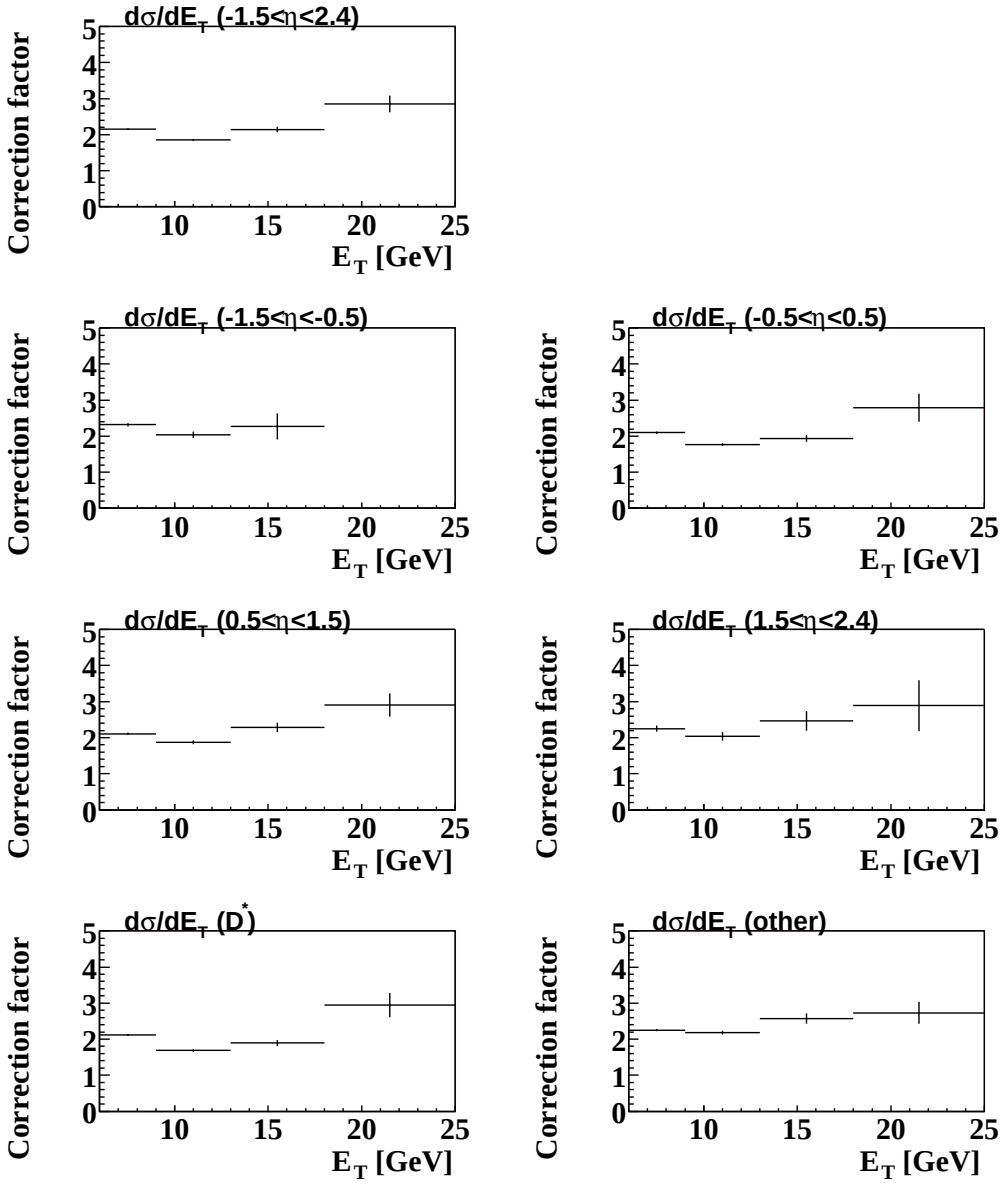

Figure 7.5: Correction factors for the $d\sigma/dE_T^{jet}$ measurements. The η^{jet} ranges are shown at the top of each plot.

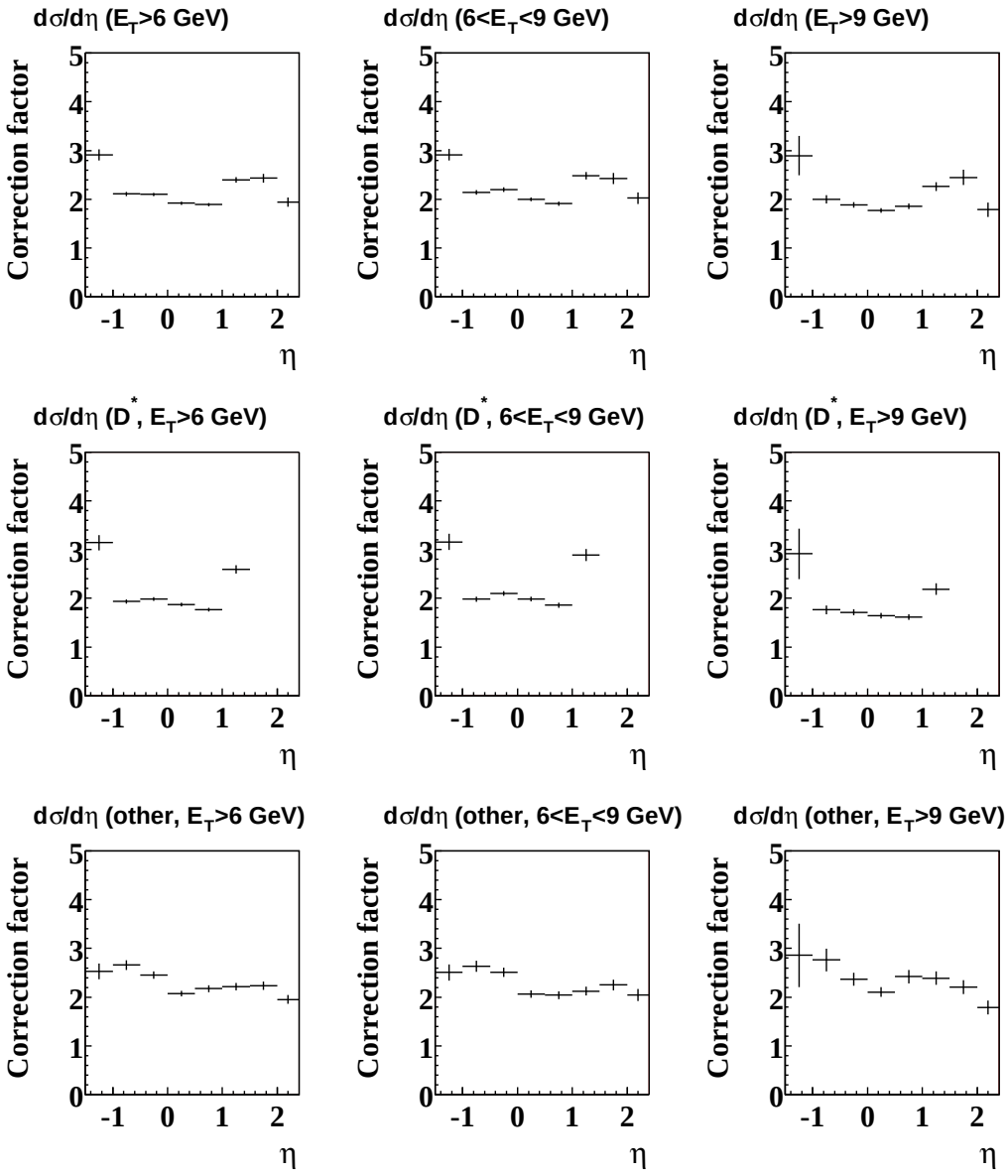

Figure 7.6: Correction factors for the $d\sigma/d\eta^{jet}$ measurements. The E_T^{jet} ranges are shown at the top of each plot.

7.2.1 Selection efficiency

The efficiency of each bin is a product of efficiencies of selection cuts and the efficiency due to the migration between bins. In order to check the efficiency of each selection cut k, we define the selection efficiency in bin i, $\mathcal{E}_i^k$ by

$$\mathcal{E}_i^k = \frac{N_i^{had \cap cut1,2,\ldots,k}}{N_i^{had \cap cut1,2\ldots,k-1}}. \tag{7.13}$$

The selection efficiency $\mathcal{E}_i^k$ is defined as the relative efficiency after applying each cut, i.e., the efficiency of the k-th cut is evaluated by taking the ratio of the number of events passing the cut k with respect to the number of events passing all preceding cuts. We start from the sample of events passing the cuts at hadron level, i.e. all generated events. In order to evaluate the effect of each cut, jet variables of hadron level are used in all cases, thus the migration effect between η^{jet} bins or E_T^{jet} bins are not considered.

Selection efficiencies were evaluated by applying the following cuts in the written order.

1. Trigger
2. Z-vertex cut
3. Electron rejection
4. W cut
5. Track selection for D^* decay products
6. D^* kinematic range

For example, $\mathcal{E}_i^1$ represents the efficiency of selecting a jet in bin i after requiring a trigger selection, with respect to all generated jets at hadron level. The $\mathcal{E}_i^2$ represents the efficiency of Z-vertex cut with respect to events which were generated and pass trigger selection, and so on.

When evaluating the effect of the track selection for D^* decay products, tracking cuts were applied to the true tracks in the MC. This was done in order to isolate the selection on the decay products from the migration effect due to finite $p_T(D^*)$ or $\eta(D^*)$. Then at the next cut, i.e. D^* kinematic range, tracking cuts and kinematic cuts of $p_T(D^*)$ and $\eta(D^*)$ are required to the reconstructed quantities.

Figure 7.7 shows the selection efficiecnies for these cuts. The efficiency of triggers (FLT, SLT and TLT) is around 70 %, decreasing at low E_T^{jet} as expected from the FLT selection. A detailed study of FLT efficiency are presented in appendix C. The efficiency of requiring Z-vertex to be reconstructed around the nominal vertex position was more than 99.9 %. The efficiencies of photoproduction selection cuts with electron rejection is

about 98 %. The efficiency of W cut, which is equivalent to the cut on y_{JB}, is about 98 % at large η^{jet}, while it decreases at negative η^{jet}. This is due to the fact that those event with a jet in the negative η^{jet} are boosted towards backward region, therefore have a large incoming momentum towards backward region. This means that, in these events, the energy of the photon emitted from the incoming electron is large, therefore the photon-proton CM energy, W becomes high. The drop of the efficiency of W cut in the backward region comes from the cut at high W. The efficiency of the tracking cuts applied to D^* decay products is 70 - 80 %. The efficiency becomes slightly lower at $|\eta^{jet}| > 1$, since tracks may get out of the CTD acceptance. Even the D^* exist within $|\eta| < 1.5$, if one of the tracks of its decay particles goes in $|\eta| > 1.75$, those events are rejected. The selection of D^* kinematic region removes only a small number of events since the resolution of $p_T(D^*)$ and $\eta(D^*)$ is good.

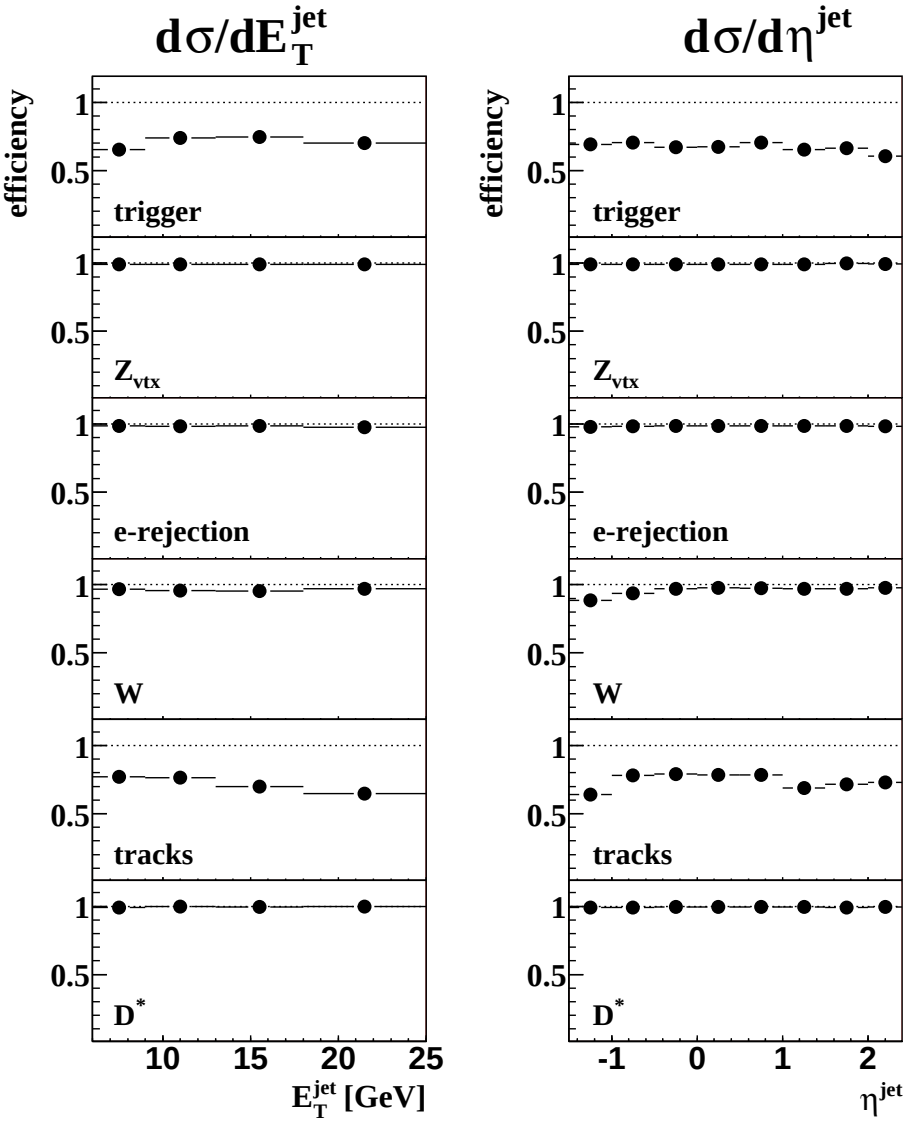

Figure 7.7: Selection efficiencies after applying each cut.

7.3 Systematic uncertainties

Systematical errors of the measured cross sections have been estimated for various sources of uncertainties. These sources can be divided into several categories.

- Resolution of the measured quantities.
- Extraction of D^* signal
- Trigger efficiency
- E_T^{jet} correction
- Uncertainty of the hadronic energy scale
- Acceptance calculation
- Luminosity measurement

The energy scale uncertainty is well correlated bin-to-bin, therefore, this is quoted seperately. For other sources of systematic uncertainties, cross sections are re-calculated by changing the procedure or varying the cuts. Newly obtained cross sections (σ_i') are compared to the nominal cross sections (σ_0) which are obtained by the optimized procedure and cuts, already described in the previous chapters. For each systematic source i, upper and lower systematical errors from that source (Δ_i^+ and Δ_i^-) are calculated by

$$\Delta_i^+ = \begin{cases} \delta_i & (\text{if } \delta_i > 0) \\ 0 & (\text{if } \delta_i < 0) \end{cases}, \tag{7.14}$$

$$\Delta_i^- = \begin{cases} 0 & (\text{if } \delta_i > 0) \\ \delta_i & (\text{if } \delta_i < 0) \end{cases}. \tag{7.15}$$

where δ_i is the deviation of the cross section given by

$$\delta_i = \sigma_i' - \sigma_0. \tag{7.16}$$

All systematic errors, except for the error coming from the energy scale uncertainty, are added in quadrature.

$$\Delta^+ = \sqrt{\sum_i \left(\Delta_i^+\right)^2}, \tag{7.17}$$

$$\Delta^- = -\sqrt{\sum_i \left(\Delta_i^-\right)^2}. \tag{7.18}$$

7.3.1 Resolution of the measured quantities

In order to estimate the effect of the finite resolution of measured quantities, thresholds of various cuts were changed to positive and negative directions. The size of the variation were taken to be a similar value as the resolution of the variables. Thresholds of the following cuts were changed in both data and MC.

- $Z_{vtx} \rightarrow \pm 5$ cm
- $p_T(\pi_s) \rightarrow \pm 0.02$ GeV/c^2
- $p_T(\pi) \rightarrow \pm 0.1$ GeV/c^2
- $p_T(K) \rightarrow \pm 0.1$ GeV/c^2
- $\eta(track) \rightarrow \pm 0.05$
- $p_T(D^*) \rightarrow \pm 0.07$ GeV
- $\eta(D^*) \rightarrow \pm 0.005$ GeV
- $E_T^{jet} \rightarrow \pm 1$ GeV
- $\eta^{jet} \rightarrow \pm 0.07$ GeV

Systematic errors from these sources were negligible.

7.3.2 D^* signal extration

In order to check whether there are any systematic effects in the background estimation under the D^* peak, the mass window and the control region for the normalization of wrong charge combination has been changed by ± 10 MeV. Systematic errors from this source was less than 5 % in most bins, however, become large at high E_T^{jet} where the statistics was low. This may double-count the statistical uncertainty, but errors were smaller than statistical errors in all bins.

7.3.3 Trigger efficiency

Efficiencies of the SLT and the TLT were 96.7 % and $\simeq$ 100 % respectively, since tighter cuts were applied in the offline selection. On the other hand, the FLT efficiency was about 88 % estimated by HERWIG and there has been some differences between data and MC in the efficiency estimation. The trigger efficiency is defined as the fraction of events passing the after requiring the trigger to the events passing all offline selection without the specific trigger requirement. The details of the trigger study is described in appendix C. Errors on the cross sections from this uncertainty was estimated to be about 2 % at the low E_T^{jet} and become negligible at high E_T^{jet}.

7.3.4 E_T^{jet} correction

To check the systematic effect from the correction procedure of the jet transverse energy, the cross section was calculated without any correction. The cross sections changed by about 20 % at low E_T^{jet}. by changing the procedure. The becomes large in forward region.

7.3.5 Acceptance calculation

The unfolding procedure described in section 7.2, depends on the correct modelling of the data by the MC. The expected distribution by the MC may be different if different models are used and also if contribution from background are different. The acceptance are recalculated by

- using PYTHIA instead of HERWIG,
- increasing b contribution by a factor 2.

We increase the b contribution, since experimental cross section measured at HERA on beauty photoproduction exceeds the theoretical cross section by a factor 2 [50]. Systematic errors from this source was negligible in most of the bins, and was at most 10 % at high E_T^{jet}, where the contribution of b production increases.

7.3.6 Hadronic energy scale

The uncertainty of the measured hadronic energy scale is known to be less than 2 % [51]. This was estimated from the comparing the transverse energy of hadrons and the scattered electron in DIS events. Although the effect of the energy scale uncertainty can be estimated by changing the measured E_T in data, due to the small statistics at high E_T the statistical uncertainty also contributes. Therefore we evaluate this effect by changing the energy scale in the MC.

7.3.7 Luminosity measurement

The uncertainty of the luminosity measurement is found to be 2 %. This is not included in the quoted systematic uncertainty nor on the plots.

7.3.8 Summary of the systematic uncertaity

Systematic uncertainty of each measured cross section is shown in appendix D. The effect of changing the threshold of cuts is negligible. The main source of uncertainty comes from the E_T correction procedure, which changes the cross sections by 20-30 % at low E_T and in forward region. The effect of the systematic uncertainty was large in the $d\sigma/d\eta^{jet}$ measurement including low E_T jets.

7.4 Results

The measured cross sections are summarized in table 7.1-7.5. In the first and the second column of the table, E_T^{jet} and η^{jet} ranges of the bins are shwon. The reference point of the differentical cross section (E_T^{ref} and η^{ref}) at which the cross section is measured, is taken as the average E_T, ($\langle E_T \rangle$) or the average η ($\langle \eta \rangle$). The reference point, the number of signals, the acceptance correction factor $\mathcal{C}_i$ and the measured cross section with its error for each bin is shown in the tables.

The results are discussed in the next chapter together with the NLO QCD calculation.

η^{jet} range	E_T^{jet} range	E_T^{ref}	N_{sig}	$\mathcal{C}$	$d\sigma/dE_T^{jet}$ ($\pm stat. \pm syst. \pm Escale$) [nb/GeV]
$[-1.5 : 2.4]$	$[6 : 9]$	7.2	4932	1.95	$1.58 \pm 0.04^{+0.17+0.07}_{-0.08-0.06} \cdot 10^{0}$
	$[9 : 13]$	10.5	1480	2.01	$3.67 \pm 0.18^{+0.18+0.25}_{-0.28-0.23} \cdot 10^{-1}$
	$[13 : 18]$	14.8	327	2.38	$7.70 \pm 0.92^{+1.24+0.98}_{-0.63-0.73} \cdot 10^{-2}$
	$[18 : 25]$	20.4	132	2.89	$2.70 \pm 0.46^{+0.58+0.33}_{-0.35-0.25} \cdot 10^{-2}$
$[-1.5 : -0.5]$	$[6 : 9]$	7.1	879	2.21	$3.21 \pm 0.17^{+0.24+0.25}_{-0.11-0.18} \cdot 10^{-1}$
	$[9 : 13]$	10.3	126	2.61	$4.08 \pm 0.62^{+0.26+0.44}_{-0.66-0.44} \cdot 10^{-2}$
	$[13 : 18]$	14.4	18	4.81	$8.79 \pm 3.32^{+1.04+2.01}_{-6.17-2.17} \cdot 10^{-3}$
	$[18 : 25]$	18.7	0	0.00	-
$[-0.5 : 0.5]$	$[6 : 9]$	7.2	2243	1.81	$6.69 \pm 0.23^{+0.98+0.27}_{-0.34-0.23} \cdot 10^{-1}$
	$[9 : 13]$	10.5	672	1.91	$1.59 \pm 0.11^{+0.06+0.11}_{-0.16-0.10} \cdot 10^{-1}$
	$[13 : 18]$	14.8	143	2.22	$3.15 \pm 0.50^{+0.54+0.42}_{-0.38-0.37} \cdot 10^{-2}$
	$[18 : 25]$	20.3	42	2.95	$8.88 \pm 2.54^{+2.97+1.24}_{-1.08-1.01} \cdot 10^{-3}$
$[0.5 : 1.5]$	$[6 : 9]$	7.2	1435	1.89	$4.46 \pm 0.22^{+0.35+0.16}_{-0.25-0.13} \cdot 10^{-1}$
	$[9 : 13]$	10.6	520	1.89	$1.22 \pm 0.11^{+0.09+0.07}_{-0.13-0.06} \cdot 10^{-1}$
	$[13 : 18]$	14.9	132	2.33	$3.06 \pm 0.63^{+0.99+0.34}_{-0.32-0.20} \cdot 10^{-2}$
	$[18 : 25]$	20.5	62	2.87	$1.26 \pm 0.33^{+0.32+0.13}_{-0.32-0.14} \cdot 10^{-2}$
$[1.5 : 2.4]$	$[6 : 9]$	7.2	371	2.49	$1.52 \pm 0.17^{+0.32+0.04}_{-0.25-0.07} \cdot 10^{-1}$
	$[9 : 13]$	10.6	160	2.32	$4.59 \pm 0.71^{+1.53+0.23}_{-0.53-0.25} \cdot 10^{-2}$
	$[13 : 18]$	15.0	32	2.75	$8.90 \pm 4.04^{+5.61+1.38}_{-3.44-0.69} \cdot 10^{-3}$
	$[18 : 25]$	20.2	27	2.79	$5.44 \pm 1.98^{+2.34+0.73}_{-1.50-0.27} \cdot 10^{-3}$

Table 7.1: The reference point, the number of observed jets, correction factor and the cross section for each bin of $d\sigma/dE_T^{jet}$

E_T^{jet} range	η^{jet} range	η^{ref}	N_{sig}	$\mathcal{C}$	$d\sigma/d\eta^{jet}$ $(\pm stat. \pm syst. \pm Escale)$ [nb]
[6 : 25]	[−1.5 : −1.0]	-1.18	174	3.18	$5.48 \pm 0.69^{+1.34+0.65}_{-1.55-0.53} \cdot 10^{-1}$
	[−1.0 : −0.5]	-0.72	847	2.08	$1.75 \pm 0.09^{+0.09+0.13}_{-0.06-0.10} \cdot 10^{0}$
	[−0.5 : 0.0]	-0.24	1438	1.96	$2.79 \pm 0.12^{+0.24+0.16}_{-0.19-0.14} \cdot 10^{0}$
	[0.0 : 0.5]	0.24	1659	1.76	$2.90 \pm 0.12^{+0.28+0.13}_{-0.13-0.12} \cdot 10^{0}$
	[0.5 : 1.0]	0.74	1319	1.76	$2.30 \pm 0.12^{+0.22+0.11}_{-0.10-0.09} \cdot 10^{0}$
	[1.0 : 1.5]	1.23	831	2.25	$1.85 \pm 0.13^{+0.07+0.08}_{-0.12-0.07} \cdot 10^{0}$
	[1.5 : 2.0]	1.72	397	2.21	$8.71 \pm 0.93^{+2.32+0.35}_{-0.79-0.43} \cdot 10^{-1}$
	[2.0 : 2.4]	2.19	196	3.09	$7.51 \pm 1.09^{+1.89+0.36}_{-1.86-0.30} \cdot 10^{-1}$
[6 : 9]	[−1.5 : −1.0]	-1.18	179	3.08	$5.46 \pm 0.66^{+0.83+0.62}_{-1.11-0.46} \cdot 10^{-1}$
	[−1.0 : −0.5]	-0.73	700	1.98	$1.37 \pm 0.08^{+0.11+0.10}_{-0.05-0.07} \cdot 10^{0}$
	[−0.5 : 0.0]	-0.24	1086	1.92	$2.07 \pm 0.10^{+0.27+0.10}_{-0.17-0.09} \cdot 10^{0}$
	[0.0 : 0.5]	0.24	1156	1.70	$1.94 \pm 0.10^{+0.33+0.06}_{-0.09-0.05} \cdot 10^{0}$
	[0.5 : 1.0]	0.73	854	1.69	$1.43 \pm 0.09^{+0.15+0.05}_{-0.06-0.04} \cdot 10^{0}$
	[1.0 : 1.5]	1.23	579	2.26	$1.30 \pm 0.10^{+0.06+0.05}_{-0.12-0.04} \cdot 10^{0}$
	[1.5 : 2.0]	1.73	250	2.19	$5.42 \pm 0.75^{+1.14+0.09}_{-0.55-0.27} \cdot 10^{-1}$
	[2.0 : 2.4]	2.19	120	3.22	$4.81 \pm 0.91^{+1.35+0.23}_{-1.53-0.12} \cdot 10^{-1}$
[9 : 25]	[−1.5 : −1.0]	-1.11	0	5.79	-
	[−1.0 : −0.5]	-0.70	148	2.57	$3.77 \pm 0.51^{+0.11+0.40}_{-0.79-0.39} \cdot 10^{-1}$
	[−0.5 : 0.0]	-0.23	351	2.09	$7.27 \pm 0.70^{+0.49+0.67}_{-0.69-0.54} \cdot 10^{-1}$
	[0.0 : 0.5]	0.25	503	1.91	$9.50 \pm 0.74^{+0.93+0.72}_{-0.87-0.70} \cdot 10^{-1}$
	[0.5 : 1.0]	0.74	464	1.90	$8.72 \pm 0.80^{+1.06+0.65}_{-0.80-0.50} \cdot 10^{-1}$
	[1.0 : 1.5]	1.23	252	2.24	$5.59 \pm 0.79^{+0.62+0.32}_{-0.71-0.28} \cdot 10^{-1}$
	[1.5 : 2.0]	1.72	146	2.26	$3.26 \pm 0.56^{+1.43+0.27}_{-0.43-0.16} \cdot 10^{-1}$
	[2.0 : 2.4]	2.19	75	2.87	$2.67 \pm 0.61^{+0.83+0.14}_{-0.49-0.18} \cdot 10^{-1}$

Table 7.2: The reference point, the number of observed jets, correction factor and the cross section for each bin of $d\sigma/d\eta^{jet}$

η^{jet} range	E_T^{jet} range	E_T^{ref}	N_{sig}	$\mathcal{C}$	$d\sigma/dE_T^{jet}$ $(\pm stat. \pm syst. \pm Escale)$ [nb/GeV]
$[-1.5:\ 2.4]$	$[\ 6:\ 9]$	7.2	2860	1.88	$8.88 \pm 0.28^{+0.13+0.39}_{-0.02-0.28} \cdot 10^{-1}$
	$[\ 9:13]$	10.5	942	1.78	$2.08 \pm 0.12^{+0.01+0.15}_{-0.02-0.13} \cdot 10^{-1}$
	$[13:18]$	14.8	185	2.04	$3.73 \pm 0.59^{+0.27+0.49}_{-0.07-0.34} \cdot 10^{-2}$
	$[18:25]$	20.4	68	2.99	$1.45 \pm 0.34^{+0.08+0.27}_{-0.11-0.22} \cdot 10^{-2}$
$[-1.5:\ 2.4]$	$[\ 6:\ 9]$	7.2	2072	2.07	$7.05 \pm 0.28^{+0.10+0.35}_{-0.03-0.35} \cdot 10^{-1}$
	$[\ 9:13]$	10.5	537	2.43	$1.61 \pm 0.14^{+0.01+0.10}_{-0.00-0.11} \cdot 10^{-1}$
	$[13:18]$	14.9	141	2.96	$4.16 \pm 0.75^{+0.13+0.49}_{-0.01-0.41} \cdot 10^{-2}$
	$[18:25]$	20.4	64	2.77	$1.26 \pm 0.30^{+0.13+0.07}_{-0.04-0.03} \cdot 10^{-2}$

Table 7.3: The reference point, the number of observed jets, correction factor and the cross section for each bin of $d\sigma/dE_T^{jet}$ for D^* jets and other jets.

E_T^{jet} range	η^{jet} range	η^{ref}	N_{sig}	$\mathcal{C}$	$d\sigma/d\eta^{jet}$ $(\pm stat. \pm syst. \pm Escale)$ [nb]
[6 : 25]	$[-1.5 : -1.0]$	-1.18	120	3.19	$3.79 \pm 0.53^{+0.13+0.42}_{-0.14-0.34} \cdot 10^{-1}$
	$[-1.0 : -0.5]$	-0.72	632	1.87	$1.17 \pm 0.07^{+0.01+0.09}_{-0.00-0.06} \cdot 10^{0}$
	$[-0.5 : 0.0]$	-0.24	1033	1.83	$1.87 \pm 0.09^{+0.01+0.10}_{-0.01-0.09} \cdot 10^{0}$
	$[0.0 : 0.5]$	0.24	1093	1.71	$1.85 \pm 0.09^{+0.02+0.08}_{-0.01-0.07} \cdot 10^{0}$
	$[0.5 : 1.0]$	0.73	790	1.65	$1.29 \pm 0.09^{+0.02+0.06}_{-0.00-0.04} \cdot 10^{0}$
	$[1.0 : 1.5]$	1.22	358	2.44	$8.63 \pm 1.02^{+0.07+0.35}_{-0.04-0.26} \cdot 10^{-1}$
	$[1.5 : 2.0]$	1.57	27	9.43	$2.59 \pm 1.28^{+0.76+0.16}_{-1.07-0.26} \cdot 10^{-1}$
	$[2.0 : 2.4]$	2.26	0	0.00	-
[6 : 9]	$[-1.5 : -1.0]$	-1.18	124	3.13	$3.85 \pm 0.52^{+0.07+0.40}_{-0.04-0.32} \cdot 10^{-1}$
	$[-1.0 : -0.5]$	-0.73	522	1.81	$9.34 \pm 0.60^{+0.10+0.71}_{-0.01-0.38} \cdot 10^{-1}$
	$[-0.5 : 0.0]$	-0.24	752	1.84	$1.36 \pm 0.07^{+0.02+0.06}_{-0.01-0.05} \cdot 10^{0}$
	$[0.0 : 0.5]$	0.24	734	1.68	$1.22 \pm 0.07^{+0.04+0.04}_{-0.00-0.02} \cdot 10^{0}$
	$[0.5 : 1.0]$	0.73	468	1.66	$7.70 \pm 0.69^{+0.17+0.19}_{-0.01-0.17} \cdot 10^{-1}$
	$[1.0 : 1.5]$	1.22	247	2.65	$6.50 \pm 0.86^{+0.17+0.15}_{-0.04-0.10} \cdot 10^{-1}$
	$[1.5 : 2.0]$	1.57	11	10.10	$1.13 \pm 1.00^{+1.81+0.01}_{-0.26-0.13} \cdot 10^{-1}$
	$[2.0 : 2.4]$	2.20	0	0.00	-
[9 : 25]	$[-1.5 : -1.0]$	-1.11	0	4.62	-
	$[-1.0 : -0.5]$	-0.70	112	2.15	$2.38 \pm 0.36^{+0.03+0.23}_{-0.07-0.23} \cdot 10^{-1}$
	$[-0.5 : 0.0]$	-0.23	281	1.85	$5.13 \pm 0.50^{+0.03+0.47}_{-0.06-0.38} \cdot 10^{-1}$
	$[0.0 : 0.5]$	0.25	358	1.74	$6.19 \pm 0.55^{+0.04+0.51}_{-0.09-0.48} \cdot 10^{-1}$
	$[0.5 : 1.0]$	0.74	322	1.63	$5.19 \pm 0.56^{+0.07+0.41}_{-0.03-0.26} \cdot 10^{-1}$
	$[1.0 : 1.5]$	1.22	109	2.12	$2.30 \pm 0.57^{+0.23+0.15}_{-0.06-0.11} \cdot 10^{-1}$
	$[1.5 : 2.0]$	1.58	16	8.51	$1.40 \pm 0.80^{+0.29+0.22}_{-0.38-0.12} \cdot 10^{-1}$
	$[2.0 : 2.4]$	2.26	0	0.00	-

Table 7.4: The reference point, the number of observed jets, correction factor and the cross section for each bin of $d\sigma/d\eta^{jet}$ for D^* jets.

E_T^{jet} range	η^{jet} range	η^{ref}	N_{sig}	$\mathcal{C}$	$d\sigma/d\eta^{jet}$ ($\pm stat. \pm syst. \pm Escale$) [nb]
[6 : 25]	$[-1.5 : -1.0]$	-1.18	54	3.12	$1.67 \pm 0.43^{+0.45+0.22}_{-0.61-0.18} \cdot 10^{-1}$
	$[-1.0 : -0.5]$	-0.73	215	2.71	$5.77 \pm 0.70^{+0.07+0.42}_{-0.03-0.42} \cdot 10^{-1}$
	$[-0.5 : 0.0]$	-0.24	404	2.30	$9.21 \pm 0.85^{+0.17+0.57}_{-0.29-0.61} \cdot 10^{-1}$
	$[0.0 : 0.5]$	0.25	566	1.89	$1.06 \pm 0.08^{+0.01+0.05}_{-0.00-0.05} \cdot 10^{0}$
	$[0.5 : 1.0]$	0.74	528	1.98	$1.04 \pm 0.09^{+0.01+0.06}_{-0.00-0.05} \cdot 10^{0}$
	$[1.0 : 1.5]$	1.24	471	2.06	$9.62 \pm 0.81^{+0.06+0.49}_{-0.36-0.47} \cdot 10^{-1}$
	$[1.5 : 2.0]$	1.74	369	2.02	$7.38 \pm 0.81^{+0.58+0.30}_{-0.06-0.35} \cdot 10^{-1}$
	$[2.0 : 2.4]$	2.19	197	3.09	$7.53 \pm 1.09^{+0.48+0.37}_{-0.38-0.30} \cdot 10^{-1}$
[6 : 9]	$[-1.5 : -1.0]$	-1.19	54	2.96	$1.60 \pm 0.40^{+0.20+0.21}_{-0.50-0.14} \cdot 10^{-1}$
	$[-1.0 : -0.5]$	-0.73	178	2.48	$4.38 \pm 0.58^{+0.06+0.27}_{-0.01-0.28} \cdot 10^{-1}$
	$[-0.5 : 0.0]$	-0.25	334	2.16	$7.14 \pm 0.67^{+0.15+0.37}_{-0.41-0.45} \cdot 10^{-1}$
	$[0.0 : 0.5]$	0.24	422	1.74	$7.25 \pm 0.62^{+0.23+0.29}_{-0.01-0.28} \cdot 10^{-1}$
	$[0.5 : 1.0]$	0.74	386	1.74	$6.65 \pm 0.63^{+0.12+0.33}_{-0.02-0.25} \cdot 10^{-1}$
	$[1.0 : 1.5]$	1.24	331	1.90	$6.23 \pm 0.61^{+0.04+0.33}_{-0.36-0.28} \cdot 10^{-1}$
	$[1.5 : 2.0]$	1.75	238	2.00	$4.73 \pm 0.66^{+0.22+0.08}_{-0.02-0.22} \cdot 10^{-1}$
	$[2.0 : 2.4]$	2.19	121	3.22	$4.84 \pm 0.91^{+0.38+0.23}_{-0.24-0.12} \cdot 10^{-1}$
[9 : 25]	$[-1.5 : -1.0]$	-1.11	0	9.33	-
	$[-1.0 : -0.5]$	-0.71	36	4.08	$1.48 \pm 0.43^{+0.03+0.21}_{-0.45-0.19} \cdot 10^{-1}$
	$[-0.5 : 0.0]$	-0.23	71	2.76	$1.94 \pm 0.55^{+0.85+0.18}_{-0.02-0.15} \cdot 10^{-1}$
	$[0.0 : 0.5]$	0.25	144	2.30	$3.29 \pm 0.51^{+0.06+0.20}_{-0.03-0.21} \cdot 10^{-1}$
	$[0.5 : 1.0]$	0.74	141	2.55	$3.58 \pm 0.63^{+0.05+0.23}_{-0.07-0.26} \cdot 10^{-1}$
	$[1.0 : 1.5]$	1.24	141	2.39	$3.34 \pm 0.55^{+0.05+0.16}_{-0.05-0.18} \cdot 10^{-1}$
	$[1.5 : 2.0]$	1.74	129	2.05	$2.62 \pm 0.48^{+0.55+0.21}_{-0.06-0.13} \cdot 10^{-1}$
	$[2.0 : 2.4]$	2.19	75	2.86	$2.66 \pm 0.61^{+0.19+0.14}_{-0.09-0.17} \cdot 10^{-1}$

Table 7.5: The reference point, the number of observed jets, correction factor and the cross section for each bin of $d\sigma/d\eta^{jet}$ for other jets.

Chapter 8

Comparison with NLO QCD predictions

8.1 NLO QCD calculation

Measured differential cross sections are compared to the NLO QCD prediction performed in the massive scheme. The NLO QCD predictions were obtained using the FORTRAN code FMNR, developed by Frixione et al. [22, 23]. The code consists of two programs; one for calculating the direct photon process and the other to calculate the resolved photon process. The calculation was performed seperately for direct and resolved processes and added at the end.

The theoretical predictions were calculated in the same kinematic region as the measurement. The jet finder was run over the final state partons ($c\bar{c}$, $c\bar{c}g$ or $c\bar{c}q$). Cuts on D^* quantities ($p_T(D^*)$ and $\eta(D^*)$) have been applied by calculating the D^* ($\bar{D}^*$) momentum from c ($\bar{c}$) quark momentum using Peterson function with $\epsilon = 0.035$, which is the value obtained from an NLO fit to the fragmentation function measured by the ARGUS experiment. The cross section for $ep \to D^*X$ has been obtained from the calculated cross section $ep \to cX$ by

$$\sigma(ep \to D^*X) = 2f(c \to D^*)\sigma(ep \to cX) \tag{8.1}$$

where $f(c \to D^*)$ is the fragmentation fraction of the D^* meson. The value obtained in [47], $f(c \to D^*) = 23.5$ % was used in this analysis, which agrees well to the value 22.3 ± 0.009 % measured in γp interaction [52]. A factor two was multiplied, since both c or $\bar{c}$ quark can fragment in to D^{*+} or D^{*-}.

The calculation was performed using CTEQ5M1 [18] and AFG-G HO [20] for the proton and the photon PDF. The renormalization scale μ_R and the factorization scales of the proton $\mu_{F,p}$ and the photon $\mu_{F,\gamma}$ were taken as

$$\mu_R^2 = \mu_{F,p}^2 = \mu_{F,\gamma}^2 = \mu_0^2 \equiv m_c^2 + \langle p_T \rangle^2 \tag{8.2}$$

where $\langle p_T \rangle^2$ is the average transverse momentum of the charm quark. The mass of the charm quark was taken as $m_c = 1.5$ GeV/c^2.

The uncertainty on the theoretical prediction was estimated by changing the parameters used in the calculation. Changing the photon PDF to GRV-G HO [19] lowered the cross section by $\simeq 5$ %. The change of the cross section was the largest when the renormalization scale and the mass of the charm quark were changed simultaneously. The upper limit of the NLO QCD calculation was obtained with $\mu_R = 0.5\mu_0$ and $m_c = 1.3$ GeV/c^2, while the lower limit was obtained with $\mu_R = 2\mu_0$ and $m_c = 1.7$ GeV/c^2.

The calculated cross sections are shown in appendix E with the hadronization correction factors described in the next two sections.

8.2 Correlation between parton and hadron level

Measured cross sections are unfolded to the hadron level cross sections as described in previous sections. On the other hand, NLO QCD calculation predicts cross sections at parton level. In order to compare data to theory, we must evaluate the effect of hadronization corrections on the parton level cross sections. Hadronization correction is estimated in the next section. In this section, correlation of jet quantities at parton level and hadron level is investigated.

In order to study the correlation, parton level jets are reconstructed by applying k_T algorithm to the final state partons after the parton shower but before the hadronization. A sample of MC events with $\eta^{jet} < 3.0$, $E_T^{jet} > 3$ GeV for both levels were prepared. The matching between parton level jets and hadron level jets was done in the same as we did for jet E_T correction (section 6.2).

Figure 8.1 shows the correlation of jet transverse energy at parton level (E_T^{par}) and hadron level (E_T^{had}). In figure 8.1 (b), relative distribution of the difference of E_T at hadron level and parton level ($(E_T^{had} - E_T^{par})/E_T^{par}$) is shown after applying cut at hadron level of $E_T^{had} > 6$ GeV. The distribution of the difference is centered around zero with a standard deviation of about 14 %. In figures 8.1 (c) and (d), mean differnces of E_T are shown as a function of E_T^{had} and η^{had} respectively. There is no strong dependence of the differnce $\left\langle (E_T^{had} - E_T^{par})/E_T^{par} \right\rangle$ on these variables.

Figure 8.2 shows the correlation of jet pseudo-rapidity at parton level and hadron level. A shift of pseudo-rapidity of jets between parton level and hadron, is clearly seen in figure 8.2 (b), where the distribution of $\eta^{had} - \eta^{par}$ is plotted. Hadron level jets are shifted to forward direction compared to parton level jets, by $\Delta\eta = 0.08$, on average. This feature can be understood qualitatively by considering the presence of proton remnant in the forward region. The connection between scattered partons and the proton remnant pulls the partons in the direction of the proton remnant after hadronization. As shown in figure 8.2 (d), this effect is seen in all region of η^{had}.

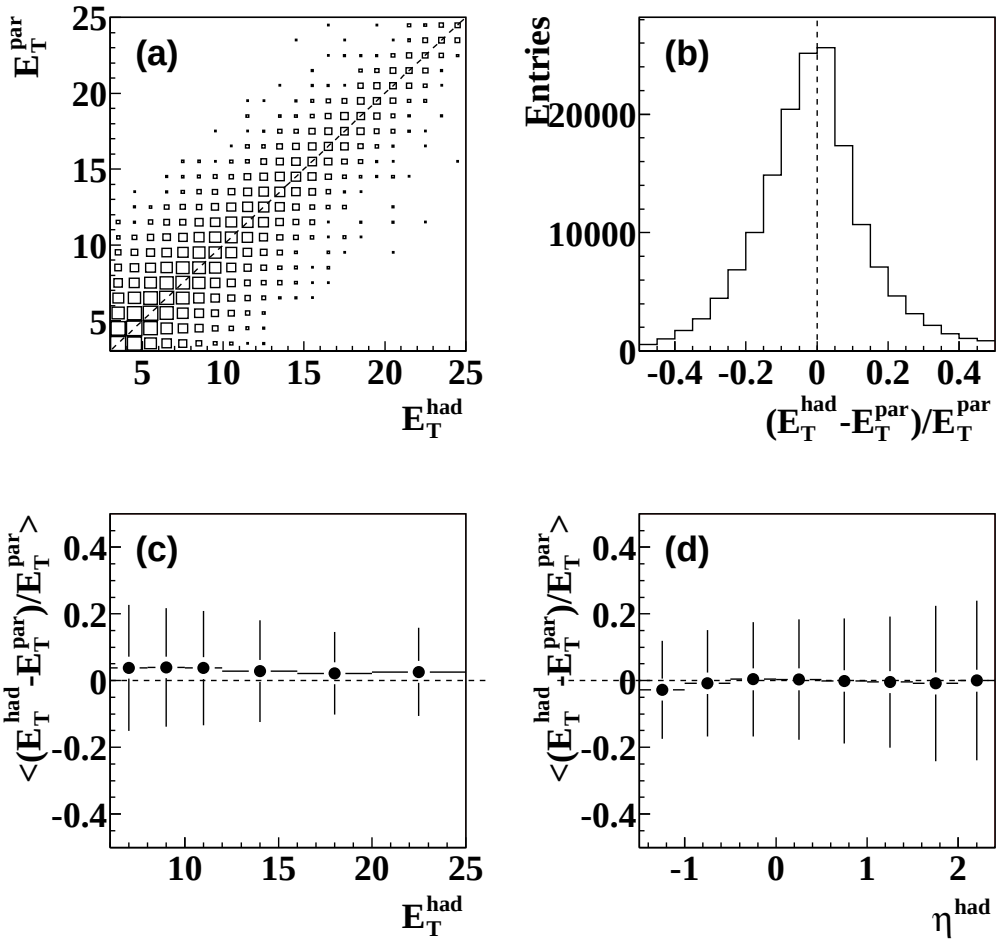

Figure 8.1: Correlation of transverse momentum of jets at parton level and hadron level after applying all cuts except for cuts on jet variables, studied using HERWIG. (a) 2 dimensional distribution of E_T^{had} and E_T^{par}. (b) Distribution of the relative difference $(E_T^{had} - E_T^{par})/E_T^{par}$. (c) Mean value of differences as a function of E_T^{had} with error bars showing the standard deviation. (d)Mean value of differences as a function of η^{had} with error bars showing the standard deviation

From these study, non-negligible hadronization corrections are expected in $d\sigma/d\eta$ measurements.

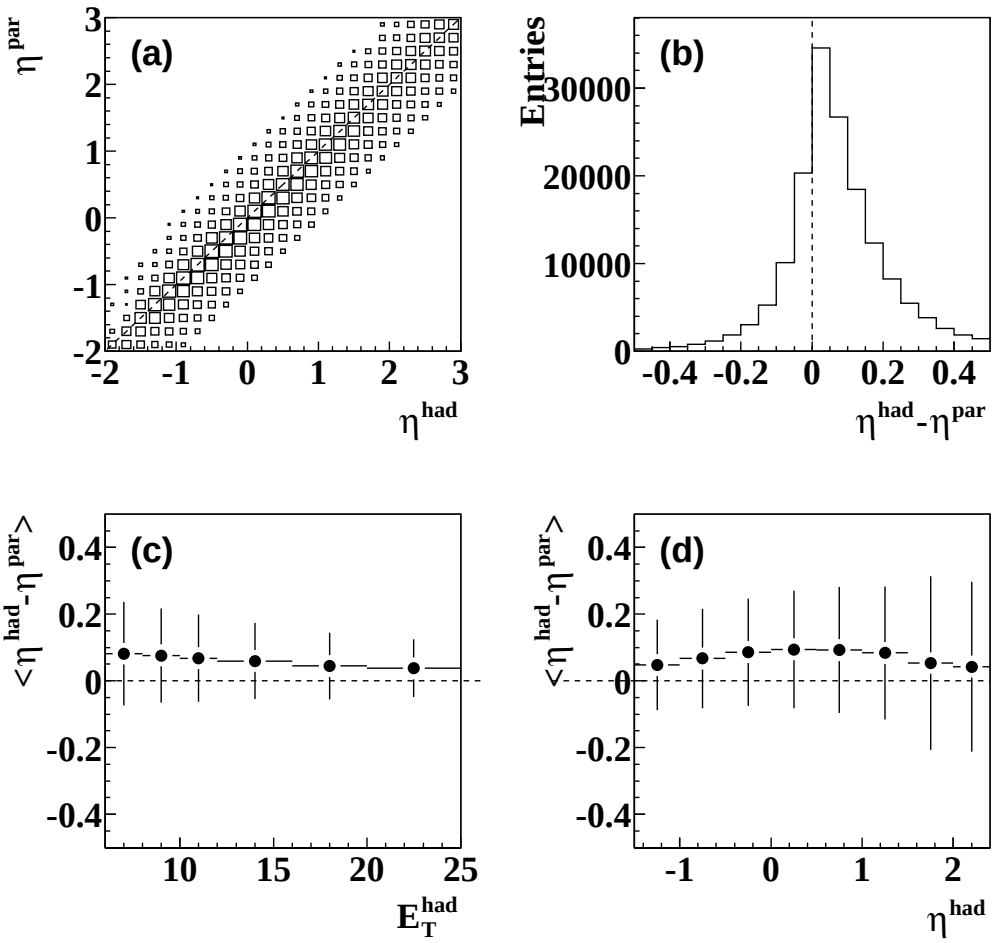

Figure 8.2: Correlation of pseudo-rapidity of jets at parton level and hadron level after applying all cuts except for cuts on jet variables, studied using HERWIG. (a) 2 dimensional distribution of η^{had} and η^{par}. (b) Distribution of the relative difference $(\eta^{had} - \eta^{par})/\eta^{par}$. (c) Mean value of differences as a function of η^{had} with error bars showing the standard deviation. (d)Mean value of differences as a function of E_T^{had} with error bars showing the standard deviation

8.3 Hadronization correction

The effect of the hadronization corrections were estimated by comparing the hadron level cross section to parton level cross section using HERWIG, considering only charm production (no b production). In order to calculate the parton level cross section in MC, the jet finder is applied to the final state partons (after the parton shower and before the hadronization).

Since the shift of η^{jet} observed between parton level and hadron level is smaller than the bin size, we adopt a bin-by-bin correction to estimate the hadronization correction for each bin. The hadronization correction factor is defined as

$$\mathcal{C}_i^{had} = \left(\frac{\sigma_i^{had}}{\sigma_i^{par}} \right)_{MC} \tag{8.3}$$

Since other cuts applied are identical to both the parton level and the hadron level, the difference between parton level and hadron level is expected to come from the migration of jets between the adjacent bins in η^{jet}. Therefore, $\mathcal{C}_i^{had}$ depends on the distribution of parton level jets. The shape of the parton level cross section between HERWIG and the NLO QCD prediction are compared in figure 8.3 for $d\sigma/d\eta^{jet}$. The parton level cross sections of NLO QCD are shown by solid lines. The parton level cross section of HERWIG (charm only, direct+resolved) are shown by filled circles. Those for HERWIG (charm only, direct) are shown by open squares. HERWIG distribution are normalized to the NLO QCD cross sections, since we are only interested in the shape, here.

The solid lines are well followed by the filled circles, i.e. the parton level cross sections of HERWIG (charm only, direct+resolved) reproduce the shape of the NLO QCD calculations reasonably well. The HERWIG (direct only) does not reproduce the NLO QCD calculation, although the NLO QCD calculation does not consider explicitly, the charm excitation process in the photon which is the dominant contribution in LO resolved process. We used the HERWIG (charm, direct+resolved) to obtain the hadronization correction factors.

Figure 8.4 shows the hadronization correction for each bin of the measured cross sections for $d\sigma/dE_T^{jet}$. The efficiency to find the parton level jet and hadron level jet in the same bin was found to be 70 to 90 % depending on η^{jet}. Hadronization correction factors are flat with respect to E_T^{jet}, although their values depend on η^{jet} ranges. This is more clearly seen in figure 8.5, where hadronization correction factors for $d\sigma/d\eta^{jet}$ are shown. There is a tendency that the correction factor is less than unity in negative η^{jet}, and is slightly above in positive η^{jet}.

Theoretical prediction of the cross section at hadron level, σ^{had} is obtained from the parton level cross sections, σ^{par} calculated with the program FMNR by

$$\left(\sigma_i^{had}\right)_{NLO} = \mathcal{C}_i^{had} \cdot \left(\sigma_i^{par}\right)_{NLO} . \tag{8.4}$$

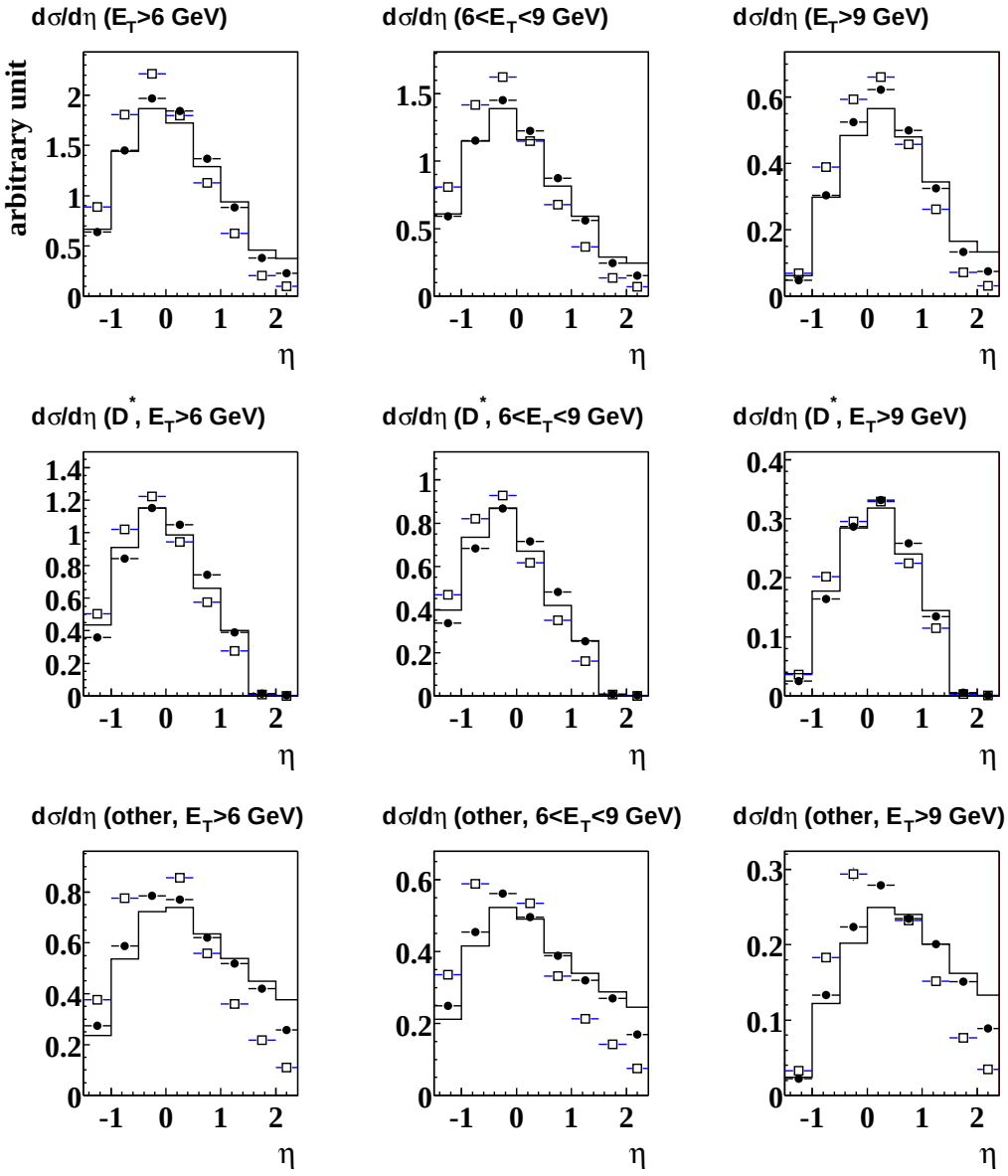

Figure 8.3: Parton level cross sections of FMNR (solid line), compared to HERWIG (direct+resolved) (filled circle) and HERWIG (direct only) (open square). All measured cross sections of $d\sigma/d\eta^{jet}$ are shown.

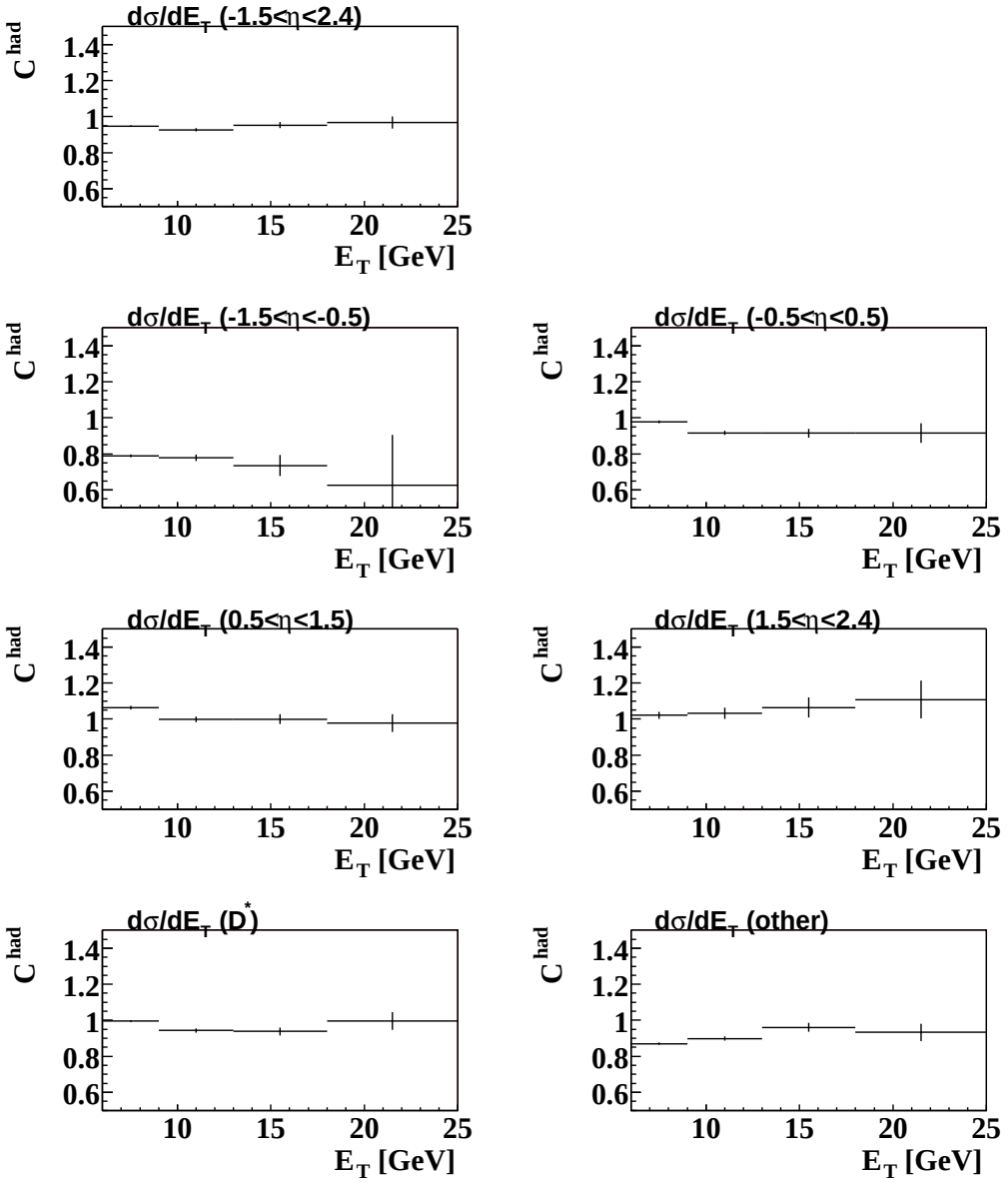

Figure 8.4: Hadronization corrrection factors in each bin of $d\sigma/dE_T$. The η^{jet} ranges are shown at the top of each plot.

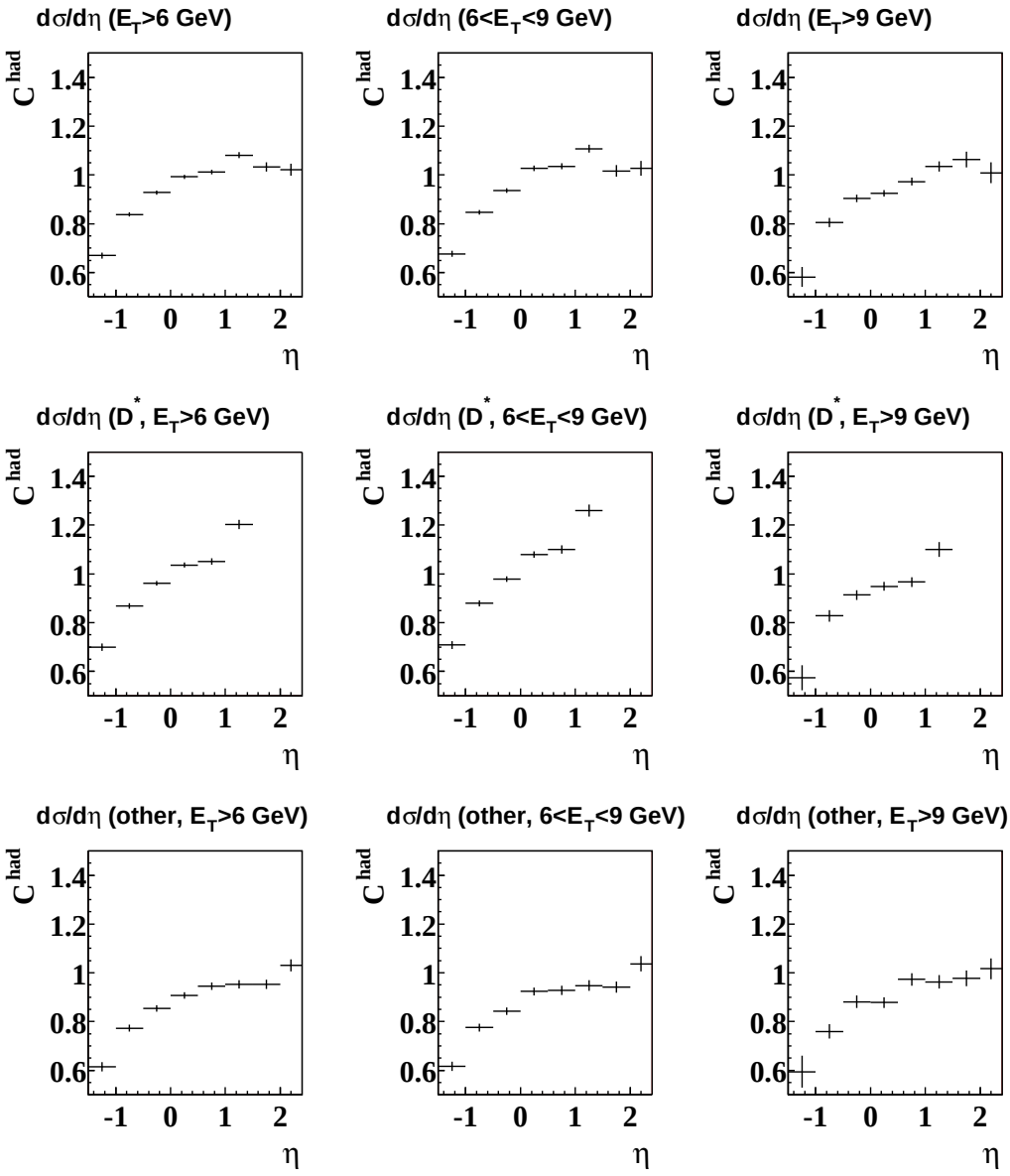

Figure 8.5: Hadronization corrrection factors in each bin of $d\sigma/\eta^{jet}$. The E_T^{jet} ranges are shown at the top of each plot.

8.4 Comparison with NLO QCD prediction

8.4.1 Inclusive jet cross sections

Figure 8.6 presents the result of $d\sigma/dE_T^{jet}$ in $-1.5 < \eta^{jet} < 2.4$ compared to the NLO QCD prediction. The measured cross sections are plotted as black dots. The central value of the NLO QCD prediction with hadronization correction is shown by a thick solid curve while upper and lower limits of NLO QCD prediction are shown with a dashed line and a dotted line respectively. The thin blue solid line indicates the NLO QCD prediction at parton level, i.e. without hadronization correction. The total errors on the measured points are indicated by the error bars, where horizontal lines indicate the size of the statistical errors. The yellow band through the data points represents the errors from the uncertainty of the hadronic energy scale.

Figure 8.7 presents $d\sigma/dE_T^{jet}$ in subranges of η^{jet}, $-1.5 < \eta^{jet} < -0.5$, $-0.5 < \eta^{jet} < 0.5$, $0.5 < \eta^{jet} < 1.5$ and $1.5 < \eta^{jet} < 2.4$. In figure 8.8, $d\sigma/d\eta^{jet}$ is shown for $E_T^{jet} > 6$ GeV and in bins of E_T^{jet}, $6 < E_T^{jet} < 9$ GeV and $E_T^{jet} > 9$ GeV. The notation of the lines and dots are the same as in 8.6.

Comparing the measurement to the NLO QCD prediction, we observe that the measured cross sections are larger than the NLO QCD predictions in the whole kinematic region, similar to the inclusive D^* analysis. The shape of the NLO QCD prediction agrees reasonably well in the whole η^{jet} region including the very forward part where the D^* measurement could not reach. There is a large scale uncertainty in the NLO QCD calculation. The NLO QCD prediction reproduce the measured cross section with extreme values of parameters.

Note that the effect of the hadronization shows a sizeable difference of $d\sigma/d\eta^{jet}$ between parton level and hadron level, in particluar at negative η^{jet}. This can be seen in figure 8.8 (b) (thin blue solid line and thick solid line). This may be the reason that the discrepancy in the inclusive D^* cross section were large at medium p_T ($3.25 < p_T(D^*) < 5$ GeV). The hadronization effect becomes smaller at higher E_T^{jet} as expected, as shown in figure 8.8 (c), which is consistent with the fact that the discrepancy in the inclusive became smaller at higher $p_T(D^*)$.

An excess of data is observed at the highest E_T^{jet} bin in figure 8.6. This is also true for all plots in figure 8.7. A discussion on this excess is given in section 8.5

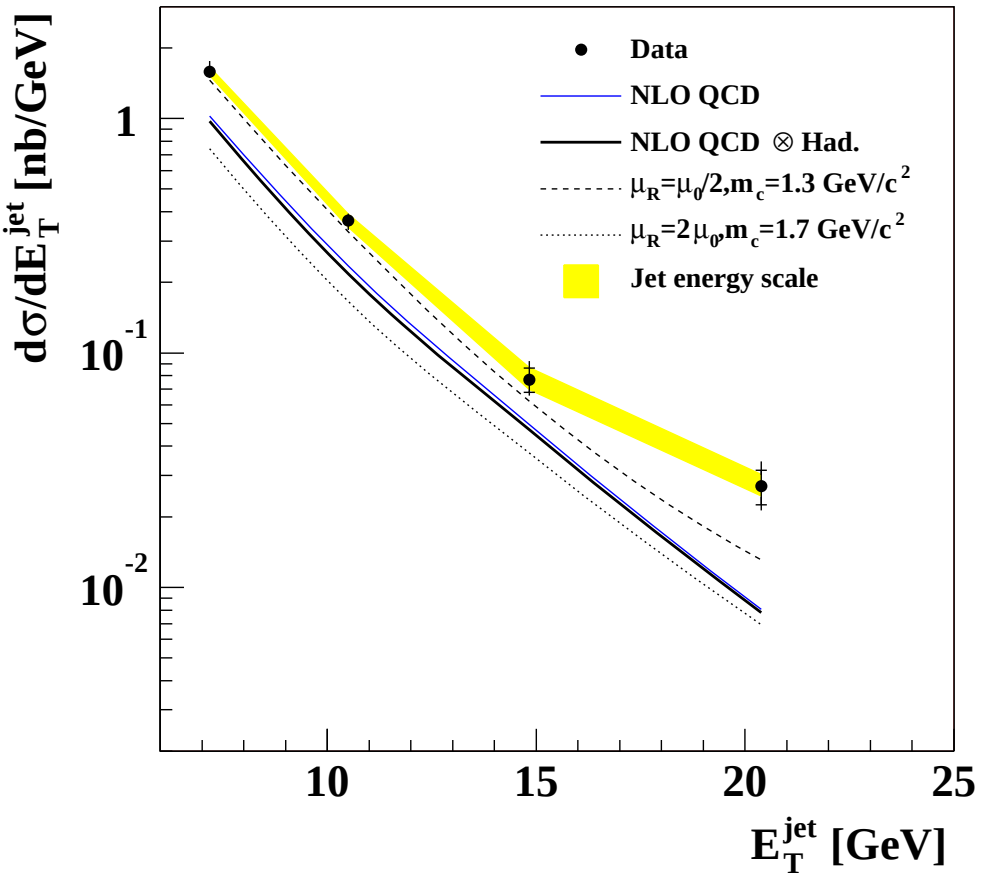

Figure 8.6: $d\sigma/dE_T^{jet}$ in $-1.5 < \eta^{jet} < -2.4$. Data (black dots) are compared to NLO QCD prediction with hadronization (thick solid line). The dashed curve (upper) shows the theoretical prediction with hadronization calculated with $\mu_R = \mu_0/2$ and $m_c = 1.3$ GeV/c^2. The dotted curve (lower) shows the theoretical prediction with hadronization calculated with $\mu_R = 2\mu_0$ and $m_c = 1.7$ GeV/c^2. The thin blue solid curve indicates the NLO QCD prediction without hadronization correction. Yellow band shows the error from the hadronic energy scale. Error bars show the total errors with the vertical lines indicating the size of the statistical error only.

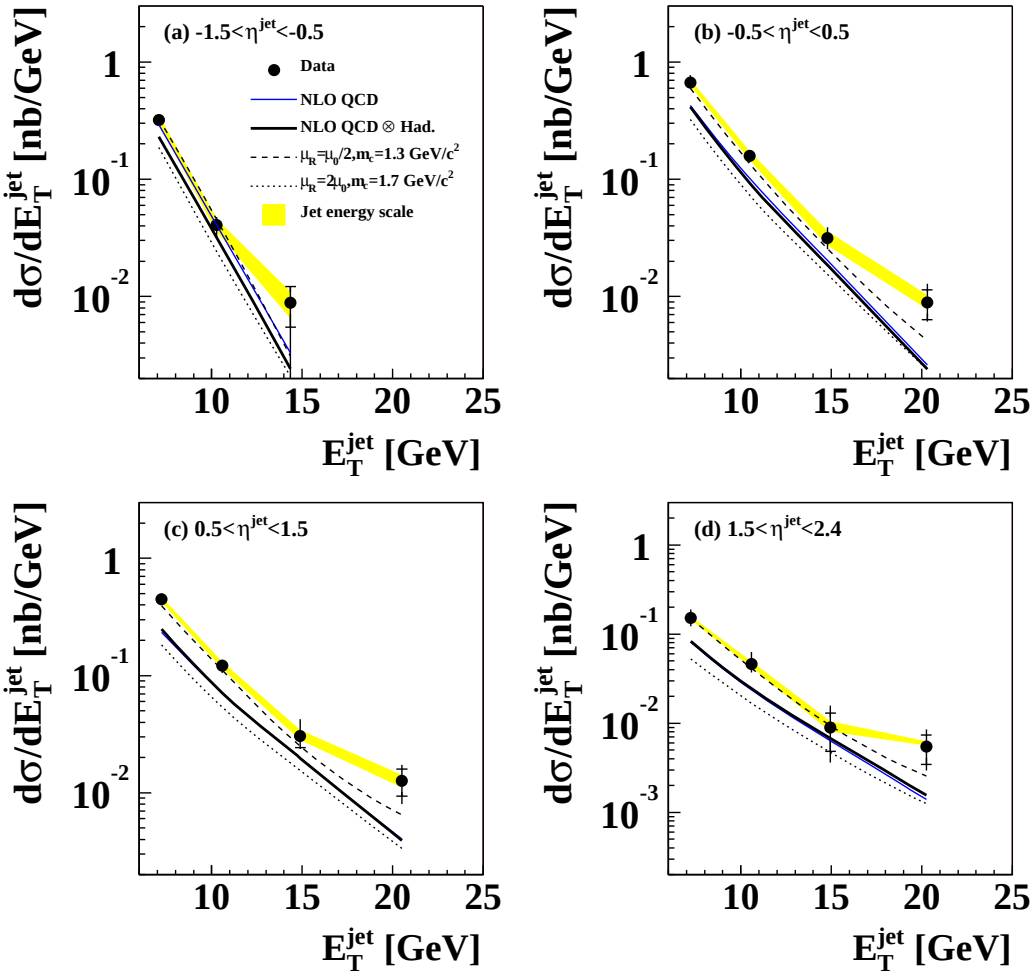

Figure 8.7: $d\sigma/dE_T^{jet}$ in $-1.5 < \eta^{jet} < -0.5$, $-0.5 < \eta^{jet} < 0.5$, $0.5 < \eta^{jet} < 1.5$ and $1.5 < \eta^{jet} < 2.4$. Data (black dots) are compared to NLO QCD prediction with hadronization (thick solid line). The dashed curve (upper) shows the theoretical prediction with hadronization calculated with $\mu_R = \mu_0/2$ and $m_c = 1.3$ GeV/c^2. The dotted curve (lower) shows the theoretical prediction with hadronization calculated with $\mu_R = 2\mu_0$ and $m_c = 1.7$ GeV/c^2. The thin blue solid curve indicates the NLO QCD prediction without hadronization correction. Yellow band shows the error from the hadronic energy scale. Error bars show the total errors with the vertical lines indicating the size of the statistical error only.

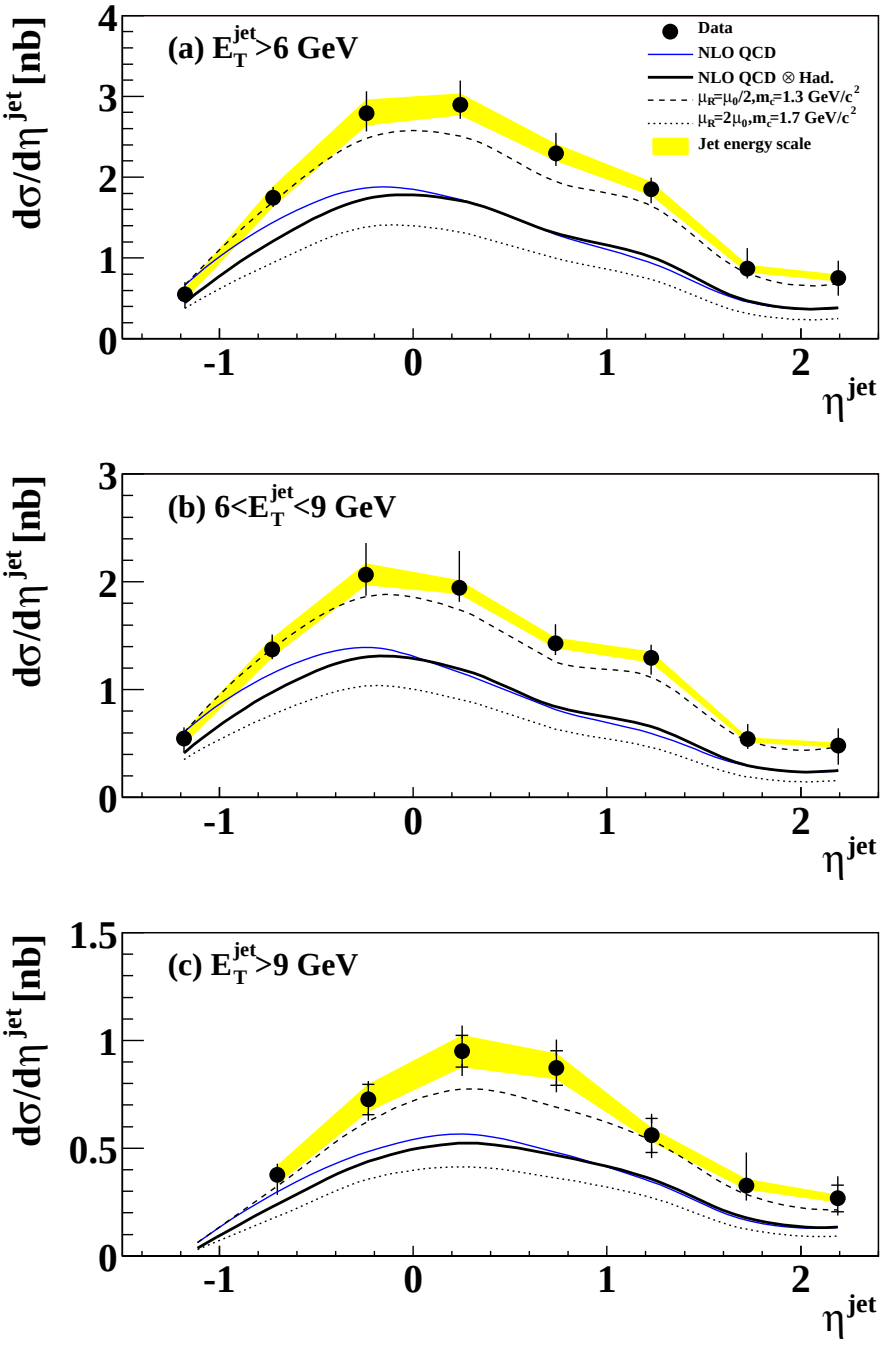

Figure 8.8: $d\sigma/d\eta^{jet}$ for $E_T^{jet} > 6$ GeV (top), $6 < E_T^{jet} < 9$ GeV (middle) and $E_T^{jet} > 9$ GeV (bottom). Data (black dots) are compared to NLO QCD prediction with hadronization (thick solid line). The dashed curve (upper) shows the theoretical prediction with hadronization calculated with $\mu_R = \mu_0/2$ and $m_c = 1.3$ GeV/c^2. The dotted curve (lower) shows the theoretical prediction with hadronization calculated with $\mu_R = 2\mu_0$ and $m_c = 1.7$ GeV/c^2. The thin blue solid curve indicates the NLO QCD prediction without hadronization correction. Yellow band shows the error from the hadronic energy scale. Error bars show the total errors with the vertical lines indicating the size of the statistical error only.

8.4.2 D^*/other jet cross sections

Figure 8.9 presents $d\sigma/dE_T$ for D^* jets and other jets compared to NLO QCD predictions. The shape of the E_T^{jet} distribution is reasonably reproduced by the NLO QCD prediction except for the last bin as in the inclusive jet presented in the last section.

Figure 8.10 shows $d\sigma/d\eta^{jet}$ for D^* jets and other jets in different E_T^{jet} regions: $E_T^{jet} > 6$ GeV, $6 < E_T^{jet} < 9$ GeV and $E_T^{jet} > 9$ GeV. The measurements are higher than NLO QCD prediction in all region but compatible within the theoretical uncertainty.

According to the LO MC, it was expected that the contribution of the resolved process gets enhanced in the forward region in $d\sigma/d\eta^{jet}$ of other jets (section 6.5.4). Since the NLO QCD calculation used in this analysis is done in massive scheme, it does not consider explicitly, the charm excitation in the photon, while it was the dominant contribution in resolved photon process as shown in charm dijet analysis (section 2.5.1). Therefore the NLO QCD prediction might underestimate the measurement in the forward region. Figure 8.10 (b),(d) and (f) shows that this is not the case, and the shape and the normalization of $d\sigma/d\eta^{jet}$ for other jets are reasonably reproduced by the extreme case where the parameters are taken as $m_c = 1.3$ GeV/c^2 and $\mu_R = \mu_0/2$.

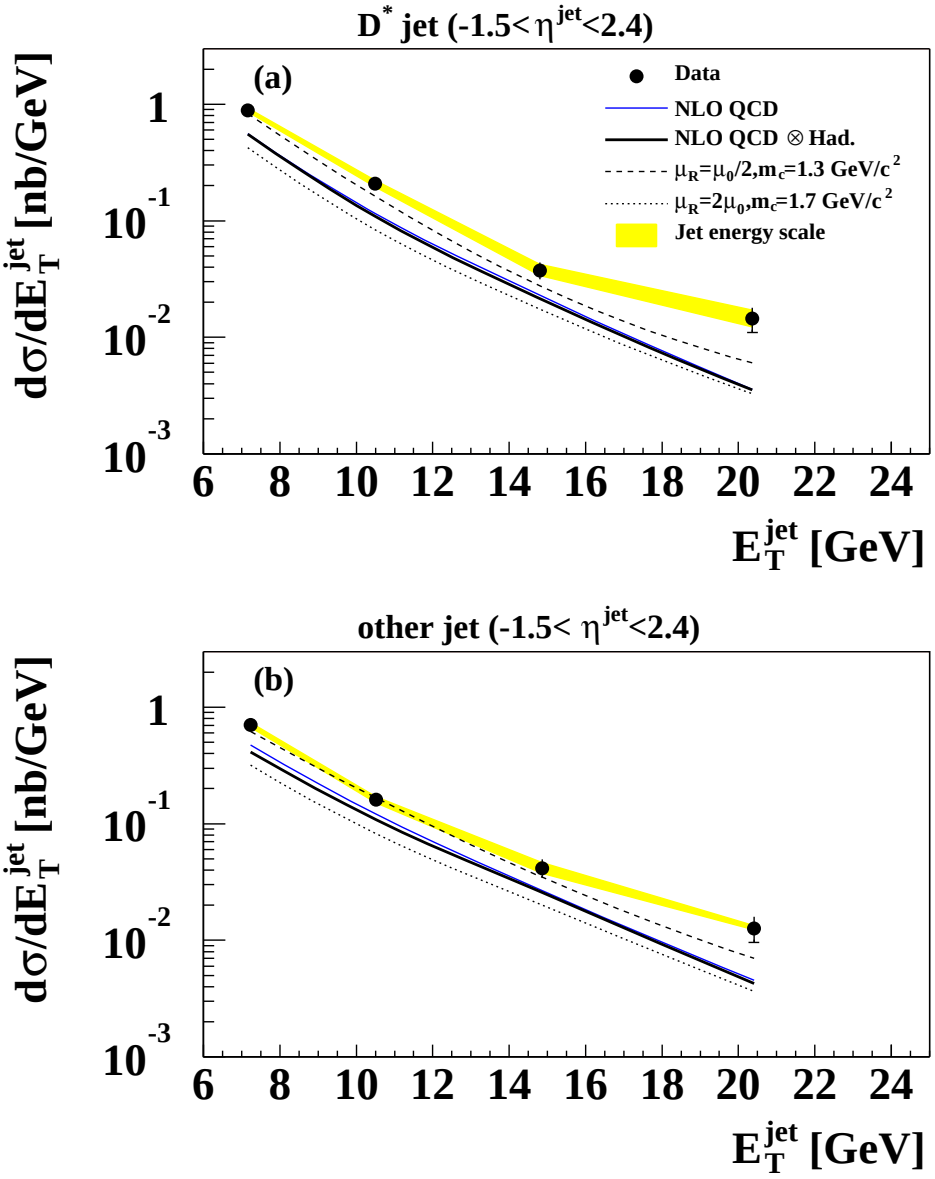

Figure 8.9: $d\sigma/dE_T^{jet}$ measured seperately for D^* jets (top) and other jets (bottom). Data (black dots) are compared to NLO QCD prediction with hadronization (thick solid line). The dashed curve (upper) shows the theoretical prediction with hadronization calculated with $\mu_R = \mu_0/2$ and $m_c = 1.3$ GeV/c^2. The dotted curve (lower) shows the theoretical prediction with hadronization calculated with $\mu_R = 2\mu_0$ and $m_c = 1.7$ GeV/c^2. The thin blue solid curve indicates the NLO QCD prediction without hadronization correction. Yellow band shows the error from the hadronic energy scale. Error bars show the total errors with the vertical lines indicating the size of the statistical error only.

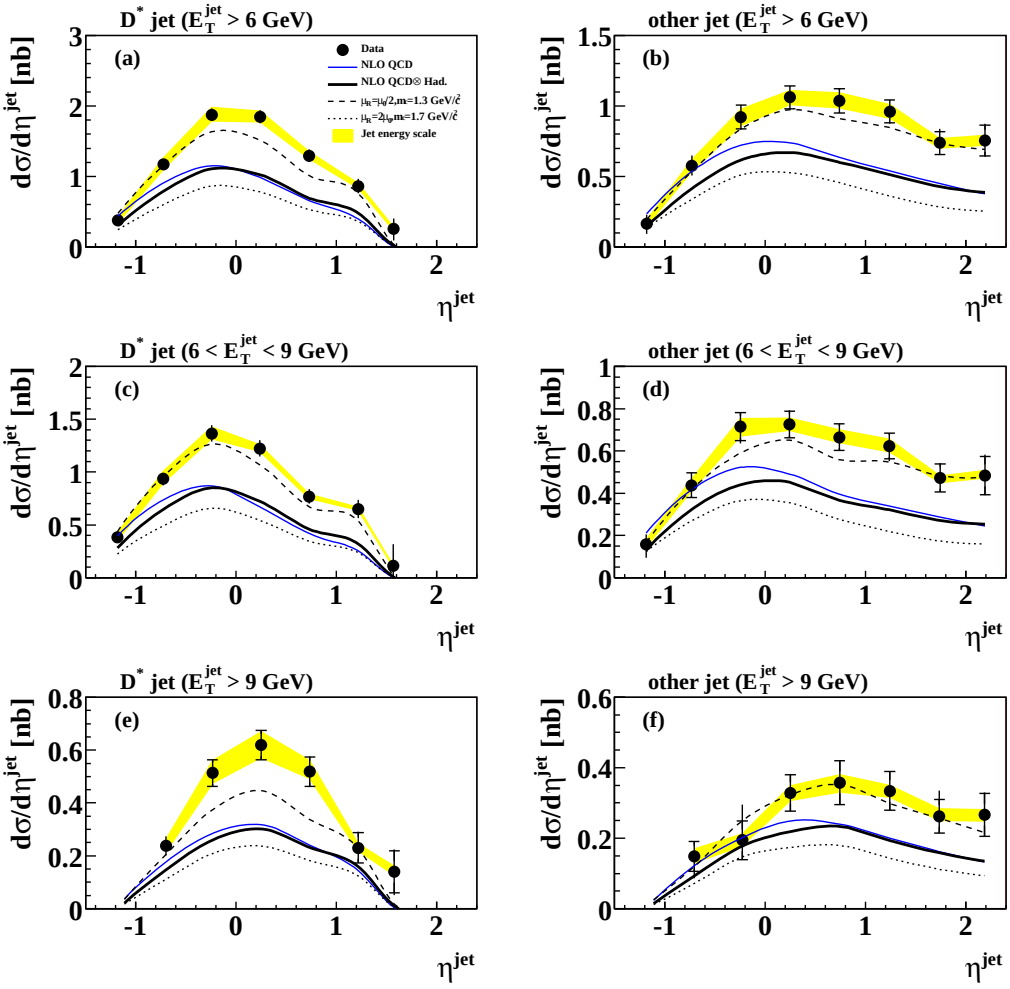

Figure 8.10: $d\sigma/d\eta^{jet}$ of D^* jets (left) and other jets (right) with different E_T^{jet} ranges. Data (black dots) are compared to NLO QCD prediction with hadronization (thick solid line). The dashed curve (upper) shows the theoretical prediction with hadronization calculated with $\mu_R = \mu_0/2$ and $m_c = 1.3$ GeV/c^2. The dotted curve (lower) shows the theoretical prediction with hadronization calculated with $\mu_R = 2\mu_0$ and $m_c = 1.7$ GeV/c^2. The thin blue solid curve indicates the NLO QCD prediction without hadronization correction. Yellow band shows the error from the hadronic energy scale. Error bars show the total errors with the vertical lines indicating the size of the statistical error only.

8.5 Discussions

We have seen that shapes of jet cross sections are reasonably described by the NLO QCD prediction. The shape of the η^{jet} cross section is dominated by low E_T^{jet} jets and by taking into account the hadronization correction, the agreement became better in the whole region. However, the measured E_T^{jet} cross section shows an excess to the NLO QCD prediction in the highest E_T^{jet} bin. In this section, we discuss the possible explanations of the excess at high E_T^{jet} and the connection to the inclusive D^* cross section.

First of all, kinematic distributions of events having a jet with $E_T^{jet} > 18$ GeV and a D^* show reasonable agreement with HERWIG, indicating that these events are likely to be physics events, not non-physics backgrounds. Also events having a jet in this region were scanned, and found no contamination of events from non-physics backgrounds, such as beam-gas events or cosmic events. As the reason of the excess at high E_T^{jet} we consider the following three possibilities.

- A statistical fluctuation,
- D^* from b production,
- A secondary charm production due to higher order effects.

In order to check the possibility of the first hypothesis, it was further examined that the D^* signal extraction in this bin was fine. Extracting D^* signal by performing a maximum likelihood fit to the Δm distribution with a Gaussian and a background function given by eq. (5.15) ($N_{D^*} = 137 \pm 37$), agreed to the extracted number of signal with wrong charge background subtraction ($N_{D^*} = 130 \pm 37$) within statistical uncertainty. The excess is about 3σ from the upper bound of the NLO QCD calculation. Although we cannot rule out this possibility, the excess at high $E_T^{jet}$is seen in all bins of η^{jet} which weakens that to be a statistical fluctuation.

In both the second and the third hypothesis, the charm quark is produced by a decay or a perturbative branching of the primary parton which was produced by the hard scattering. Here we call them a *secondary charm*. Figure 8.11 shows distributions of variables related to the D^* for events having a jet with $E_T^{jet} > 18$ GeV. Distributions of $p_T(D^*)$ and $\eta(D^*)$ are shown in figure 8.11 (a) and (b). In figure 8.11 (c), the ratio of the transverse momentum of the D^* and the matching jet, $p_T(D^*)/E_T^{jet}$ is shown. The variable $p_T(D^*)/E_T^{jet}$ represents the fractional momentum of the jet carried by the D^* which is expected to have a peak at $p_T(D^*)/E_T^{jet} > 0.5$ for primary charm production, as in figure 6.2. The data points are shown by dots, HERWIG (charm + bottom) by the solid line and the contribution from primary b production in HERWIG is shown by the hatched histogram. Clearly, $p_T(D^*)$ and $p_T(D^*)/E_T^{jet}$ distributions are not described by the MC in shape. The data show more entries at low $p_T(D^*)$ or $p_T(D^*)/E_T^{jet}$.

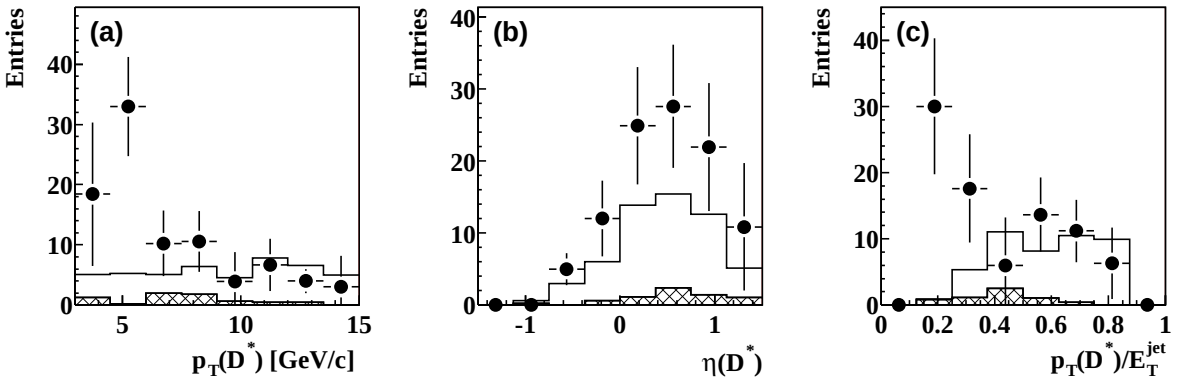

Figure 8.11: D^* variables for events having a jet in the highest E_T^{jet} bin. (a) Transverse momentum of the D^*, (b) pseudo-rapidity of the D^* and (c) the ratio $p_T(D^*)/E_T^{jet}$. The data (dots), HERWIG (c+b) (solid lines) and HERWIG (b) (hatched) are shown together.

As described in section 6.4, the measured cross section includes contribution from b production, while the NLO QCD calculation does not. The fraction of b contribution in the measurement increases at high E_T^{jet} reaching up to 12 % in the highest E_T^{jet} bin. Taking into account of the fact that measured b cross sections are higher than theoretical expectations, b fraction may be as high as 20-30 %. However, this is still too small to explain the excess at high E_T^{jet}. Furthermore, although figure 8.11 (c) shows that the contribution from b production has a peak at lower $p_T(D^*)/E_T^{jet}$ value than charm production, it still fails to describe the shape of the distribution. Therefore, the b production should contribute to the observed excess that alone seems not to explain it all.

The third hypothesis considers the secondary charm production from the primary parton. Such process has been observed at LEP experiments [53]–[55], where they observed $c\bar{c}$ production from gluon splitting, i.e. $e^+e^- \to q\bar{q}g; g \to c\bar{c}$ at CM energy in the region of Z^0 mass [54, 55]. They found that the rate of this process to the total hadronic decay of Z^0 amounts to about 3 %. Similar process may also take place in photoproduction at HERA at high energy. In such cases, the momentum of the charm quark becomes smaller than that of the primary parton, or the jet. Thus $p_T(D^*)/E_T^{jet}$ would peak at smaller values than that from primary charm production, as in figure 8.11 (c). Although a further study is needed to derive a definitive conclusion about the physics process involved, the excess at high E_T^{jet} and the $p_T(D^*)/E_T^{jet}$ distribution indicates the presence of a secondary charm production. It would be interesting to investigate it with higher statistics and extend the measurement to higher E_T^{jet} since the rate of the secondary charm production might depend on E_T^{jet}.

Figure 8.11 (a)-(c) suggest that the excess observed at high E_T^{jet} in jet cross section

would appear at low $p_T(D^*)$ ($\simeq 3-6$ GeV) and positive $\eta(D^*)$ which corresponds to the region where an excess was observed in D^* cross sections. This would contribute a few % to the excess observed in the forward region in D^* cross sections.

Chapter 9

Conclusion

Inclusive jet cross sections have been measured for the first time in $D^{*\pm}$ photoproduction. The kinematic region of the measurement was restricted to $Q^2 < 1$ GeV^2, $130 < W < 280$ GeV, $p_T(D^*) > 3$ GeV/c, $|\eta(D^*)| < 1.5$, $E_T^{jet} > 6$ GeV and $-1.5 < \eta^{jet} < 2.4$. The measured cross sections were presented as a function of E_T^{jet} and η^{jet}.

Theoretical predictions of the cross sections were calculated in the same kinematic region as the experiment using the NLO QCD calculation performed in the massive scheme. The scales μ_R, $\mu_{F,\gamma}$ and $\mu_{F,p}$ were taken as $\mu_0 = \sqrt{m_c^2 + \langle p_T \rangle^2}$ and the charm quark mass was taken as $m_c = 1.5$ GeV/c^2 in the calculation. Hadronization correction was applied to the NLO QCD prediction to obtain the theoretical prediction at hadron level. It was found that the hadronization effect becomes important at low E_T^{jet}.

The measured cross sections are larger than the NLO QCD prediction in the whole region as in the inclusive D^* cross sections [14]. In contrast to the inclusive D^* cross sections, the shape of the cross sections are reasonably described by the NLO QCD prediction within the theoretical uncertainty. This measurement extended the pseudo-rapidity region into the forward region, compared to the inclusive D^* measurement, to study particle distribution in D^* events. The contribution of the c quark from the photon was expected to become dominant in the forward region. Although the NLO QCD prediction does not consider this process explicitly, it is able to reproduce the shape of the jet cross section in the forward region as well.

An excess is observed at the highest measured E_T^{jet} by about 3σ. By comparing the transverse momentum of the D^* and that of the matching jet, the excess at high E_T^{jet} is found to have relatively low $p_T(D^*)$ where the excess was observed in the D^* cross section. The contribution at low $p_T(D^*)/E_T^{jet}$ indicates the existence of a secondary charm production in photoproduction at HERA.

Acknowledgements

I am very grateful to my supervisor Prof. K. Tokushuku for his guidance and support throughout my graduate student course, as well as giving me the opportunity to study in the ZEUS Collaboration. Also I appreciate his careful reading of the draft and lots of useful comments on it.

I would like to thank the coordinators of the heavy flavor group, Dr. M. Wing, Dr. L. Gladilin, Dr. R. Hall-Wilton and Dr. M. Corradi. I wish to express my special thanks to Dr. M. Wing for giving me many useful advises on the details of the analysis and for organizing the charm subgroup meeting. Dr. L. Gladilin has also gave me many advises on the analyis and helped me a lot on the NLO QCD calculation. I am grateful to Mr. J. Loizides for the detailed discussions on the analysis. I enjoyed working with him.

I am grateful to Dr. Y. Yamazaki for his advises where his insight in physics was very helpful. I would like to thank the members of ZEUS Tokyo group, Prof. S. Yamada, Prof. R. Hamatsu, Prof. S. Kitamura, Prof. T. Tsurugai, Prof. Y. Iga, Prof. M. Kuze, Dr. K. Nagano, Mr. K. Matsuzawa, Mr. S. Kagawa, Ms. M. Kataoka, Mr. T. Tawara, Ms. S. Kato, Mr. Y. Ri, Mr. R. Hori, Mr. O. Ota and Mr. H. Fujimoto, for their support and collaboration.

Last but not least, I would like to express my thanks to my family for their understanding, support and encouragement.

Appendix A

EFO algorithm

The EFO algorithm is divided in two steps. First, neighboring CAL cells are merged into a cluster of cells. This procedure is called *clustering*.

A.1 Clustering of CAL cells

The clustering is performed in two steps [56]: (1) neighboring cells in the same CAL section (EMC, HAC1 and HAC2) are clustered in 2 dimensional plane (*cell-island*), (2) then cells in different sections (EMC and HAC1, or HAC1 and HAC2) are merged in 3 dimensional space(*cone-island*).

A.1.1 Cell-island

The algorithm to make cell-island is based on the energy gradient between adjacent cells. A cell's energy is compared to the eight adjacent cells around itself. If the energy of the cell is higher than all other cells around itself, then the cell is called a *local maximum*. If the cell is not the highest energy cell, the cell is merged to the highest energy cells around it. After evaluating all cells, there are several local maxima. Each local maxima has a cluster of cells around it. The group of cells belonging to the same local maximum are regarded as the cell-island. This situation is schematically shown in figure A.1.1.

A.1.2 Cone-island

The next step of the clustering is to form a cone-island. Clustering over different sections (FCAL/BCAL boundary, BCAL/RCAL boundary or EMC/HAC sections) are allowed. A cone from the vertex position is considered in the $\theta - \phi$ plane. If two cell-islands have an openning angle from the vertex position, close enough, these two cells are merged.

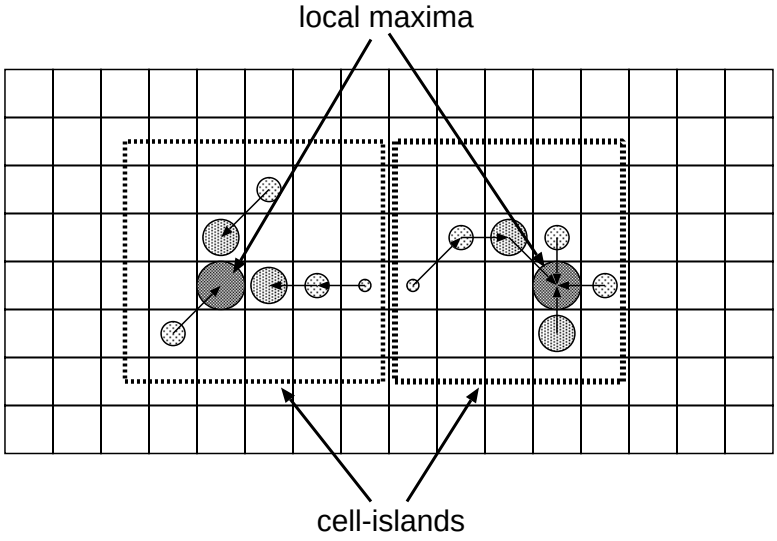

Figure A.1: A schematic diagram showing how cell-islands are formed.

A.2 Matching of tracks and cone-islands

To match tracks and cone-islands, only charged tracks with a momentum in the range $0.1 < p_T < 20$ GeV which are fitted to the event vertex and traverse at least 4 CTD superlayers are considered. The track is extrapolated to the inner surface of the CAL and distance of closest approach (DCA) between the track and the island is calculated. A track is matched to an island if the DCA is less than 20 cm or the DCA is smaller than the size of an island. The size of an island is defined as the maximum distance between the position of the island and positions of cells belonging to that island, in the plane perpendicular to the line drawn from the event vertex to the island.

After matching tracks and cone-islands, we must decide which information to use for the measurement of 4-momentum of the EFO. Which information to use is determined as the following.

- Unmatched tracks
  Use the CTD measurement for the momentum of the EFO. The energy is calculated by assuming a mass of a charged pion to this EFO.

- Unmatched islands
  The CAL measurement is used and the EFO is regarded as a neutral particle with no mass, i.e. $E = |p|$.

- One, two or three tracks matches one or two islands
  In this case, both measurements are available. The CTD information is used if the

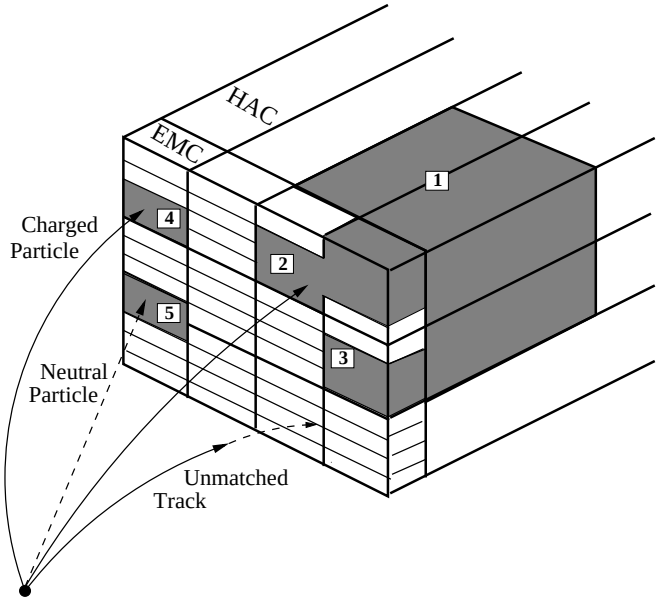

Figure A.2: A figure illustrating the clustering into a cone-island (cell-islands 1, 2 and 3 are merged) and the track-island matching.

following conditions are both satisfied.

1. $E_{cal}/p < 1.0 + 1.2 \cdot \sigma(E_{cal}/p)$
2. $\sigma(p)/p < \sigma(E_{cal})/E_{cal}$

The first condition ensures that the energy of the island comes only from the matched track. A factor 1.2 multiplied to $\sigma(E_{cal}/p)$ is used to account for the underestimation of the uncertainty on E_{cal}/p obtained from test beam measurement. The second condition requires that the uncertainty on the track momentum measurement is smaller than the uncerntainty on the energy measurement in the CAL. If the island is at the boundary of B/FCAL or B/RCAL, the requirement on the resolution is loosened ($\sigma(p)/p < 1.2 \cdot \sigma(E_{cal})/E_{cal}$), since the resolution of E is poor in these regions.

If more than one track (island) matches, then the sum of p (E_{cal}) is used.

If the following three conditions are satisfied, the EFO is regarded as a muon and the CTD information is used.

1. $E_{cal} < 5$ GeV
2. $E_{cal}/p < 0.25$
3. $p_T < 30$ GeV/c

In case a single track matches to one or two islands and the energy measurement of the island is favored, energy measurement is taken from the CAL but the angular information of the CTD is used.

- More than 3 tracks matches an island
  The CAL information is used as for unmatched islands.

Appendix B

Description of the trigger logic

B.0.1 FLT

The trigger logic in the FLT used for this analysis is an OR of two GFLT slots; slot 42 and slot 59. Both of the slots require a large energy deposit in the CAL and an existence of a good track with slightly different thresholds used in each slot. Standard vetoes with background counters are imposed to reject beam-gas backgrounds.

Slot 42 requires a large energy deposit in the CAL with a loose track requirement. The total energy in the CAL (E^{FLT}_{CAL}), energy in EMC sections of CAL (E^{FLT}_{EMC}), energy in RCAL EMC sections (E^{FLT}_{REMC}) and energy in BCAL EMC sections (E^{FLT}_{BEMC}) are evaluated. The CFLT performs a zero suppression of cell energies such that the energies are set to zero if it is less than 464 MeV. After the zero suppression, energies of cells are summed up excluding cells beloging to towers of 3 inner rings in the FCAL and 1 inner ring in the RCAL around the beam hole. These cells are excluded since the energies measured at those cells are affected by the beam-gas events. Also the event timing should be consistent with timing of physics events.

Slot 42 requires the following conditions.

- Large energy deposit in CAL.
  - $E^{FLT}_{CAL} > 15$ GeV or
  - $E^{FLT}_{EMC} > 10$ GeV or
  - $E^{FLT}_{BEMC} > 2$ GeV or
  - $E^{FLT}_{REMC} > 2$ GeV
- At least one good FLT track which comes from the nominal interaction point ($-50 < z < 80$ cm)
- Timing information measured by VETO, C5 counter and SRTD are not consistent with the beam-gas timing.

Slot 59 requires a better quality of the tracking with a looser cut on energy deposits than slot 42. It requires the following conditions.

- A large energy deposit in CAL.
  - $E^{FLT}_{CAL} > 2$ GeV and ($E^{FLT}_{REMC} > 0.5$ GeV or $E^{FLT}_{BEMC} > 2$ GeV) or
  - $E^{FLT}_{CAL} > 8$ GeV and $E^{FLT}_{FCAL}/E^{FLT}_{CAL} < 0.65$.
- At least 9 FLT tracks found and the fraction of the number of good FLT tracks to the total number of FLT tracks is greater than 50 %.
- Timing information measured by VETO, C5 counter and SRTD are not consistent with the beam-gas timing.

B.0.2 SLT

At the SLT, events are vetoed if the timing obtained from the FCAL (t_{FCAL}), RCAL (t_{RCAL}), top half of the BCAL (t^{top}_{BCAL}) and bottom half of the BCAL (t^{bottom}_{BCAL}) satisfy one of the following relations.

- $t_{RCAL} > -8$ ns.
- $t_{FCAL} - t_{RCAL} < 8$ ns.
- $t^{bottom}_{BCAL} - t^{bottom}_{BCAL} > -10$ ns.

Timings are calibrated such that the $t = 0$ corresponds to the timing of physics events. The first two cuts are used to remove backgrounds from proton beam-bas events. The last one is to remove cosmic events.

A cut on $\sum_{CAL} E - P_z$,

- $\sum_{CAL} E - P_z < 75$ GeV

is also required to further remove backgrounds.

To select D^* photoproduction events, the following conditions must be all satisfied.

- $-60 <$ CTD SLT vertex < 60 cm or no CTD information
- $\sum_{CAL} E - P_z > 7$ GeV
- $\sum_{CAL} E_T$ (excluding FCAL inner ring) > 6 GeV
- $\sum_{CAL} P_z / \sum_{CAL} E < 0.96$
- $N_{track} \geq 5$ and $N_{vtxtrk} \geq 3$

- $N_{track} \geq 16$ or $\sum_{1,2} P_T > 1.2$ GeV.

The variable, $\sum_{1,2} P_T$ is the sum of tranverse momenta of the two tracks with the highest transverse momenta. The lower cut on $E - P_z$ is applied to removed proton beam-gas events, since these events are boosted towards positive z direction, therefore $E \simeq P_z$. Cuts on $\sum_{CAL} E_T$ and $\sum_{CAL} P_z / \sum_{CAL} E < 0.96$ require that there should be a large energy deposit in the central part of the detector. Cuts on tracking quantities are required, since the event must contain many tracks in order to reconstruc a D^*.

This branch of the SLT logic, requires that slots 42 and 59 of the FLT are fired.

B.0.3 TLT

The following global veto logic is applied at the TLT.

- $|t_{RCAL}| < 6$ ns.
- $|t_{FCAL}| < 8$ ns.
- $t_{FCAL} - t_{RCAL} < 8$ ns.
- $|t_{GLOBAL}| < 8$ ns.

where t_{GLOBAL} represent the timing obtained from all CAL cells. These cuts further remove non-*ep* backgrounds.

At the TLT, full tracking information is available and the offline tracking code, modified to achieve higher perfomance, is used. D^* reconstructed as described in section 5.6.3 is performed with wider mass windows of

- $1.4 < m(D^0) < 2.2$ GeV/c^2
- $\Delta m < 0.17$ GeV/c^2

Appendix C

FLT efficiency

The FLT used in this analysis consists of a logical OR of several conditions. As described in section 5.5, event is accepted by the FLT if one of the following conditions are satisfied.

A. $E_{CAL}^{FLT} > 15$ GeV

B. $E_{EMC}^{FLT} > 10$ GeV

C. $E_{BEMC}^{FLT} > 3$ GeV

D. $E_{REMC}^{FLT} > 2$ GeV

E. `TRK_dstar` and $E_{CAL}^{FLT} > 2$ GeV and ($E_{BEMC}^{FLT} > 2$ GeV or $E_{REMC}^{FLT} > 0.5$ GeV)

F. `TRK_dstar` and $E_{CAL}^{FLT} > 8$ GeV and $DSTAR\_FCAL^{FLT} > 0$ GeV

where the logic `TRK_dstar` is a requirement of the fraction of the number of FLT tracks coming from the vertex to the number of all FLT tracks. The variable $DSTAR\_FCAL^{FLT}$ is defined as

$$DSTAR\_FCAL^{FLT} = 0.65 \times E_{CAL}^{FLT} - E_{FCAL}^{FLT}$$

We ignore the requirement that there should be at least one good FLT track, since this condition was always held for events passing the offline cuts.

The efficiency of the FLT has been studied using HERWIG. A sample of events passing all offline cuts without the trigger requirement has been prepared for the study. Table C summarizes the fraction of events passing each sublogic with respect to all events passing the offline cuts. The table also contains the fraction of the firing probability of each variable. The efficiency of the FLT is estimated to be 88 %.

Figure C and C show the fraction of events survived after requiring a cut to a certain variable, as a function of E_T^{jet} or η^{jet}. For example, figure C (a) shows that only 20 % of jets with $6 < E_T^{jet} < 9$ GeV are taken after requiring the condition $E_{CAL}^{FLT} > 15$ GeV. For

sublogic	fired (%)	only itself (%)
slot 42 or slog 59	88.0	-
slot 42	73.1	21.2
slot 59	66.3	14.5
A	32.8	0.84
B	27.5	0.04
C	54.2	7.57
D	23.2	2.75
E	64.2	5.16
F	55.7	1.71
variable	fired (%)	
$E_{CAL}^{FLT} > 2$	99.9	
$E_{BEMC}^{FLT} > 2$	76.2	
$E_{REMC}^{FLT} > 0.5$	49.4	
$E_{CAL}^{FLT} > 8$	83.2	
$DSTAR\_FCAL^{FLT} fbb > 0$	94.3	

Table C.1: Summary of the firing probability of FLT variables based on events passing all offline cuts.

jets with $9 < E_T^{jet} < 13$ GeV, about 60 % are taken after the cut. For jets with $E_T^{jet} > 18$ GeV, almost 100 % of events are saved.

From figure C (e),(f),(g), one can see that the most of the events are taken by the condition '$E_{CAL}^{FLT} > 8$ GeV & $DSTAR\_FCAL^{FLT}$' or $E_{BEMC}^{FLT} > 2$ GeV. This is also true by looking at figure C. Moreover, from figure C (g), one finds that some fraction of jets in the central region ($-1 < \eta^{jet} < 1$) are rejected by requiring $E_{CAL}^{FLT} > 8$ GeV. For a fixed E_T, E becomes large at large η^{jet}, therefore efficiency gets higher in forward region for $E_{CAL}^{FLT} > 8$ GeV requirement. However, it was found that part of those jets rejected by $E_{CAL}^{FLT} > 8$ GeV requirement are saved by $E_{BEMC} > 2$ GeV. As shown in figure C (e), the efficiency of this cut is high for jets in the central region.

C.1 Efficiency curve

The trigger study has been done to check whether the MC simulates the efficiencies well. If the efficiency of the MC differs from that of the data, then we may get the wrong correction factor to unfold the cross section. This introduces a systematic effect on the measured cross sections. In order to compare the efficiencies of data and MC, we check them against the offline values of the FLT component data.

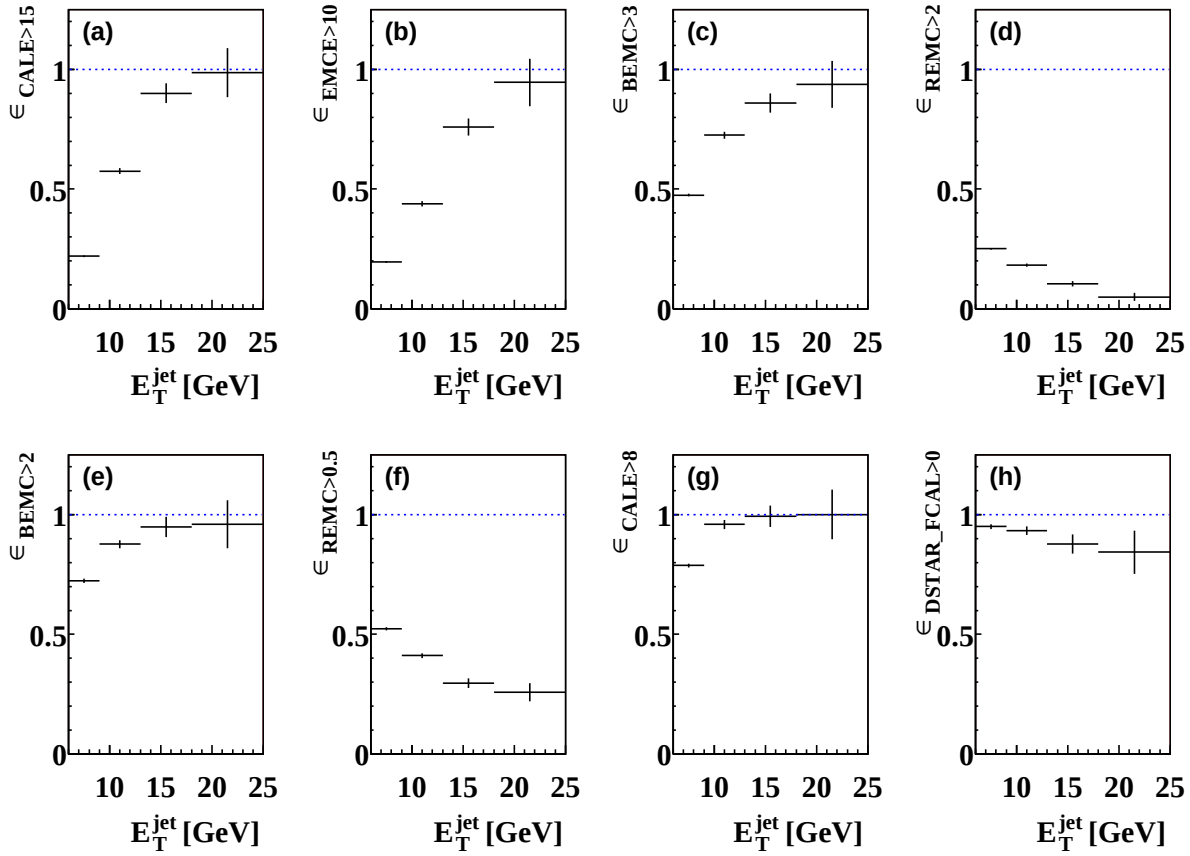

Figure C.1: Effect of cuts on FLT calorimeter quantities on the E_T^{jet} distribution.

For example, in order to evaluate the efficiency of the logic, $E_{CAL} > 15$, we plot the fraction of events passing the $E_{CAL}^{FLT} > 15$ cut with respect to $E_{CAL}^{offline}$. Thus obtained curve (*efficiency curve*) should be zero at $E_{CAL}^{offline} \lesssim 15$ and go up to unity at $E_{CAL}^{offline} \gtrsim 15$. This is shown in figure C.1 (a). The turning point of the efficiency curve in figure C.1 (a) is at 23 GeV. This is significantly higher than 15 GeV, which is the threshold applied at the FLT. This discrepancy comes from the fact that in the Calorimeter FLT (CFLT) [57], a zero suppresion is performed for towers whose energy is less than 464 MeV, i.e. energies of towers less than 464 MeV are not counted in the energy sums of FLT quantities. Due to this procedure, energy is underestimated in the FLT. Figure C.1 tells that there could be about 8 GeV difference between the FLT and offline CAL quantities.

Efficiency curves for other FLT variables are shown with respect to their offline quantities in figure C.1. Efficiency curves obtained from data are shown by dots while those obtained from HERWIG are shown by the histogram.

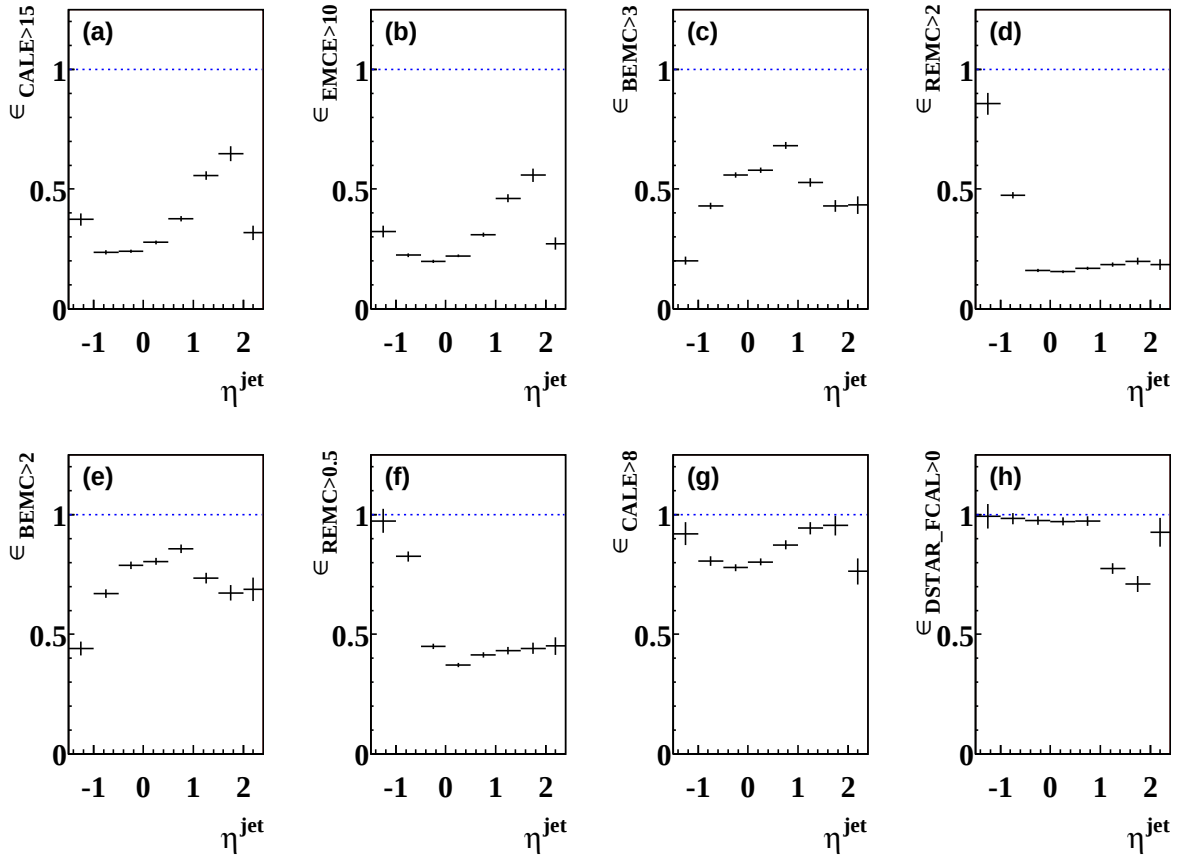

Figure C.2: Effect of cuts on FLT calorimeter quantities on the η^{jet} distribution.

Efficiency curves are fitted by a functional form given by

$$\epsilon = 0.5\left(1 + \tanh(\frac{x - p_0}{p_1})\right) \tag{C.1}$$

Fitted curves are shown by the black solid line for data and by red dashed line for HERWIG in figure C.1.

As already mentioned, difference between the efficiency curve obtained for data and MC is observed for E_{CAL}. The differences are observed in other variables as well, such as E_{BEMC} or $DSTAR\_FCAL$.

In figure C.1, differences between data and MC of the turning points of the efficiency curves are plotted against the energy. This difference shows a linear dependence to the energy scale. Therefore it is likely that there are difference of the energy scale in the FLT between data and MC.

C.2 Estimation of systemtatic uncertainty

Efficiency curves obtained in the previous section can be used to select events instead of using the FLT decision. For example, the FLT requirement of $E_{CAL}^{FLT} > 15$ can be replaced by giving each event a weight $w_{CALE}(E_{CAL}^{offline})$.

The FLT logic used in this analysis consists of an OR of 6 logics as described earlier. We must calculate the efficiency of the event from the efficiency of each variable. If there are no correlations between the variables the combined efficiency of logic A and B are given by

$$\epsilon_{A\cup B} = 1 - (1-\epsilon_A)(1-\epsilon_B) \quad \text{(C.2)}$$

$$\epsilon_{A\cap B} = \epsilon_A \cdot \epsilon_B \quad \text{(C.3)}$$

for OR and AND logics respectively. If logic A and B have 100 % positive correlation, the combined efficiency are given by

$$\epsilon_{A\cup B} = \max(\epsilon_A, \epsilon_B) \quad \text{(C.4)}$$

$$\epsilon_{A\cap B} = \min(\epsilon_A, \epsilon_B) \quad \text{(C.5)}$$

In the case for this analysis, the FLT logic can be written as follows depending on the tracking condition.

- At least one good track but doesn't satisfy `TRK_dstar` condition.
  - $E_{CAL}^{FLT} > 15$ GeV
  - $E_{EMC}^{FLT} > 10$ GeV
  - $E_{BEMC}^{FLT} > 3$ GeV
  - $E_{REMC}^{FLT} > 2$ GeV
- `TRK_dstar` is satisfied.
  - $E_{CAL}^{FLT} > 15$ GeV
  - $E_{EMC}^{FLT} > 10$ GeV
  - $E_{BEMC}^{FLT} > 2$ GeV
  - $E_{REMC}^{FLT} > 0.5$ GeV
  - $DSTAR\_FCAL^{FLT} > 0$ GeV

Then the overall efficiency becomes

$$\begin{aligned}\epsilon = \quad & 1-(1-\epsilon_{E^{FLT}_{CAL}>15})(1-\epsilon_{E^{FLT}_{EMC}>10}) \\ & (1-\epsilon_{E^{FLT}_{BEMC}>3})(1-\epsilon_{E^{FLT}_{REMC}>2})\end{aligned} \tag{C.6}$$

for events with at least one good FLT track but does not satisfy `TRK_dstar` condition. And

$$\begin{aligned}\epsilon = \quad & 1-(1-\epsilon_{E^{FLT}_{CAL}>15})(1-\epsilon_{E^{FLT}_{EMC}>10})(1-\epsilon_{E^{FLT}_{BEMC}>2}) \\ & (1-\epsilon_{E^{FLT}_{REMC}>0.5})(1-\epsilon_{E^{FLT}_{CAL}>8}\cdot\epsilon_{DSTAR\_FCAL>0})\end{aligned} \tag{C.7}$$

for events satisfying `TRK_dstar` condition.

Systematic uncertainty due to the FLT efficiency was estimated as the difference of the correction factors obtained, by using efficiency curves fitted to the MC and by using efficiency curves fitted to the data. It was found that this effect is about 2 % in the lowest E_T bin and gets smaller as E_T gets higher. The systematic uncertainty was estimated by calculating the combined efficiecy considering all variables as uncorrelated or all 100 % positively correlated. The systematic uncertainties were found to be similar to the one obtained with using eq. (C.6) and eq. (C.7).

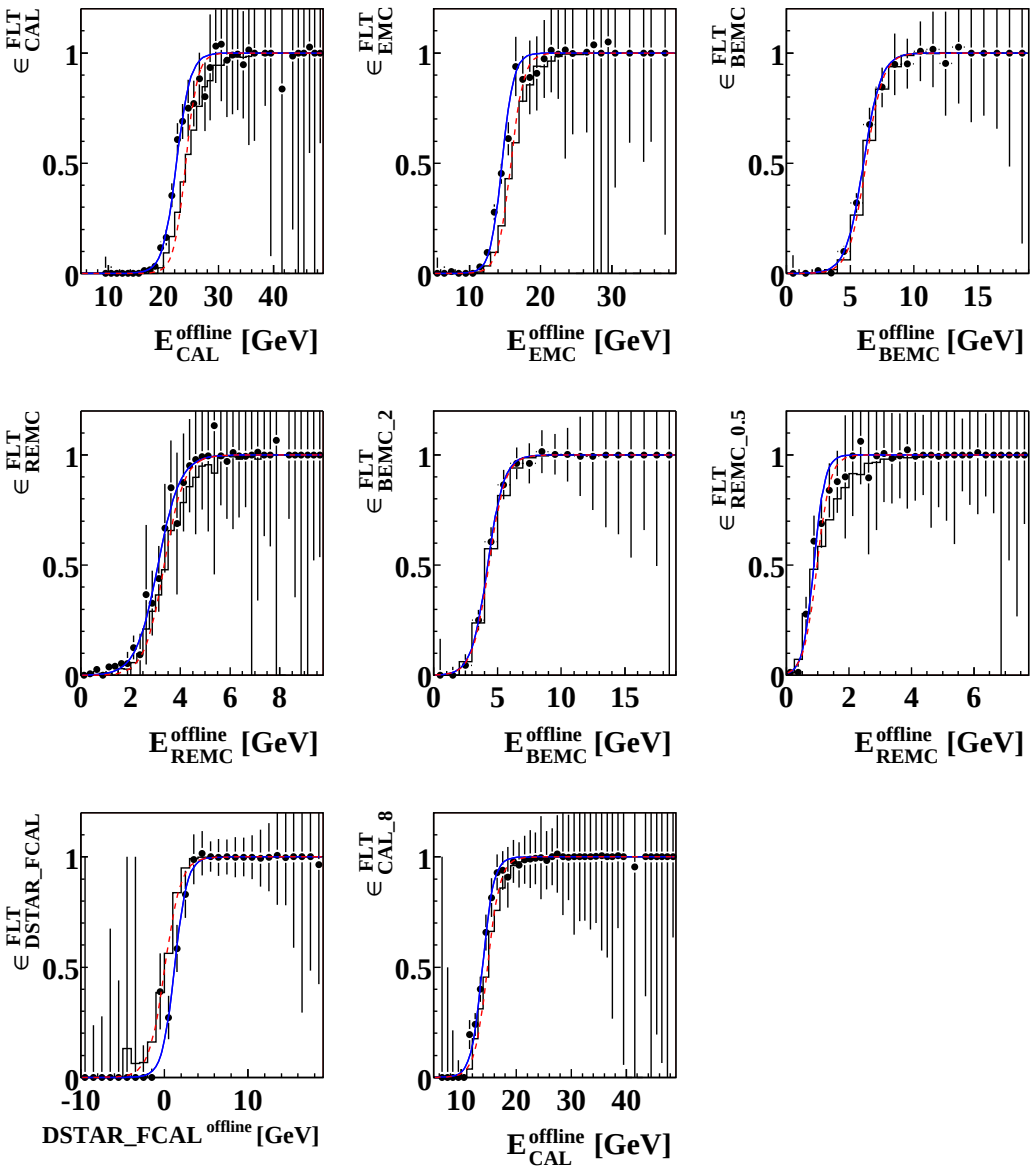

Figure C.3: Efficiency curves of FLT variables plotted with respect to their offline quantities.

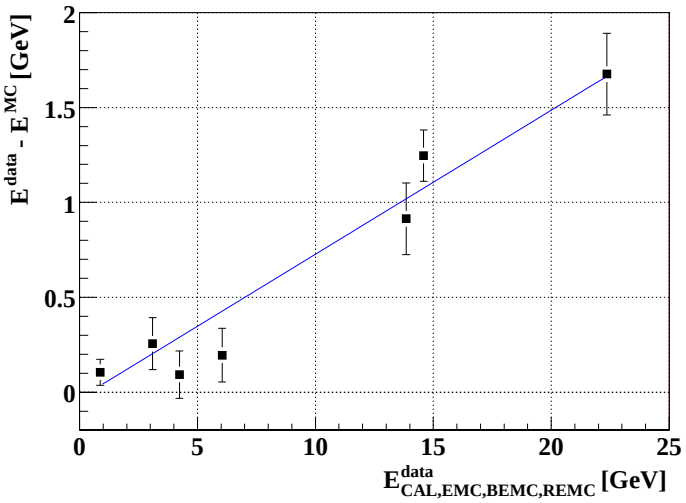
$E^{data} - E^{MC}$ [GeV]
$E^{data}_{CAL,EMC,BEMC,REMC}$ [GeV]
2
1.5
1
0.5
0
0
5
10
15
20
25

Figure C.4:

Appendix D

Systematic uncertainties for each cross section

In this chapter, the systematic uncertainties from sources described in section 7.3 are shown for each measurement.

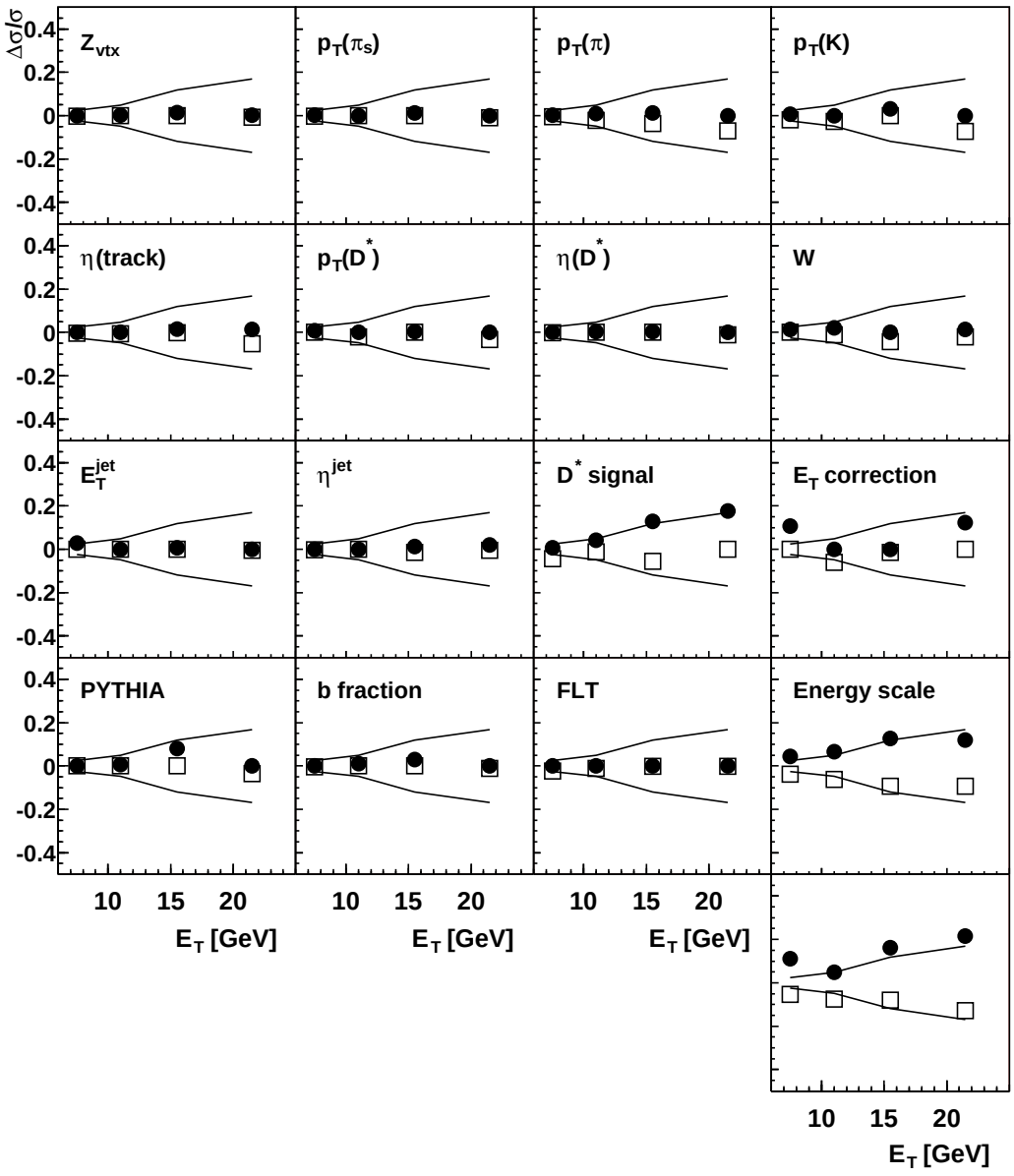

Figure D.1: Systematic uncertainty in the measurement of $d\sigma/dE_T^{jet}$ in η^{jet} range of $-1.5 < \eta^{jet} < 2.4$. Curves in the plots show the size of the statistical errors. Filled circle represent the upper errors and open squares represent the lower errors. The total systematic error is shown in the last plot.

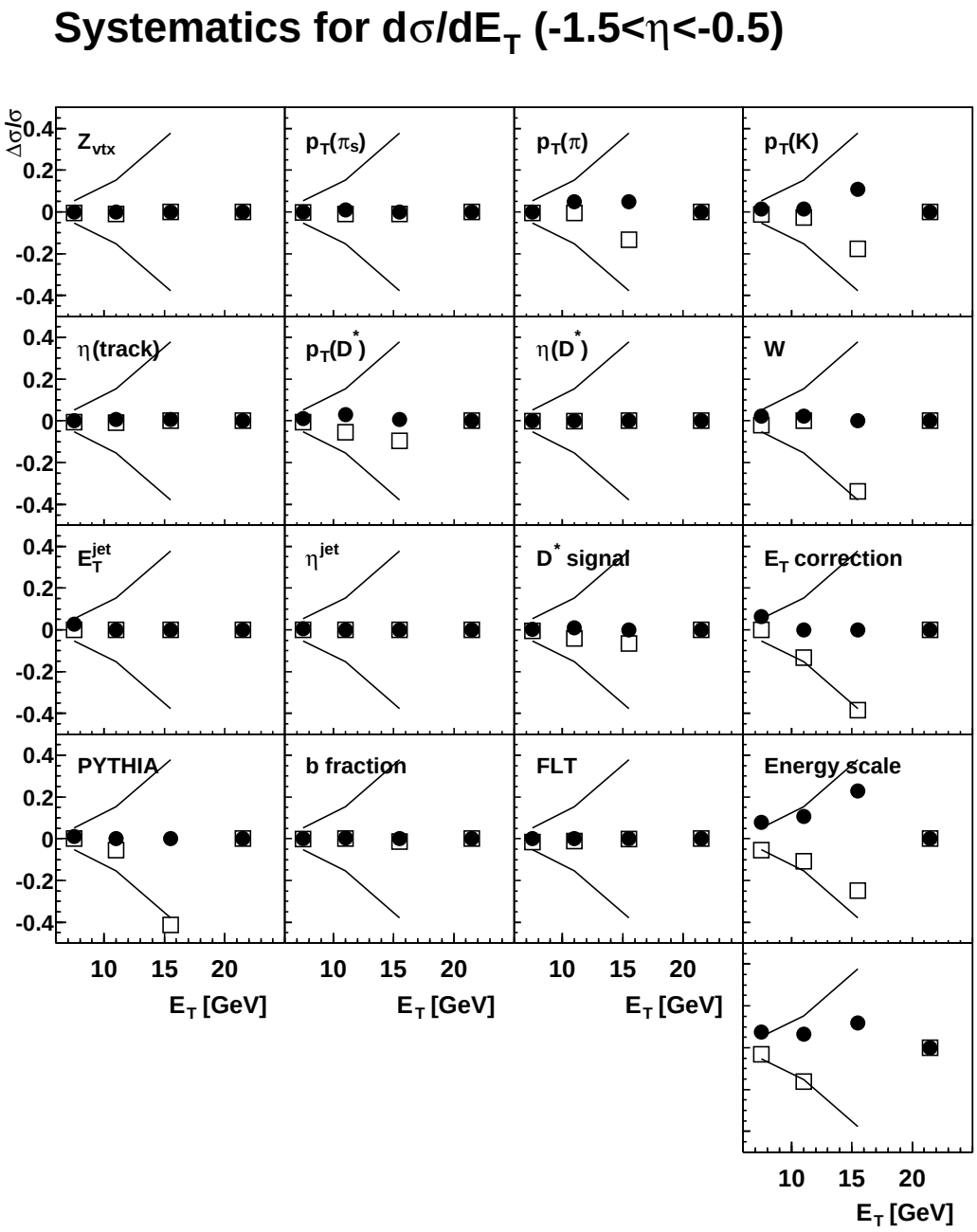

Figure D.2: Systematic uncertainty in the measurement of $d\sigma/dE_T^{jet}$ in η^{jet} range of $-1.5 < \eta^{jet} < -0.5$. Curves in the plots show the size of the statistical errors. Filled circle represent the upper errors and open squares represent the lower errors. The total systematic error is shown in the last plot.

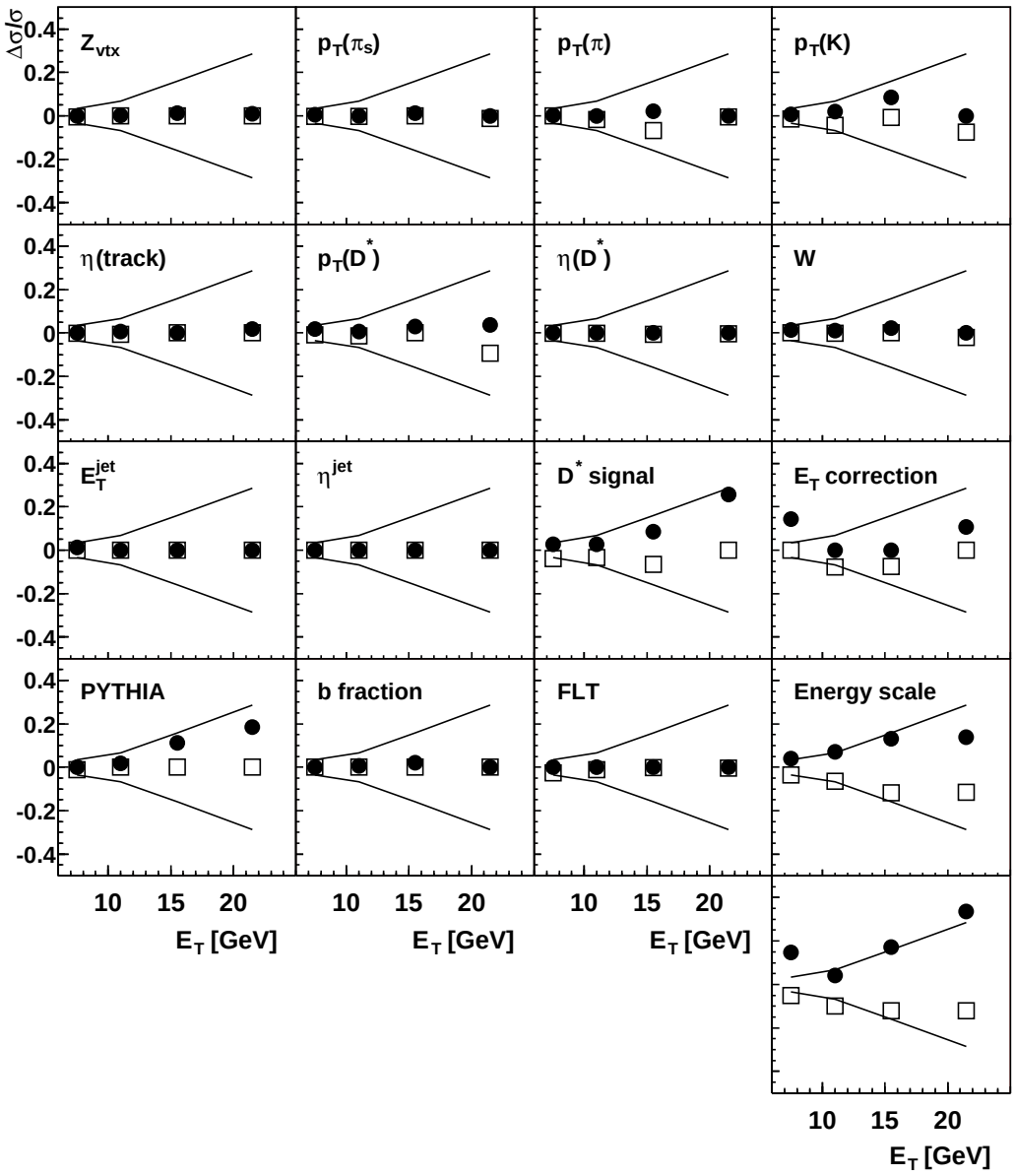

Figure D.3: Systematic uncertainty in the measurement of $d\sigma/dE_T^{jet}$ in η^{jet} range of $-0.5 < \eta^{jet} < 0.5$. Curves in the plots show the size of the statistical errors. Filled circle represent the upper errors and open squares represent the lower errors. The total systematic error is shown in the last plot.

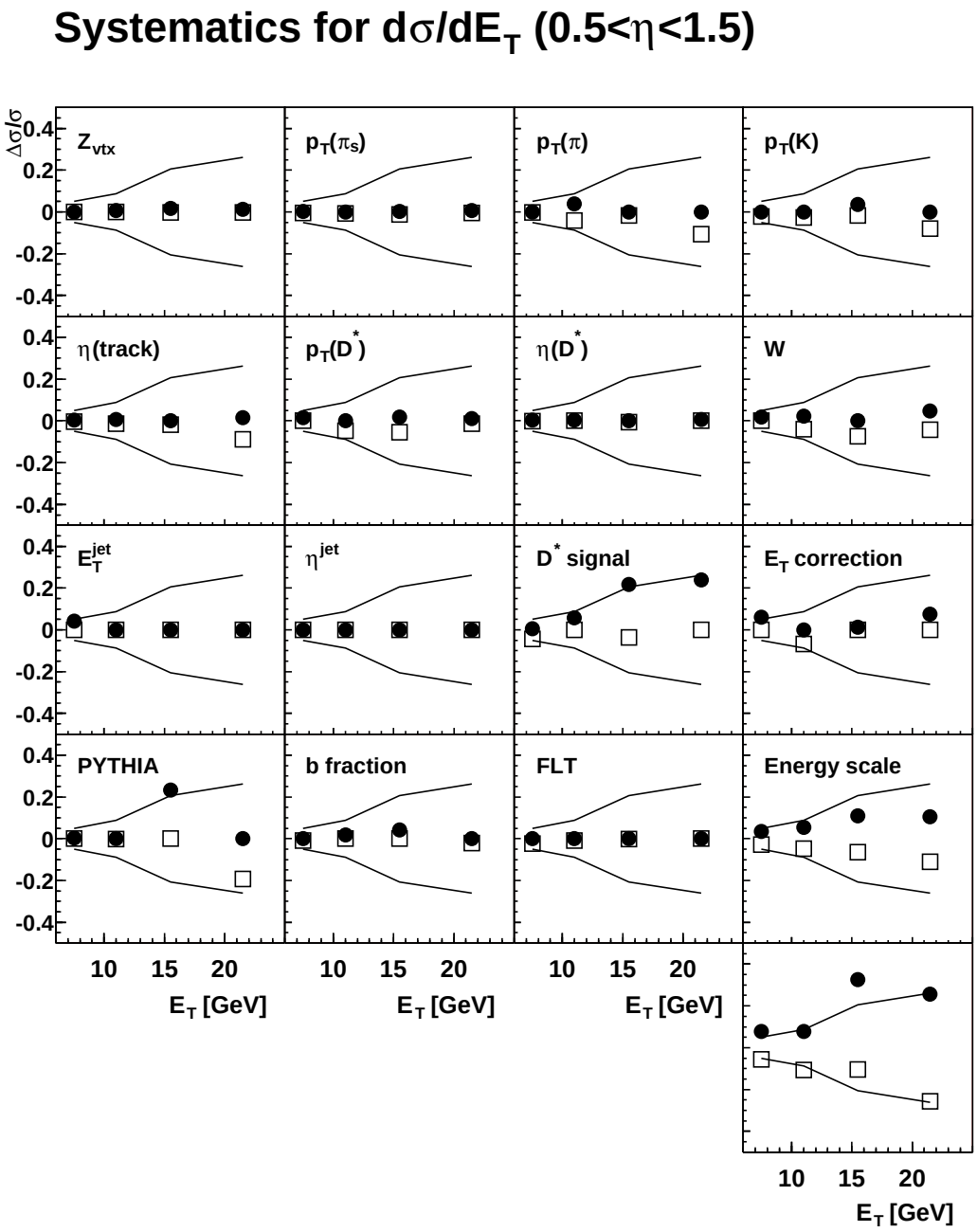

Figure D.4: Systematic uncertainty in the measurement of $d\sigma/dE_T^{jet}$ in η^{jet} range of $0.5 < \eta^{jet} < 1.5$. Curves in the plots show the size of the statistical errors. Filled circle represent the upper errors and open squares represent the lower errors. The total systematic error is shown in the last plot.

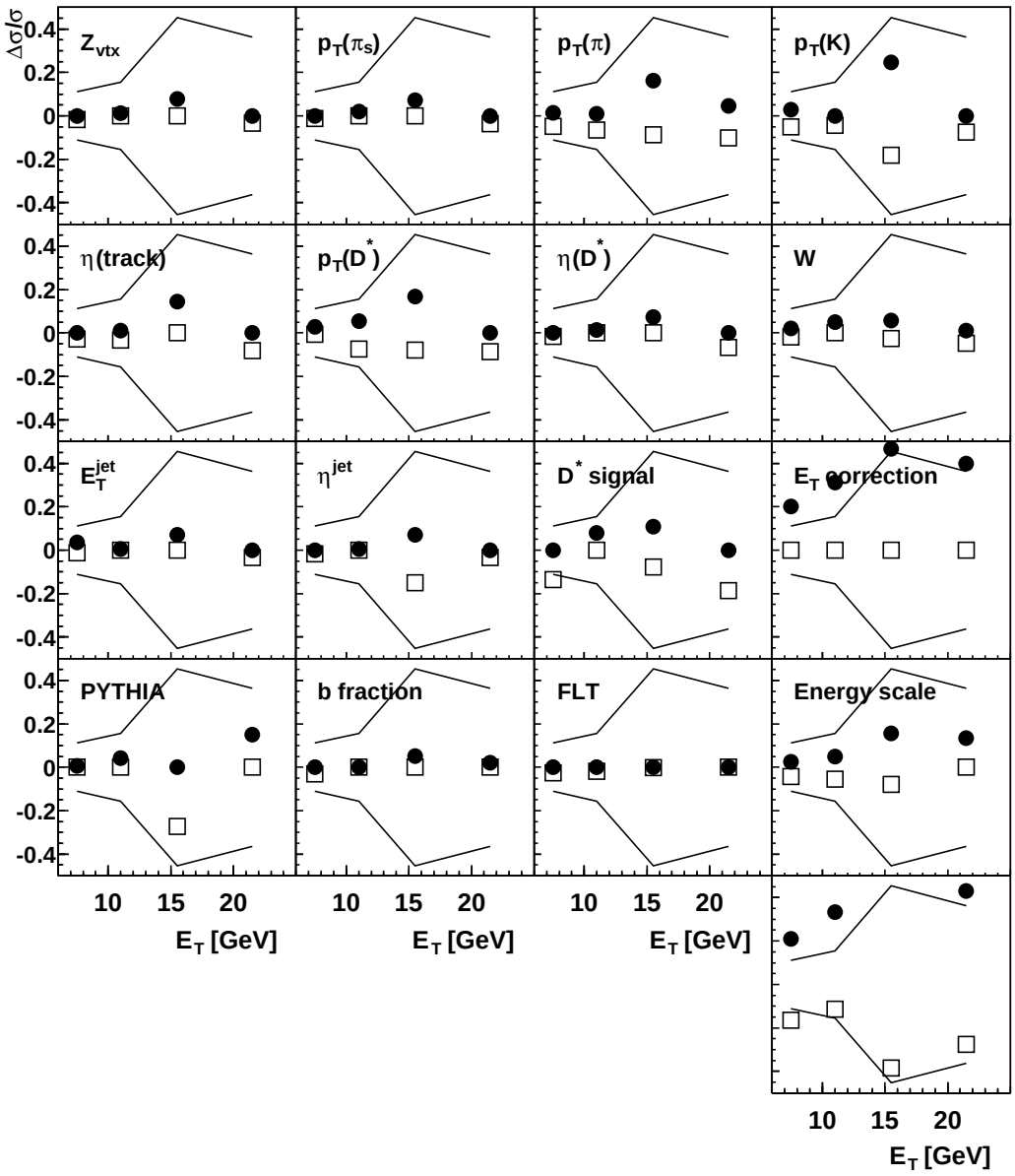

Figure D.5: Systematic uncertainty in the measurement of $d\sigma/dE_T^{jet}$ in η^{jet} range of $1.5 < \eta^{jet} < 2.4$. Curves in the plots show the size of the statistical errors. Filled circle represent the upper errors and open squares represent the lower errors. The total systematic error is shown in the last plot.

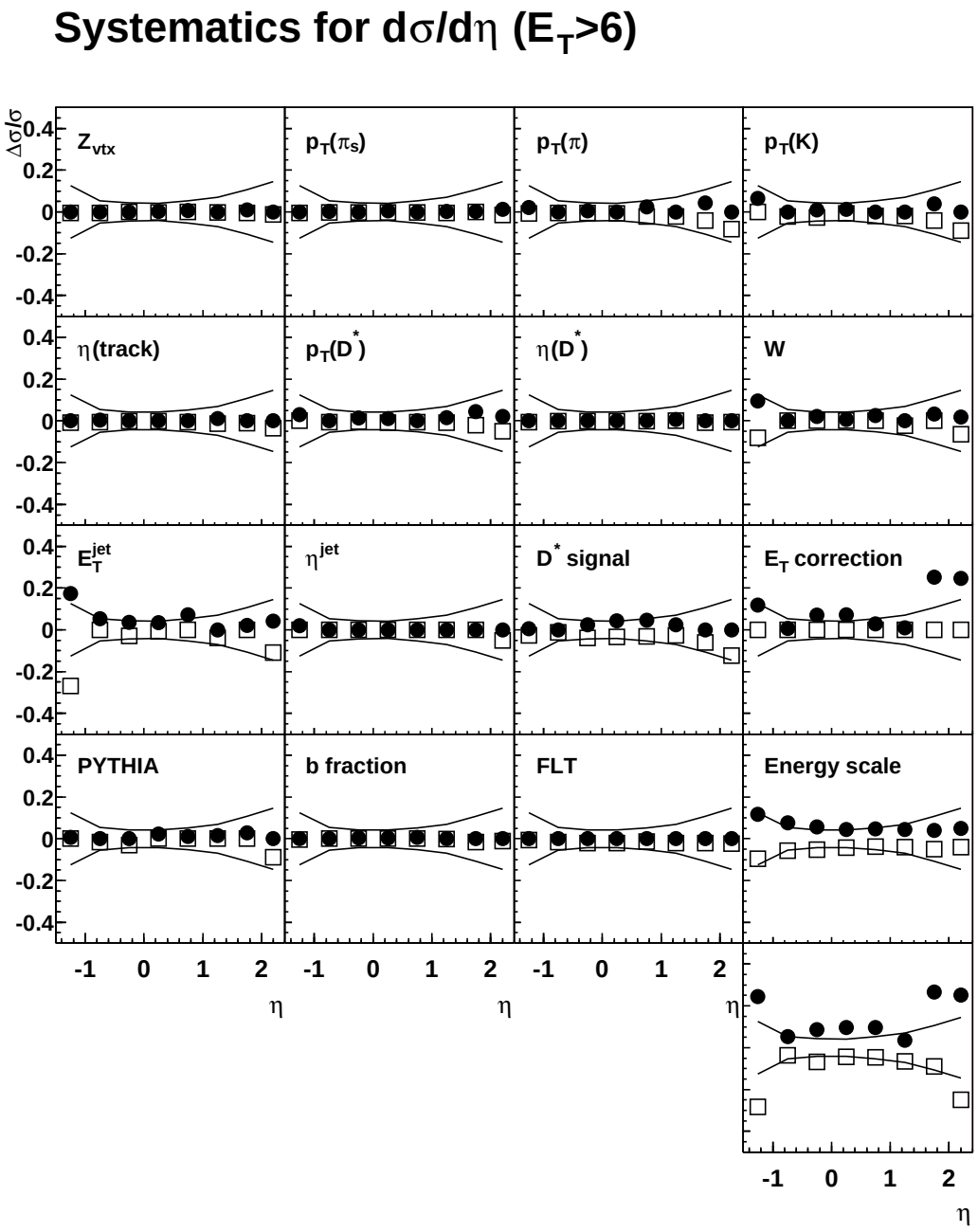

Figure D.6: Systematic uncertainty in the measurement of $d\sigma/d\eta^{jet}$ in E_T^{jet} range of $E_T >$ 6 GeV. Curves in the plots show the size of the statistical errors. Filled circle represent the upper errors and open squares represent the lower errors. The total systematic error is shown in the last plot.

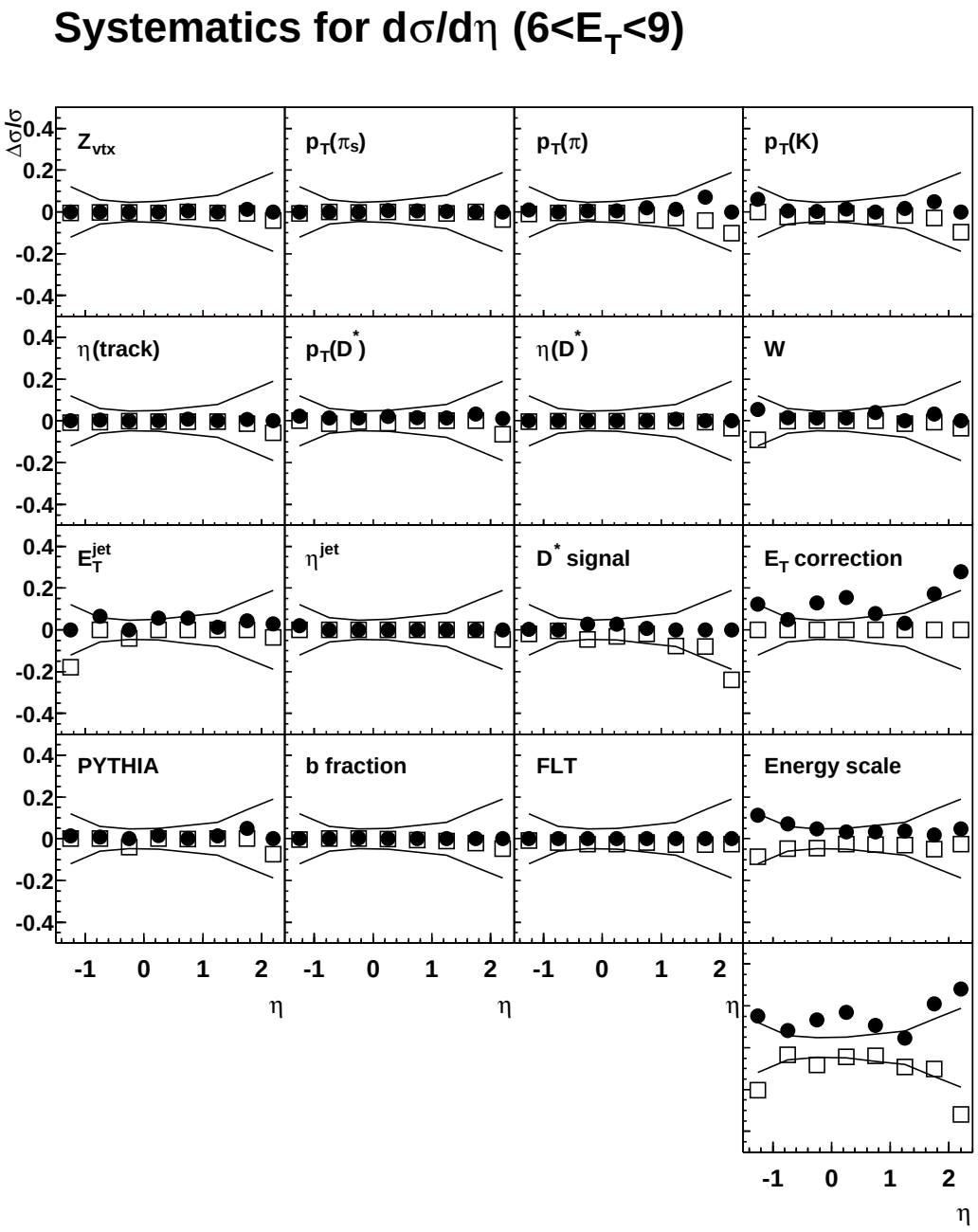

Figure D.7: Systematic uncertainty in the measurement of $d\sigma/d\eta^{jet}$ in E_T^{jet} range of $6 < E_T < 9$ GeV. Curves in the plots show the size of the statistical errors. Filled circle represent the upper errors and open squares represent the lower errors. The total systematic error is shown in the last plot.

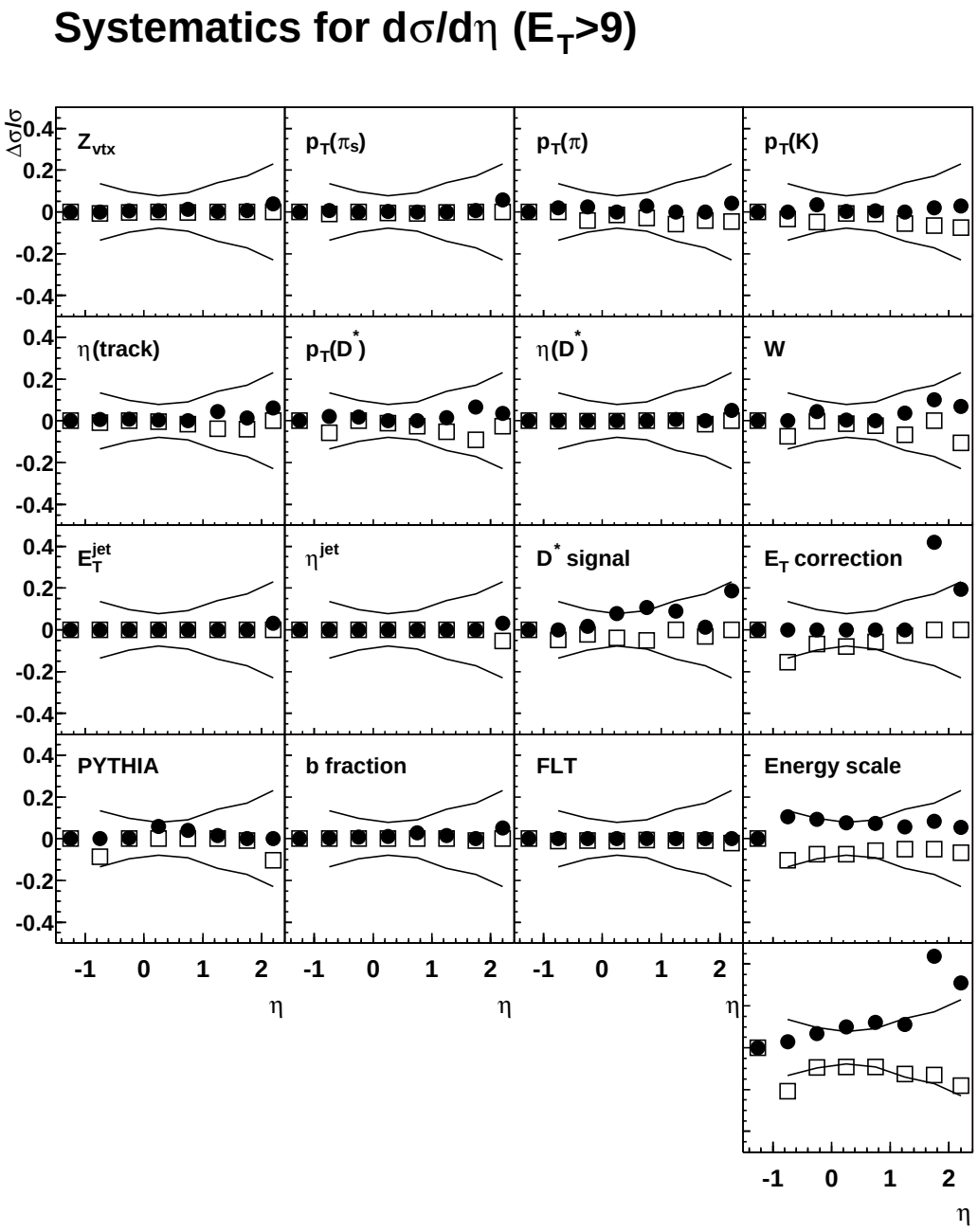

Figure D.8: Systematic uncertainty in the measurement of $d\sigma/d\eta^{jet}$ in E_T^{jet} range of $E_T >$ 9 GeV. Curves in the plots show the size of the statistical errors. Filled circle represent the upper errors and open squares represent the lower errors. The total systematic error is shown in the last plot.

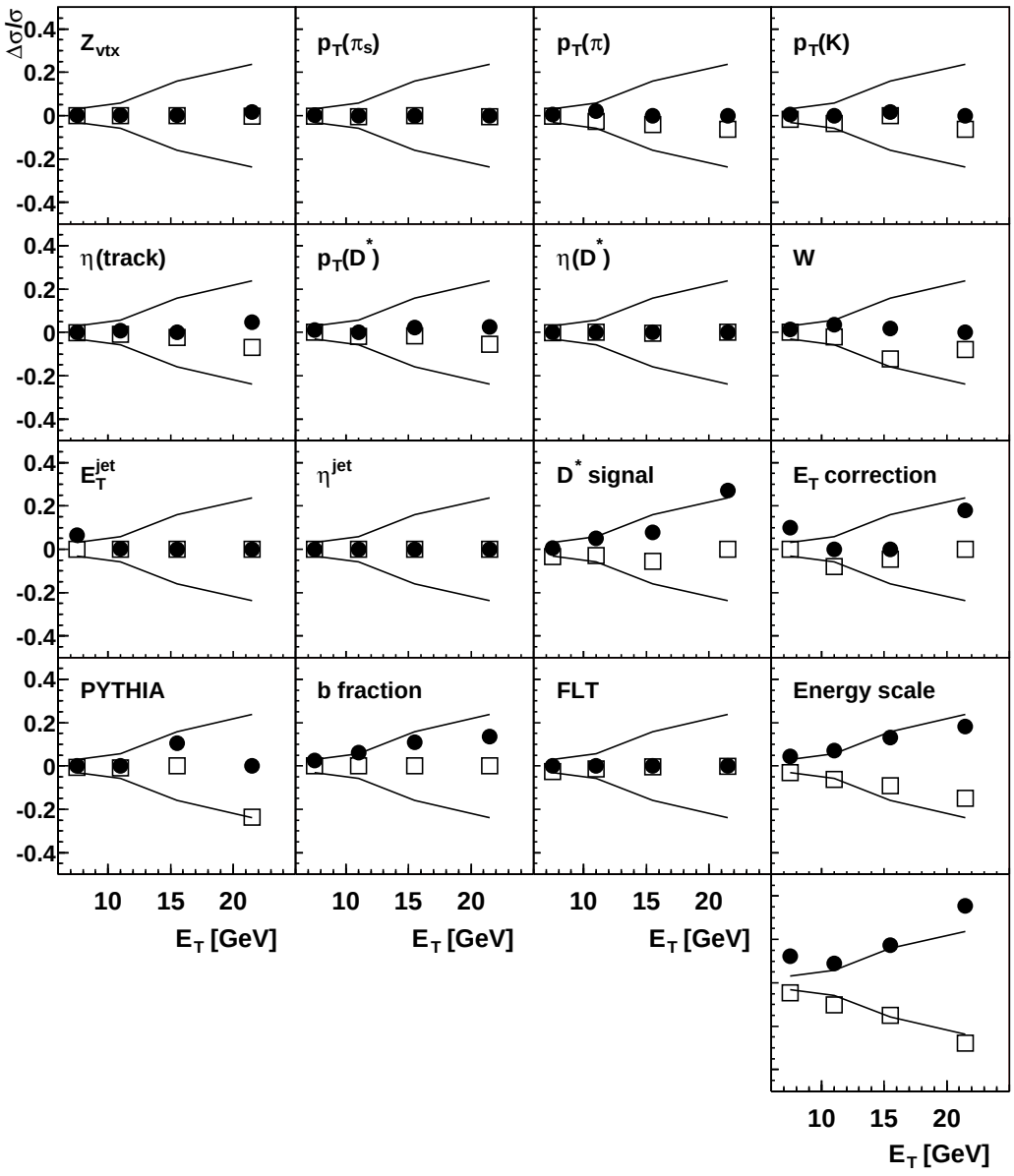

Figure D.9: Systematic uncertainty in the measurement of $d\sigma/dE_T^{jet}$ of D^* jets in η^{jet} range of $-1.5 < \eta^{jet} < 2.4$. Curves in the plots show the size of the statistical errors. Filled circle represent the upper errors and open squares represent the lower errors. The total systematic error is shown in the last plot.

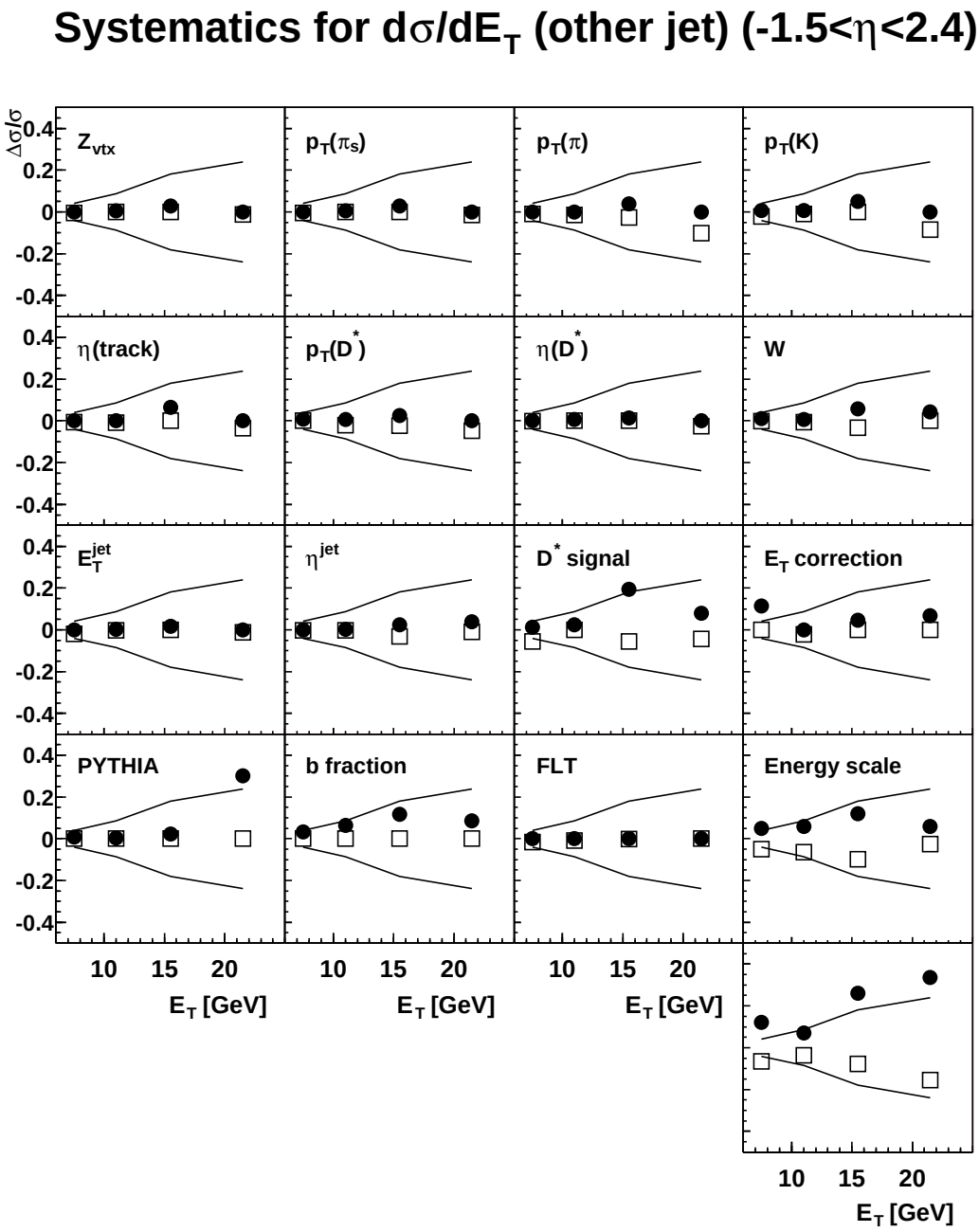

Figure D.10: Systematic uncertainty in the measurement of $d\sigma/dE_T^{jet}$ of other jets in η^{jet} range of $-1.5 < \eta^{jet} < 2.4$. Curves in the plots show the size of the statistical errors. Filled circle represent the upper errors and open squares represent the lower errors. The total systematic error is shown in the last plot.

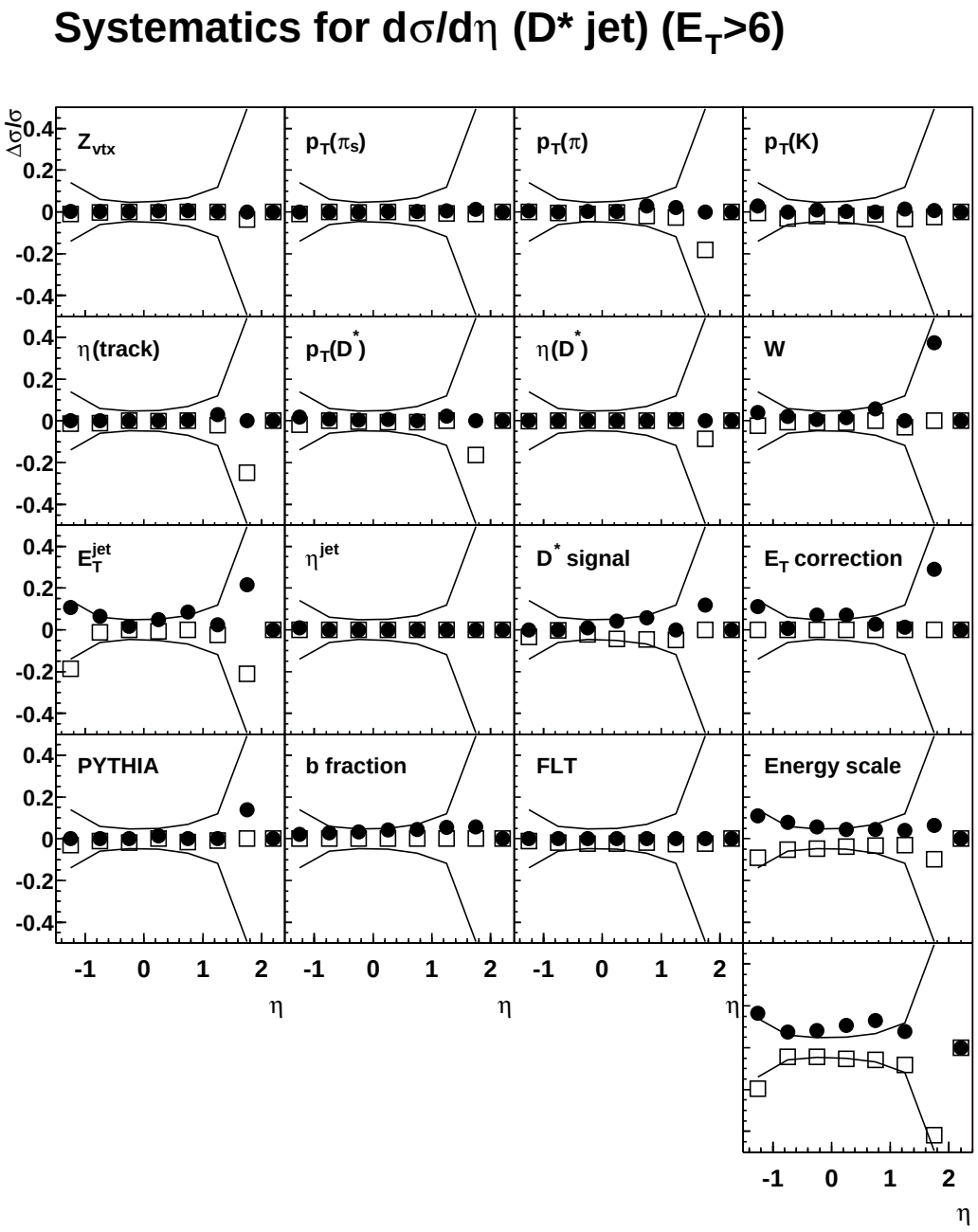

Figure D.11: Systematic uncertainty in the measurement of $d\sigma/d\eta^{jet}$ of D^* jets in E_T^{jet} range of $E_T^{jet} > 6$ GeV. Curves in the plots show the size of the statistical errors. Filled circle represent the upper errors and open squares represent the lower errors. The total systematic error is shown in the last plot.

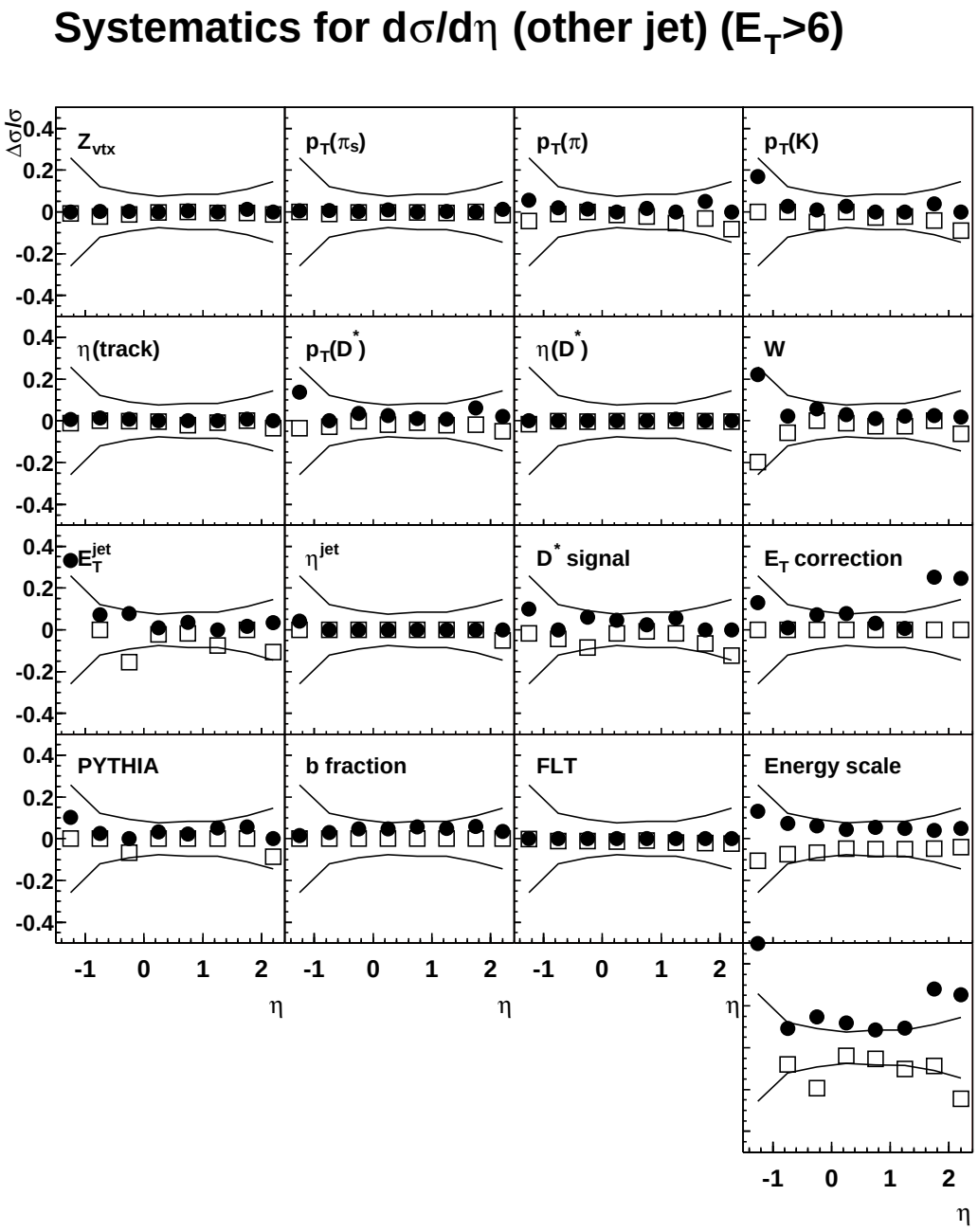

Figure D.12: Systematic uncertainty in the measurement of $d\sigma/d\eta^{jet}$ of other jets in E_T^{jet} range of $E_T^{jet} > 6$ GeV. Curves in the plots show the size of the statistical errors. Filled circle represent the upper errors and open squares represent the lower errors. The total systematic error is shown in the last plot.

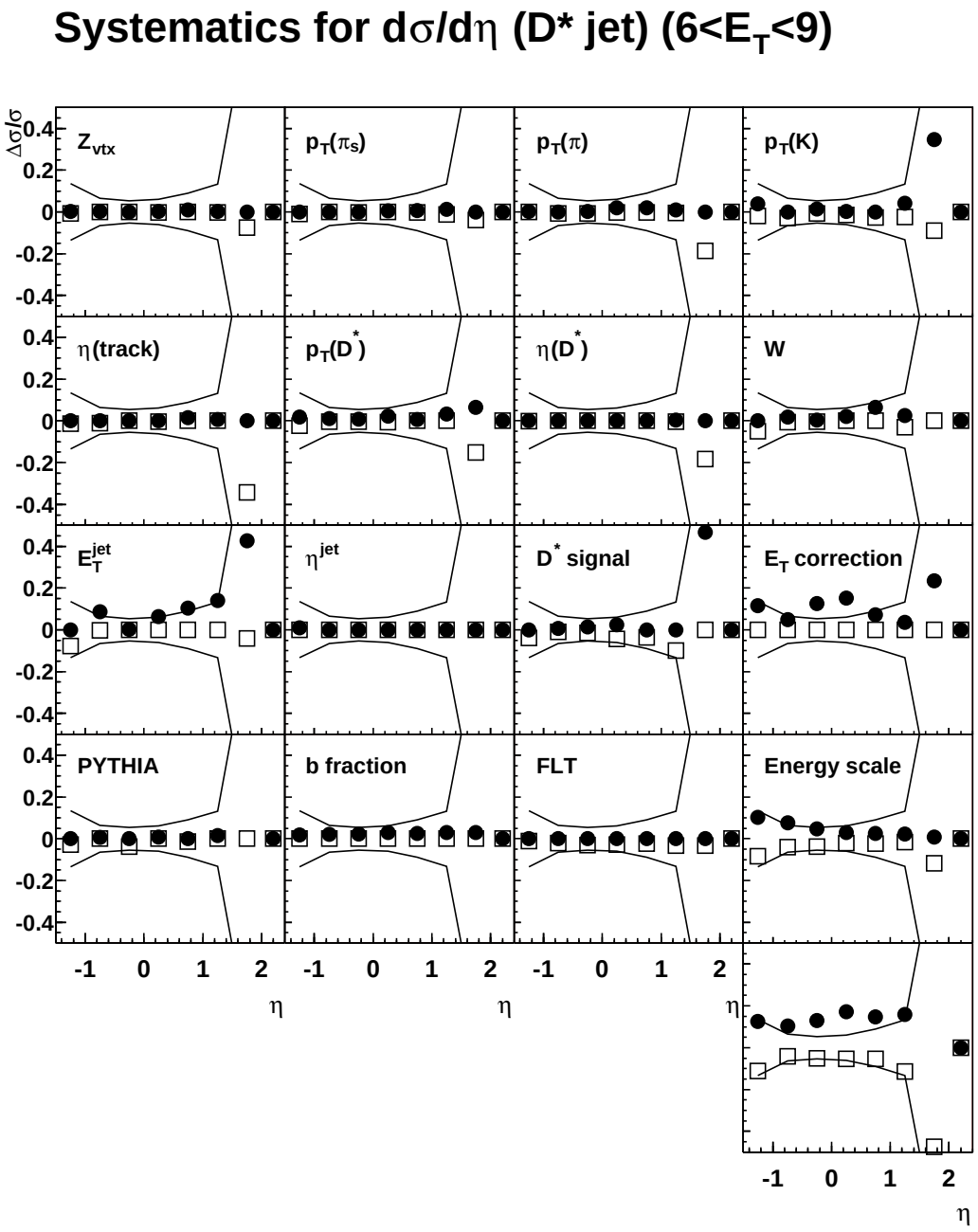

Figure D.13: Systematic uncertainty in the measurement of $d\sigma/d\eta^{jet}$ of D^* jets in E_T^{jet} range of $6 < E_T^{jet} < 9$ GeV. Curves in the plots show the size of the statistical errors. Filled circle represent the upper errors and open squares represent the lower errors. The total systematic error is shown in the last plot.

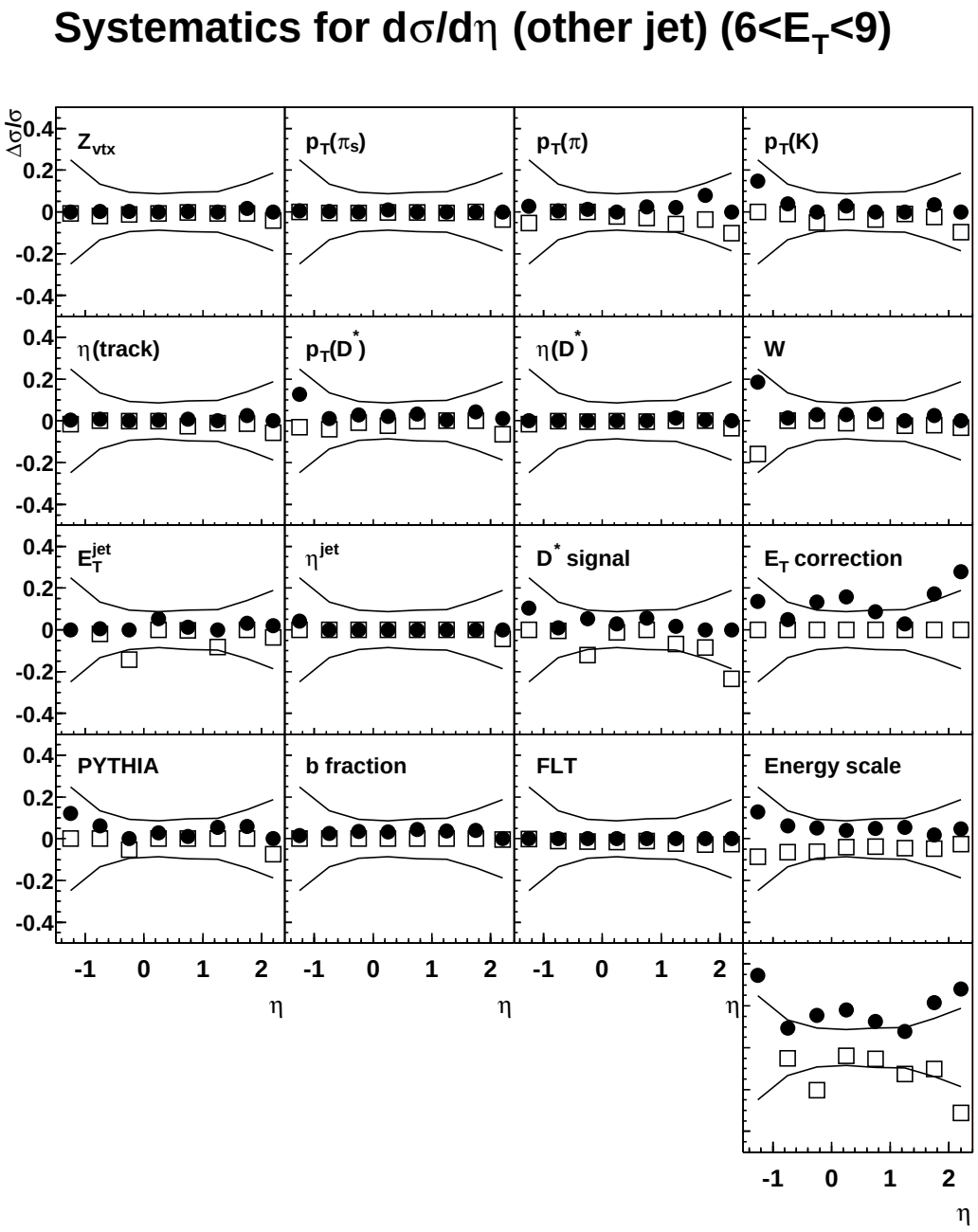

Figure D.14: Systematic uncertainty in the measurement of $d\sigma/d\eta^{jet}$ of other jets in E_T^{jet} range of $6 < E_T^{jet} < 9$ GeV. Curves in the plots show the size of the statistical errors. Filled circle represent the upper errors and open squares represent the lower errors. The total systematic error is shown in the last plot.

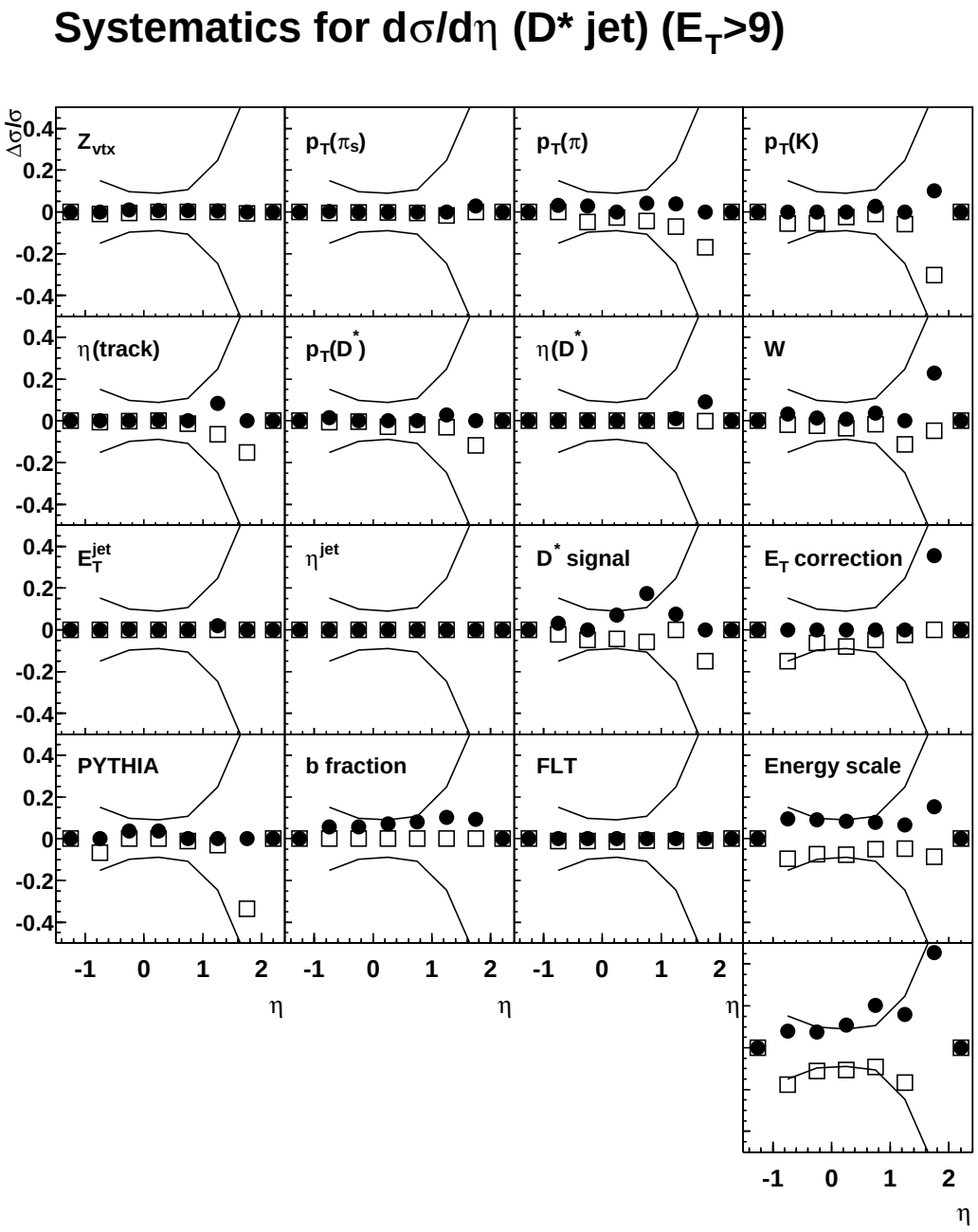

Figure D.15: Systematic uncertainty in the measurement of $d\sigma/d\eta^{jet}$ of D^* jets in E_T^{jet} range of $E_T^{jet} > 9$ GeV. Curves in the plots show the size of the statistical errors. Filled circle represent the upper errors and open squares represent the lower errors. The total systematic error is shown in the last plot.

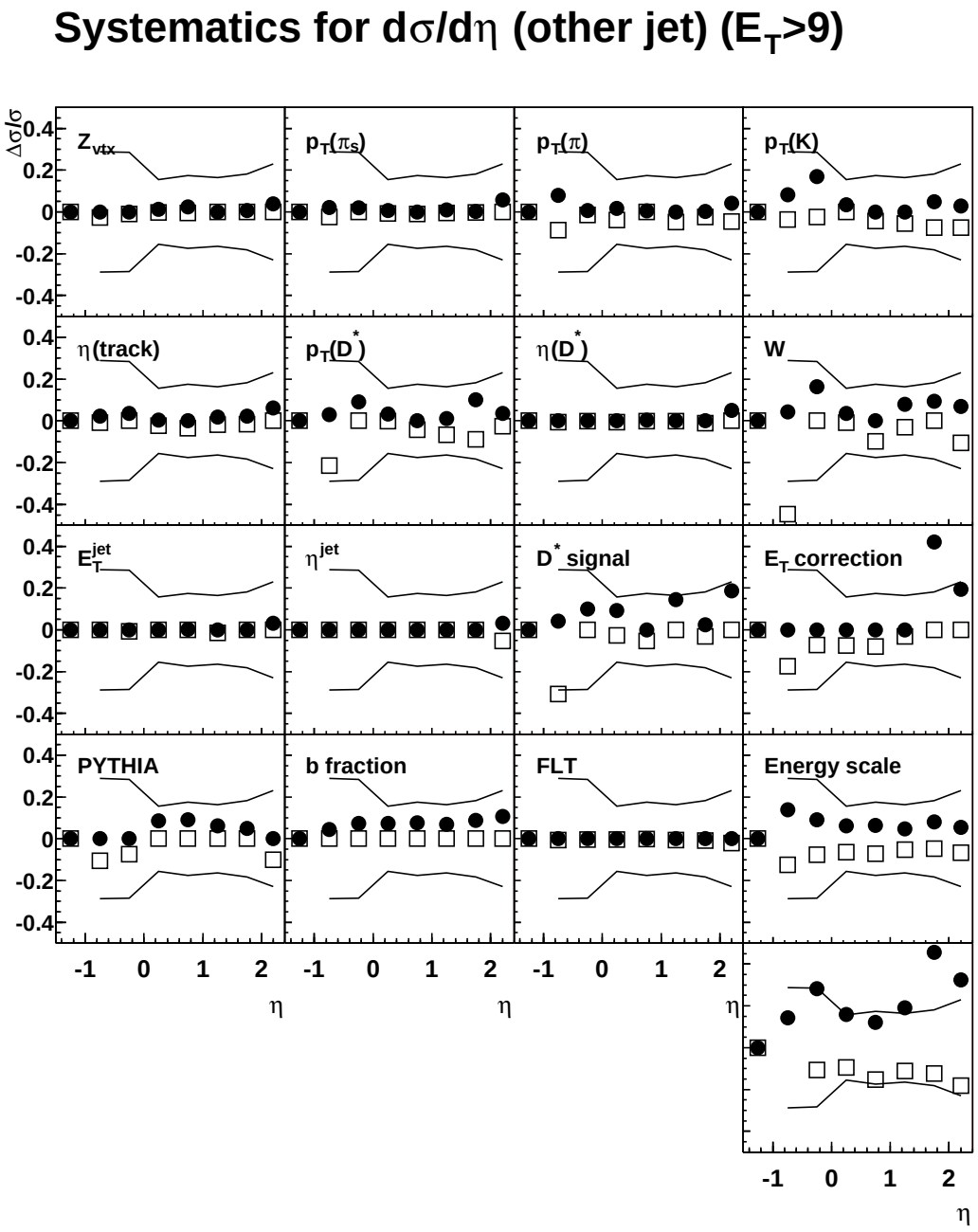

Figure D.16: Systematic uncertainty in the measurement of $d\sigma/d\eta^{jet}$ of other jets in E_T^{jet} range of $E_T^{jet} > 9$ GeV. Curves in the plots show the size of the statistical errors. Filled circle represent the upper errors and open squares represent the lower errors. The total systematic error is shown in the last plot.

Appendix E

NLO QCD predictions

The cross sections obtained by the NLO QCD calculation as described in section 8.1, are summarized in tables E.1-E.5. The cross sections shown are the ones after applying the the hadronization correction. The hadronization correction factors are also shown in the tables.

η^{jet} range	E_T^{jet} range	$\mathcal{C}^{had}$	σ_0 [nb/GeV]	σ_U [nb/GeV]	σ_L [nb/GeV]
$[-1.5 : 2.4]$	$[6 : 9]$	0.95	$9.73 \cdot 10^{-1}$	$14.61 \cdot 10^{0}$	$7.44 \cdot 10^{-1}$
	$[9 : 13]$	0.93	$2.18 \cdot 10^{-1}$	$3.29 \cdot 10^{-1}$	$1.66 \cdot 10^{-1}$
	$[13 : 18]$	0.95	$4.70 \cdot 10^{-2}$	$6.22 \cdot 10^{-2}$	$3.74 \cdot 10^{-2}$
	$[18 : 25]$	0.97	$7.81 \cdot 10^{-3}$	$13.09 \cdot 10^{-2}$	$6.94 \cdot 10^{-3}$
$[-1.5 : -0.5]$	$[6 : 9]$	0.79	$2.31 \cdot 10^{-1}$	$3.30 \cdot 10^{-1}$	$1.87 \cdot 10^{-1}$
	$[9 : 13]$	0.78	$3.17 \cdot 10^{-2}$	$4.54 \cdot 10^{-2}$	$2.41 \cdot 10^{-2}$
	$[13 : 18]$	0.73	$2.42 \cdot 10^{-3}$	$3.09 \cdot 10^{-3}$	$2.09 \cdot 10^{-3}$
	$[18 : 25]$	0.62	$5.93 \cdot 10^{-5}$	$7.97 \cdot 10^{-5}$	$5.25 \cdot 10^{-5}$
$[-0.5 : 0.5]$	$[6 : 9]$	0.98	$4.15 \cdot 10^{-1}$	$6.00 \cdot 10^{-1}$	$3.24 \cdot 10^{-1}$
	$[9 : 13]$	0.92	$9.30 \cdot 10^{-2}$	$13.59 \cdot 10^{-1}$	$7.30 \cdot 10^{-2}$
	$[13 : 18]$	0.91	$1.86 \cdot 10^{-2}$	$2.54 \cdot 10^{-2}$	$1.54 \cdot 10^{-2}$
	$[18 : 25]$	0.92	$2.39 \cdot 10^{-3}$	$4.17 \cdot 10^{-3}$	$2.38 \cdot 10^{-3}$
$[0.5 : 1.5]$	$[6 : 9]$	1.06	$2.49 \cdot 10^{-1}$	$3.93 \cdot 10^{-1}$	$1.83 \cdot 10^{-1}$
	$[9 : 13]$	1.00	$7.13 \cdot 10^{-2}$	$11.08 \cdot 10^{-1}$	$5.38 \cdot 10^{-2}$
	$[13 : 18]$	1.00	$1.97 \cdot 10^{-2}$	$2.49 \cdot 10^{-2}$	$1.55 \cdot 10^{-2}$
	$[18 : 25]$	0.98	$3.93 \cdot 10^{-3}$	$6.46 \cdot 10^{-3}$	$3.34 \cdot 10^{-3}$
$[1.5 : 2.4]$	$[6 : 9]$	1.02	$8.28 \cdot 10^{-2}$	$15.07 \cdot 10^{-1}$	$5.28 \cdot 10^{-2}$
	$[9 : 13]$	1.03	$2.43 \cdot 10^{-2}$	$4.11 \cdot 10^{-2}$	$1.68 \cdot 10^{-2}$
	$[13 : 18]$	1.06	$6.82 \cdot 10^{-3}$	$9.36 \cdot 10^{-3}$	$4.72 \cdot 10^{-3}$
	$[18 : 25]$	1.11	$1.55 \cdot 10^{-3}$	$2.56 \cdot 10^{-3}$	$1.25 \cdot 10^{-3}$

Table E.1: Hadronization correction factor, and center value (σ_0), upper value (σ_U), and lower value (σ_L) of the cross section obtained from NLO QCD calculation for $d\sigma/dE_T^{jet}$. The cross section values are the ones after multiplying the hadronization correction.

E_T^{jet} range	η^{jet} range	$\mathcal{C}^{had}$	σ_0 [nb]	σ_U [nb]	σ_L [nb]
[6 : 25]	[−1.5 : −1.0]	0.67	$4.47 \cdot 10^{-1}$	$6.64 \cdot 10^{-1}$	$3.80 \cdot 10^{-1}$
	[−1.0 : −0.5]	0.84	$1.21 \cdot 10^{0}$	$1.69 \cdot 10^{0}$	$0.94 \cdot 10^{-1}$
	[−0.5 : 0.0]	0.93	$1.73 \cdot 10^{0}$	$2.48 \cdot 10^{0}$	$1.38 \cdot 10^{0}$
	[0.0 : 0.5]	0.99	$1.71 \cdot 10^{0}$	$2.51 \cdot 10^{0}$	$1.32 \cdot 10^{0}$
	[0.5 : 1.0]	1.01	$1.31 \cdot 10^{0}$	$1.95 \cdot 10^{0}$	$1.00 \cdot 10^{-1}$
	[1.0 : 1.5]	1.08	$1.01 \cdot 10^{0}$	$1.64 \cdot 10^{0}$	$0.73 \cdot 10^{-1}$
	[1.5 : 2.0]	1.03	$4.72 \cdot 10^{-1}$	$8.12 \cdot 10^{-1}$	$3.13 \cdot 10^{-1}$
	[2.0 : 2.4]	1.02	$3.85 \cdot 10^{-1}$	$6.85 \cdot 10^{-1}$	$2.51 \cdot 10^{-1}$
[6 : 9]	[−1.5 : −1.0]	0.68	$4.12 \cdot 10^{-1}$	$6.02 \cdot 10^{-1}$	$3.52 \cdot 10^{-1}$
	[−1.0 : −0.5]	0.85	$9.73 \cdot 10^{-1}$	$13.77 \cdot 10^{0}$	$7.65 \cdot 10^{-1}$
	[−0.5 : 0.0]	0.94	$1.30 \cdot 10^{0}$	$1.86 \cdot 10^{0}$	$1.03 \cdot 10^{0}$
	[0.0 : 0.5]	1.03	$1.19 \cdot 10^{0}$	$1.74 \cdot 10^{0}$	$0.91 \cdot 10^{-1}$
	[0.5 : 1.0]	1.04	$8.43 \cdot 10^{-1}$	$12.57 \cdot 10^{0}$	$6.34 \cdot 10^{-1}$
	[1.0 : 1.5]	1.11	$6.58 \cdot 10^{-1}$	$11.14 \cdot 10^{0}$	$4.65 \cdot 10^{-1}$
	[1.5 : 2.0]	1.02	$2.96 \cdot 10^{-1}$	$5.28 \cdot 10^{-1}$	$1.90 \cdot 10^{-1}$
	[2.0 : 2.4]	1.03	$2.52 \cdot 10^{-1}$	$4.72 \cdot 10^{-1}$	$1.58 \cdot 10^{-1}$
[9 : 25]	[−1.5 : −1.0]	0.58	$3.57 \cdot 10^{-2}$	$6.14 \cdot 10^{-2}$	$2.89 \cdot 10^{-2}$
	[−1.0 : −0.5]	0.81	$2.40 \cdot 10^{-1}$	$3.25 \cdot 10^{-1}$	$1.83 \cdot 10^{-1}$
	[−0.5 : 0.0]	0.90	$4.38 \cdot 10^{-1}$	$6.25 \cdot 10^{-1}$	$3.56 \cdot 10^{-1}$
	[0.0 : 0.5]	0.92	$5.23 \cdot 10^{-1}$	$7.74 \cdot 10^{-1}$	$4.13 \cdot 10^{-1}$
	[0.5 : 1.0]	0.97	$4.66 \cdot 10^{-1}$	$6.91 \cdot 10^{-1}$	$3.62 \cdot 10^{-1}$
	[1.0 : 1.5]	1.04	$3.57 \cdot 10^{-1}$	$5.36 \cdot 10^{-1}$	$2.70 \cdot 10^{-1}$
	[1.5 : 2.0]	1.06	$1.77 \cdot 10^{-1}$	$2.86 \cdot 10^{-1}$	$1.24 \cdot 10^{-1}$
	[2.0 : 2.4]	1.01	$1.34 \cdot 10^{-1}$	$2.15 \cdot 10^{-1}$	$0.93 \cdot 10^{-2}$

Table E.2: Hadronization correction factor, and center value (σ_0), upper value (σ_U), and lower value (σ_L) of the cross section obtained from NLO QCD calculation for $d\sigma/d\eta^{jet}$. The cross section values are the ones after multiplying the hadronization correction.

η^{jet} range	E_T^{jet} range	$\mathcal{C}^{had}$	σ_0 [nb/GeV]	σ_U [nb/GeV]	σ_L [nb/GeV]
$[-1.5:\ 2.4]$	$[\ 6:\ 9]$	1.00	$5.54 \cdot 10^{-1}$	$8.34 \cdot 10^{-1}$	$4.24 \cdot 10^{-1}$
	$[\ 9:13]$	0.94	$1.09 \cdot 10^{-1}$	$1.62 \cdot 10^{-1}$	$0.84 \cdot 10^{-2}$
	$[13:18]$	0.94	$2.15 \cdot 10^{-2}$	$2.76 \cdot 10^{-2}$	$1.75 \cdot 10^{-2}$
	$[18:25]$	1.00	$0.35 \cdot 10^{-2}$	$0.61 \cdot 10^{-3}$	$0.33 \cdot 10^{-3}$
$[-1.5:\ 2.4]$	$[\ 6:\ 9]$	0.87	$4.13 \cdot 10^{-1}$	$6.17 \cdot 10^{-1}$	$3.17 \cdot 10^{-1}$
	$[\ 9:13]$	0.90	$1.09 \cdot 10^{-1}$	$1.66 \cdot 10^{-1}$	$0.82 \cdot 10^{-2}$
	$[13:18]$	0.96	$2.56 \cdot 10^{-2}$	$3.47 \cdot 10^{-2}$	$2.01 \cdot 10^{-2}$
	$[18:25]$	0.93	$0.42 \cdot 10^{-2}$	$0.70 \cdot 10^{-3}$	$0.36 \cdot 10^{-3}$

Table E.3: Hadronization correction factor, and center value (σ_0), upper value (σ_U), and lower value (σ_L) of the cross section obtained from NLO QCD calculation for $d\sigma/dE_T^{jet}$ for D^*/other jets. The cross section values are the ones after multiplying the hadronization correction.

E_T^{jet} range	η^{jet} range	$\mathcal{C}^{had}$	σ_0 [nb]	σ_U [nb]	σ_L [nb]
[6 : 25]	[−1.5 : −1.0]	0.70	$3.03 \cdot 10^{-1}$	$4.75 \cdot 10^{-1}$	$2.45 \cdot 10^{-1}$
	[−1.0 : −0.5]	0.87	$0.79 \cdot 10^{0}$	$1.16 \cdot 10^{0}$	$0.60 \cdot 10^{-1}$
	[−0.5 : 0.0]	0.96	$1.11 \cdot 10^{0}$	$1.63 \cdot 10^{0}$	$0.86 \cdot 10^{-1}$
	[0.0 : 0.5]	1.04	$1.02 \cdot 10^{0}$	$1.51 \cdot 10^{0}$	$0.78 \cdot 10^{-1}$
	[0.5 : 1.0]	1.05	$0.69 \cdot 10^{0}$	$1.01 \cdot 10^{0}$	$0.53 \cdot 10^{-1}$
	[1.0 : 1.5]	1.20	$4.80 \cdot 10^{-1}$	$7.64 \cdot 10^{-1}$	$3.62 \cdot 10^{-1}$
	[1.5 : 2.0]	2.85	$0.22 \cdot 10^{-1}$	$0.38 \cdot 10^{-2}$	$0.14 \cdot 10^{-2}$
	[2.0 : 2.4]	0.09	$0.00 \cdot 10^{0}$	$0.00 \cdot 10^{-6}$	$0.00 \cdot 10^{-6}$
[6 : 9]	[−1.5 : −1.0]	0.71	$2.82 \cdot 10^{-1}$	$4.38 \cdot 10^{-1}$	$2.27 \cdot 10^{-1}$
	[−1.0 : −0.5]	0.88	$6.47 \cdot 10^{-1}$	$9.59 \cdot 10^{-1}$	$4.91 \cdot 10^{-1}$
	[−0.5 : 0.0]	0.98	$0.85 \cdot 10^{0}$	$1.26 \cdot 10^{0}$	$0.66 \cdot 10^{-1}$
	[0.0 : 0.5]	1.08	$0.72 \cdot 10^{0}$	$1.07 \cdot 10^{0}$	$0.54 \cdot 10^{-1}$
	[0.5 : 1.0]	1.10	$4.60 \cdot 10^{-1}$	$6.73 \cdot 10^{-1}$	$3.46 \cdot 10^{-1}$
	[1.0 : 1.5]	1.26	$3.21 \cdot 10^{-1}$	$5.39 \cdot 10^{-1}$	$2.37 \cdot 10^{-1}$
	[1.5 : 2.0]	2.83	$0.11 \cdot 10^{-1}$	$0.20 \cdot 10^{-2}$	$0.07 \cdot 10^{-3}$
	[2.0 : 2.4]	0.00	$0.00 \cdot 10^{0}$	$0.00 \cdot 10^{0}$	$0.00 \cdot 10^{0}$
[9 : 25]	[−1.5 : −1.0]	0.57	$0.02 \cdot 10^{0}$	$0.04 \cdot 10^{-2}$	$0.02 \cdot 10^{-2}$
	[−1.0 : −0.5]	0.83	$1.47 \cdot 10^{-1}$	$2.05 \cdot 10^{-1}$	$1.11 \cdot 10^{-1}$
	[−0.5 : 0.0]	0.91	$2.60 \cdot 10^{-1}$	$3.74 \cdot 10^{-1}$	$2.08 \cdot 10^{-1}$
	[0.0 : 0.5]	0.95	$3.02 \cdot 10^{-1}$	$4.46 \cdot 10^{-1}$	$2.37 \cdot 10^{-1}$
	[0.5 : 1.0]	0.97	$2.32 \cdot 10^{-1}$	$3.37 \cdot 10^{-1}$	$1.82 \cdot 10^{-1}$
	[1.0 : 1.5]	1.10	$1.59 \cdot 10^{-1}$	$2.29 \cdot 10^{-1}$	$1.24 \cdot 10^{-1}$
	[1.5 : 2.0]	2.89	$0.11 \cdot 10^{-1}$	$0.18 \cdot 10^{-2}$	$0.07 \cdot 10^{-3}$
	[2.0 : 2.4]	0.22	$0.00 \cdot 10^{0}$	$0.00 \cdot 10^{-6}$	$0.00 \cdot 10^{-6}$

Table E.4: Hadronization correction factor, and center value (σ_0), upper value (σ_U), and lower value (σ_L) of the cross section obtained from NLO QCD calculation for $d\sigma/d\eta^{jet}$ for D^* jets. The cross section values are the ones after multiplying the hadronization correction.

E_T^{jet} range	η^{jet} range	$\mathcal{C}^{had}$	σ_0 [nb]	σ_U [nb]	σ_L [nb]
[6 : 25]	[−1.5 : −1.0]	0.61	$1.45 \cdot 10^{-1}$	$1.94 \cdot 10^{-1}$	$1.35 \cdot 10^{-1}$
	[−1.0 : −0.5]	0.77	$4.14 \cdot 10^{-1}$	$5.36 \cdot 10^{-1}$	$3.39 \cdot 10^{-1}$
	[−0.5 : 0.0]	0.85	$6.16 \cdot 10^{-1}$	$8.36 \cdot 10^{-1}$	$5.10 \cdot 10^{-1}$
	[0.0 : 0.5]	0.91	$0.67 \cdot 10^{0}$	$0.97 \cdot 10^{-1}$	$0.53 \cdot 10^{-1}$
	[0.5 : 1.0]	0.94	$0.60 \cdot 10^{0}$	$0.91 \cdot 10^{-1}$	$0.46 \cdot 10^{-1}$
	[1.0 : 1.5]	0.95	$5.14 \cdot 10^{-1}$	$8.46 \cdot 10^{-1}$	$3.62 \cdot 10^{-1}$
	[1.5 : 2.0]	0.95	$4.28 \cdot 10^{-1}$	$7.37 \cdot 10^{-1}$	$2.85 \cdot 10^{-1}$
	[2.0 : 2.4]	1.03	$3.88 \cdot 10^{-1}$	$6.91 \cdot 10^{-1}$	$2.53 \cdot 10^{-1}$
[6 : 9]	[−1.5 : −1.0]	0.62	$1.31 \cdot 10^{-1}$	$1.68 \cdot 10^{-1}$	$1.23 \cdot 10^{-1}$
	[−1.0 : −0.5]	0.78	$3.23 \cdot 10^{-1}$	$4.17 \cdot 10^{-1}$	$2.69 \cdot 10^{-1}$
	[−0.5 : 0.0]	0.84	$4.40 \cdot 10^{-1}$	$5.90 \cdot 10^{-1}$	$3.64 \cdot 10^{-1}$
	[0.0 : 0.5]	0.92	$4.53 \cdot 10^{-1}$	$6.51 \cdot 10^{-1}$	$3.55 \cdot 10^{-1}$
	[0.5 : 1.0]	0.93	$3.67 \cdot 10^{-1}$	$5.59 \cdot 10^{-1}$	$2.77 \cdot 10^{-1}$
	[1.0 : 1.5]	0.95	$3.21 \cdot 10^{-1}$	$5.48 \cdot 10^{-1}$	$2.20 \cdot 10^{-1}$
	[1.5 : 2.0]	0.94	$2.71 \cdot 10^{-1}$	$4.82 \cdot 10^{-1}$	$1.74 \cdot 10^{-1}$
	[2.0 : 2.4]	1.04	$2.54 \cdot 10^{-1}$	$4.76 \cdot 10^{-1}$	$1.60 \cdot 10^{-1}$
[9 : 25]	[−1.5 : −1.0]	0.59	$0.01 \cdot 10^{0}$	$0.03 \cdot 10^{-2}$	$0.01 \cdot 10^{-2}$
	[−1.0 : −0.5]	0.76	$0.92 \cdot 10^{-1}$	$1.20 \cdot 10^{-1}$	$0.71 \cdot 10^{-2}$
	[−0.5 : 0.0]	0.88	$1.78 \cdot 10^{-1}$	$2.50 \cdot 10^{-1}$	$1.47 \cdot 10^{-1}$
	[0.0 : 0.5]	0.88	$2.19 \cdot 10^{-1}$	$3.23 \cdot 10^{-1}$	$1.74 \cdot 10^{-1}$
	[0.5 : 1.0]	0.97	$2.33 \cdot 10^{-1}$	$3.52 \cdot 10^{-1}$	$1.79 \cdot 10^{-1}$
	[1.0 : 1.5]	0.96	$1.93 \cdot 10^{-1}$	$2.98 \cdot 10^{-1}$	$1.43 \cdot 10^{-1}$
	[1.5 : 2.0]	0.98	$1.58 \cdot 10^{-1}$	$2.56 \cdot 10^{-1}$	$1.12 \cdot 10^{-1}$
	[2.0 : 2.4]	1.02	$1.35 \cdot 10^{-1}$	$2.16 \cdot 10^{-1}$	$0.93 \cdot 10^{-2}$

Table E.5: Hadronization correction factor, and center value (σ_0), upper value (σ_U), and lower value (σ_L) of the cross section obtained from NLO QCD calculation for $d\sigma/d\eta^{jet}$ for other jets. The cross section values are the ones after multiplying the hadronization correction.

Bibliography

[1] F. Halzen and A.D. Martin, *Quarks and Leptons: An Introductory Course in Modern Particle Physics*, John Wiley & Sons, 1984.

[2] H. Georgi and H.D. Politzer, Phys. Rev. **D 9**, 416 (1974).

[3] D. Gross and F. Wilczek, Phys. Rev. **D 9**, 980 (1974).

[4] T. Muta, *FOUNDATION OF QUANTUM CHROMODYNAMICS* 2nd edition, World Scientific Lecture Notes in Physics - Vol.57, World Scientific, 1998.

[5] S. Frixione et al, Phys. Lett. **B 348**, 633 (1995);
S. Frixione et al., Nucl. Phys. **B 454**, 3 (1995).

[6] B.A. Kniehl, G. Kramer and M. Spira, Z. Phys. **C 76**, 689 (1997);
J. Binneweis, B.A. Kniehl and G. Kramer, Z. Phys. **C 76**, 677 (1997);
J. Binneweis, B.A. Kniehl and G. Kramer, Phys. Rev. **D 58**, 014014 (1998);
M. Cacciari and M. Greco, Z. Phys. **C 69**, 459 (1996);
M. Cacciari, M. Greco, S. Rolli and A. Tanzini, Phys. Rev. **D 55**, 2736 (1997);
M. Cacciari and M. Greco, Phys. Rev. **D 55**, 7134 (1997).

[7] CDF Collaboration, Phys. Lett. **B 68**, 3403 (1992);
CDF Collaboration, Phys. Lett. **B 69**, 3704 (1992);
CDF Collaboration, Phys. Lett. **B 71**, 500 (1993);
CDF Collaboration, Phys. Lett. **B 71**, 2396 (1993);
CDF Collaboration, Phys. Lett. **B 71**, 2537 (1993);
CDF Collaboration, Phys. Rev. **D 50**, 4252 (1994).

[8] DØ Collaboration, Phys. Rev. Lett. **74**, 3548 (1995);
DØ Collaboration, Phys. Lett. **B 370**, 239 (1996).

[9] The L3 Collaboration, Phys. Lett. **B 503**, 503 (2001).

[10] The OPAL Collaboration, Contributed paper to PHOTON 2000, Ambleside, UK, Preprint hep-ex/0010060, 2000.

[11] The ALEPH Collaboration, Eur. Phys. J. **C 28**, 437 (2003).

[12] The L3 Collaboration, Phys. Lett. **B 453**, 83 (1999);
The L3 Collaboration, CERN-EP/2002-012.

[13] The OPAL Collaboration, Eur. Phys. J. **C 16**, 579 (2000).

[14] ZEUS Collaboration, Contributed paper no. 786 to ICHEP 2002, Amsterdam.

[15] ZEUS Collaboration, Eur. Phys. **C 12** (2000) 1, 35.

[16] C.F. Weizsäcker, Z. Phys. **88**, 612 (1934);
E.J. Williams, Phys. Rev. **45**, 729 (1934).

[17] L.N. Lipatov, Sov. J. Nucl. Phys. **20**,95 (1975);
V.N. Gribov and L.Nl Lipatov, Sov. J. Nucl. Phys. **15**, 438 (1972);
G. Altarelli and G. Parisi, Nucl. Phys. **B 126**, 298 (1977);
Yu.L. Dokshitzer, Sov. Phys. JETP **46**, 641 (1977).

[18] CTEQ Coll., H.L. Lai et al., Eur. Phys. J. **C 12**, 375 (2000).

[19] M. Glück, E. Reya, A. Vogt, Phys. Rev. **D 46**, 1973 (1992).

[20] P. Aurenche, J.P. Guillet and M. Fontannaz, Z. Phys. **C 64**, 621 (1994).

[21] M. Cacciari, *ON HEAVY QUARKS PHOTOPRODUCTION AND* $c \to D^*$ *FRAGMENTATION FUNCTIONS*, DESY 97-156, Preprint hep-ph/9708282.

[22] S. Frixione, M. Mangano, P. Nason, G. Ridolfi, Nucl. Phys. **B 412**, 225 (1994).

[23] M. Mangano, P. Nason, G. Ridolfi, Nucl. Phys. **B 373**, 295 (1992).

[24] C. Peterson et al., Phys. Rev. **D 27**, 105 (1983).

[25] P. Nason and C. Oleari, Phys. Lett. **B 447**, 327 (1999);
P. Nason and C. Oleari, Preprint hep-ph/9903541, 1999.

[26] ARGUS Collaboration, H. Albrecht et al., Z. Phys. **C 52**, 353 (1991).

[27] H1 Collaboration, Z. Phys. **C 72**, 593 (1996);
H1 Collaboration, Phys. Lett. **B 528**, 199 (2002).

[28] H1 Collaboration, Nucl. Phys. **B 472**, 32 (1996).

[29] ZEUS Collaboration, Eur .Phys. J. **C 6**, 67 (1999).

[30] M. Cacciari, S. Frixione and P. Nason, JHEP **0103**, 006 (2001).

[31] ZEUS Collaboration, Phys. Lett. **B 565**, 87 (2003).

[32] ZEUS Collaboration., M. Derrick, et al., The ZEUS Detector, Status Report 1993, DESY (1993), available on `http://www-zeus.desy.de/bluebook/bluebook.html`.

[33] B. Foster et al., Nucl. Inst. Meth. **A 338**, 254 (1994).

[34] ZEUS Collaboration, Calorimeter group, U. Behrens et al., Nucl. Inst. Meth. **A 289**, 115 (1990).

[35] A. Savin, *Study of calorimeter noise in the 1996 data.* ZEUS-Note 98-007 (internal ZEUS note), 1998.

[36] ZEUS Luminisity Group, *Luminosity Measurement in the ZEUS Experiment* ZEUS-Note 01-004 (internal ZEUS note), 2001

[37] K. Olkiewicz, A. Eskreys, *Off-line Luminosity Calculation in the ZEUS Experiment in 1997, 1998 and 1999.* ZEUS-Note 99-044 (internal ZEUS note), 1999.

[38] W.H. Smith et al., *The ZEUS Trigger System* ZEUS-Note 89-084, 1989.

[39] R.K. Ellis, W.J. Stirling and B.R. Webber, *QCD and Collider Physics*, Cambridge Monographs on Particle Physics, Nuclear Physics and Cosmology, Vol.8. Cambridge University Press, 1996.

[40] G. Marchesini et al., Comp. Phys. Comm. **67**, 465 (1992);
G. Corcella et al., JHEP **0101**, 010 (2001).

[41] T. Sjöstrand, Comp. Phys. Comm. **82**, 74 (1994).

[42] R. Brun et al., *GEANT 3.13.* CERN DD/EE/84-1, 1987.

[43] Niels Tuning, *ZUFOs: Hadronic final state reconstruction with calorimeter, tracking and backsplash correction* ZEUS-Note 01-021, 2001

[44] F. Jacquet and A. Blondel, *Proceedings of the Study for an ep Facility for Europe*, U. Amaldi (ed.), p.391. Hamburg, Germany (1979). Also in preprint DESY 79/48.

[45] S. Catani, Yu.L. Dokshitzer, M.H. Seymour and B.R. Webber, Nucl. Phys. **B 406**, 187 (1993);
S.D. Ellis and D.E. Soper, Phys. Rev. **D 48**, 3160 (1993).

[46] Particle Data Group, D.E. Groom et al., Phys. Rev. **D 66**, 1 (2002).

[47] L. Gladilin, Preprint hep-ex/9912064, 1999.

[48] H. Abramowicz, A. Caldwell and R. Sinkus, Nucl. Inst. Meth. **A 365**, 508 (1995).

[49] M. Wodarczyk, Measurement of the F_2 structure function of the proton at HERA from 1996 to 1997 ZEUS Data, PhD thesis, University of Wisconsin, 1999.

[50] ZEUS Collaboration, Eur. Phys. J. **C 18**, 625 (2001);
ZEUS Collaboration, Contributed paper no. 785 to ICHEP 2002, Amsterdam.

[51] M. Moritz, C. Cormack, ZEUS internal meeting. 2001.

[52] ZEUS Collaboration, Contributed paper no. 564 to EPS 2003, Aahcen.

[53] The OPAL Collaboration, Z. Phys. **C 67**, 27 (1995).

[54] The OPAL Collaboration, Eur. Phys. J. **C 13**, 1 (2000).

[55] ALEPH Collaboration, Phys. Lett. **B 561**, 213 (2003).

[56] G.M. Briskin, *Diffractive dissociation in ep deep inelastic scattering.*, Ph.D. Thesis, Tel Aviv University, 1998.

[57] W.H. Smith et al., *ZEUS CALORIMETER FIRST LEVEL TRIGGER* ZEUS-Note 89-085, 1989.